

NAVAL POSTGRADUATE SCHOOL

Monterey, California



DISSERTATION

EXPERIMENTAL INVESTIGATION OF LOW SPEED FLOW OVER FLAPPING AIRFOILS AND AIRFOIL COMBINATIONS

by

Osama Mohamed Kamal Mohamed Mahmoud

September 2001

Dissertation Supervisor:

Max F. Platzer

Approved for public release; distribution is unlimited.

REPORT DOCUMENTATION PAGE

Form Approved OMB No. 0704-0188

Public reporting burden for this collection of information is estimated to average 1 hour per response, including the time for reviewing instruction, searching existing data sources, gathering and maintaining the data needed, and completing and reviewing the collection of information. Send comments regarding this burden estimate or any other aspect of this collection of information, including suggestions for reducing this burden, to Washington Headquarters Services, Directorate for Information Operations and Reports, 1215 Jefferson Davis Highway, Suite 1204, Arlington, Va 22202-4302, and to the Office of Management and Budget, Paperwork Reduction Project (0704-0188) Washington DC 20503.

1. AGENCY USE ONLY (<i>Leave blank</i>)	2. REPORT DATE	3. REPORT TYPE AND DATES COVERED	
	September 2001	Doctor's Dissertation	
4. TITLE AND SUBTITLE EXPERIMENTAL INVESTIGATION OF LOW SPEED FLOW OVER FLAPPING AIRFOILS AND AIRFOIL COMBINATIONS		5. FUNDING NUMBERS	
6. AUTHORS Osama Mohamed Kamal Mohamed Mahmoud			
7. PERFORMING ORGANIZATION NAME(S) AND ADDRESS(ES) Naval Postgraduate School Monterey CA 93943-5000		8. PERFORMING ORGANIZATION REPORT NUMBER	
9. SPONSORING/MONITORING AGENCY NAME(S) AND ADDRESS(ES)		10. SPONSORING/MONITORING AGENCY REPORT NUMBER	
11. SUPPLEMENTARY NOTES The views expressed in this thesis are those of the author and do not reflect the official policy or position of the Department of Defense or the U.S. Government.			
12a. DISTRIBUTION/AVAILABILITY STATEMENT Approved for public release; distribution is unlimited.		12b. DISTRIBUTION CODE	
13. ABSTRACT(<i>maximum 200 words</i>) A wind tunnel investigation of low speed flow over flapping airfoils and airfoil combinations was performed using flow visualization and laser Doppler velocimetry. Specifically, three cases were studied: A NACA0014 airfoil oscillating in a sinusoidal plunge mode, A NACA0014 airfoil oscillating in a sinusoidal plunge mode near a ground plane, and two NACA0014 airfoils arranged in a biplane configuration and oscillating in counterphase in a sinusoidal plunge mode. The plunge amplitude-to-airfoil chord ratio was 0.4, the reduced frequency of oscillation was 1.0 and the Reynolds number based on airfoil chord was set at 8760. Conditionally sampled measurements of the axial flow velocity were taken at numerous flow field points providing detailed information about the flow features generated by this type of flapping motion. These measurements were complemented by time-averaged flow field data and by visualization of the instantaneous flow field at various points during the flapping cycle. Furthermore, the thrust generated by the sinusoidal plunge motion was measured with a laser range finder. The results shows that vortex shedding occurs both from the airfoil leading and trailing edge.			
14. SUBJECT TERMS Unsteady flow measurements, LDV, Flapping wings, Airfoil in Ground Effect, Micro Air Vehicles		15. NUMBER OF PAGES	
		16. PRICE CODE	
17. SECURITY CLASSIFICATION OF REPORT Unclassified	18. SECURITY CLASSIFICATION OF THIS PAGE Unclassified	19. SECURITY CLASSIFICATION OF ABSTRACT Unclassified	20. LIMITATION OF ABSTRACT UL

Approved for public release; distribution is unlimited.

**EXPERIMENTAL INVESTIGATION OF LOW SPEED FLOW OVER
FLAPPING AIRFOILS AND AIRFOIL COMBINATIONS**

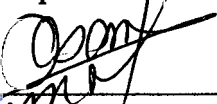
Osama Mohamed Kamal Mohamed Mahmoud
Major, Egyptian Army
B.S., Military Technical College, CAIRO, EGYPT, 1989
M.S., Military Technical College, CAIRO, EGYPT, 1994

Submitted in partial fulfillment of the
requirements for the degree of

**DOCTOR OF PHILOSOPHY IN AERONAUTICAL AND
ASTRONAUTICAL ENGINEERING**

from the

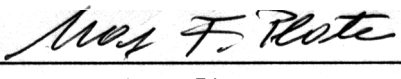
NAVAL POSTGRADUATE SCHOOL
September 2001



Author:

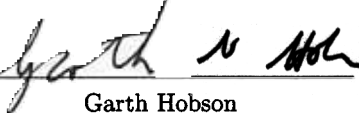
 Osama Mohamed Kamal Mohamed Mahmoud

Approved by:

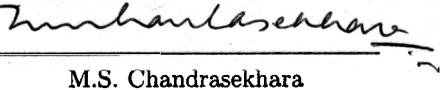
 Max F. Platzer

Professor of Aeronautics

Dissertation Supervisor and Committee Chair

 Garth Hobson

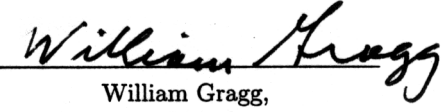
Professor of Aeronautics

 M.S. Chandrasekhara

Professor of Aeronautics

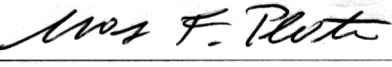
 Oscar Biblarz

Professor of Aeronautics

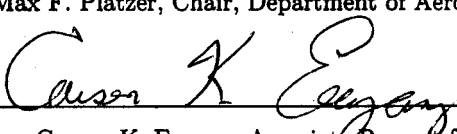
 William Gragg,

Professor of Mathematics

Approved by:

 Max F. Platzer, Chair, Department of Aeronautics & Astronautics

Approved by:

 Carson K. Eoyang, Associate Provost for Academic Affairs

ABSTRACT

A wind tunnel investigation of low speed flow over flapping airfoils and airfoil combinations was performed using flow visualization and laser Doppler velocimetry. Specifically, three cases were studied: A NACA0014 airfoil oscillating in a sinusoidal plunge mode, A NACA0014 airfoil oscillating in a sinusoidal plunge mode near a ground plane, and two NACA0014 airfoils arranged in a biplane configuration and oscillating in counterphase in a sinusoidal plunge mode. The plunge amplitude-to-airfoil chord ratio was 0.4, the reduced frequency of oscillation was 1.0 and the Reynolds number based on airfoil chord was set at 8760.

Conditionally sampled measurements of the axial flow velocity were taken at numerous flow field points providing detailed information about the flow features generated by this type of flapping motion. These measurements were complemented by time-averaged flow field data and by visualization of the instantaneous flow field at various points during the flapping cycle. Furthermore, the thrust generated by the sinusoidal plunge motion was measured with a laser range finder. The results shows that vortex shedding occurs both from the airfoil leading and trailing edge.

TABLE OF CONTENTS

I.	INTRODUCTION	1
	A. BRIEF HISTORY OF FLAPPING WING RESEARCH	1
	B. THE PHYSICS OF THRUST GENERATION DUE TO WING FLAPPING	4
	C. THE PHENOMENON OF DYNAMIC STALL	6
	D. MOTIVATION FOR THIS INVESTIGATION	7
II.	COMPUTATIONAL ANALYSIS	9
	A. NAVIER-STOKES ANALYSIS	9
	B. BIPLANE CONFIGURATION	9
	C. SINGLE FLAPPING WING IN PURE PLUNGE	12
III.	EXPERIMENTAL TOOLS	33
	A. GENERAL DESCRIPTION OF THE SYSTEM	33
	1. Wind Tunnel Description	33
	2. Pitot Static Tube	33
	3. Laser Doppler Velocimetry (LDV)	34
	4. LDV Apparatus	35
	5. Flow Seeding	36
	6. Model Description	36
	B. THE THRUST MEASURING TECHNIQUE	40
	C. UNSTEADY FLOW MEASUREMENTS	41

D. TRIGGERING SIGNAL	41
E. CONVENTIONS	42
IV. FLOW VISUALIZATION	45
A. SMOKE WIRE SYSTEM	45
B. CASE STUDIES	46
1. NACA0014 Airfoil At Zero Angle Of Attack	46
2. NACA0014 Airfoil at 4° Angle Of Attack	48
3. Biplane Configuration	48
C. RESULTS	52
V. EXPERIMENTAL RESULTS	59
A. THRUST MEASUREMENTS	59
B. STEADY FLOW MEASUREMENTS	59
1. First Case: $U=2$ m/s, $\alpha = 0^\circ$	62
2. Second Case: $U=5$ m/s, $\alpha = 0^\circ$	62
3. Third Case: $U=2$ m/s, $\alpha = 4^\circ$	62
C. UNSTEADY FLOW MEASUREMENTS	70
1. Biplane Configuration	70
2. Wing in Ground Effect	95
3. Single Wing Configuration	108
VI. ANALYSIS OF THE EXPERIMENTAL RESULTS	117
A. STEADY FLOW MEASUREMENTS	117
B. THRUST MEASUREMENTS	118
C. FLAPPING BIPLANE FLOW MEASUREMENTS	118

D. FLOW MEASUREMENTS FOR FLAPPING AIRFOIL IN GROUND EFFECT	121
E. SINGLE FLAPPING AIRFOIL FLOW MEASUREMENTS .	121
VII. CONCLUSIONS AND RECOMMENDATIONS	129
APPENDIX A: CALIBRATION OF WIND TUNNEL	131
APPENDIX B: UNSTEADY MEASUREMENTS FOR THE BIPLANE CASE	145
APPENDIX C: UNSTEADY MEASUREMENTS FOR SINGLE FLAPPING WING	155
APPENDIX D: UNSTEADY MEASUREMENTS FOR THE FLAPPING WING IN PRESENCE OF GROUND PLANE	161
LIST OF REFERENCES	171
INITIAL DISTRIBUTION LIST	175

LIST OF FIGURES

1.1 Thrust-Indicative Wake Pattern, after [12]	5
1.2 Drag-Indicative Wake Pattern, after [12]	6
2.1 The Flapping Motion in the Biplane Configuration	13
2.2 Vorticity and Pressure Distribution for Biplane Configuration, NACA 0014, $\alpha = 0^\circ, M_\infty = 0.1, k = 1, Re_\infty = 1 \times 10^4, \Phi = 0^\circ$	14
2.3 Vorticity and Pressure Distribution for Biplane Configuration, NACA 0014, $\alpha = 0^\circ, M_\infty = 0.1, k = 1, Re_\infty = 1 \times 10^4, \Phi = 45^\circ$	15
2.4 Vorticity and Pressure Distribution for Biplane Configuration, NACA 0014, $\alpha = 0^\circ, M_\infty = 0.1, k = 1, Re_\infty = 1 \times 10^4, \Phi = 90^\circ$	16
2.5 Vorticity and Pressure Distribution for Biplane Configuration, NACA 0014, $\alpha = 0^\circ, M_\infty = 0.1, k = 1, Re_\infty = 1 \times 10^4, \Phi = 135^\circ$	17
2.6 Vorticity and Pressure Distribution for Biplane Configuration, NACA 0014, $\alpha = 0^\circ, M_\infty = 0.1, k = 1, Re_\infty = 1 \times 10^4, \Phi = 180^\circ$	18
2.7 Vorticity and Pressure Distribution for Biplane Configuration, NACA 0014, $\alpha = 0^\circ, M_\infty = 0.1, k = 1, Re_\infty = 1 \times 10^4, \Phi = 225^\circ$	19
2.8 Vorticity and Pressure Distribution for Biplane Configuration, NACA 0014, $\alpha = 0^\circ, M_\infty = 0.1, k = 1, Re_\infty = 1 \times 10^4, \Phi = 270^\circ$	20
2.9 Vorticity and Pressure Distribution for Biplane Configuration, NACA 0014, $\alpha = 0^\circ, M_\infty = 0.1, k = 1, Re_\infty = 1 \times 10^4, \Phi = 315^\circ$	21
2.10 Vorticity and Pressure Around a Single Wing in Pure Plunge, NACA 0014, $\alpha = 0^\circ, M_\infty = 0.1, k = 1, Re_\infty = 1 \times 10^4, \Phi = 0^\circ$	24

2.11 Vorticity and Pressure Around a Single Wing in Pure Plunge, NACA 0014, $\alpha = 0^\circ, M_\infty = 0.1, k = 1, Re_\infty = 1 \times 10^4, \Phi = 45^\circ$	25
2.12 Vorticity and Pressure Around a Single Wing in Pure Plunge, NACA 0014, $\alpha = 0^\circ, M_\infty = 0.1, k = 1, Re_\infty = 1 \times 10^4, \Phi = 90^\circ$	26
2.13 Vorticity and Pressure Around a Single Wing in Pure Plunge, NACA 0014, $\alpha = 0^\circ, M_\infty = 0.1, k = 1, Re_\infty = 1 \times 10^4, \Phi = 135^\circ$	27
2.14 Vorticity and Pressure Around a Single Wing in Pure Plunge, NACA 0014, $\alpha = 0^\circ, M_\infty = 0.1, k = 1, Re_\infty = 1 \times 10^4, \Phi = 180^\circ$	28
2.15 Vorticity and Pressure Around a Single Wing in Pure Plunge, NACA 0014, $\alpha = 0^\circ, M_\infty = 0.1, k = 1, Re_\infty = 1 \times 10^4, \Phi = 225^\circ$	29
2.16 Vorticity and Pressure Around a Single Wing in Pure Plunge, NACA 0014, $\alpha = 0^\circ, M_\infty = 0.1, k = 1, Re_\infty = 1 \times 10^4, \Phi = 270^\circ$	30
2.17 Vorticity and Pressure Around a Single Wing in Pure Plunge, NACA 0014, $\alpha = 0^\circ, M_\infty = 0.1, k = 1, Re_\infty = 1 \times 10^4, \Phi = 315^\circ$	31
3.1 Wind Tunnel Schematic Diagram	34
3.2 Isometric View of Upturned Flapping Mechanism.	37
3.3 Top View of Flapping Mechanism.	38
3.4 Profile View of Flapping Mechanism.	38
3.5 Thrust measurement arrangement	41
3.6 Trigger signal and the plunge motion	43
4.1 Smoke Wire Arrangement With the Copper Nodes on the Smoke Wire . .	47
4.2 Flow Around NACA0014 at $\alpha = 0^\circ, U_\infty = 2.24 \text{ m/s}, \text{Re}=10000$	48
4.3 Vortex Shedding Around NACA0014 at $\alpha = 4^\circ, U_\infty = 2.24 \text{ m/s}, \text{Re}=10000$	49

4.4 (a) Vortex Shedding Around Biplane with Minimum Distance between the Two Wings, Re=10000. The Time Step Between Frames =1/30 sec	50
4.5 (b) Vortex Shedding Around Biplane with Minimum Distance between the Two Wings, Re=10000, with time step=1/30 sec	51
4.6 Vortex Shedding Around Biplane with Maximum Distance between the Wings, Re=10000	52
4.7 Vortex Shedding Around Biplane During Flapping, $\Phi = 0^\circ$ and $\Phi = 30^\circ$, k=1, U=2.24 m/s, Re=10000	53
4.8 Vortex Shedding Around Biplane During Flapping, $\Phi = 135^\circ$ and $\Phi = 180^\circ$, k=1, U=2.24 m/s, Re=10000	54
4.9 Vortex Shedding Around Biplane During Flapping, $\Phi = 225^\circ$ and $\Phi = 360^\circ$, k=1, U=2.24 m/s, Re=10000	55
4.10 Vortex Shedding Around Biplane During Flapping, $\Phi = 0^\circ$, $\Phi = 45^\circ$ and $\Phi = 135^\circ$, k=1, U=2.24 m/s, Re=10000	56
4.11 Vortex Shedding Around Biplane During Flapping, $\Phi = 180^\circ$, $\Phi = 225^\circ$ and $\Phi = 270^\circ$, k=1, U=2.24 m/s, Re=10000	57
5.1 Thrust coefficient for single flapping wing in pure plunge with error included as error bar, $h=0.4C$,	60
5.2 Thrust coefficient versus reduced frequency, k, for single flapping wing in pure plunge, with measurements error included as error bar, $h=0.4C$	61
5.3 Axial Velocity at U=2 m/s and $\alpha = 0^\circ$	63
5.4 Velocity Profile at Different Axial Locations over NACA0014, U=2 m/s and $\alpha = 0^\circ$	64
5.5 Velocity Profile over NACA0014 at U=2 m/s and $\alpha = 0^\circ$	65

5.6 Nondimensional Turbulence Intensity over NACA0014 at $U=2$ m/s and $\alpha = 0^\circ$	66
5.7 Nondimensional Axial Velocity Component at $U=5$ m/s and $\alpha = 0^\circ$	67
5.8 Nondimensional Axial Velocity Component at $U=5$ m/s and $\alpha = 0^\circ$	68
5.9 Nondimensional Turbulence Intensity at $U=5$ m/s and $\alpha = 0^\circ$	69
5.10 Axial Velocity at $U_\infty = 2m/s$ and $\alpha = 4^\circ$	71
5.11 Axial Velocity Profile at Measured Axial Locations, $U_\infty = 2m/s$ and $\alpha = 4^\circ$	72
5.12 Axial Velocity Profile at $U_\infty = 2m/s$ and $\alpha = 4^\circ$	73
5.13 Normalized Turbulence Intensity at $U_\infty = 2m/s$ and $\alpha = 4^\circ$	74
5.14 Average Velocity Profile,Biplane Configuration	75
5.15 Measured Axial Velocity Component, u , at $X/C=-0.25$	76
5.16 Nondimensional turbulence intensity at $X/C=-0.25$	77
5.17 Measured Axial Velocity Component, u , at $X/C=0$, the Leading Edge	78
5.18 Nondimensional Turbulence Intensity at the Leading Edge	79
5.19 Measured Axial Velocity Component, u , at $X/C=0.25$	80
5.20 Nondimensional Turbulence Intensity at $X/C=0.25$	81
5.21 The Measured Velocity over the Complete Domain at $X/C = 0.5$	82
5.22 Nondimensional Turbulence Intensity, Ti/U_∞ at $X/C = 0.5$	83
5.23 The Measured Axial Velocity Component over the Complete Domain at $X/C=0.75$	84
5.24 Nondimensional Turbulence Intensity at $X/C=0.75$	85
5.25 Measured Velocity over the Complete Domain	86
5.26 Nondimensional Turbulence Intensity	87
5.27 Measured Velocity over the Complete Domain at $X/C = 1.5$	88

5.27 Nondimensional Turbulence Intensity at $X/C = 1.5$	89
5.28 Measured Velocity over the Complete Domain at $X/C=2.0$	90
5.29 Nondimensional Turbulence Intensity	91
5.30 Measured Velocity over the Complete Domain at $X/C = 3.0$	92
5.33 Flow Around NACA0014 in the Upper Flapping Stroke for Biplane Configuration	93
5.34 Flow Around NACA0014 in the Lower Flapping Stroke for Biplane Configuration	94
5.35 Boundary Layer over the Ground Plane	96
5.36 Nondimensional Axial Velocity at $X/C=-0.25$ for Flapping Wing in Presence of Ground Effect	98
5.37 Flapping Wing in Presence of Ground Effect, $X/C=0$	99
5.38 Flapping Wing in Presence of Ground Effect, $X/C=0.25$	100
5.39 Flapping Wing in Presence of Ground Effect, $X/C=0.5$	101
5.40 Flapping Wing in Presence of Ground Effect, $X/C=0.75$	102
5.41 Flapping Wing in Presence of Ground Effect, $X/C=1$	103
5.42 Flapping Wing in Presence of Ground Effect, $X/C=1.5$	104
5.43 Flapping Wing in Presence of Ground Effect at $X/C=2.0$	105
5.44 Flapping Wing in Ground Plane During Upstroke.	106
5.45 Flapping Wing in Ground Plane During Downstroke.	107
5.46 Single Flapping Wing During Upstroke, $k=1$, $u=2[m/s]$, $f=5[Hz]$, $Re=8760$	109
5.47 Single Flapping Wing During Downstroke, $k=1$, $u=2[m/s]$, $f=5[Hz]$, $Re=8760$	

5.48 Average Velocity Profile and the Associated Turbulence Intensity Around Single Flapping Wing, $k=1$, $u=2$ m/s, $f=5$ Hz	111
5.49 Single Flapping Wing at $X/C=-0.2$, $k=1$, $u=2$ [m/s], $f=5$ [Hz], $Re=8760$. .	112
5.50 Single Flapping Wing at $X/C=0.0$, $k=1$, $u=2$ [m/s], $f=5$ [Hz], $Re=8760$. .	113
5.51 Single Flapping Wing at $X/C=0.2$, $k=1$, $u=2$ [m/s], $f=5$ [Hz], $Re=8760$. .	114
5.52 Single Flapping Wing at $X/C = 0.6$, $k=1$, $u=2$ m/s, $f=5$ Hz, $Re=8760$. .	115
5.53 Single Flapping Wing at $X/C = 1.0$, $k=1$, $u=2$ m/s, $f=5$ Hz, $Re=8760$. .	116
A.1 Locations Probed by The Pitot Tube Along The Wind Tunnel Test Section	
A.2 Nondimensional Axial Velocity Obtained by the Pitot Tube	134
A.3 Nondimensional Axial Velocity Component Measured by Pitot Tube at Dif- ferent Axial Locations	136
A.4 Nondimensional Axial Velocity Component Measured by Pitot Tube at Dif- ferent lateral Locations	137
A.5 Nondimensional Axial Velocity Component Measured by Pitot Tube at Dif- ferent Vertical Locations	138
A.6 Measured Velocity	139
A.7 Turbulence Intensity %	139
A.8 The Scanned Plane	141
A.9 u/U_∞	141
A.10 u/U_∞	142
A.11 Turbulence Intensity	143
A.12 Measured Axial Velocity Component, u , at Different Locations.	144
B.1 Measured Axial Velocity, u , at $X/C=-0.25$	

B.2	Measured Axial Velocity, u , at the leading edge	147
B.3	Measured Axial Velocity, u , at $X/C=0.25$	148
B.4	Measured Axial Velocity, u , at $X/C = 0.5$	149
B.5	Measured Axial Velocity, u , at $X/C = 0.75$	150
B.6	Measured Axial Velocity, u , at $X/C = 1.0$	151
B.7	Measured Axial Velocity, u , at $X/C = 1.5$	152
B.8	Measured Axial Velocity, u , at $X/C=2.0$	153
B.9	Measured Axial Velocity, u , at $X/C=3.0$	154
C.1	Single Flapping Wing at $X/C=-0.2$, $k=1$, $u=2[m/s]$, $f=5[Hz]$, $Re=8760$. .	156
C.2	Single Flapping Wing at $X/C=0$, $k=1$, $u=2[m/s]$, $f=5[Hz]$, $Re=8760$. .	157
C.3	Single Flapping Wing at $X/C=0.2$, $k=1$, $u=2[m/s]$, $f=5[Hz]$, $Re=8760$. .	158
C.4	Single Flapping Wing at $X/C=0.6$, $k=1$, $u=2[m/s]$, $f=5[Hz]$, $Re=8760$. .	159
C.5	Single Flapping Wing at $X/C=1.0$, $k=1$, $u=2[m/s]$, $f=5[Hz]$, $Re=8760$. .	160
D.1	Flapping Wing in Ground Effect at $X/C=-0.25$	162
D.2	Flapping Wing in Ground Effect at $X/C=0$	163
D.3	Flapping Wing in Ground Effect at $X/C=0.25$	164
D.4	Flapping Wing in Ground Effect at $X/C=0.5$	165
D.5	Flapping Wing in Ground Effect at $X/C=0.75$	166
D.6	Flapping Wing in Ground Effect at $X/C=1.0$	167
D.7	Flapping Wing in Ground Effect at $X/C=1.5$	168
D.8	Flapping Wing in Ground Effect at $X/C=2$	169

LIST OF TABLES

3.1 Flapping Model Parameters	39
4.1 Shedding Frequency for Flapping Wing in Biplane Configuration	58
5.1 Biplane Configuration	75
5.2 Flapping Wing in Ground Effect	97
5.3 Single Flapping Wing	108
6.1 Measured Axial Velocity Component, u/U_∞ , at Different Plunge Phase Angle, Φ , $Z/C = -0.7$, $k=1$, $Re=8760$, $h=0.4$, $X/C=-0.25$	123
6.2 Measured Axial Velocity Component, u/U_∞ , at Different Plunge Phase Angle, Φ , $Z/C = -0.7$, $k=1$, $Re=8760$, $h=0.4$, $X/C=0$, Leading Edge	124
6.3 Measured Axial Velocity Component, u/U_∞ , at Different Plunge Phase Angle, Φ , $Z/C = -0.7$, $k=1$, $Re=8760$, $h=0.4$, $X/C=0.25$	125
6.4 Measured Axial Velocity Component, u/U_∞ , at Different Plunge Phase Angle, Φ , $Z/C = -0.7$, $k=1$, $Re=8760$, $h=0.4$, $X/C=0.5$	126
6.5 Measured Axial Velocity Component, u/U_∞ , at Different Plunge Phase Angle, Φ , $Z/C = -0.7$, $k=1$, $Re=8760$, $h=0.4$, $X/C=0.75$	127
6.6 Measured Axial Velocity Component, u/U_∞ , at Different Plunge Phase Angle, Φ , $Z/C = -0.7$, $k=1$, $Re=8760$, $h=0.4$, $X/C=1$, Trailing Edge	128
A.1 Wind Tunnel Calibration	132
A.2 Standard Deviation for the Measured Axial Velocity Component	142

LIST OF ABBREVIATIONS, ACRONYMS, AND SYMBOLS

CFD = Computational fluid dynamics

LDV = Laser Doppler Velocimetry

RMR = Rotary Machinery Resolver

Re = Reynolds Number

α = Angle of attack (geometric)

Φ = Plunge phase angle, deg

h = Plunge amplitude

k = Reduced frequency $\omega C/U_\infty$

C = Airfoil chord

f = Flapping frequency, Hz

u = Axial component of velocity

X = Distance in axial direction.

Y = Distance in lateral direction

ACKNOWLEDGMENT

The author wishes to express his deep appreciation and gratitude to Prof. Max Platzer, for his encouragement during this research study. His continuous guidance and inspiration were critical to the completion of this study.

Prof. Kevin D. Jones contributed a lot of technical advice and direct assistance with the experimental work.

Many thanks to Prof. M.S. Chandrasekhara, whose brilliant experimental work was a guide post for the author. His critical guidance and insightful critiques were essential to my progress in this study.

This work would have been impossible without Prof. Garth Hobson's loan of the flow atomizer, and his help installing the Rotary Machinery Resolver. His experience allowed us to fine tune the experiment.

Finally, the author wishes to dedicate this work to his mother and father for their love, care, guidance and continuous support.

I. INTRODUCTION

A. BRIEF HISTORY OF FLAPPING WING RESEARCH

The desire “to fly like the birds” is almost as old as humanity itself. Indeed, Leonardo da Vinci was so fascinated by the flapping flight phenomenon that he made many sketches of bats and summarized his flapping wing studies in a book manuscript. However, little progress was made during the following centuries until the German flight pioneer Otto Lilienthal undertook systematic glider flight tests with flapping wings and published his findings in 1889. Knoller [17] and Betz [2] appear to have been the first ones to offer an explanation for the development of thrust due to wing flapping. Katzmayr [15] first presented wind tunnel experiments which showed that a wing mounted in an oscillating air flow experienced a thrust force. Birnbaum [3] first succeeded to develop a theory which correctly predicted the lift and thrust forces developed by flapping wings. In the following decades Kuessner and Theodorsen [27] were able to eliminate the restriction of Birnbaum’s theory from low-frequency oscillations. This Theodorsen-Kuessner oscillatory thin-airfoil theory thereafter became the standard tool to analyze airfoil flutter problems. Garrick [8], applied Theodorsen’s theory to the analysis of flapping wing propulsion, which remains the classical reference work to this day.

The rapid development of fixed-wing airplanes in conjunction with the obvious mechanical complications introduced by flapping wings soon discouraged the further development of ornithopters. Indeed, the demonstration of a successful manned ornithopter is still an aeronautical engineering challenge which is being pursued by flapping wing enthusiasts,

such as DeLaurier [6] and his team at the University of Toronto, among others. Further discouragement came from Garrick's results which showed that flapping wings have low propulsion efficiencies unless oscillated at very low frequencies. However, Schmidt [25] tried to overcome this concern during and after World War II by developing a device which he called "wave propeller". He argued that the vortices generated by a flapping wing carry energy which can be converted into additional thrust by a wing mounted in the wake of a flapping wing. The aft-wing thus is exposed to an oscillatory flow which generates thrust by virtue of the Katzmayr effect. Schmidt claimed to have achieved wave propeller efficiencies comparable to conventional propeller efficiencies.

Nevertheless, the practical development potential of flapping wings for either pure propulsion or as an integrated lift/propulsion system was regarded as unattractive until very recently. Flapping wing studies therefore largely remained restricted to scientists interested in bird flight or fish propulsion problems.

An unexpected revival of interest in the systematic study of flapping wing flight phenomena occurred only a few years ago with the announcement of a major initiative by the Defense Advanced Research Projects Agency (DARPA) to encourage the development of micro-air vehicles (MAVs). The use of flapping wings for vehicles with dimensions not exceeding six inches in length or span is an obvious option because of the low efficiency of conventional propellers at low Reynolds number. Therefore, this DARPA initiative sparked a number of investigations which have been reviewed in June 2000 at a special symposium held at the University of Notre Dame to be published by AIAA in 2001. This publication is referred to for a detailed review of the current status of these studies and we therefore limit ourselves to a brief description of the major developments in recent years.

Of special note is the replacement of the Theodorsen-Kuessner oscillatory thin-airfoil

theory by an approach which enables the computation of incompressible potential flow past oscillating airfoils of arbitrary shape. This is being accomplished by the placement of sources and vortices on the airfoil surface rather than along the chord line. This so-called panel method was pioneered by Giesing [9], who generalized the method of Hess and Smith [10], for steady airfoil flow. It was further developed at the Naval Postgraduate School, as described by Teng [26], Platzer et al [22], and Jones et al [16]. The rapid increase in computer power over the past few years also made it possible to apply Navier-Stokes computations to the analysis of flapping airfoil aerodynamics, thus making it possible to compute strong viscous effects, as shown by Tuncer and Platzer [30], Tuncer et al [29], Tuncer and Platzer [28], Isogai et al [11], and Ramamurti and Sandberg [24]. Also, a number of investigators succeeded to analyze three-dimensional effects. Of special note here is the early work of Lan [19], who applied the vortex lattice method and showed that the interaction between a flapping fore and aft-wing can be quite beneficial. Peng-fei Liu [20] developed a three-dimensional panel code and, most recently, Neef (private communications) even succeeded to analyze three-dimensional flapping wing effects using a Navier-Stokes code. Experimentally, Freymuth provided valuable flow visualizations of the vortical wakes generated by plunging or pitching airfoils. Jones et al [12] and Lai and Platzer [18] showed in their flow visualization studies that the vortical wake becomes asymmetric as soon as the reduced plunge velocity exceeds a critical value. Jones et al [16], and Anderson et al [1] made thrust measurements which provide information about the dependence on flapping frequency and amplitude.

B. THE PHYSICS OF THRUST GENERATION DUE TO WING FLAPPING

As already mentioned, Knoller [17] and Betz [2] were the first ones to offer an explanation for the birds' ability to generate a propulsive force by means of flapping their wings. Consider the airfoil in sinusoidal flapping while also flying forward. As the airfoil moves through its mean position during the downward stroke, it is effectively exposed to a flow with positive angle of incidence. Similarly, it sees a negative incidence angle during the upstroke. If, for simplicity, the resulting aerodynamic force is assumed to be essentially perpendicular to the instantaneous approach flow angle, then decomposition into a force component parallel to the flight velocity vector will produce a small sinusoidally varying thrust force.

It is understood that this explanation is greatly simplified. The actual flow which is produced is considerably more complicated, even if only attached inviscid flow is assumed. As is well known, every change in incidence will produce a starting vortex which is shed from the trailing edge. Therefore, a sinusoidally oscillating airfoil will generate a vortex street behind the airfoil. This phenomenon can be simulated quite easily with the above mentioned unsteady panel codes. The vortex street consists of an upper row of counterclockwise vortices and a row of lower clockwise vortices Fig. 1.1. This vortex street therefore is just the opposite of the well known Karman vortex street. If time-averaging is applied at some location cutting the wake in the normal direction to the free-stream a jet profile is obtained, whereas the same operation applied to the Karman vortex street would produce a wake profile, Fig. 1.2 . The vortex street produced by the flapping foil in effect produces a jet flow. This is to be expected since the thrust experienced by the airfoil must be found

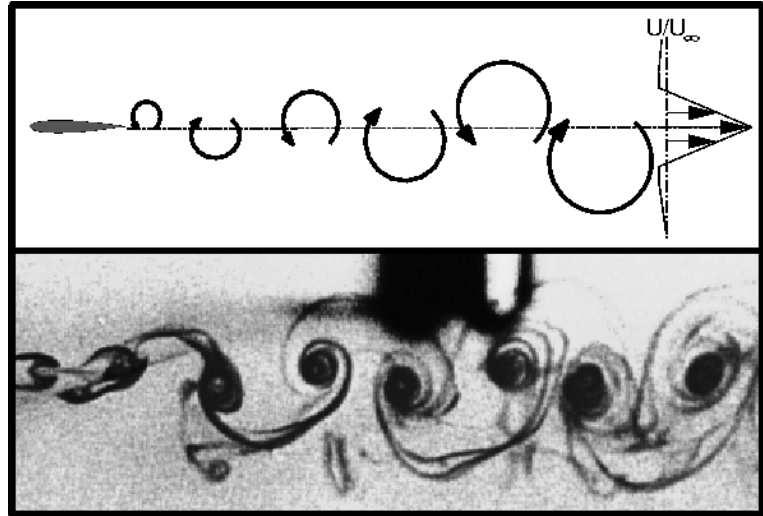


Figure 1.1. Thrust-Indicative Wake Pattern, after [12]

as momentum increase in the fluid. As shown by Jones et al [12], this jet flow can indeed be measured and is in good agreement with the panel code predictions. Jones et al also found, however, that the symmetric vortex street switches into a deflected street as soon as the non-dimensional plunge velocity exceeds a critical value, again in good agreement between the flow visualizations and the panel code predictions.

This encouraging agreement between the measurements and the inviscid flow predictions of Jones et al [16] might give the impression that the physics of flapping airfoils is understood reasonably well and that the prediction of the achievable thrust can be made with considerable confidence. Unfortunately, even disregarding the three-dimensional flow effects introduced by finite-span wings, the range of validity of inviscid flow predictions is severely limited by the onset of dynamic stall. This seems to be particularly true at the low Reynolds numbers typically required for micro-air vehicles.

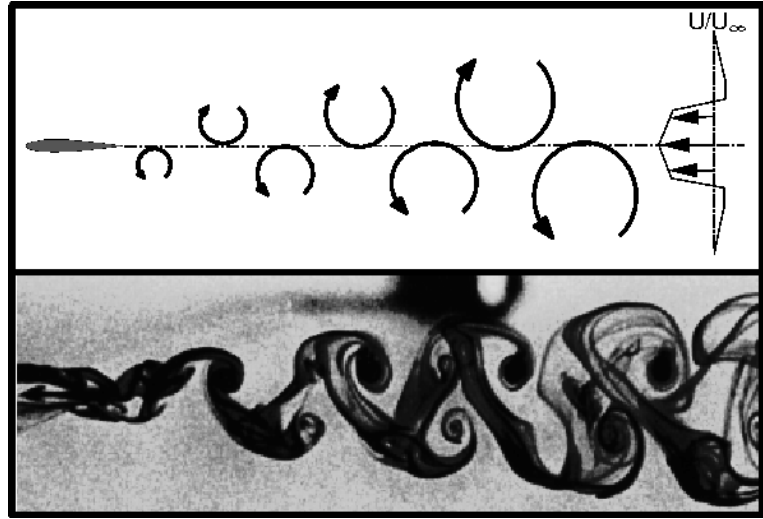


Figure 1.2. Drag-Indicative Wake Pattern, after [12]

C. THE PHENOMENON OF DYNAMIC STALL

Helicopter aerodynamicists are quite familiar with the phenomenon of dynamic stall. A helicopter blade in forward flight can experience dynamic stall while it is in the so-called retreating blade position, exposing the blade to high incidence angles. For this reason, the aerodynamics of pitching airfoils experiencing dynamic stall has been studied to a considerable extent both experimentally and computationally. The current state-of-the-art can be found in the recent review papers of Carr and Chandrasekhara [4], and Ekaterinaris and Platzer [7]. During the downstroke, a stall vortex forms near the leading edge which moves over the upper surface and eventually leaves the airfoil, strongly interacting with the trailing edge vortex which forms at the trailing edge. As soon as the stall vortex leaves the airfoil, rapid lift loss and changes in pitching moment occur, leading to a severe hysteresis loop in lift, drag and pitching moment.

Most dynamic stall studies have been limited to pitching airfoils because of the importance of this motion for helicopter blades. However, for thrust generation it is well

known (and has been shown in detail by Jones and Platzer [14]) that a pure plunging or a combined pitch/plunge motion is required in order to produce significant thrust forces. Very few experiments involving dynamic stall due to pure plunge have as yet been carried out, but several Navier-Stokes computations have been completed by Tuncer and Platzer, Isogai et al, and Ramamurti and Sandberg, as already noted above. These computations clearly show the possibility of dynamic stall for values of flapping frequency, amplitude, and Reynolds number typical for MAV flight.

D. MOTIVATION FOR THIS INVESTIGATION

Because of the very limited experimental information available for plunging airfoils it is the objective of this investigation to conduct detailed experiments which provide flow visualization and quantitative measurements of the flow near and downstream of flapping airfoils. As shown by Jones and Platzer [14], the performance of flapping airfoils is enhanced if two airfoils are flapping in counterphase, effectively producing the favorable ground effect experienced by birds flying near the water surface. Therefore, three experiments are carried out,

1. Two airfoils plunging sinusoidally in counterphase.
2. A single airfoil plunging sinusoidally near a ground plane.
3. A single airfoil plunging sinusoidally.

so that the differences caused by these three configurations can be understood in sufficient detail.

THIS PAGE INTENTIONALLY LEFT BLANK

II. COMPUTATIONAL ANALYSIS

A. NAVIER-STOKES ANALYSIS

In the companion computational study by Castro [5], a thin-layer Navier-Stokes code was used to compute the two dimensional flow over flapping airfoils. Two cases of his study were investigated in the present work, with Laser Doppler Velocimetry (LDV) and flow visualization. These two cases are:

- Biplane configuration in pure plunge motion, $k=1$, $M_\infty = 0.1$, $Re = 10000$, $\alpha = 0^\circ$,
 $h=0.4$
- Single wing configuration in pure plunge motion, $k=1$, $M_\infty = 0.1$, $Re = 10000$, $\alpha = 0^\circ$,
 $h=0.4$

His results are introduced in the next two sections, mainly to provide some insight into the basic flow features which one expects to find in the experiments. However, it is important to recall that the computations are based on a fully laminar flow assumption.

B. BIPLANE CONFIGURATION

The wings' flapping motion is presented in Fig. 2.1. In the biplane case, the flow behavior around the upper airfoil is the same as around the lower one. It is antisymmetric about the plane of symmetry. Hence, from now on, the flow around the upper airfoil will be the one that will be described and the word airfoil will mean the upper one.

The non-dimensional velocity around the biplane configuration is presented as vec-

tors at 8 different plunge phase angles Φ , namely 0° , 45° , 90° , 135° , 180° , 225° , 270° , and 315° . The non-dimensional velocity is presented as vectors, while the vorticity and the pressure distribution are presented as flood contours in Fig. 2.2, Fig. 2.3, Fig. 2.4, Fig. 2.5, Fig. 2.6, Fig. 2.7, Fig. 2.8, and Fig. 2.9.

The flapping cycle starts at $\Phi = 0^\circ$, Fig. 2.2. The wing is in the uppermost position and starts to move toward the plane of symmetry. At this position, $\Phi = 0^\circ$, the flow near the lower surface of the airfoil has two counter-clockwise vortices surrounding a clockwise vortex. These vortices were generated during the upstroke, as will be explained in more detail. The velocity near the upper surface is close to the freestream velocity. In the near wake region (half period, since $k=1$, $c=1$, hence $L = 2\pi$), the velocity decreases. Further downstream there is a clockwise vortex which originated from the dynamic stall vortex shed during the previous cycle.

As the airfoil moves down to $\Phi = 45^\circ$, the effective angle of attack starts to increase on the upper surface causing a small pressure drop, Fig. 2.3. Also, the stagnation point moves to the lower surface close to the leading edge. Meanwhile, the three vortices which were sitting near the lower surface start to get shed downstream, such that the first one moves to the near wake region causing the velocity to increase just behind the trailing edge. The pressure increases between the two airfoils as the velocity decreases. Meanwhile, in the far wake region the vortex keeps moving downstream.

The airfoil reaches the mean flapping position at $\Phi = 90^\circ$, Fig. 2.4. By then all the vortices are completely shed downstream away from the airfoil surface. The effective angle of attack increases and the stagnation point moves further downstream at the lower surface. The velocity increases on the upper surface within the first quarter chord and a vortex starts to be formed. The pressure increases between the two airfoils causing a velocity increase

just behind the trailing edge which helps to shed the vortices into the near wake region.

In the far wake, the velocity starts to decrease below the free stream value and a region of higher pressure starts to be generated near the plane of symmetry.

As the airfoil keeps moving down, $\Phi = 135^\circ$, the vortex generated on the upper surface becomes stronger, Fig. 2.5. As a matter of fact, four vortices start to develop, two clockwise and one counter-clockwise within the first half chord. A smaller clockwise vortex is generated close to the trailing edge. The velocity decreases on the lower surface and the pressure increases to cover an area which extends to half chord behind the trailing edge.

As the airfoil reaches the lowest position in the flapping stroke, $\Phi = 180^\circ$, Fig. 2.6, the four vortices on the upper surface become fully developed and the airfoil is in complete dynamic stall. The velocity between the two airfoils is slightly higher than the free stream value. In both the near and far wake regions, two vortices can still clearly be seen. The stagnation point has moved forward toward the leading edge but is still on the lower surface. The pressure is a little lower than the free stream value.

The down stroke ends at $\Phi = 180^\circ$.

As the airfoil starts to move up, the effective angle of attack switches from positive to negative values. Hence, the stagnation point starts to move to the upper surface which can be seen at $\Phi = 225^\circ$, Fig. 2.7. The vortices on the upper surface start to be shed downstream clearing the trailing edge. The velocity increases in the area between the two airfoils causing a drop in pressure. In the near wake region, the shed clockwise vortex behind the trailing edge causes a drop in velocity near the plane of symmetry. The velocity starts to increase gradually toward the far wake.

As the airfoil approaches the mean position during the upstroke, $\Phi = 270^\circ$, Fig. 2.8, the effective angle of attack increases causing the velocity to increase near the lower surface.

A shed clockwise vortex is seen in the near wake which creates a low pressure zone that draws the flow toward it. Meanwhile, this vortex slows the flow velocity dramatically near the plane of symmetry. As the flow approaches the far wake, the velocity increases slightly near the plane of symmetry, but away from the plane of symmetry the flow direction changes in a wavy form due to the existence of the vortex at one chord behind the airfoil and the shed one at the 4.5 chord length.

As the airfoil moves upward during the upstroke, the effective angle of attack keeps increasing. This becomes obvious at $\Phi = 315^\circ$, Fig. 2.9. As a result, the velocity increases on the lower surface which creates three counter-clockwise vortices and a small clockwise one. The stagnation point starts to move downstream on the upper surface. The pressure decreases a little in the area between the two airfoils. The lower surface of the airfoil is almost in complete dynamic stall.

As the airfoil arrives at the uppermost point, $\Phi = 360^\circ = 0^\circ$, Fig. 2.2, the flow near the lower surface of the airfoil is in complete dynamic stall. Multiple vortices exist on the lower surface while the fourth is already shed downstream.

C. SINGLE FLAPPING WING IN PURE PLUNGE

Similarly, the flow around a single flapping wing in pure plunge was computed. The flow fields are shown in Fig. 2.10, Fig. 2.11, Fig. 2.12, Fig. 2.13, Fig. 2.14, Fig. 2.15, Fig. 2.16, and Fig. 2.17 at 8 plunge phase angles, namely, 0° , 45° , 90° , 135° , 180° , 225° , 270° , and 315° .

The airfoil flaps in pure sinusoidal plunging motion. It flaps in the same fashion as the top airfoil in Fig. 2.1.

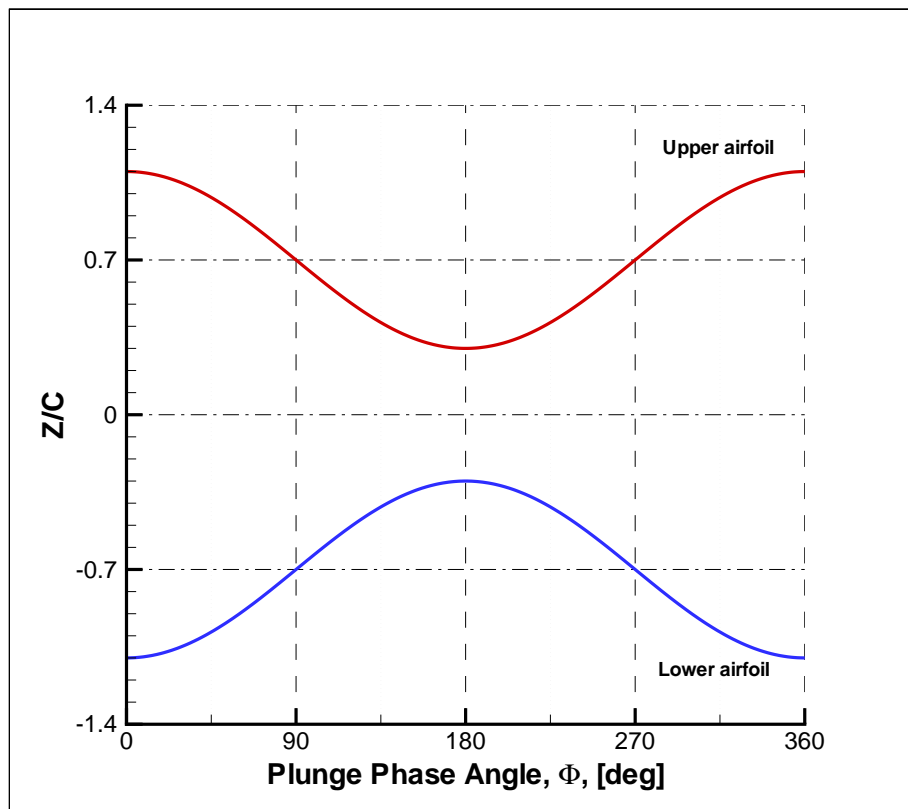


Figure 2.1. The Flapping Motion in the Biplane Configuration

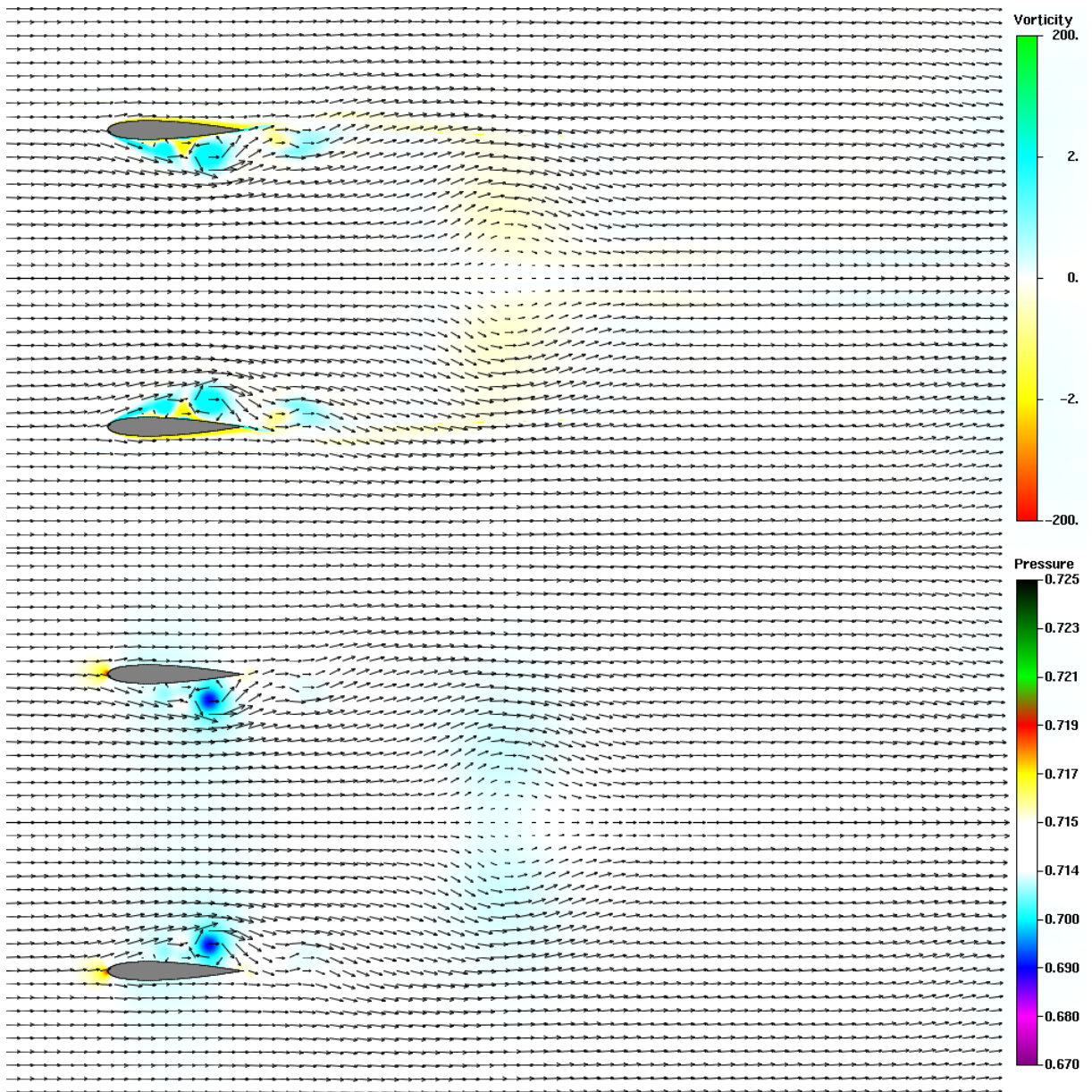


Figure 2.2. Vorticity and Pressure Distribution for Biplane Configuration, NACA 0014, $\alpha = 0^\circ$, $M_\infty = 0.1$, $k = 1$, $Re_\infty = 1 \times 10^4$, $\Phi = 0^\circ$.

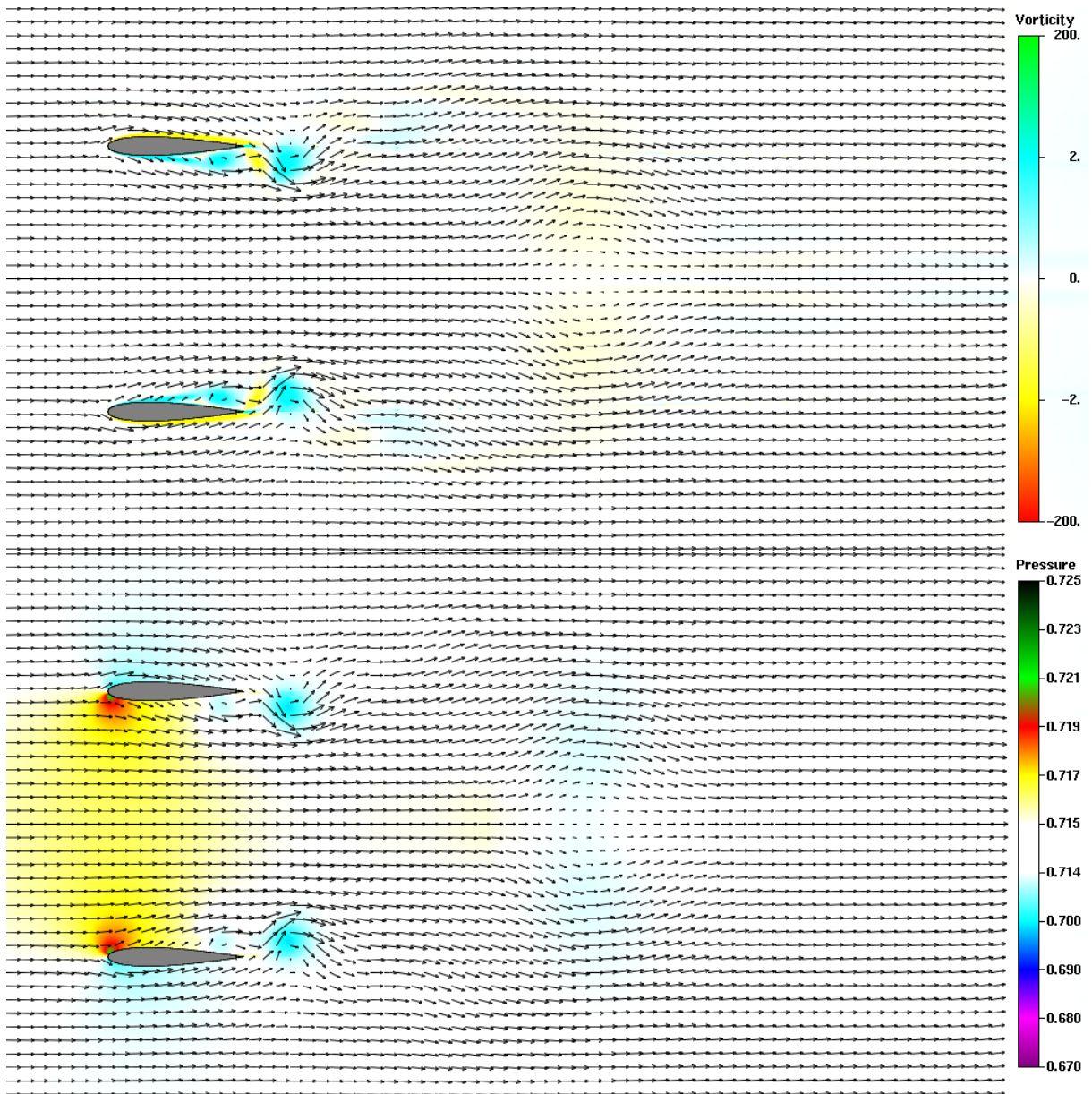


Figure 2.3. Vorticity and Pressure Distribution for Biplane Configuration, NACA 0014, $\alpha = 0^\circ$, $M_\infty = 0.1$, $k = 1$, $Re_\infty = 1 \times 10^4$, $\Phi = 45^\circ$.

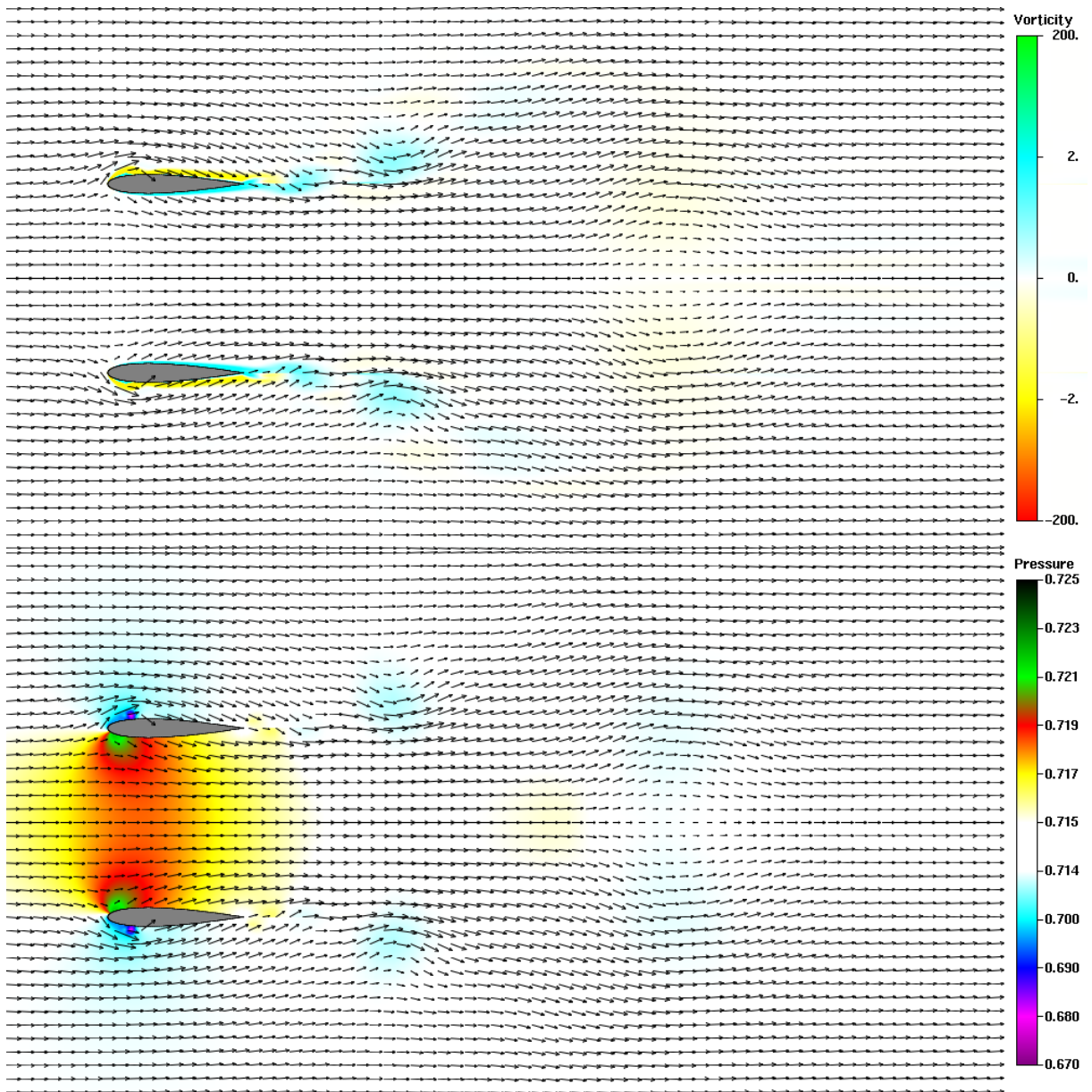


Figure 2.4. Vorticity and Pressure Distribution for Biplane Configuration, NACA 0014, $\alpha = 0^\circ$, $M_\infty = 0.1$, $k = 1$, $Re_\infty = 1 \times 10^4$, $\Phi = 90^\circ$.

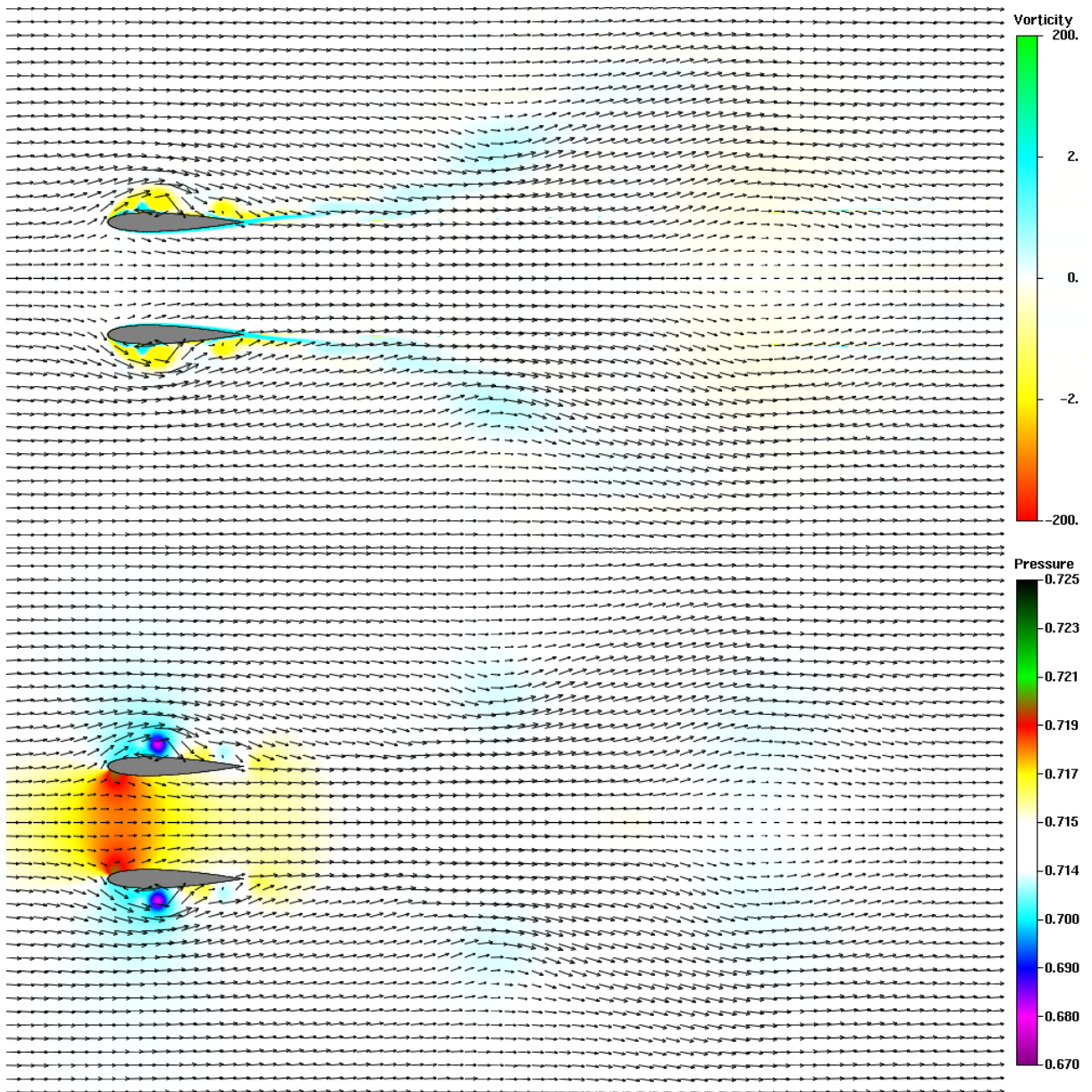


Figure 2.5. Vorticity and Pressure Distribution for Biplane Configuration, NACA 0014, $\alpha = 0^\circ$, $M_\infty = 0.1$, $k = 1$, $Re_\infty = 1 \times 10^4$, $\Phi = 135^\circ$.

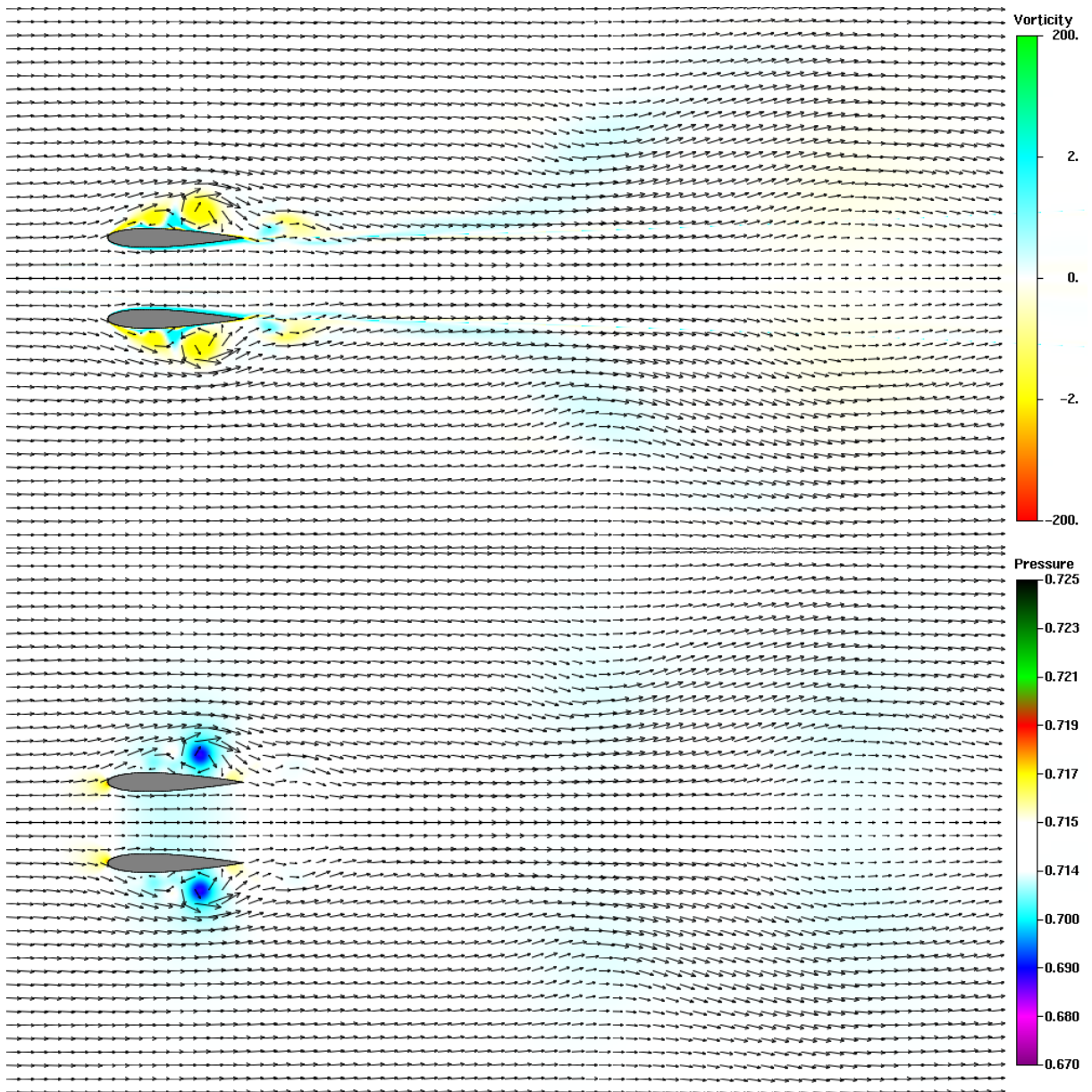


Figure 2.6. Vorticity and Pressure Distribution for Biplane Configuration, NACA 0014, $\alpha = 0^\circ$, $M_\infty = 0.1$, $k = 1$, $Re_\infty = 1 \times 10^4$, $\Phi = 180^\circ$.

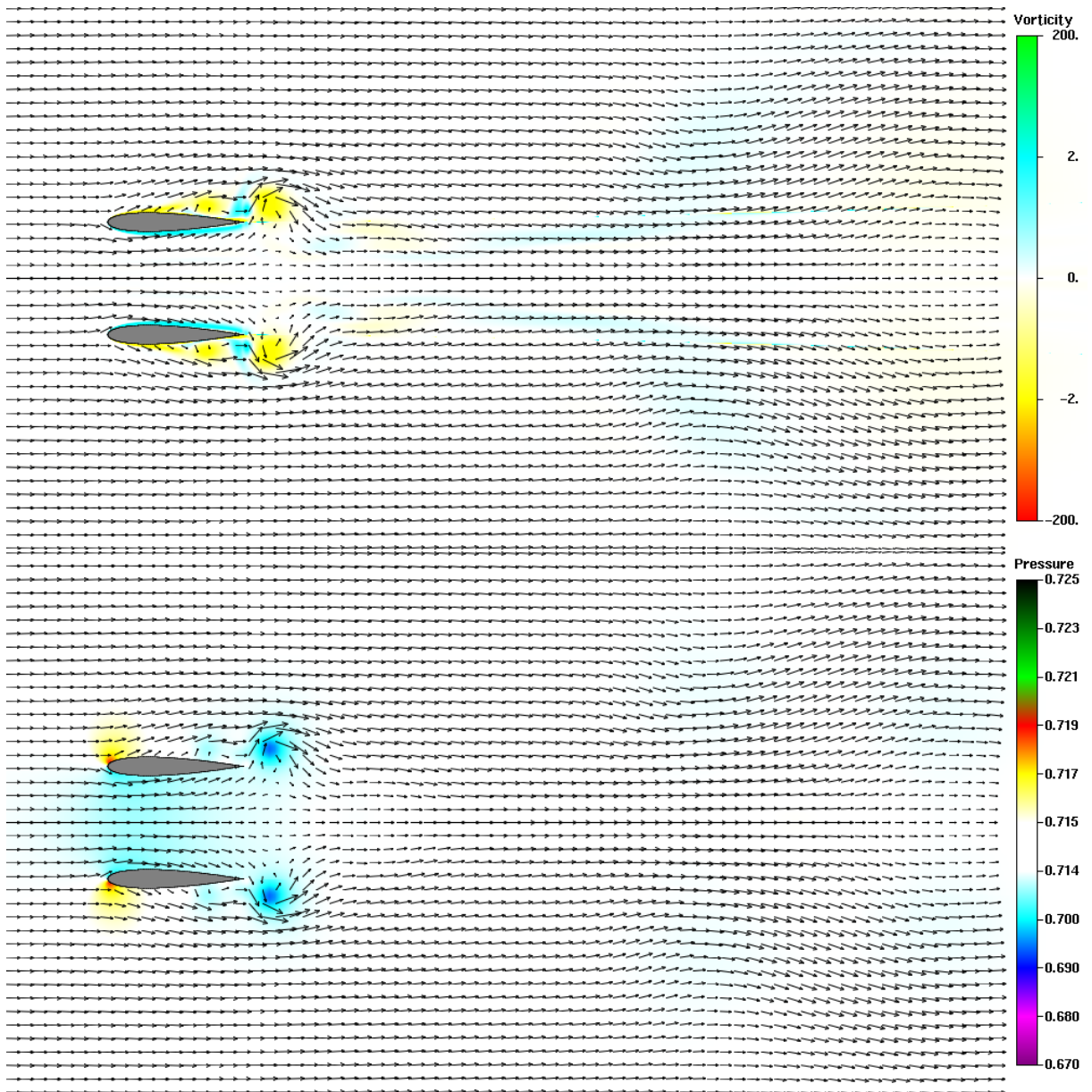


Figure 2.7. Vorticity and Pressure Distribution for Biplane Configuration, NACA 0014, $\alpha = 0^\circ$, $M_\infty = 0.1$, $k = 1$, $Re_\infty = 1 \times 10^4$, $\Phi = 225^\circ$.

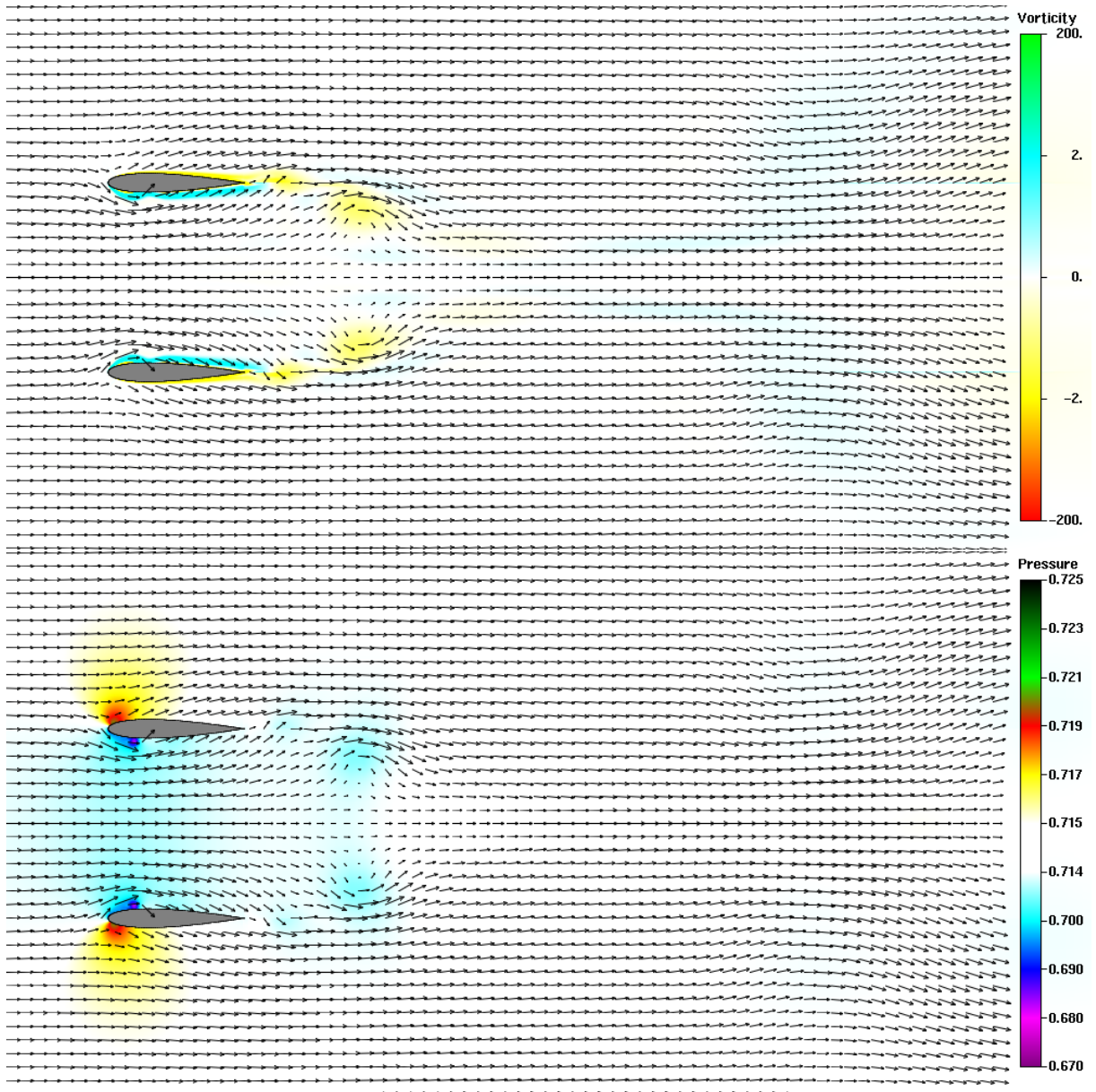


Figure 2.8. Vorticity and Pressure Distribution for Biplane Configuration, NACA 0014,
 $\alpha = 0^\circ$, $M_\infty = 0.1$, $k = 1$, $Re_\infty = 1 \times 10^4$, $\Phi = 270^\circ$.

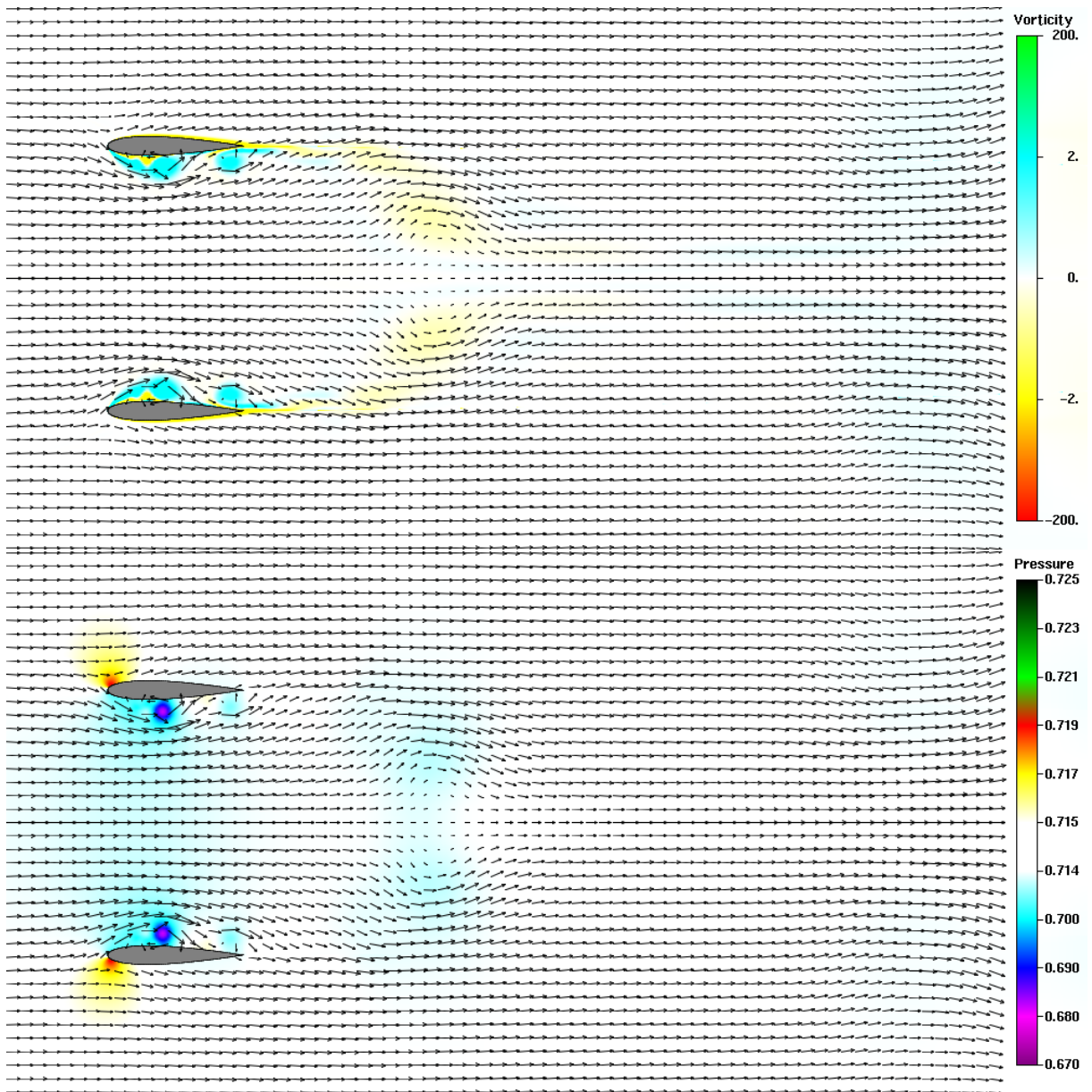


Figure 2.9. Vorticity and Pressure Distribution for Biplane Configuration, NACA 0014, $\alpha = 0^\circ$, $M_\infty = 0.1$, $k = 1$, $Re_\infty = 1 \times 10^4$, $\Phi = 315^\circ$.

The flapping cycle starts with the wing in the uppermost position at $\Phi = 0^\circ$, Fig. 2.10. At that position, the stagnation point is located near the leading edge. Two clockwise and one counterclockwise vortices exist near the lower surface of the airfoil. These vortices were generated during the previous upstroke.

As the airfoil starts the downstroke, $\Phi = 45^\circ$, the effective angle of attack increases causing the stagnation point to move to the lower surface behind the leading edge, Fig. 2.11. The velocity increases on the upper surface causing a slight decrease in pressure. The three vortices which existed on the lower surface have moved downstream and two of them have already cleared the airfoil surface. The pressure on the upper surface is less than that on the lower surface.

As the airfoil approaches the mid-flapping position at $\Phi = 90^\circ$, the effective angle of attack keeps increasing and the stagnation point moves further downstream from the leading edge on the lower surface, Fig. 2.12. On the upper surface a vortex starts to develop within the first quarter chord. Meanwhile all vortices have been shed away from the lower surface. The pressure value keeps increasing on the lower surface especially within the quarter chord behind the leading edge.

As the airfoil keeps moving down during the downstroke, $\Phi = 135^\circ$, the vortices on the upper surface keep growing, Fig. 2.13. Two clockwise vortices and one counter-clockwise vortex lying between them can be well distinguished. Another vortex is generated on the upper surface just before the trailing edge.

As the airfoil approaches the lowest point in the downstroke, $\Phi = 180^\circ$, the flow near the upper surface is in full dynamic stall, Fig. 2.14. The three vortices on the upper surface are well developed while the one that was at the trailing edge has been shed downstream.

The stagnation point is located near the leading edge. The pressure on the upper surface is less than on the lower surface.

As the wing starts the upstroke, the effective angle of attack changes from positive to negative and the stagnation points starts to move downstream on the upper surface, $\Phi = 225^\circ$, Fig. 2.15. The velocity increases on the lower surface causing a slight drop in pressure. Meanwhile, on the upper surface, the pressure starts to build up. The previously generated vortices start moving toward and past the trailing edge.

As the airfoil approaches the mid-flapping position during the upstroke, $\Phi = 270^\circ$, Fig. 2.16, the negative effective angle of attack keeps increasing causing the stagnation point to move downstream on the upper surface. A high pressure zone is well developed on the upper surface and concentrated mainly around the stagnation point within the first quarter chord. The velocity increases on the lower surface causing a pressure drop and a vortex starts to develop.

As the airfoil keeps moving during the upstroke, $\Phi = 315^\circ$, Fig. 2.17, the velocity keeps increasing on the lower surface. Four vortices are now completely developed.

As the wing reaches the uppermost point, it starts a new cycle as presented at $\Phi = 0^\circ$, Fig. 2.10

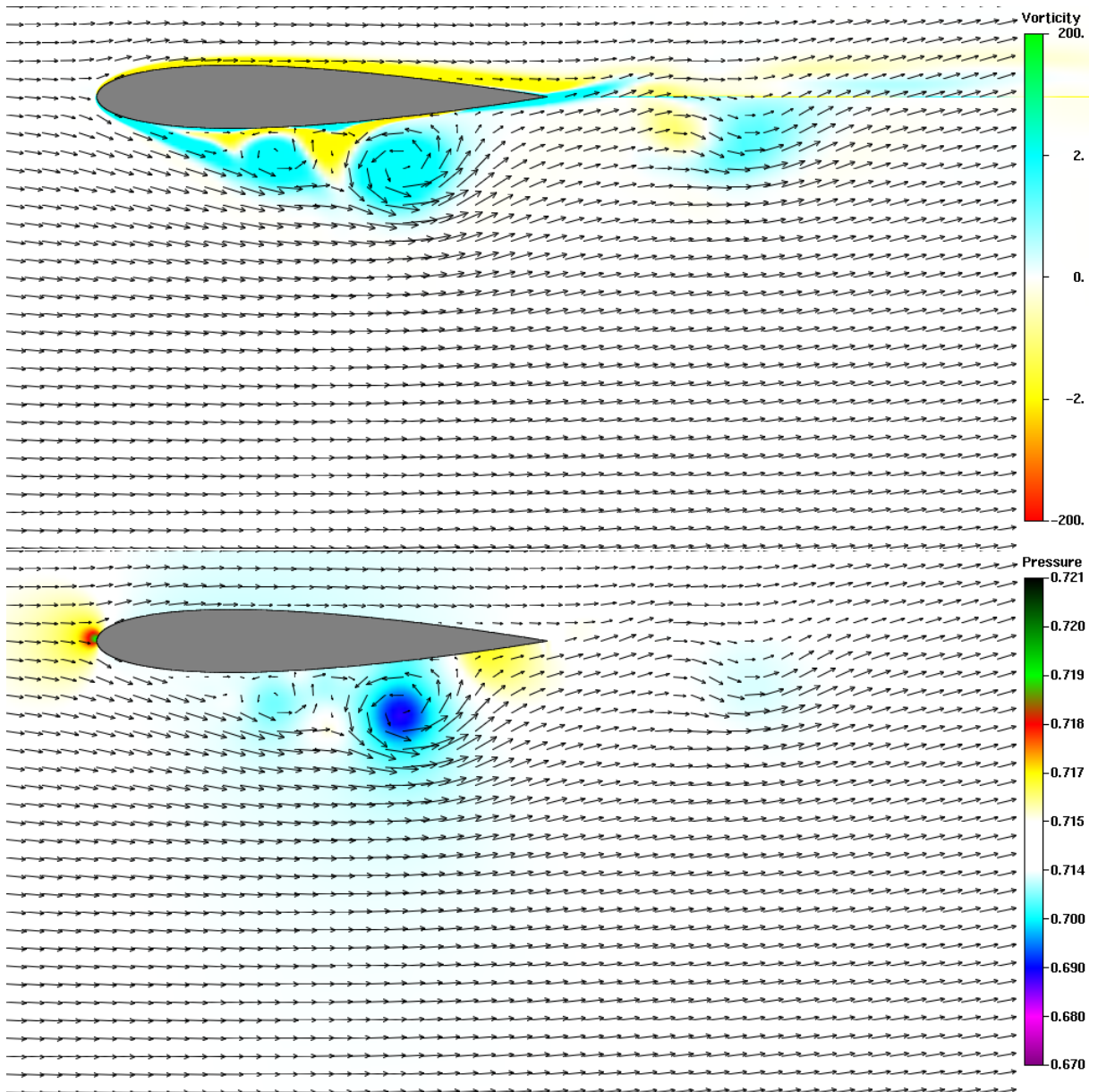


Figure 2.10. Vorticity and Pressure Around a Single Wing in Pure Plunge, NACA 0014,
 $\alpha = 0^\circ$, $M_\infty = 0.1$, $k = 1$, $Re_\infty = 1 \times 10^4$, $\Phi = 0^\circ$.

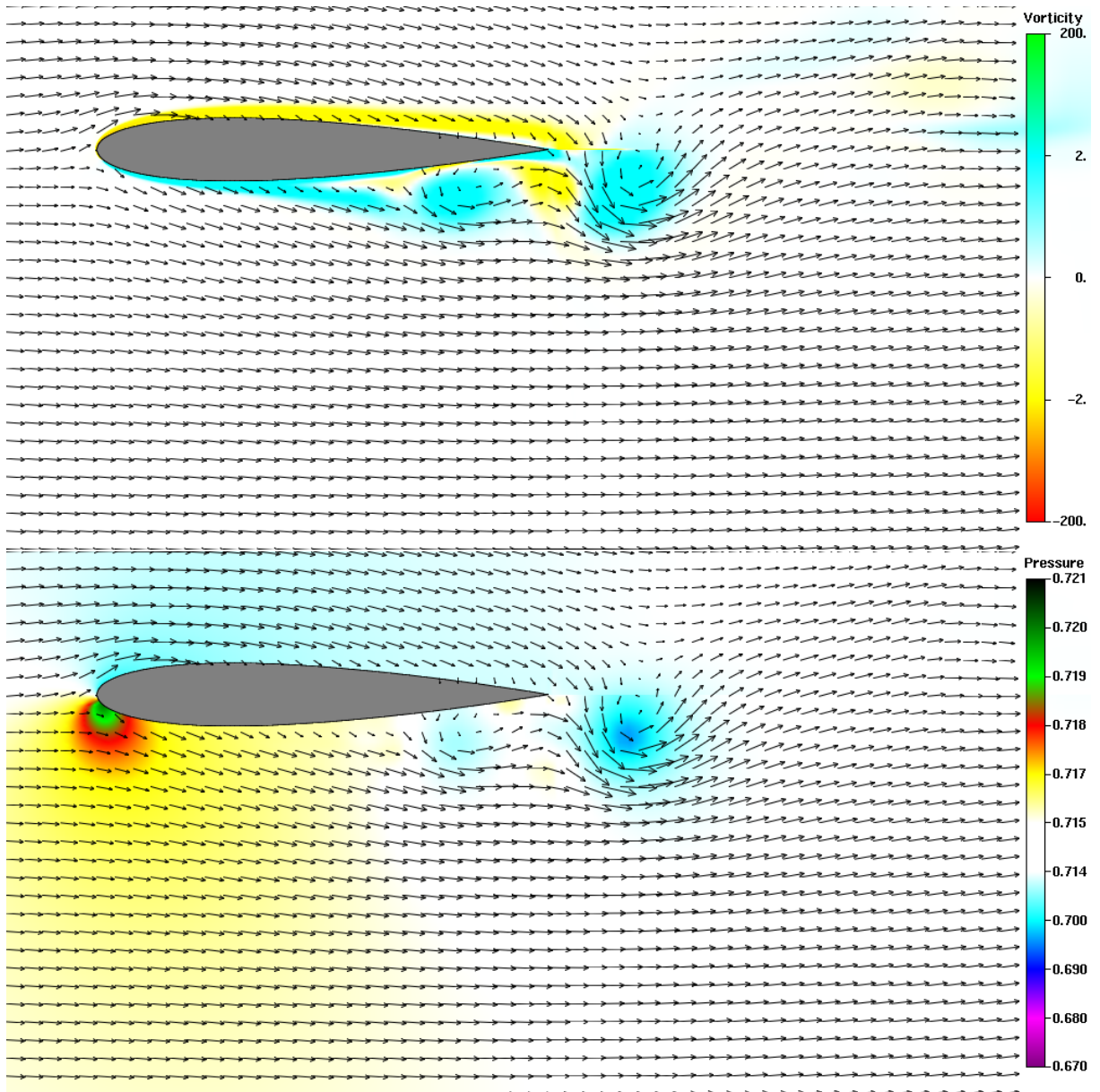


Figure 2.11. Vorticity and Pressure Around a Single Wing in Pure Plunge, NACA 0014, $\alpha = 0^\circ$, $M_\infty = 0.1$, $k = 1$, $Re_\infty = 1 \times 10^4$, $\Phi = 45^\circ$.

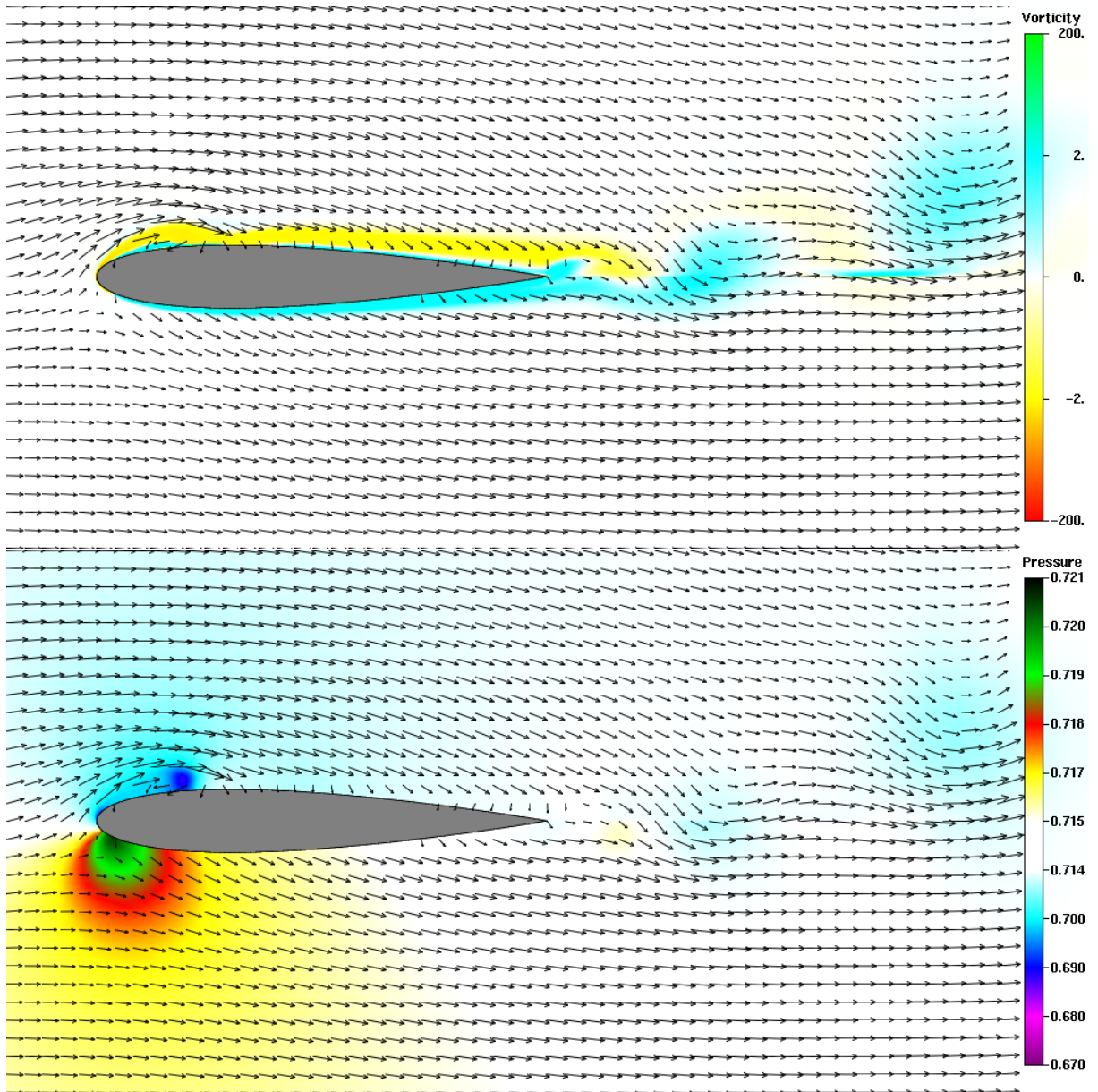


Figure 2.12. Vorticity and Pressure Around a Single Wing in Pure Plunge, NACA 0014, $\alpha = 0^\circ$, $M_\infty = 0.1$, $k = 1$, $Re_\infty = 1 \times 10^4$, $\Phi = 90^\circ$.

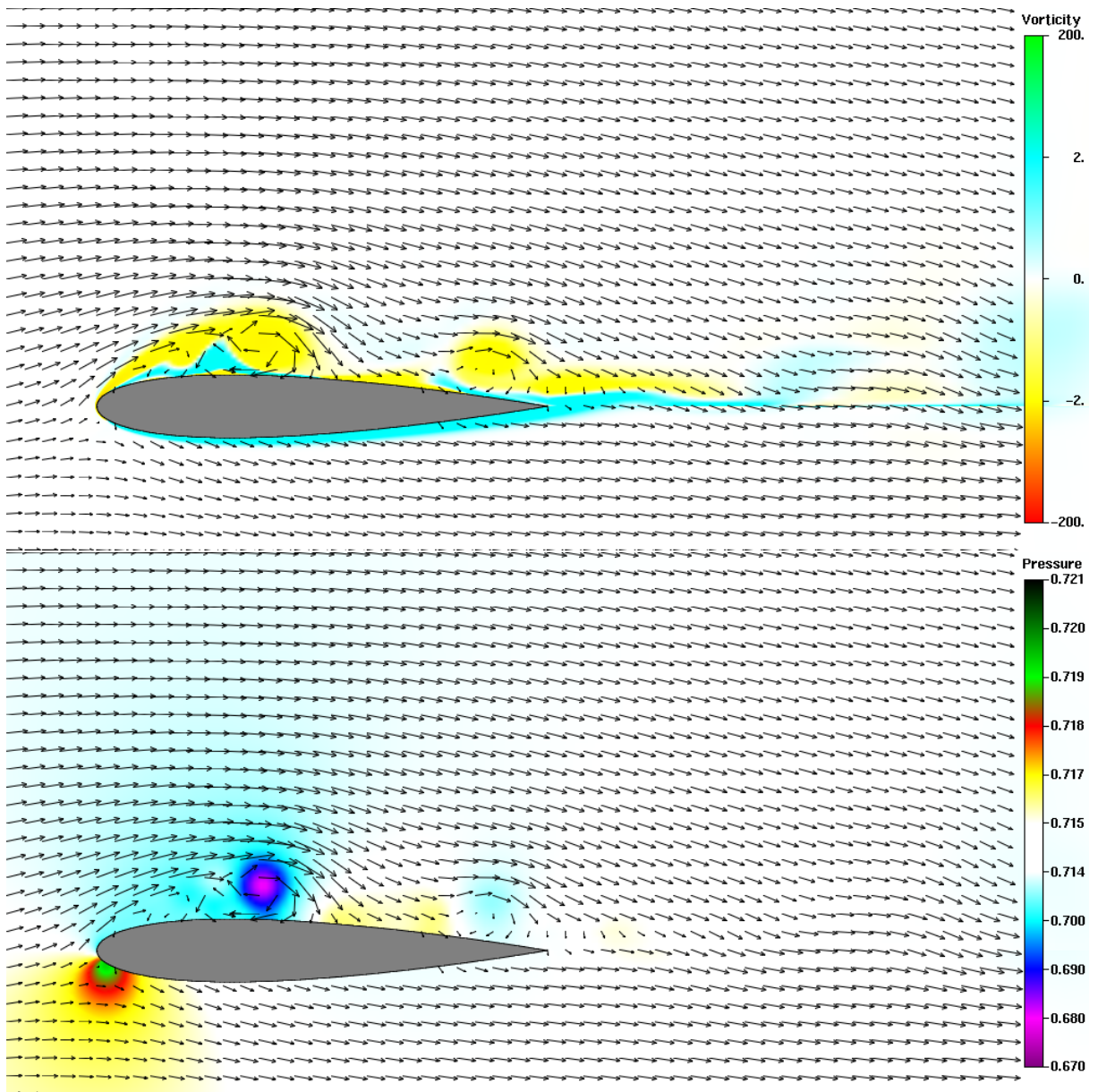


Figure 2.13. Vorticity and Pressure Around a Single Wing in Pure Plunge, NACA 0014, $\alpha = 0^\circ$, $M_\infty = 0.1$, $k = 1$, $Re_\infty = 1 \times 10^4$, $\Phi = 135^\circ$.

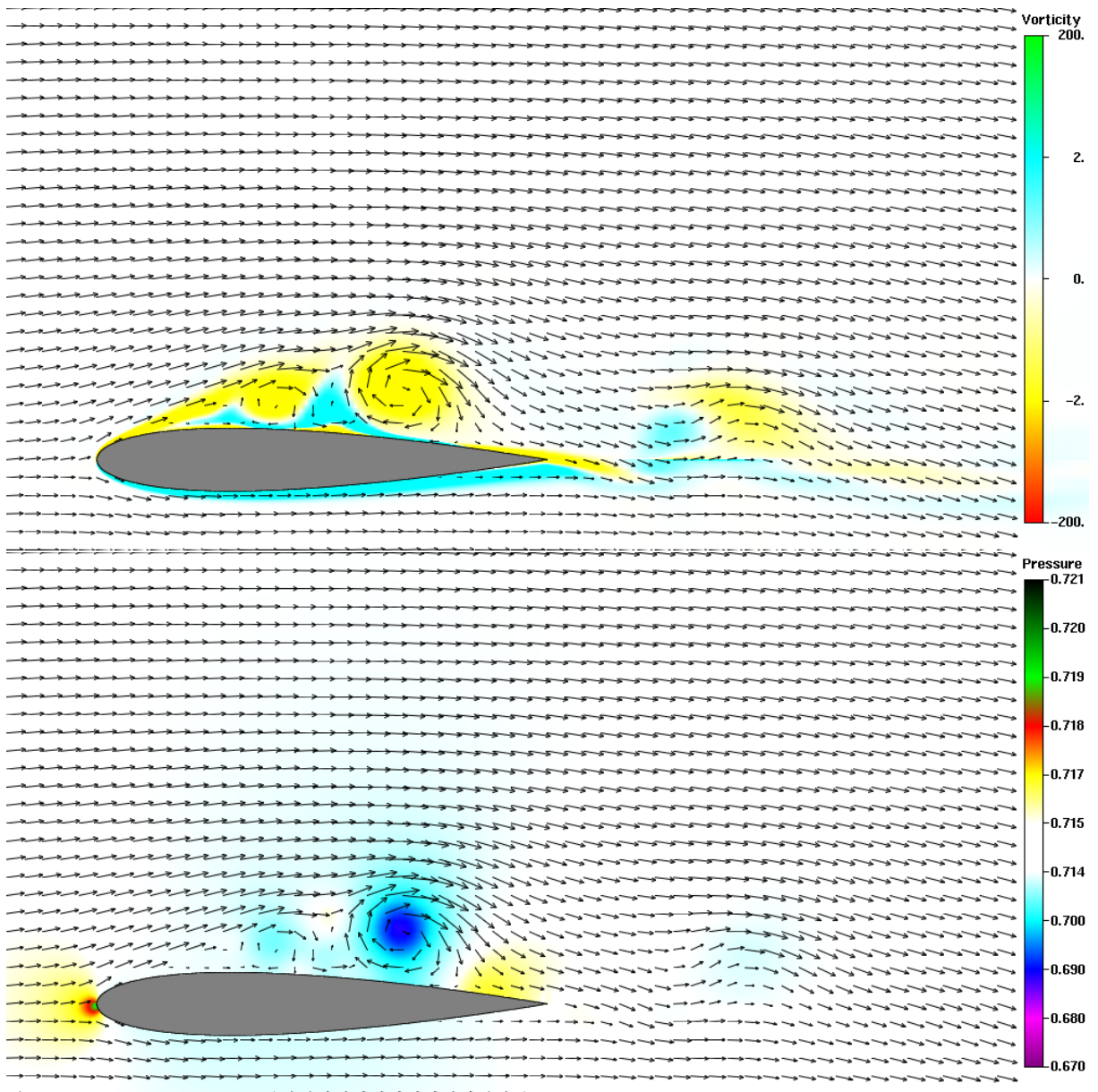


Figure 2.14. Vorticity and Pressure Around a Single Wing in Pure Plunge, NACA 0014, $\alpha = 0^\circ$, $M_\infty = 0.1$, $k = 1$, $Re_\infty = 1 \times 10^4$, $\Phi = 180^\circ$.

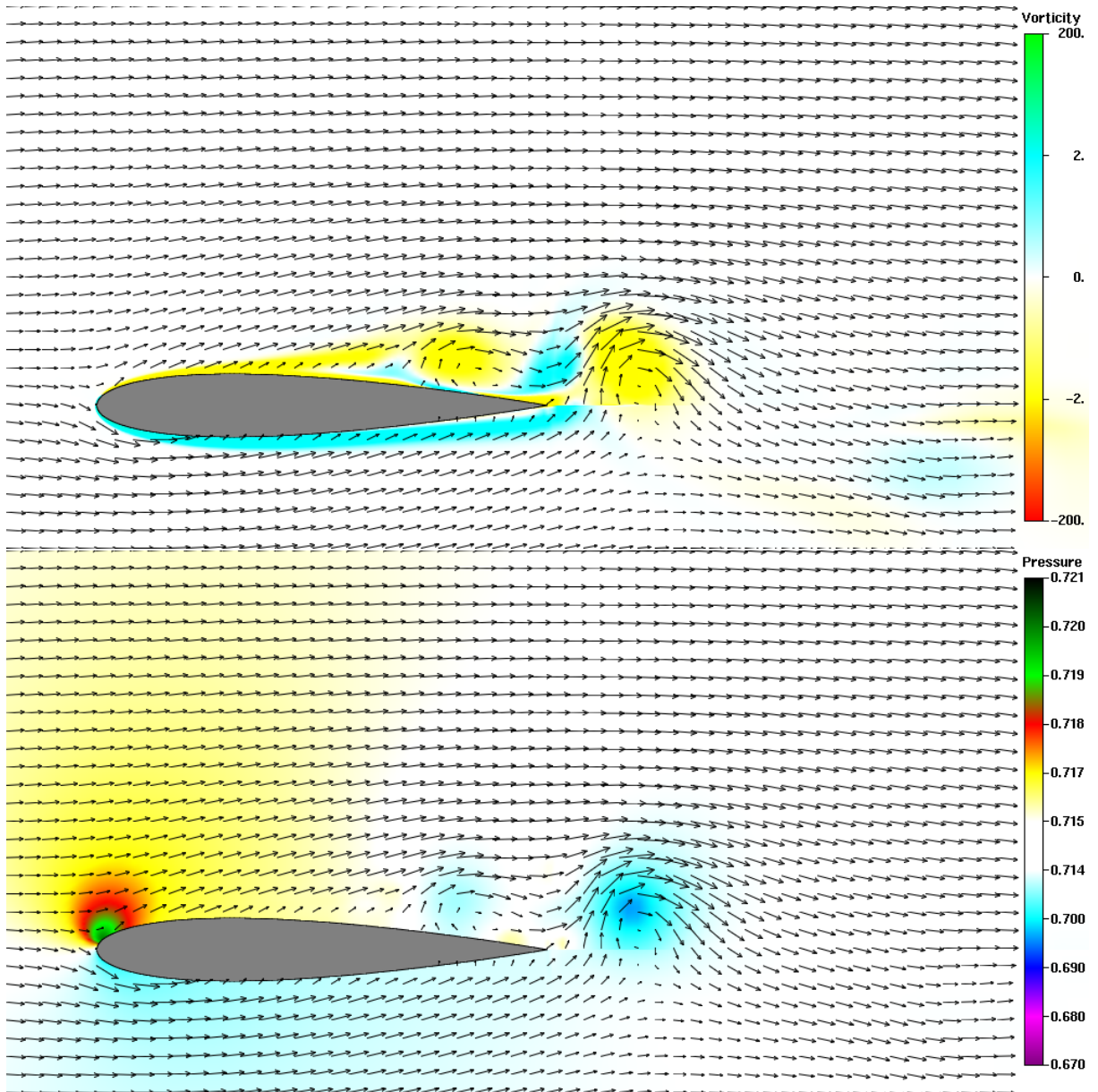


Figure 2.15. Vorticity and Pressure Around a Single Wing in Pure Plunge, NACA 0014, $\alpha = 0^\circ$, $M_\infty = 0.1$, $k = 1$, $Re_\infty = 1 \times 10^4$, $\Phi = 225^\circ$.

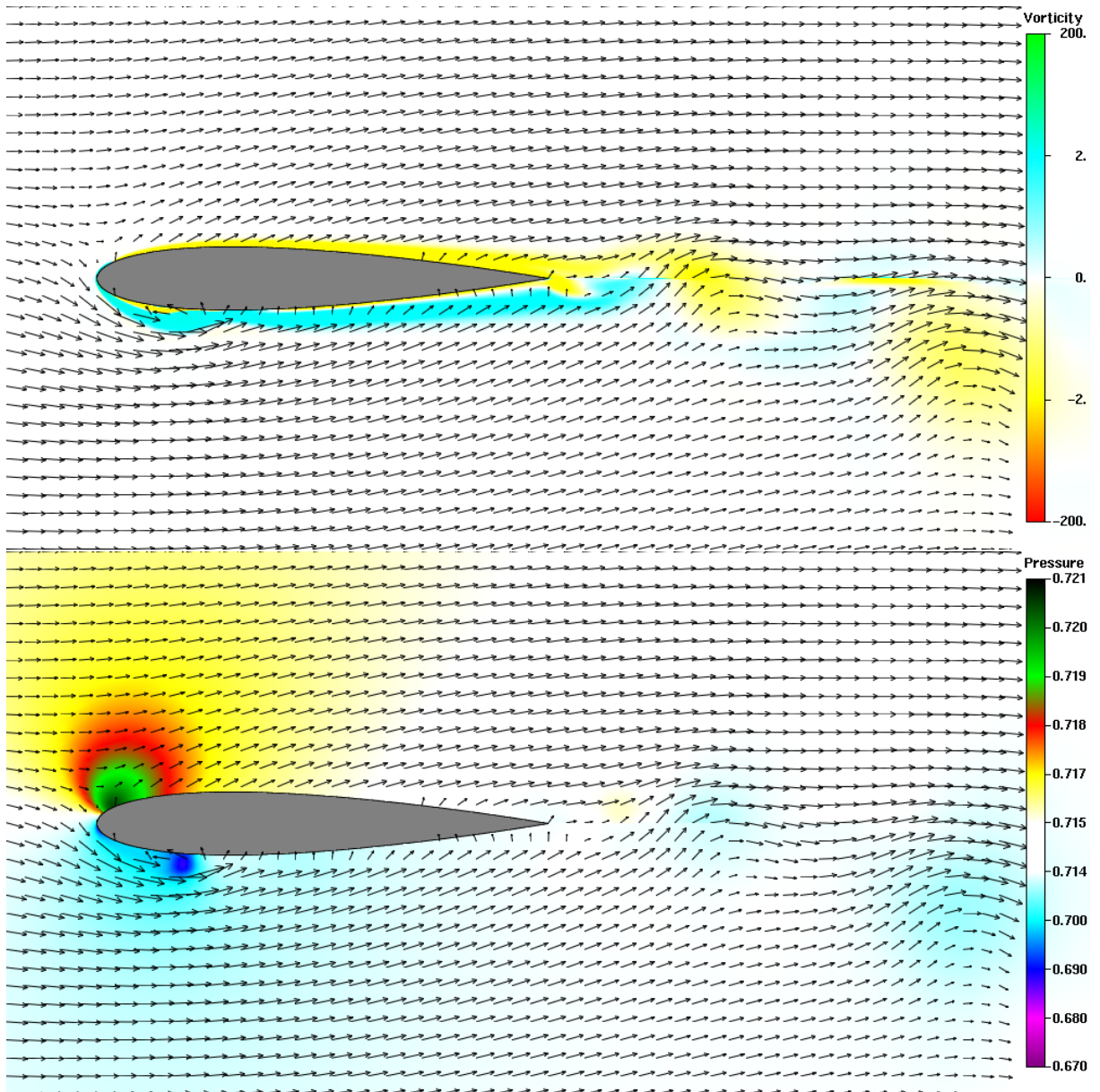


Figure 2.16. Vorticity and Pressure Around a Single Wing in Pure Plunge, NACA 0014,
 $\alpha = 0^\circ$, $M_\infty = 0.1$, $k = 1$, $Re_\infty = 1 \times 10^4$, $\Phi = 270^\circ$.

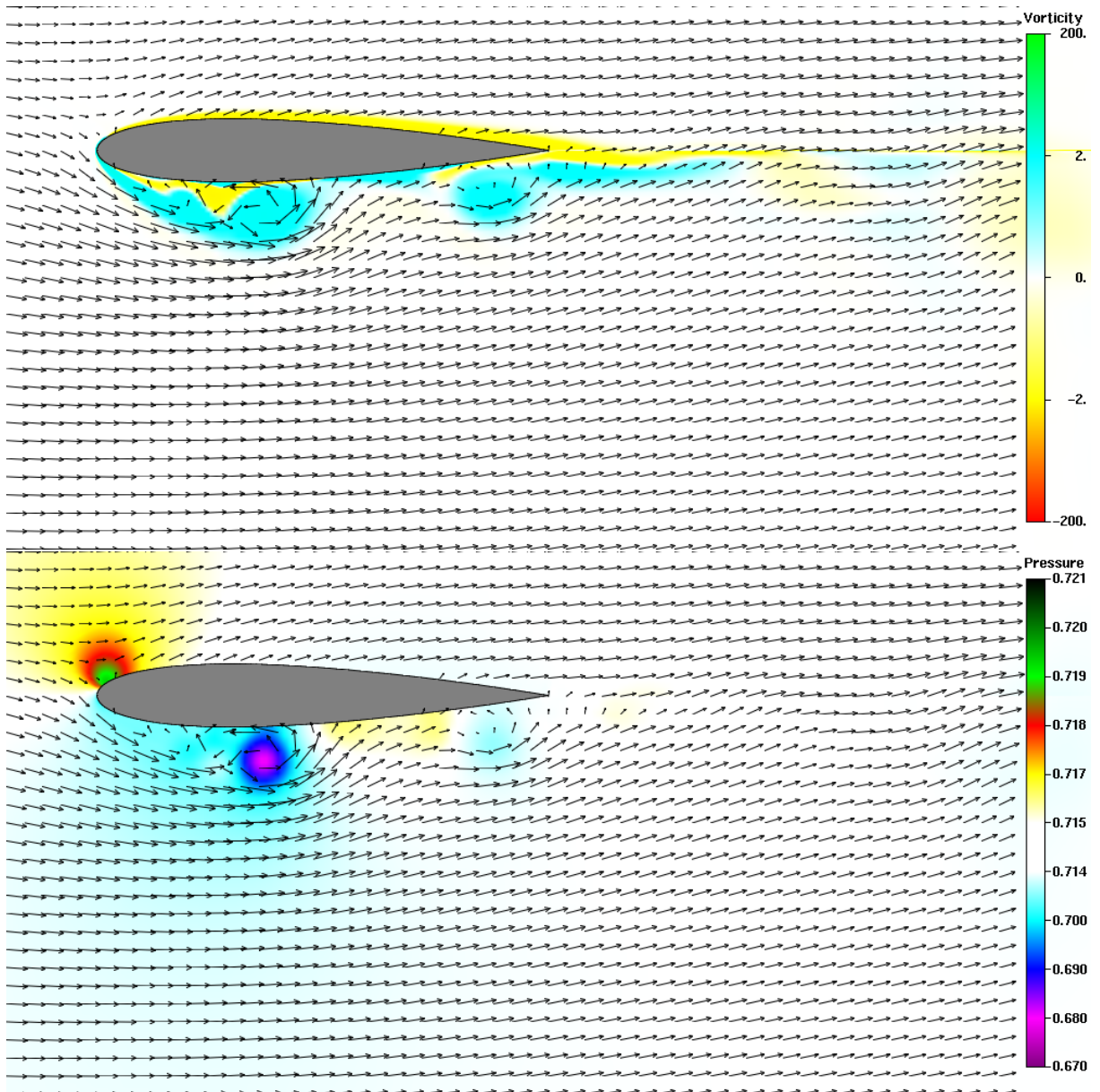


Figure 2.17. Vorticity and Pressure Around a Single Wing in Pure Plunge, NACA 0014,
 $\alpha = 0^\circ$, $M_\infty = 0.1$, $k = 1$, $Re_\infty = 1 \times 10^4$, $\Phi = 315^\circ$.

THIS PAGE INTENTIONALLY LEFT BLANK

III. EXPERIMENTAL TOOLS

A. GENERAL DESCRIPTION OF THE SYSTEM

1. Wind Tunnel Description

The low-speed, continuous, in-draft wind tunnel used in the present investigation is shown in Fig. 3.1. Air is ingested from inside the building through a square 4.5 x 4.5 m inlet, converging through a 9:1 bell shaped contraction to a 1.5 x 1.5 m test section. Tunnel speed is controlled by a variable pitch fan driven by a constant speed electric motor. Motor and fan vibration are isolated from the test section by rubber sleeves on each side of the motor/fan assembly. The tunnel velocity range is 0 to 9.5 m/s.

2. Pitot Static Tube

A pitot static tube was installed above the model for general adjustments of tunnel velocity. The pitot-static tube is connected to a MKS Baratron type 223B differential pressure transducer. The transducer provides a voltage that is linear with the differential pressure, yielding 1 volt at 1 torr. The flow-speed is then given by Eq. (3.1)

$$U_{\infty} = \sqrt{\frac{2\Delta p}{\rho_{\infty}}} \quad (3.1)$$

The transducer has a reported accuracy of 0.5% of the full-scale reading which, due to the nature of Eq. (3.1), results in rather large errors in the measurement of low velocities but quite small errors in the measurement at high velocities. The pitot-static tube has been calibrated using LDV, and was shown to be sufficiently accurate.

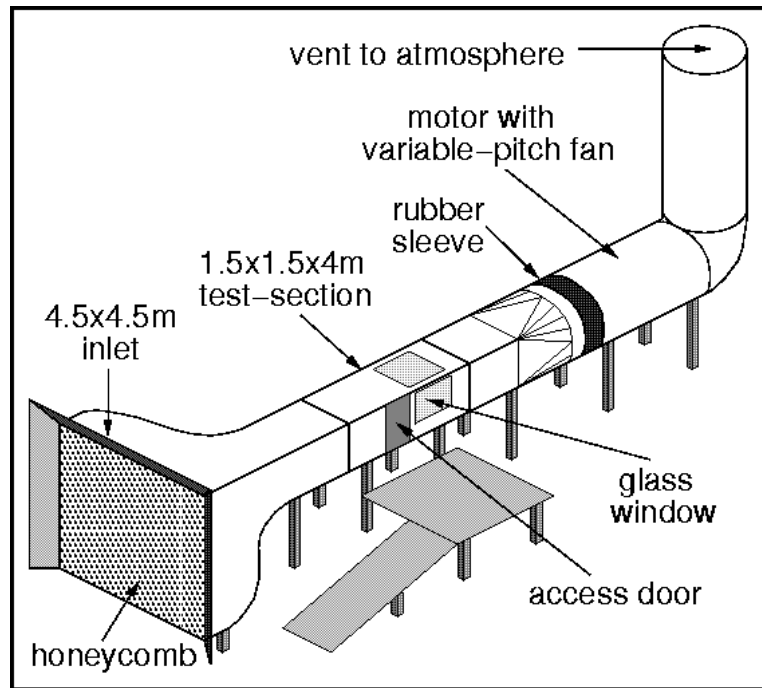


Figure 3.1. Wind Tunnel Schematic Diagram

The pitot static tube has errors associated with the measurement of both the static and total pressure. The pitot tube used here has an outer diameter of 8mm, 8 static ports aligned symmetrically, 64mm (8 diameters) downstream of the tip base, and a stem approximately 120mm (15 diameters) downstream of the static ports. According to Pope [23] the geometry of the probe should yield about a 0.5% overprediction of the static pressure.

3. Laser Doppler Velocimetry (LDV)

LDV is an optical method that utilizes the Doppler principle, measuring the frequency shift of laser light scattered by a particle in the flow. A dual-beam, on-axis, backward-scatter system is used to measure the air velocity and turbulence intensity in the NPS low-speed, open circuit smoke tunnel.

In the dual-beam arrangement utilized, a beam of laser light is split in two, the

frequency of one of the beams is shifted, and both beams are transmitted such that they cross each other, thereby generating the so-called probe volume. Particles moving through the probe volume scatter the laser light. The scattered light is collected, and sent via an optical receiving fiber to a Photo Multiplier Tube (PMT). A photo detector in the PMT converts the light pulse into a voltage signal at the Doppler frequency. The signal produced by the photo detector is sent to the IFA 755 signal processor via a frequency downshifter. The signal processor determines the Doppler frequency by performing a burst spectrum analysis of the signal. The Doppler frequency is then sent to computer via direct memory access (DMA) interface. The PACE software records the signal for later processing into velocity information. The LDV probe is mounted on a 3-axis traverse mechanism outside the tunnel at the test section window. The LDV probe is fitted with a 750 mm lens allowing LDV measurements to the center of the tunnel.

4. LDV Apparatus

The LDV system uses a 5W, water-cooled Coherent Innova Series Argon-ion laser for the light source. A TSI Model 9201 Colorburst multicolor beam separator unit is used to separate the laser colors (green - 514.5 nm , blue- 488 nm , and purple - 476 nm), split the beams and frequency shift one beam in each color. After splitting the beams, one of the two blue beams and one of the two green beams were frequency shifted by 40 MHz. The purple channel was blocked. The beams were coupled into a 2-component, 4-beam, Model 9832 fiber optic probe through a Model 9271 coupler (one for each beam). The beams were transmitted to the probe via optical receiving fiber. Probe beam spacing is 50 mm and the lens focal length is 750 mm. A multi-mode receiving fiber located in the probe received and forwarded the reflected light to a Model 9160 photo multiplier tube (PMT). Although the

probe is a two-component unit, only one component of the receiving optics was available. The output of the PMT is connected to a 9186A frequency downshifter. The downshifter is connected to a TSI Model IFA-755 signal processor. The signal processor distinguishes the signal burst from the noise based upon the signal-to-noise-ratio. The processor determines frequency, phase, burst transit time, and burst arrival time and sends these signals to the computer. The DMA board and PACE windows software package on the computer converts the signals into velocity, and is used for data display and storage.

5. Flow Seeding

Flow seeding was performed using a TSI 9306 six-jet atomizer, operating with compressed air producing particles with approximately 1 micron in size.

6. Model Description

For the steady flow measurements, a wing with a NACA 0014 airfoil was fixed to a mechanism, which allows variable angles of attack. The wing chord is 64 mm with a span of 635 mm.

For the unsteady flow and thrust measurements, a flapping wing mechanism was used. It was designed by Dr. Kevin Jones at the Naval Postgraduate school in 1997. Its construction and dynamics are described in [13] from which this description is taken. Isometric, profile and top views are shown in Fig. The structure of the fuselage is made of aluminum, the front and rear nacelles of balsa-wood, and the wings of wood. The device is configured to flap one or two wings. When flapping two wings, the wings are positioned one above the other. The two flapping wings are configured to execute a two degree of freedom motion, with both pitch and plunge amplitudes adjustable. The phase angle between pitch

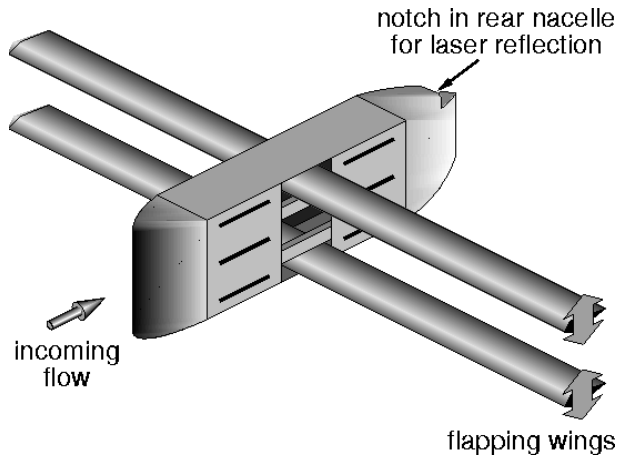


Figure 3.2. Isometric View of Upturned Flapping Mechanism.

and plunge is also adjustable. Stationary wings may be attached before or after the flapping wings in the slots depicted, Fig. 3.2.

The flapping wings are attached to moving beams, which are driven by eight actuator wheels. A pin attached to each of the eight wheels rides in a slot at the end of each beam. This attachment changes the circular motion of the wheels into the flapping motion of the beams. The beams may be attached to the wheels at a selected wheel radius to control plunge amplitude, Fig. 3.3 and Fig. 3.4. Wing pitch is controlled by adjusting the phase between the fore and aft wheels. The eight wheels are attached to four worm gears. The gears mesh with two worms that are driven by an Astro-Flight Cobalt 40 model airplane motor. The motor is powered by a variable voltage/current power supply. Lund [21] recommended that the motor voltage should be limited to 26V for a maximum of one minute. This voltage limit restricted maximum flapping frequency to 7Hz during the thrust measurements. However, for the unsteady flow measurements around the flapping wing, longer run times were needed to be able to get enough samples. Therefore, the flapping frequency was limited to 5Hz.

This 26V corresponds to a motor rpm of 21,000 with a 50:1 gear reduction. Current

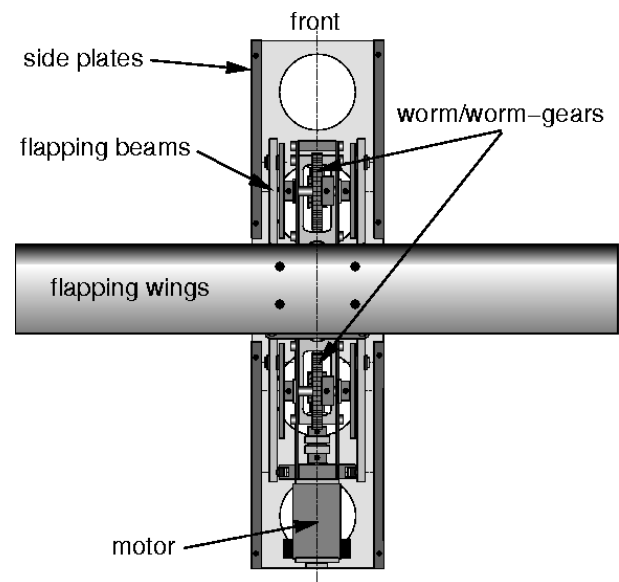


Figure 3.3. Top View of Flapping Mechanism.

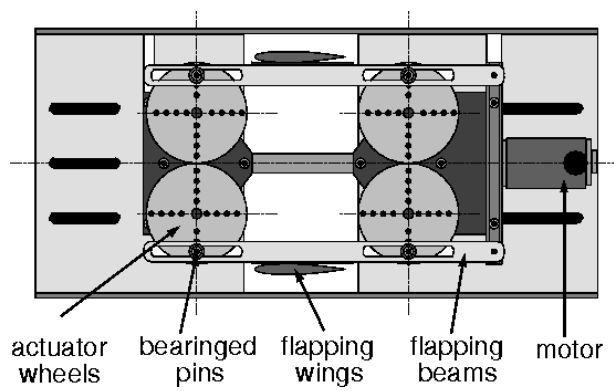


Figure 3.4. Profile View of Flapping Mechanism.

Table 3.1. Flapping Model Parameters

Wing Configuration		Single, Bi-wing flapping, no stationary wings
Wing Type		Symmetric, approximating NACA 0014
Wing Span	b^*	1270 mm
Fuselage Width		70 mm
Useful Lifting Span	b	1200 mm
Wing Chord	c	64 mm
Aspect Ratio	$AR = b^2/S = b/c$	19.84 full span, 18.75 useful span
Taper Ratio	$\lambda = c_t/c_o$	1
Sweep Angle	Λ	0
Mean Wing Separation		1.4c
Plunge Amplitude	h	$h \cong 0.4 = 25.4$ mm
Pitching Motion	$\Delta\alpha$	None, $\alpha_{geom} = 0^\circ$

drawn was always less than 5A. A wing section with a NACA0014 airfoil was used in all the experimental work. The wings were manufactured by the Miniature Aircraft Supply model helicopter company and were made of balsa wood and laminated hardware, and covered with a thin, smooth plastic sheet. The wings can be bolted to the flapping beams, or attached as stationary wings in the slots upstream or downstream of the flapping wings. The stationary wing feature is useful for experiments to explore Schmidt's wave propeller. The parameters of the flapping mechanism is summarized in Table 3.1

B. THE THRUST MEASURING TECHNIQUE

The experimental arrangement for measuring thrust is depicted in Fig. 3.5. The model is suspended with four thin cables 112.8 cm in length. The cables allow displacement along the streamwise axis, but hinder motion in other axes. In order to determine thrust, the model displacement due to flapping is required. Drag induced by the tunnel flow deflects the model rearward. Flapping the wings of the model moves it forward. The net displacement, measured by a laser rangefinder, positioned on a two-axis traverse behind the model, reflecting the beam from a notch in the model's rear nacelle, is a measure of the thrust.

After setting tunnel velocity, the laser rangefinder was positioned at its zero voltage center point, 13 cm behind the model. Since the model's rearward displacement due to drag increased with velocity, the rangefinder was reset to its center point at each tunnel velocity.

In order to obtain the desired flapping frequency, the strobe light was set to the required frequency and the motor voltage adjusted until the beams flapping the wings appeared to be stationary. The model was equipped with a micro switch which triggers a square signal once per revolution. This signal was used to obtain the exact flapping frequency of the model through the digital oscilloscope.

During flapping, the laser rangefinder voltage was recorded concurrently with the frequency micro-switch voltage by the digital oscilloscope. The rangefinder and frequency micro-switch data were recorded with a sample rate of 1000 Hz for a period of approximately 32 seconds. This ensured collecting enough data.

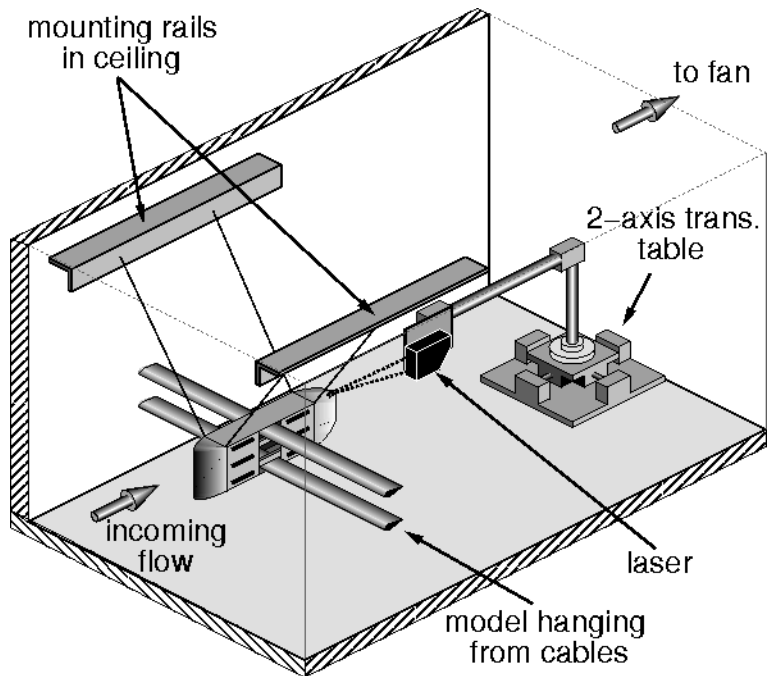


Figure 3.5. Thrust measurement arrangement

C. UNSTEADY FLOW MEASUREMENTS

Measuring the instantaneous axial velocity component, u , was essential to know the flow characteristics during the wing flapping cycle. The Rotary Machinery Resolver, RMR, along with the micro switch circuit allowed conditional sampling for the velocity picked up by the LDV system.

D. TRIGGERING SIGNAL

A triggering signal was generated by a micro switch which sends a one per revolution pulse. An electric circuit was built to get a clean square signal. The RMR uses the rising part of the square signal as a reference for position "ZERO" and the following rising signal

as position "ZERO". In the present work, the time interval between the two signals was divided into 360 bins which were used to store the velocity measured by the LDV.

Ideally, the position "ZERO" should represent the wing at zero amplitude. But due to space limitations inside the model, it was impossible to meet this condition. So, the relation between the triggering signal and the actual wing position was required to obtain meaningful results. The laser range finder was installed underneath the wing and the model set to flap for a while and a set of flapping cycles along with the triggering signal was recorded. The obtained results are presented in Fig. 3.6.

It was found that the trigger signal was generated such that it will trigger at $\phi = 95.17^\circ$ considering that the position ZERO is the position when the wing is in the uppermost position, which was the convention used in this work. In the present work, the maximum amplitude was $0.4C$ which equals 0.0256 [m]. Hence, the triggering signal was initiated when the wing was at a plunge distance of 0.0023 m after passing the mean plunge position during the downstroke.

E. CONVENTIONS

In the present work the following conventions were used:

- The wing starts the flapping cycle, $\Phi = 0$, from the uppermost position.
- The airfoil leading edge was always placed at $X/C = 0$, and the trailing edge was placed at $X/C = 1$
- In the steady measurements, the airfoil chord was placed at $Z/C = 0$
- In the unsteady measurements, the mid flapping position was placed at $Z/C = 0$.

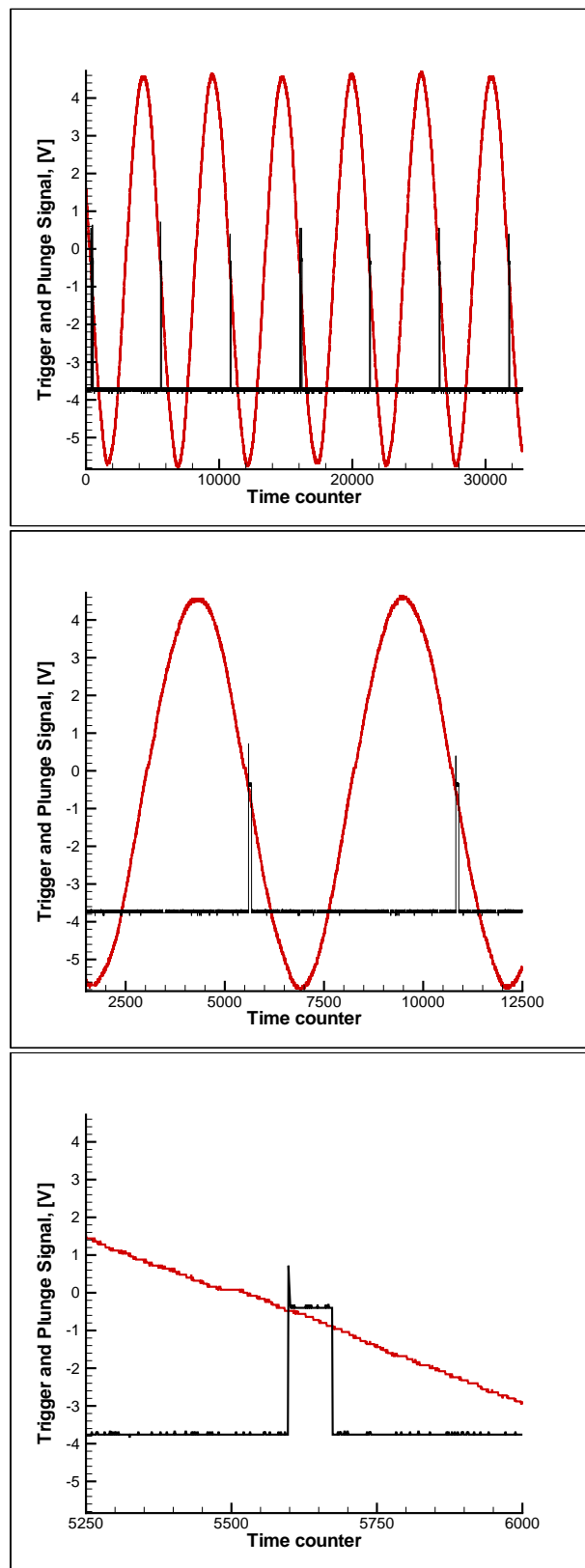


Figure 3.6. Trigger signal and the plunge motion

THIS PAGE INTENTIONALLY LEFT BLANK

IV. FLOW VISUALIZATION

It was of interest to visualize the flow around the NACA0014 airfoil which was used in the present work. The flow visualization was done by generating smoke upstream of the wing and taking pictures by still and video cameras. A simple mechanism was built to change the angle of attack.

A. SMOKE WIRE SYSTEM

Flow visualization was performed using a smoke wire, with 0.3 mm diameter Ni-Chrome (NI80_CR20) wire stretched between two posts, and spring loaded to account for the wire elongation when heated, Fig. 4.1. The resistive wire was heated by applying a voltage across its length. The voltage was provided by a Variac set to provide 15-20V. The voltage setting was dependent upon tunnel speed and fog fluid flow rate.

Smoke was generated by dripping Roscoe fog liquid down the wire prior to heating it. Supplying the fog fluid was done through a brass tube welded to the fixture at one end of the wire. A clear silicon tube was attached to this brass tube which delivered the fog fluid from a pressurized container outside the test section. The container was pressurized using a bike pump through one of two adapters bolted through the jug's cap. The transparent silicone tube was attached to the second adapter and fog fluid flow was controlled by a pair of hemostat clamps.

To generate streaklines, thin copper wire (0.25 mm diameter) was wrapped around the Ni_Chrome wire at intervals and soldered to keep it in place. For the smokewire used, the wire/solder beads were spaced at 1 cm intervals, Fig. 4.1. The fog fluid tended to pool

on the beads, and it took some time for the wire to burn off these deposits, providing 5 to 10 seconds of continuous smoke. Close inspection shows that most of the streaklines are really two, closely spaced lines. Typically, the fluid pools above and below the beads, and it is these two deposits that burn and create the pairs of lines. The nickel chromium wire was fixed to a wing with airfoil NACA0014 by two posts such that a 2" distance was kept between the wire and the wing to avoid any interference. The flow was illuminated using a Smith-Vector Corp 750W Photographic Light.

A Sony DCR-VX1000 digital video camera was used to capture video images of the model in flapping motion and the wing at different angles of attack. A video capturing card was used to go through the images and grab the best pictures to present the flow behavior. Also, a Kodak DC 260 digital camera was used to capture some of the images.

B. CASE STUDIES

Two main study cases were investigated by flow visualization. The first was the fixed single NACA0014 airfoil at 0° and 4° angle of attack. The second case was the biplane configuration, which was investigated for three different cases, as will be explained later.

1. NACA0014 Airfoil At Zero Angle Of Attack

The angle of attack was set to zero, and the tunnel speed to $U_\infty = 2.24m/s$ which means that the Reynolds number was in the order of 10,000. The flow around the airfoil is presented in Fig. 4.2. A small separation area was noticed near the trailing edge at the upper surface.

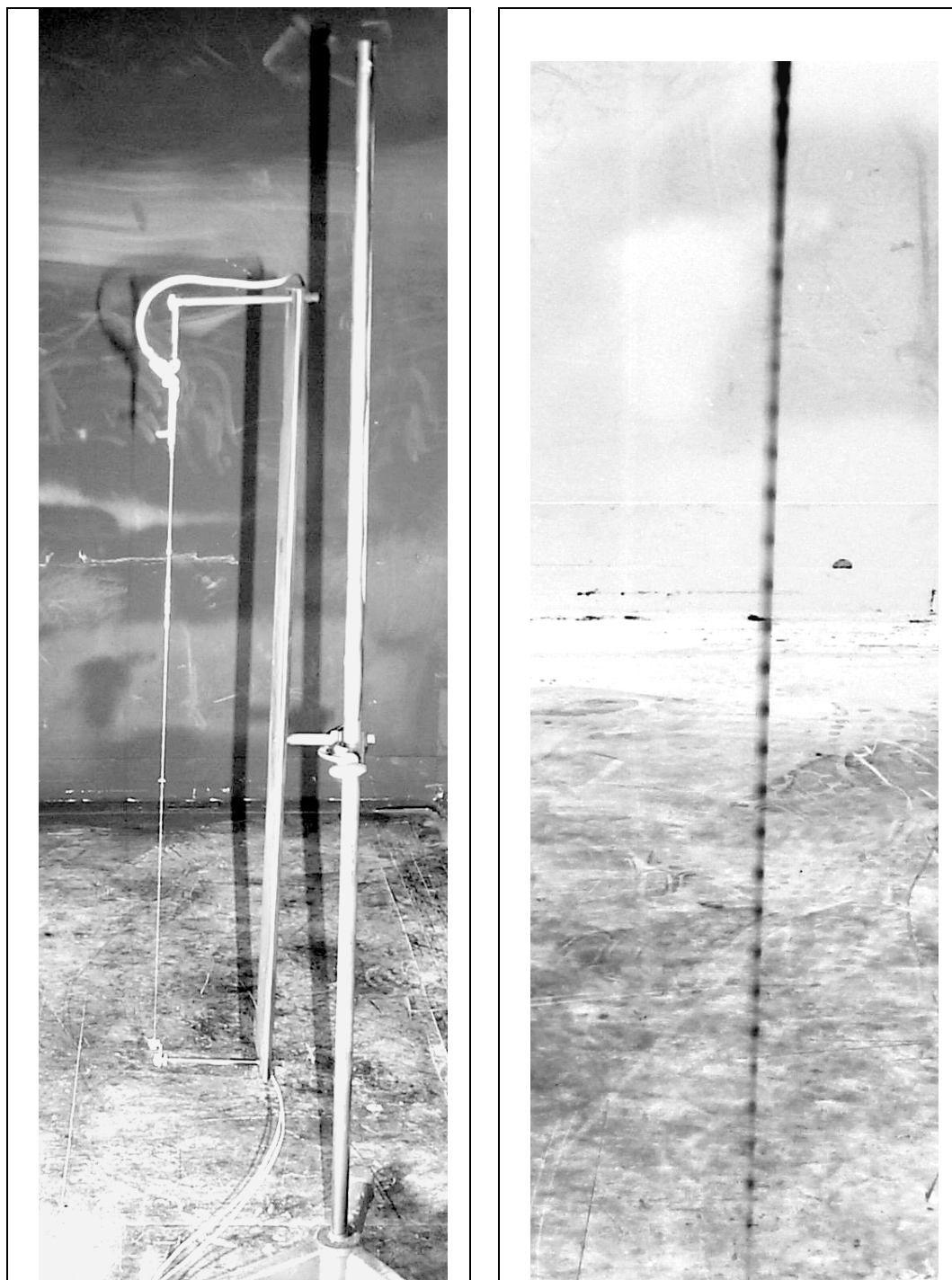


Figure 4.1. Smoke Wire Arrangement With the Copper Nodes on the Smoke Wire

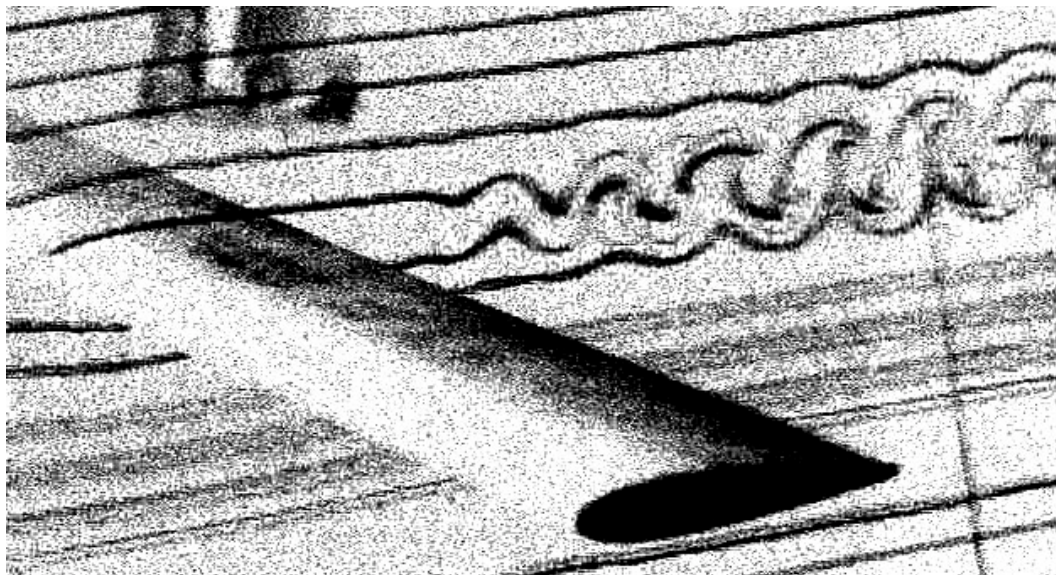


Figure 4.2. Flow Around NACA0014 at $\alpha = 0^\circ$, $U_\infty = 2.24$ m/s, $Re=10000$

2. NACA0014 Airfoil at 4° Angle Of Attack

At the same tunnel speed, $U_\infty = 2.24$ m/s, the angle of attack was increased to 4° and the video camera was used to record the flow around the airfoil. A grabber computer card was used to extract the pictures from the recorded tape.

A selected photo for the flow is shown in Fig. 4.3. They depict the development of the vortices around the airfoil and their shedding downstream into the wake.

3. Biplane Configuration

The biplane configuration was investigated for 3 different cases. The tunnel speed for all of these cases was $U_\infty = 2.24$ m/s and $Re=10,000$.

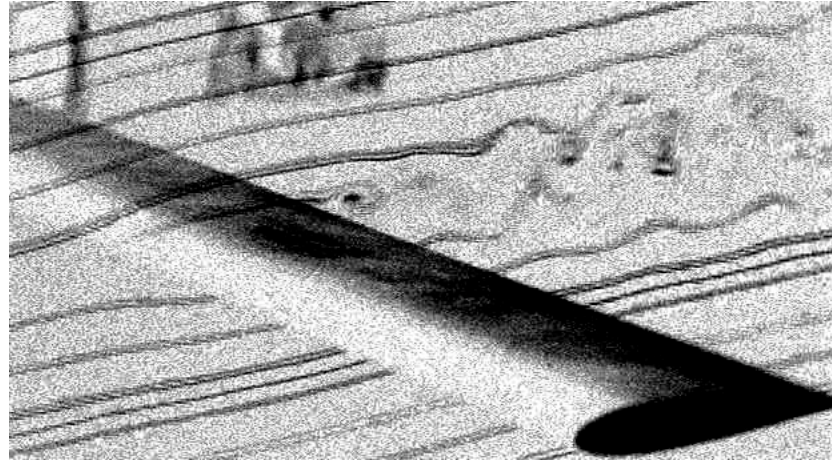


Figure 4.3. Vortex Shedding Around NACA0014 at $\alpha = 4^\circ$, $U_\infty = 2.24 \text{ m/s}$, $\text{Re}=10000$

a. Case1: minimum distance between the wings

In this case, the two wings were set such that the distance between them was the minimum distance. The video camera was used to capture the presented consecutive frames with time step 1/30 of a second. These pictures are shown in Fig. 4.4, and Fig. 4.5.

b. Case2: Maximum distance between the wings

In this investigation, the distance between the two flapping wings was set to the maximum value. The wind tunnel speed was kept the same as for the previous case. A selected photo is presented in Fig. 4.6

c. Case3: Wing flapping at $k=1$, $f=5.6 \text{ Hz}$

The model was set to flap at $f=5.6 \text{ Hz}$, corresponding to a reduced frequency, $k=1$. A series of consecutive frames is presented to show the flow behavior during two flapping cycles. The first cycle is presented in Fig. 4.7, Fig. 4.8, and Fig. 4.9. The second cycle is presented in Fig. 4.10 and Fig. 4.11.

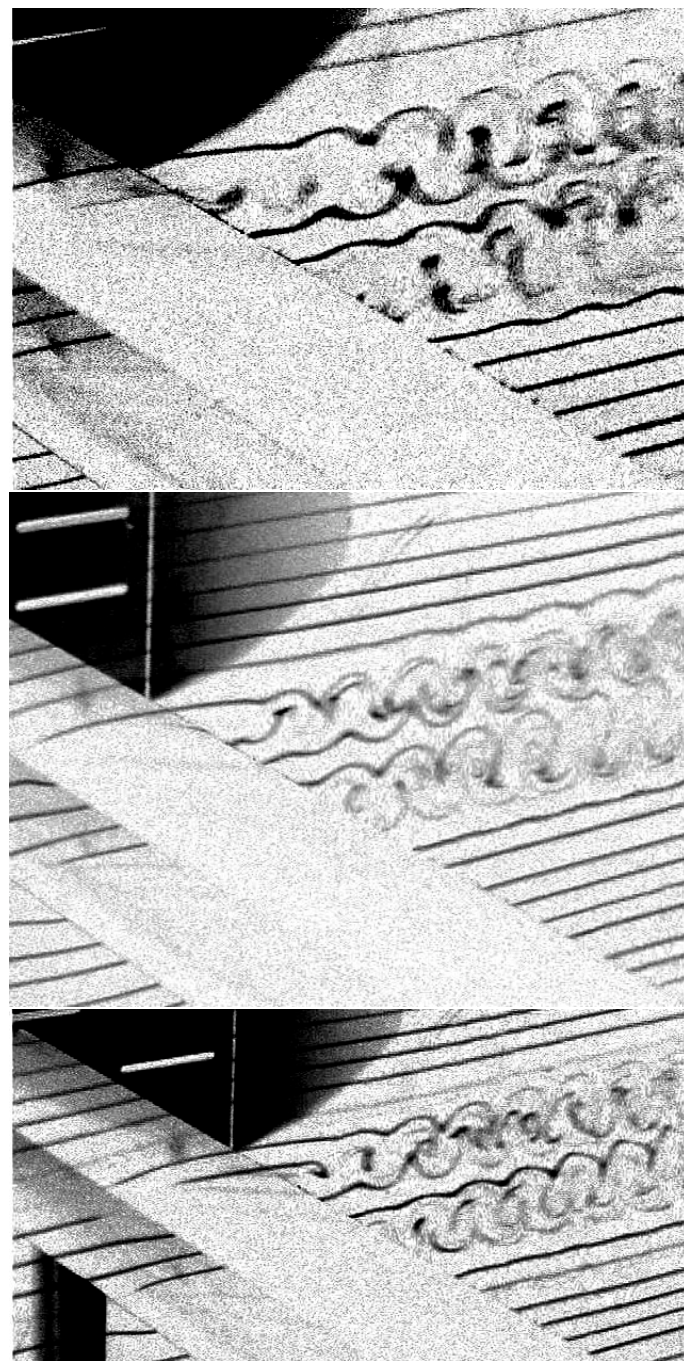


Figure 4.4. (a) Vortex Shedding Around Biplane with Minimum Distance between the Two Wings, $Re=10000$. The Time Step Between Frames = $1/30$ sec

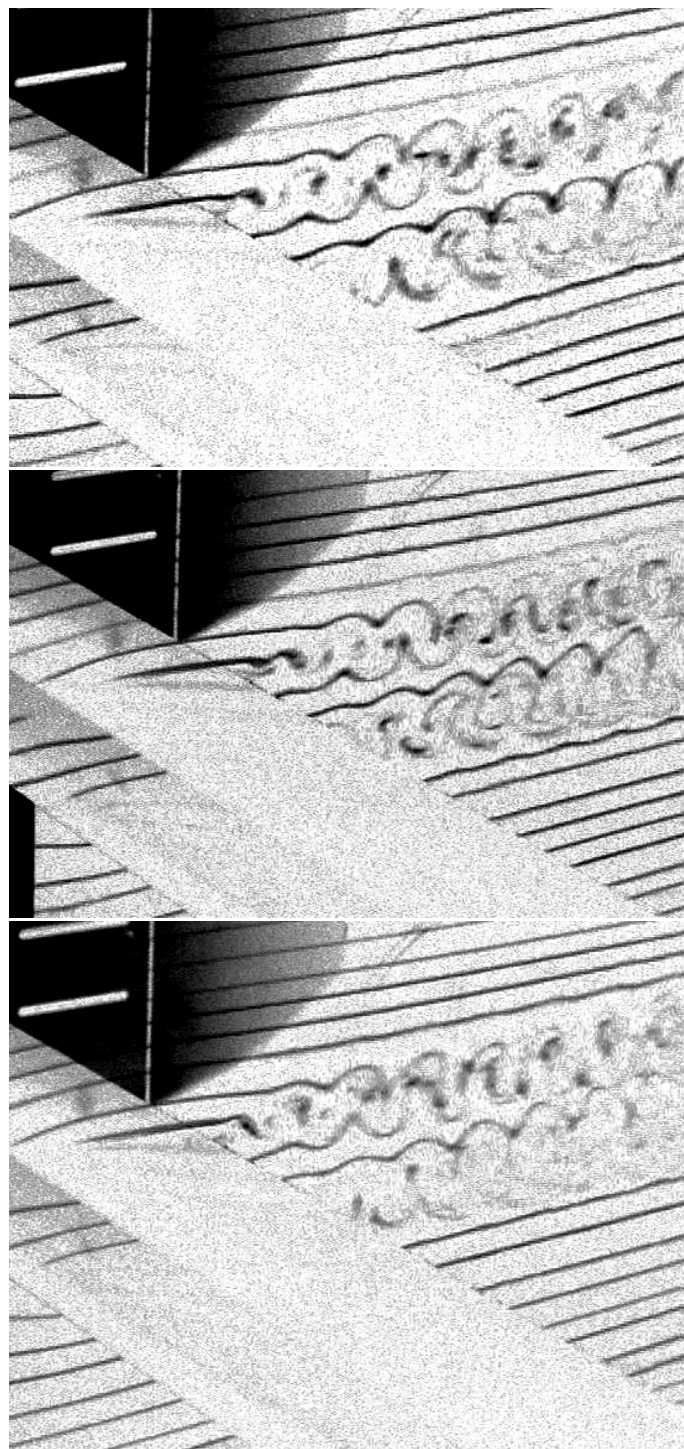


Figure 4.5. (b) Vortex Shedding Around Biplane with Minimum Distance between the Two Wings, $Re=10000$, with time step=1/30 sec

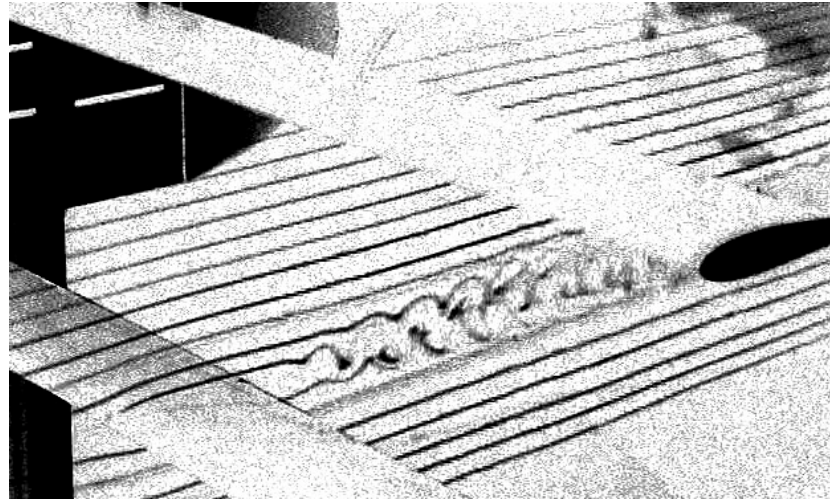


Figure 4.6. Vortex Shedding Around Biplane with Maximum Distance between the Wings,
 $Re=10000$

C. RESULTS

During the experiment the strobe light along with the frame speed for the video camera was altered to be able to capture the flow details around the airfoil. When the frame speed was set to 1/60 of a second , it was impossible to capture any details, only the average stream lines were captured. When the frame speed was increased to 1/500 of a second, the camera was able to capture the flow details. Hence, the strobe light was used to visually freeze the flow. As a result, the vortices that are shed downstream start to appear stationary, the strobe light frequencies were recorded and the shedding frequency was calculated as shown in Table 4.1

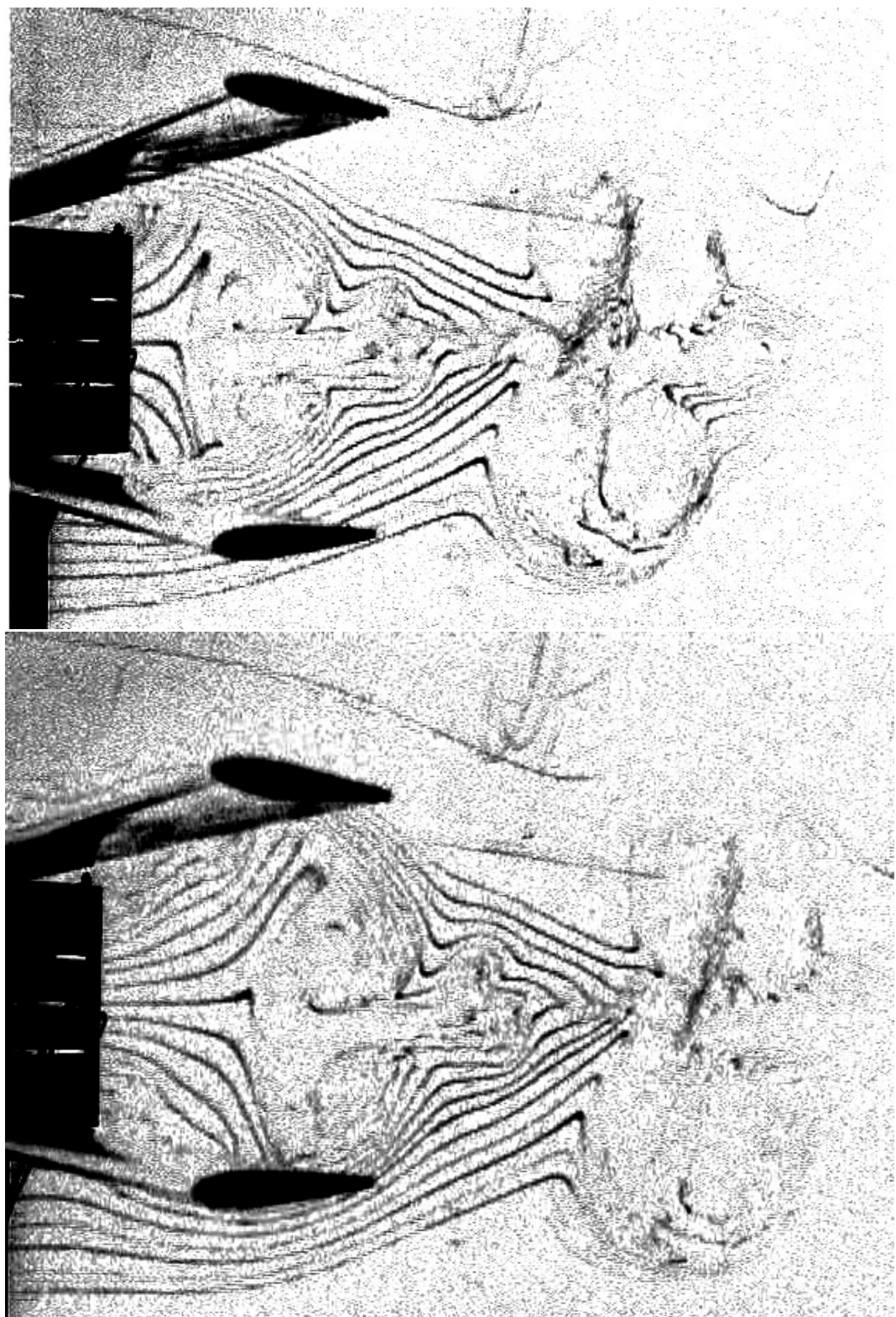


Figure 4.7. Vortex Shedding Around Biplane During Flapping, $\Phi = 0^\circ$ and $\Phi = 30^\circ$, $k=1$,

$U=2.24$ m/s, $Re=10000$

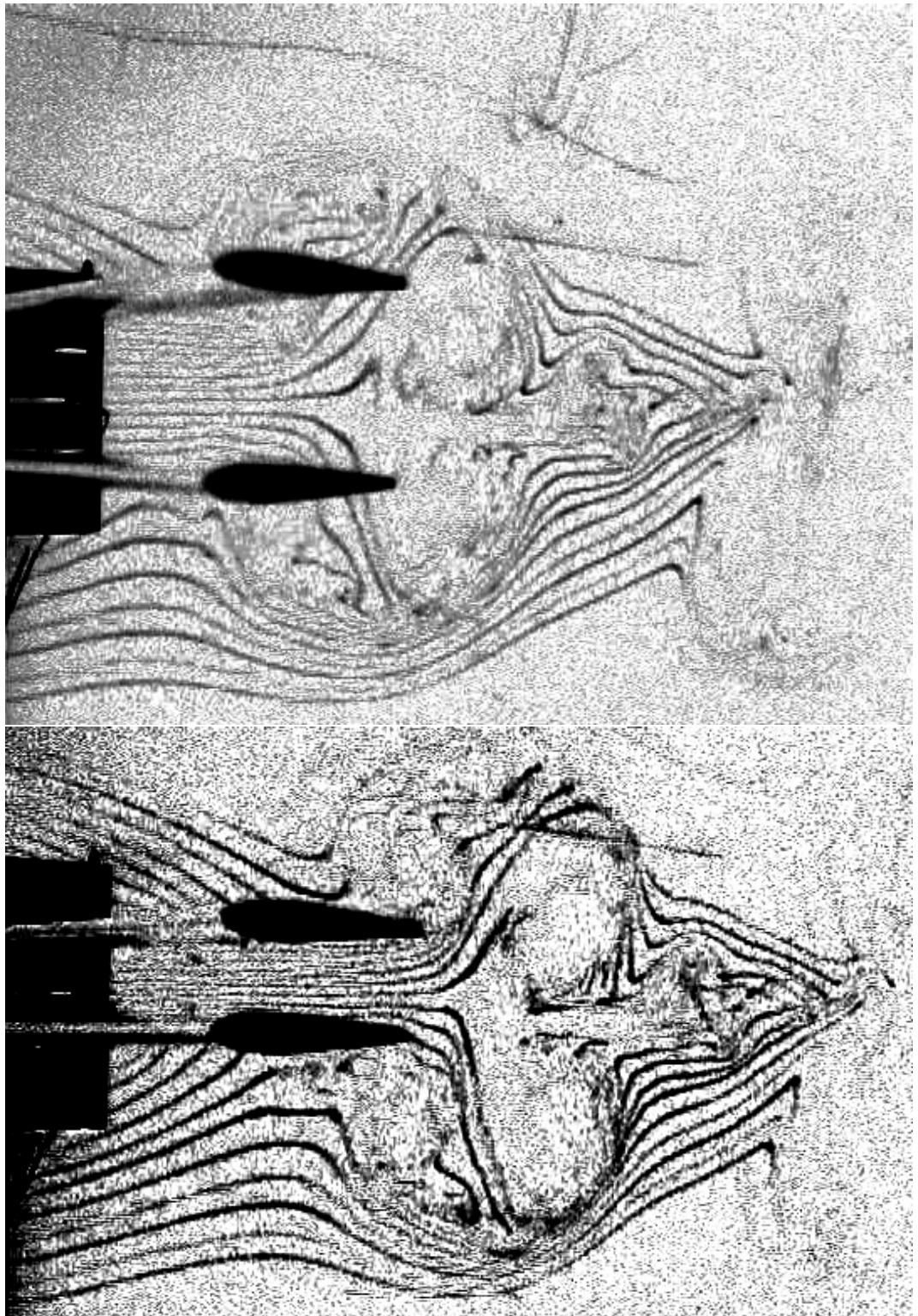


Figure 4.8. Vortex Shedding Around Biplane During Flapping, $\Phi = 135^\circ$ and $\Phi = 180^\circ$,
 $k=1$, $U=2.24$ m/s, $Re=10000$

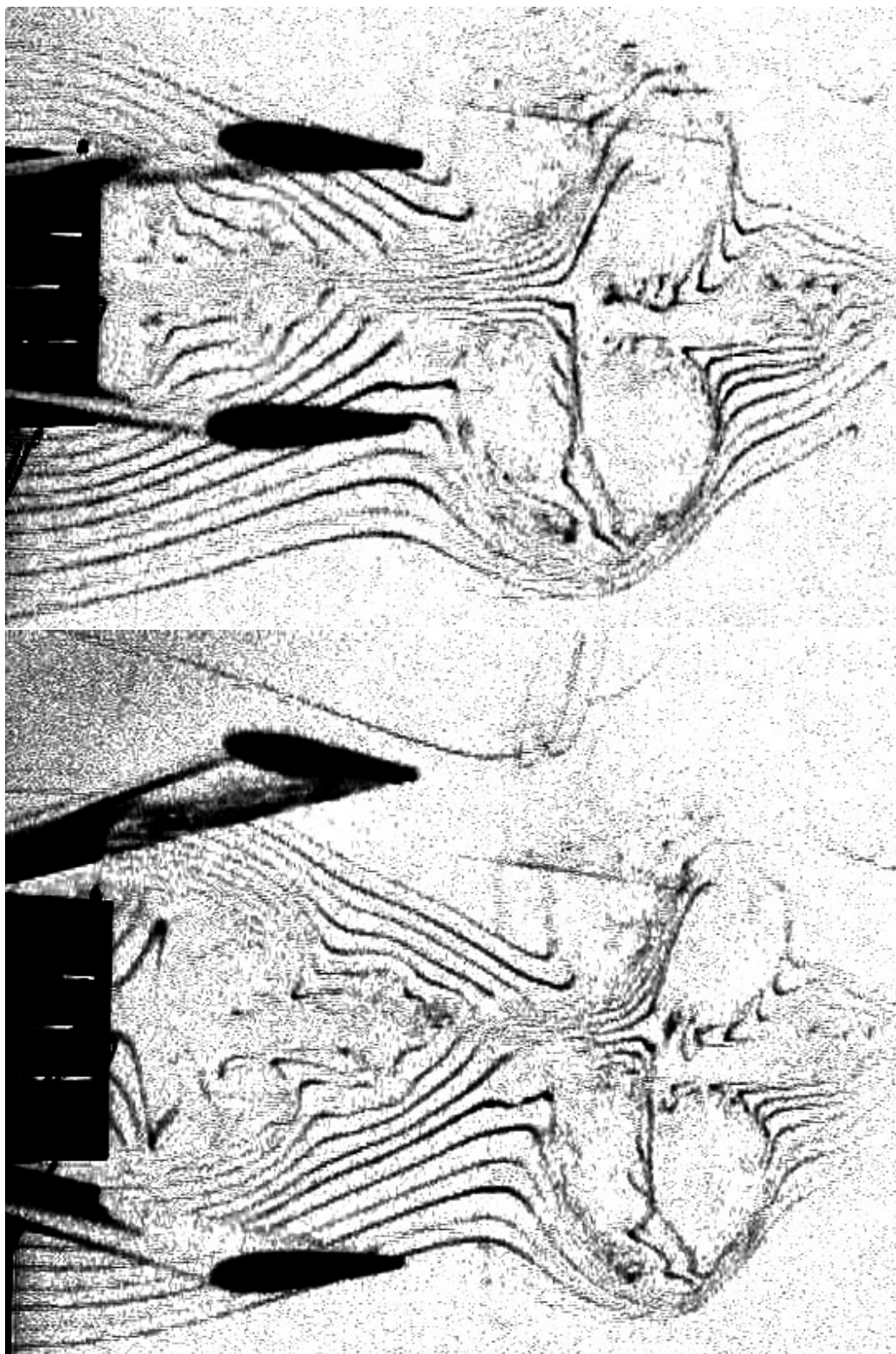


Figure 4.9. Vortex Shedding Around Biplane During Flapping, $\Phi = 225^\circ$ and $\Phi = 360^\circ$,
 $k=1$, $U=2.24$ m/s, $Re=10000$

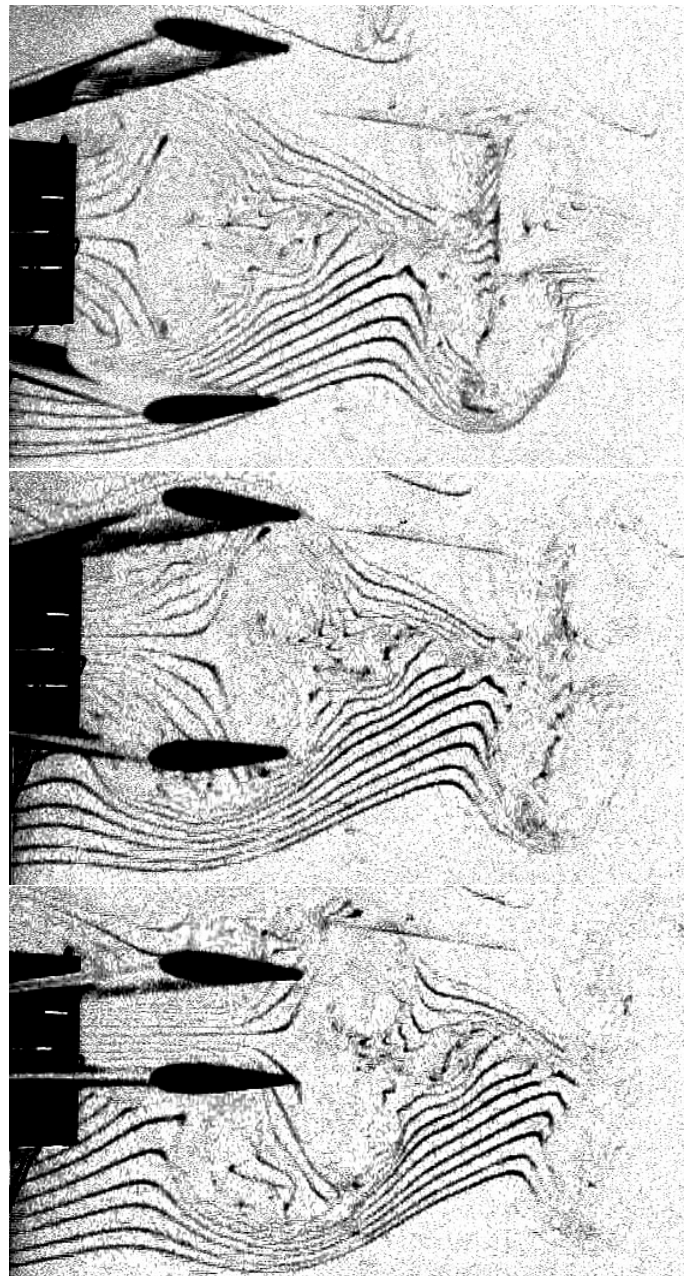


Figure 4.10. Vortex Shedding Around Biplane During Flapping, $\Phi = 0^\circ$, $\Phi = 45^\circ$ and $\Phi = 135^\circ$, $k=1$, $U=2.24$ m/s, $Re=10000$

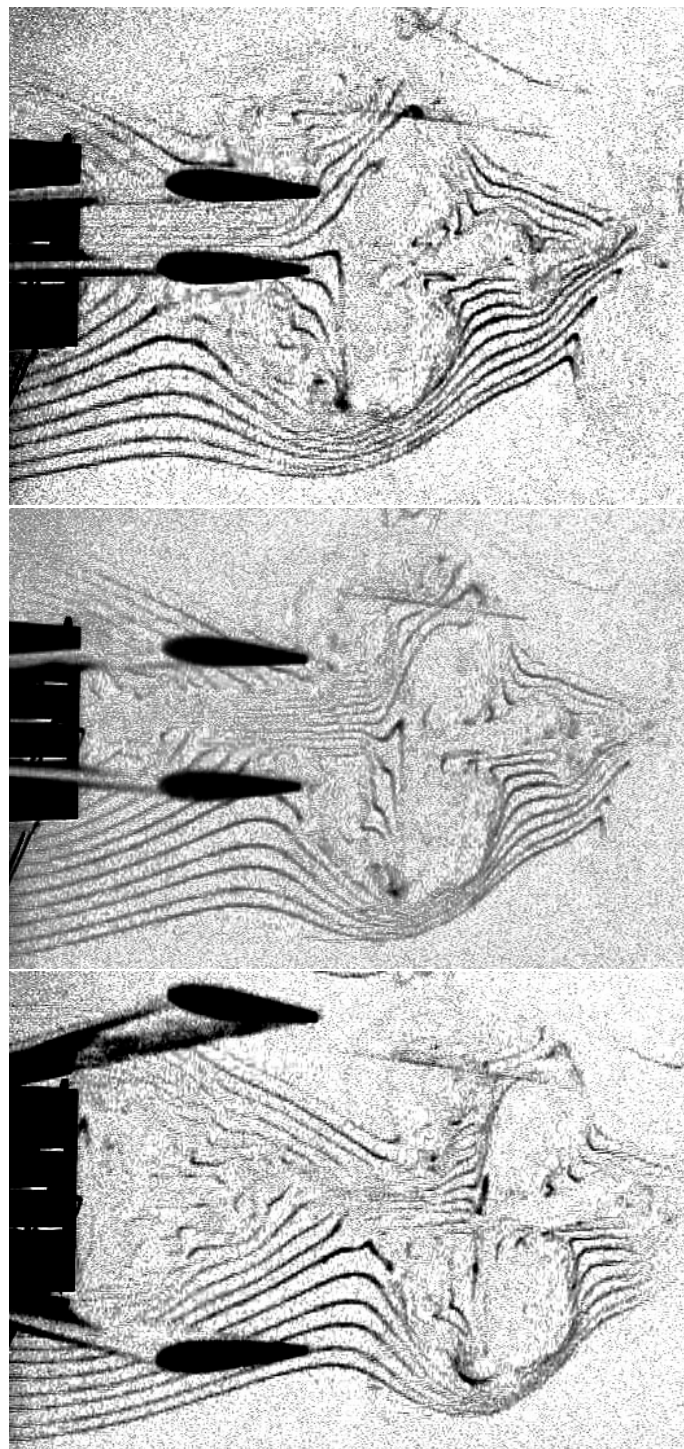


Figure 4.11. Vortex Shedding Around Biplane During Flapping, $\Phi = 180^\circ$, $\Phi = 225^\circ$ and $\Phi = 270^\circ$, $k=1$, $U=2.24$ m/s, $Re=10000$

Table 4.1. Shedding Frequency for Flapping Wing in Biplane Configuration

Reynolds Number	α [deg]	Shedding Frequency, Hz
5000	0	10.4
	4	9.7
7500	0	12.8
	4	8.14
10000	0	14.66
	4	8.0
15000	0	13.49

V. EXPERIMENTAL RESULTS

A. THRUST MEASUREMENTS

Jones [13] already provided extensive thrust measurements for the biplane configuration and several micro-air vehicle configurations. Therefore, in the present work, thrust generation by single plunging wings only was investigated. The effect of changing the flapping frequency on the thrust value was investigated. The effect of changing Reynolds number on the thrust force was investigated as well. The model was set to flap at frequencies between 2 to 7[Hz] with increment of 1[Hz]. The wind tunnel speed was varied from 3 to 9.5[m/s] with increment of 0.5[m/s]. The maximum flapping amplitude was 0.4C.

The effect of increasing the flapping frequency on the thrust coefficient is illustrated in Fig. 5.1 for different Reynolds numbers. The error involved in the thrust measurements was included as error bars.

In Fig. 5.2, the effect of varying Reynolds number on thrust coefficient is illustrated. The error in thrust measurement is included as error bars.

B. STEADY FLOW MEASUREMENTS

It was important to know detailed information about the flow behavior around the wing at the low speed of interest. A wing with a NACA0014 airfoil section was attached to a mechanism which allows a variable angle of attack. The LDV system was used to investigate the flow around the airfoil for three different cases. At zero angle of attack, the flow was probed at a free stream speed of 2 and 5 m/s, while for the third case the wing was at 4°

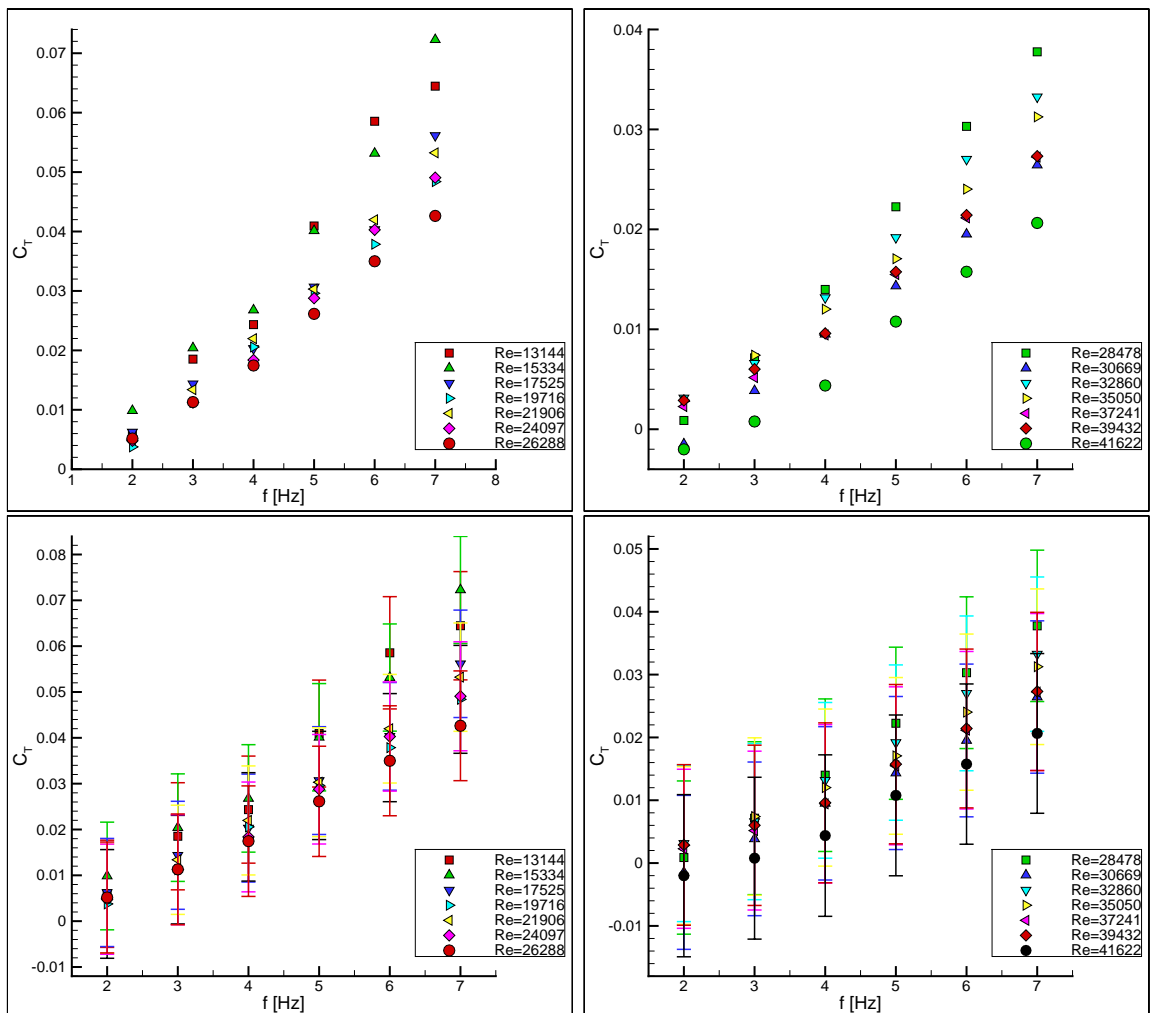


Figure 5.1. Thrust coefficient for single flapping wing in pure plunge with error included as error bar, $h=0.4C$,

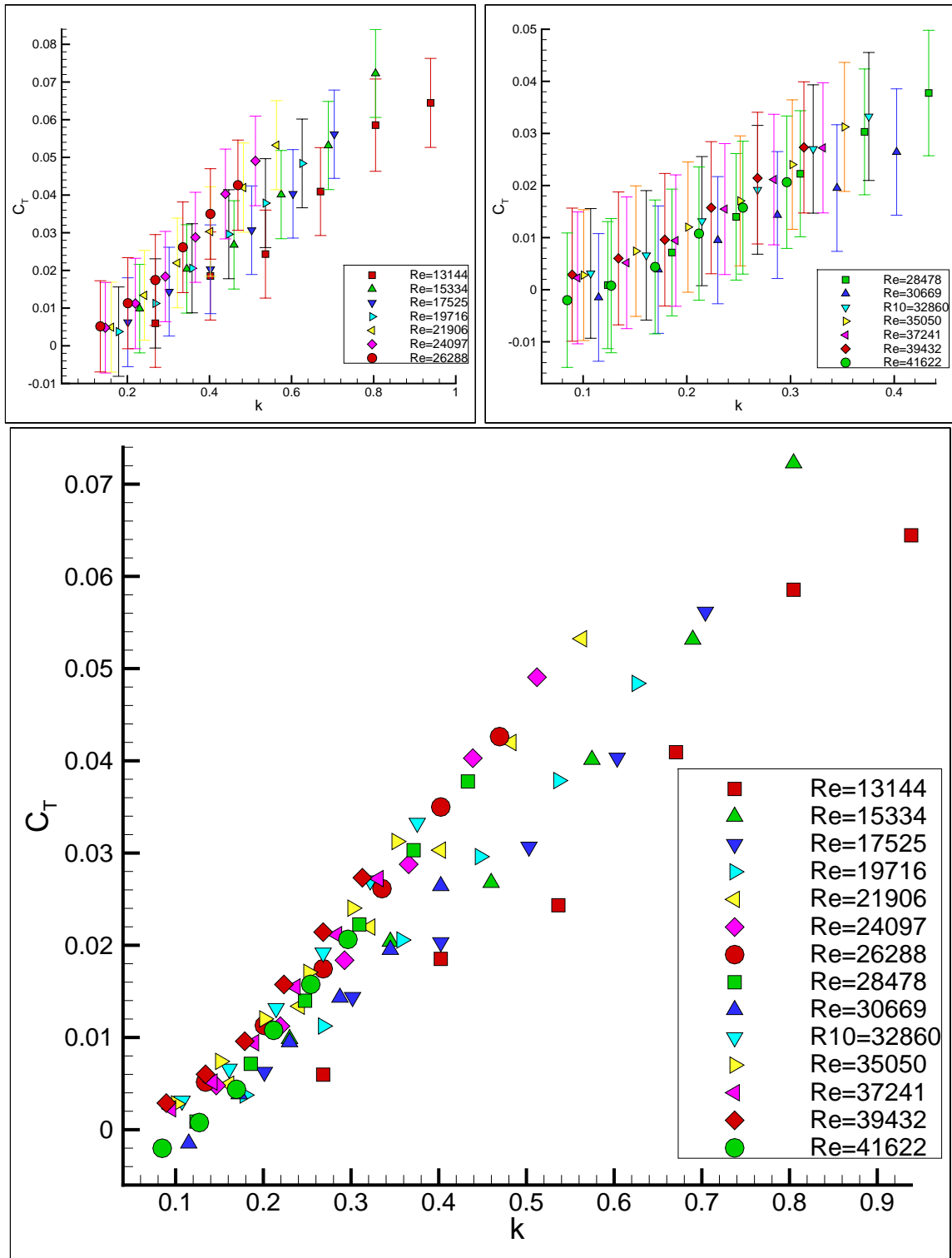


Figure 5.2. Thrust coefficient versus reduced frequency, k , for single flapping wing in pure plunge, with measurements error included as error bar, $h=0.4C$

angle of attack and the free stream velocity was 2 m/s. For each case, 10 axial locations were investigated to cover from quarter chord upstream to two chords downstream of the trailing edge. At each axial location, 11 locations were probed in the vertical direction.

1. First Case: $U=2$ m/s, $\alpha = 0^\circ$

The measured axial velocity is non-dimensionalized and is illustrated as a contour and carpet plot in Fig. 5.3. The velocity profiles at each axial location are presented in Fig. 5.4 while the velocity profile over the entire domain is shown in Fig. 5.5. The measured turbulence intensity in the free stream was 2.8906. The turbulence intensity was normalized by this value and presented in Fig. 5.6 as carpet and contour plots.

2. Second Case: $U=5$ m/s, $\alpha = 0^\circ$

The non-dimensional axial velocity component u/U is shown in Fig. 5.7 as a contour plot and as a velocity profile. Also, the non-dimensional axial velocity component u/U at different axial locations X/C is presented in Fig. 5.8. The turbulence intensity at the free stream measured and found to be 2.6929. This value was used to normalize the measured turbulence intensities and presented in Fig. 5.9.

3. Third Case: $U=2$ m/s, $\alpha = 4^\circ$

For this case, the angle of attack was increased to 4 degrees. The flow was investigated at 9 axial locations. At each axial location, 27 vertical locations were probed such that, $-1 \leq Z/C \leq 1$. The velocity values are shown as a carpet and contour plot in Fig. 5.10. The axial velocity profiles are presented in Fig. 5.11. The velocity profiles at different axial location are given in Fig. 5.12.

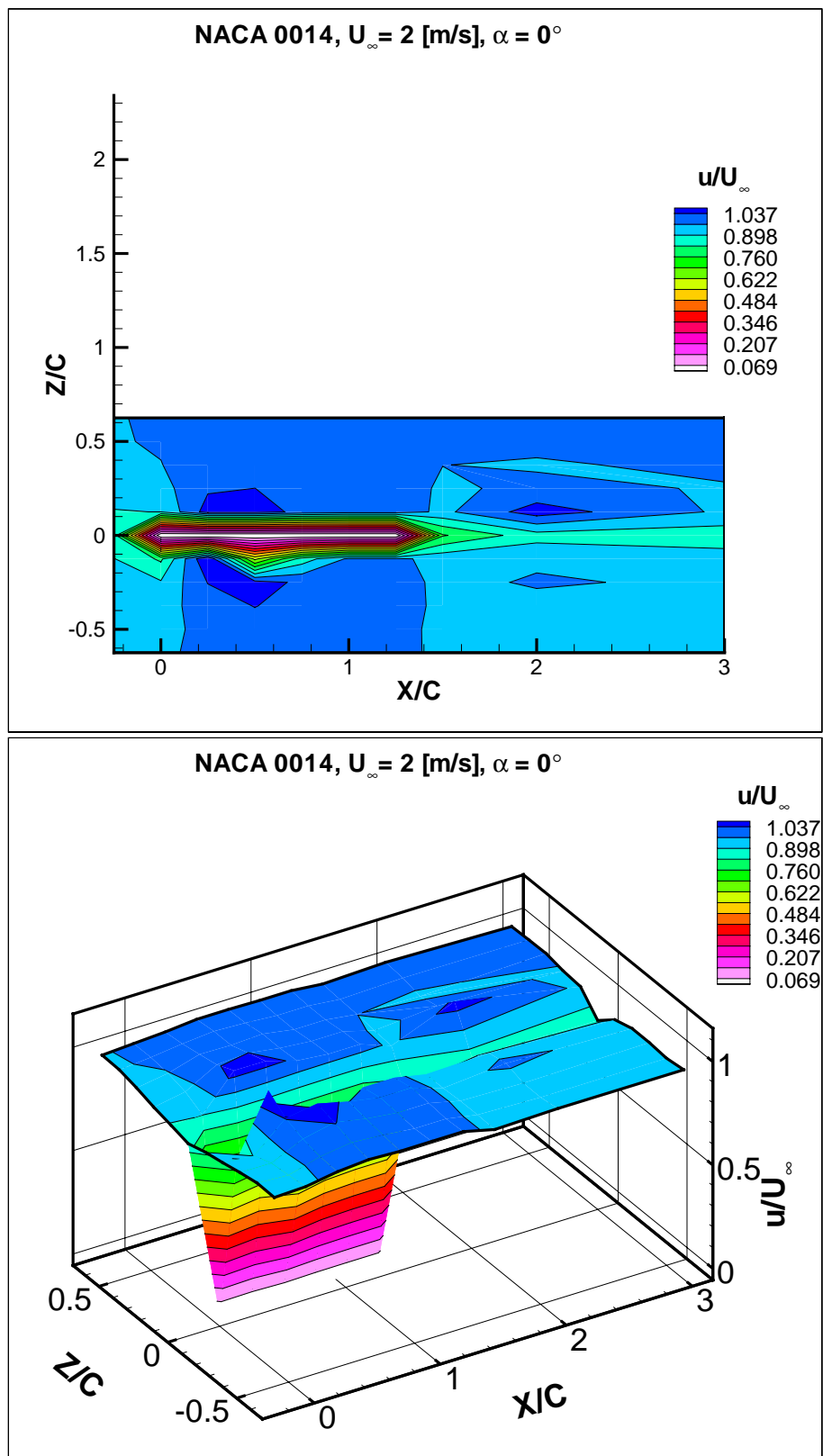


Figure 5.3. Axial Velocity at $U=2$ m/s and $\alpha = 0^\circ$

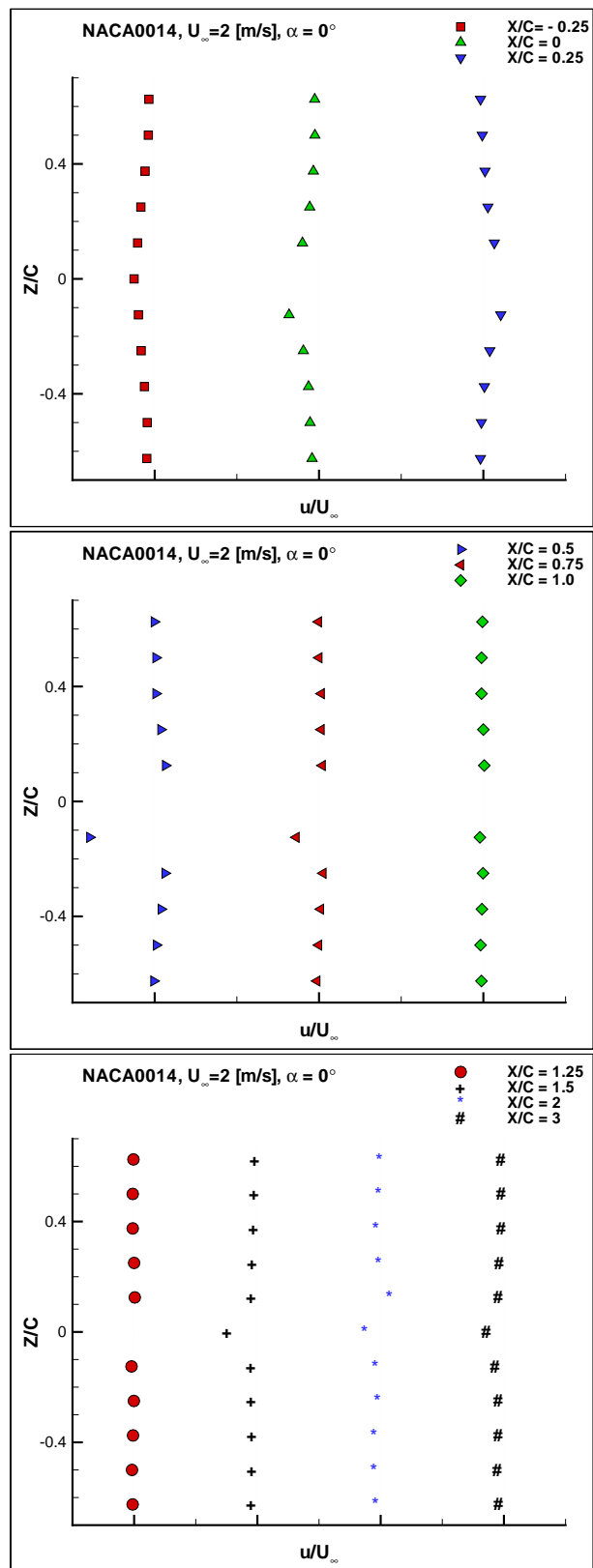


Figure 5.4. Velocity Profile at Different Axial Locations over NACA0014, $U=2$ m/s and $\alpha = 0^\circ$

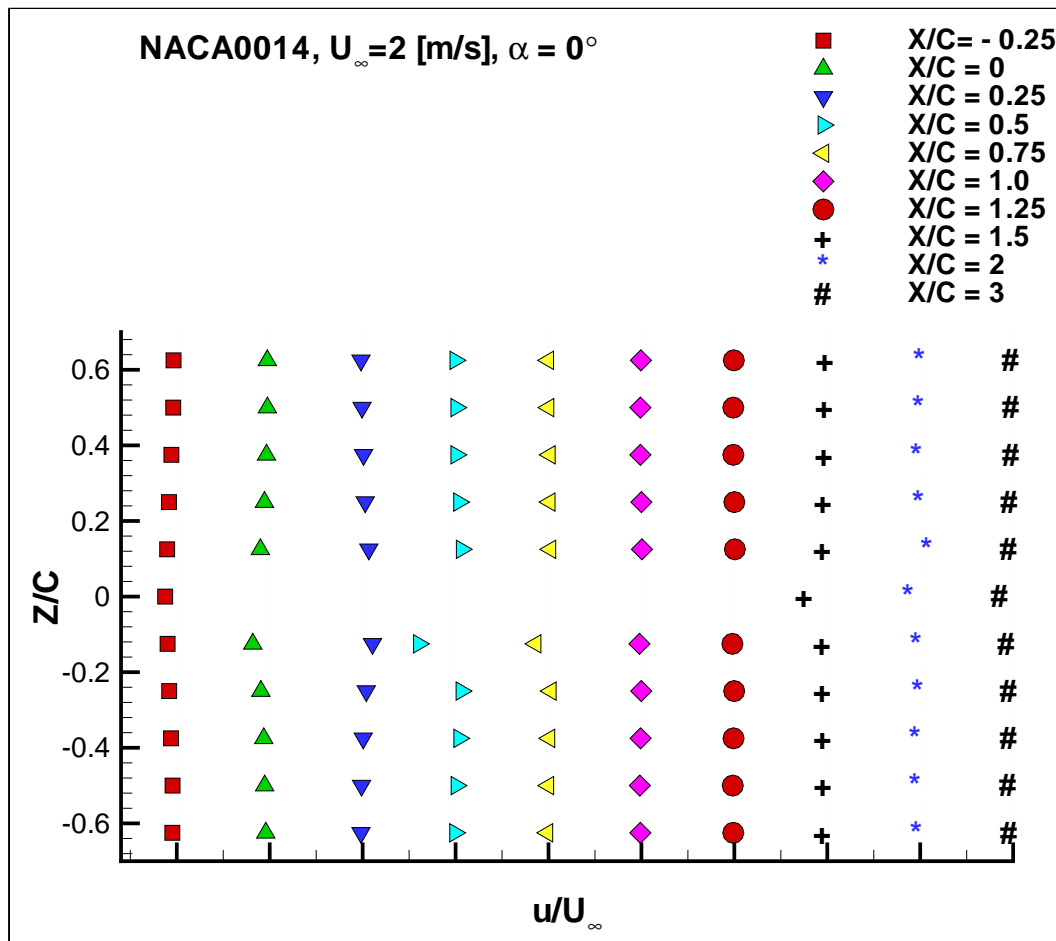


Figure 5.5. Velocity Profile over NACA0014 at $U=2$ m/s and $\alpha = 0^\circ$

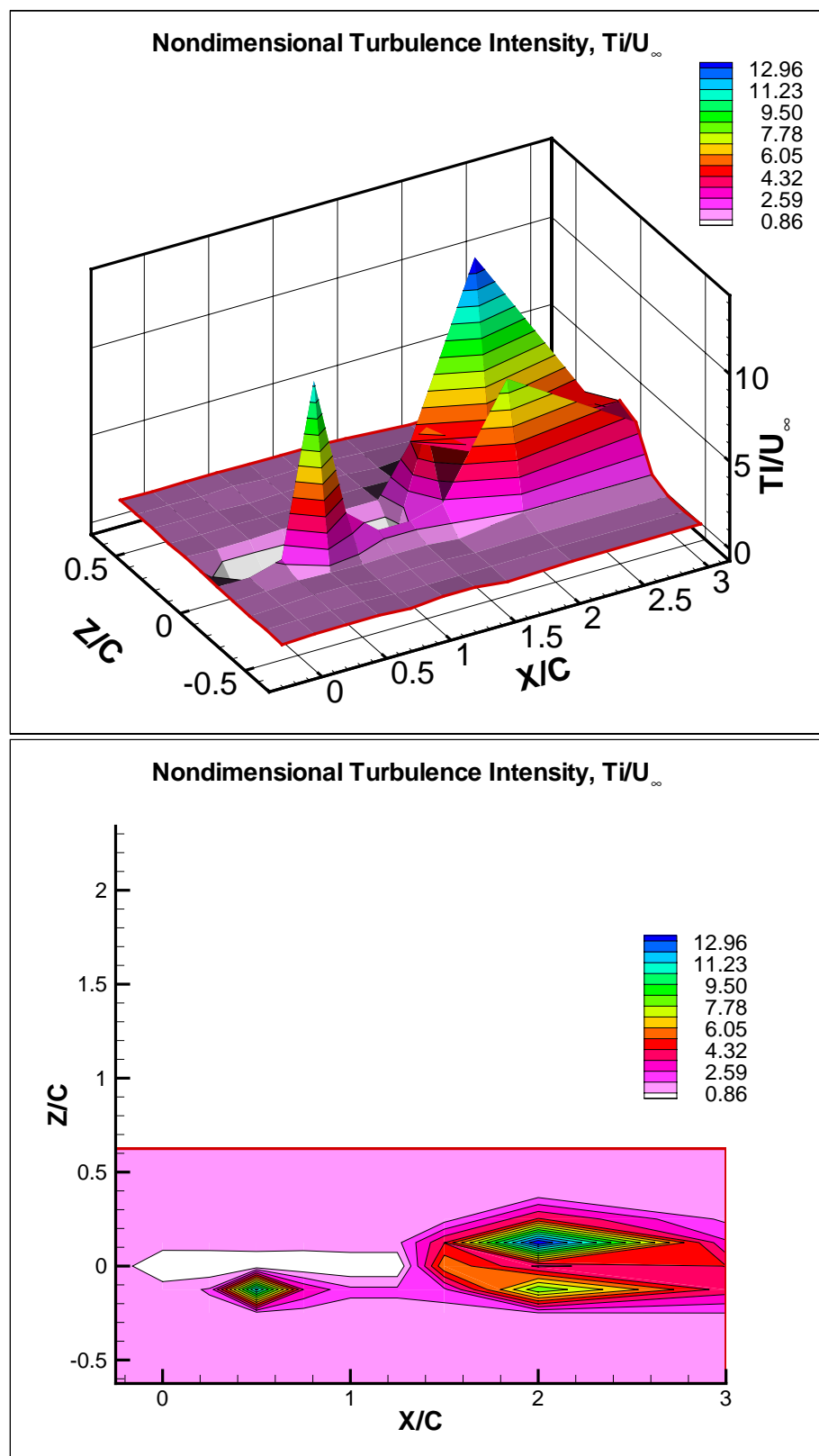


Figure 5.6. Nondimensional Turbulence Intensity over NACA0014 at $U=2$ m/s and $\alpha = 0^\circ$

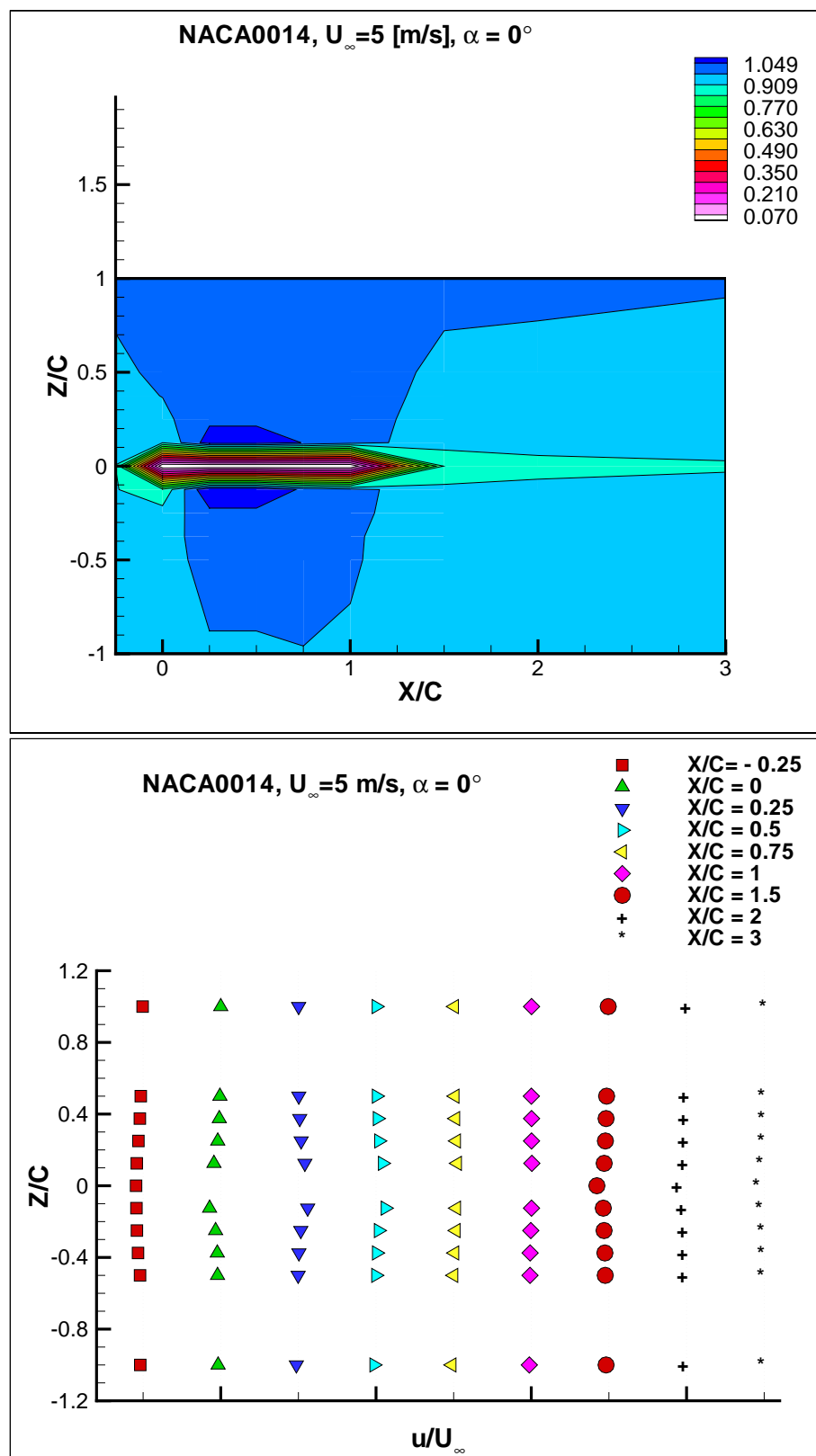


Figure 5.7. Nondimensional Axial Velocity Component at $U=5$ m/s and $\alpha = 0^\circ$

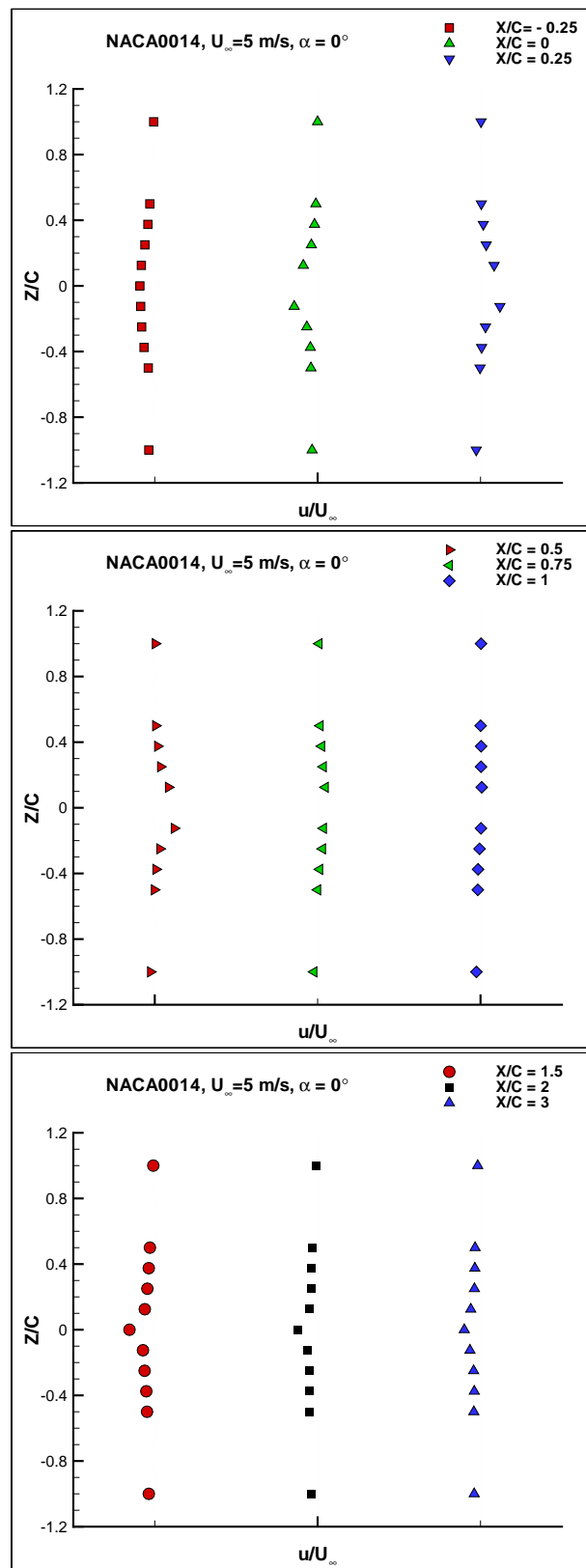


Figure 5.8. Nondimensional Axial Velocity Component at $U=5$ m/s and $\alpha = 0^\circ$

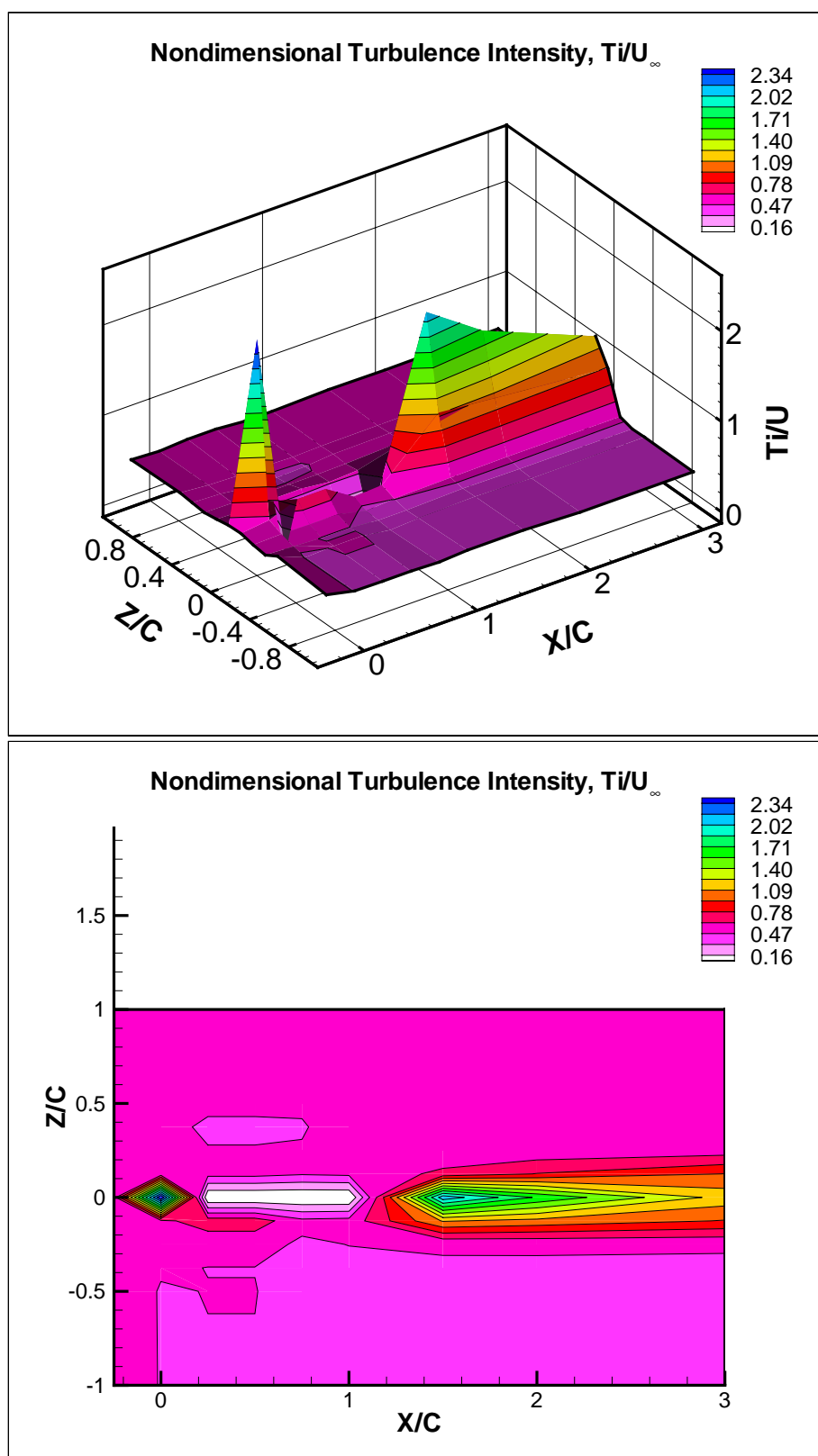


Figure 5.9. Nondimensional Turbulence Intensity at $U=5$ m/s and $\alpha = 0^\circ$

The turbulence intensity was normalized by the measured turbulence intensity at the free stream which was 2.6929 and is presented in Fig. 5.13.

C. UNSTEADY FLOW MEASUREMENTS

The flapping model was used as the test model for the unsteady measurements. LDV was used along with the RMR to measure the axial velocity component and stamp it with the wing position through the triggering signal generated by the micro-switch.

1. Biplane Configuration

The flow around the biplane configuration during flapping was investigated. The wind tunnel speed was 2 m/s and the flapping frequency was 5 Hz, which corresponds to a reduced frequency, k , of 1. The Reynolds number was of 8763. Nine locations were investigated along the airfoil in the downstream direction. At each location, 17 points were measured. In total, 153 points were measured. At each point, the LDV was set up to obtain 10000 samples or 8 minutes measuring time, whichever happens faster. It was found that 10000 samples were enough to give acceptable statistics.

The area investigated was 3.25 chord lengths in the downstream direction and 4.2 chord lengths in the vertical direction. The locations investigated were $X/C=-0.25, 0, 0.25, 0.5, 0.75, 1.0, 1.5, 2.0$ and 3.0 . At each location, 17 points were investigated such that point number 9 was located mid-way between the two flapping wing.

The measured axial velocity component, u , at each position Z/C is presented as a function of the plunge phase angle, Φ . In the same time, the measured u is presented as carpet and contour plots at each axial location. Nondimensional turbulence intensity,

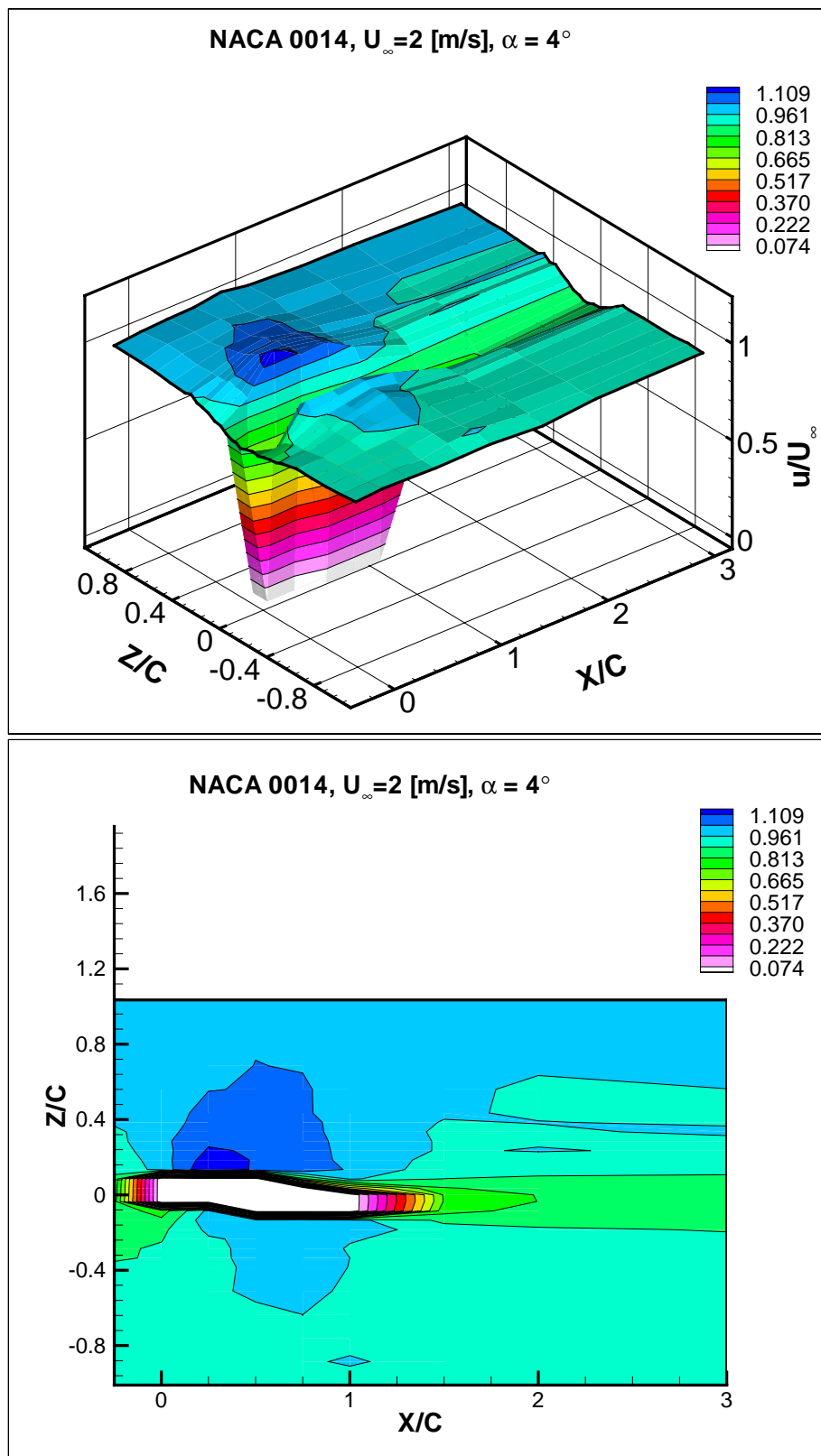


Figure 5.10. Axial Velocity at $U_{\infty} = 2\text{m/s}$ and $\alpha = 4^\circ$

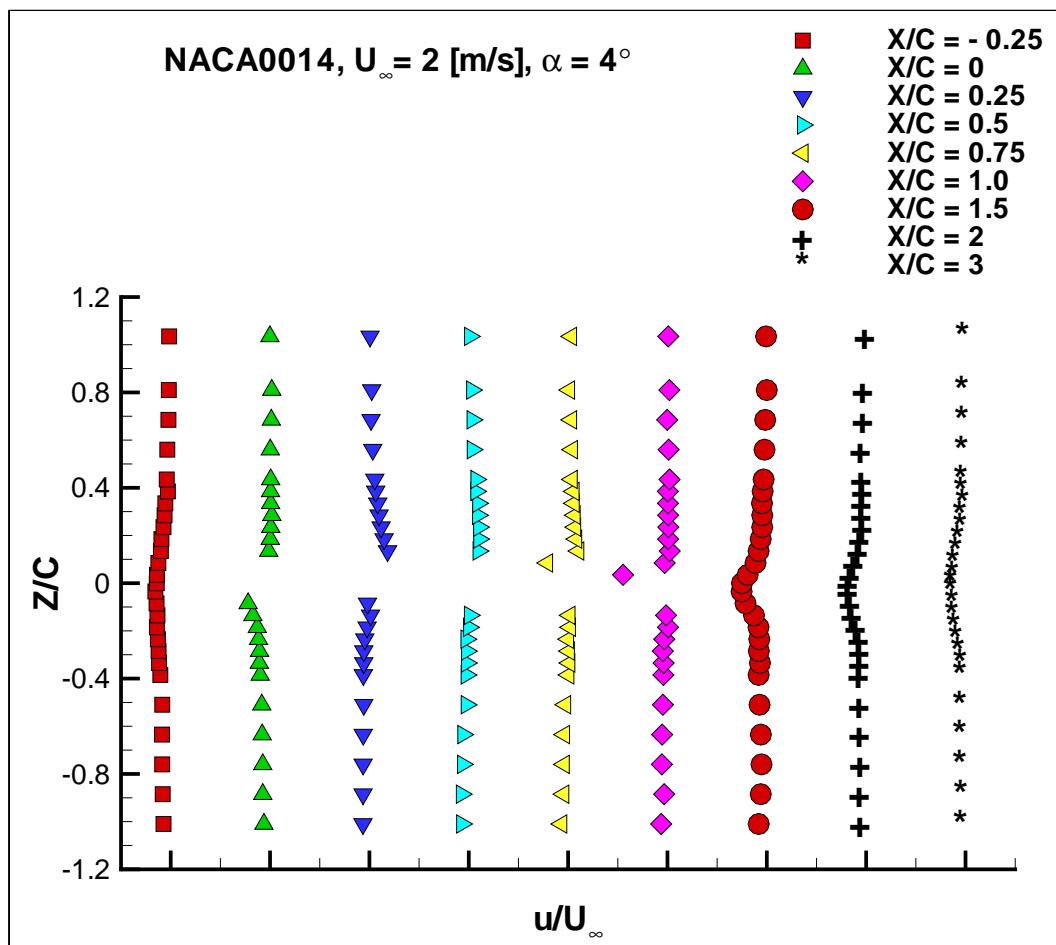


Figure 5.11. Axial Velocity Profile at Measured Axial Locations, $U_\infty = 2$ m/s and $\alpha = 4^\circ$

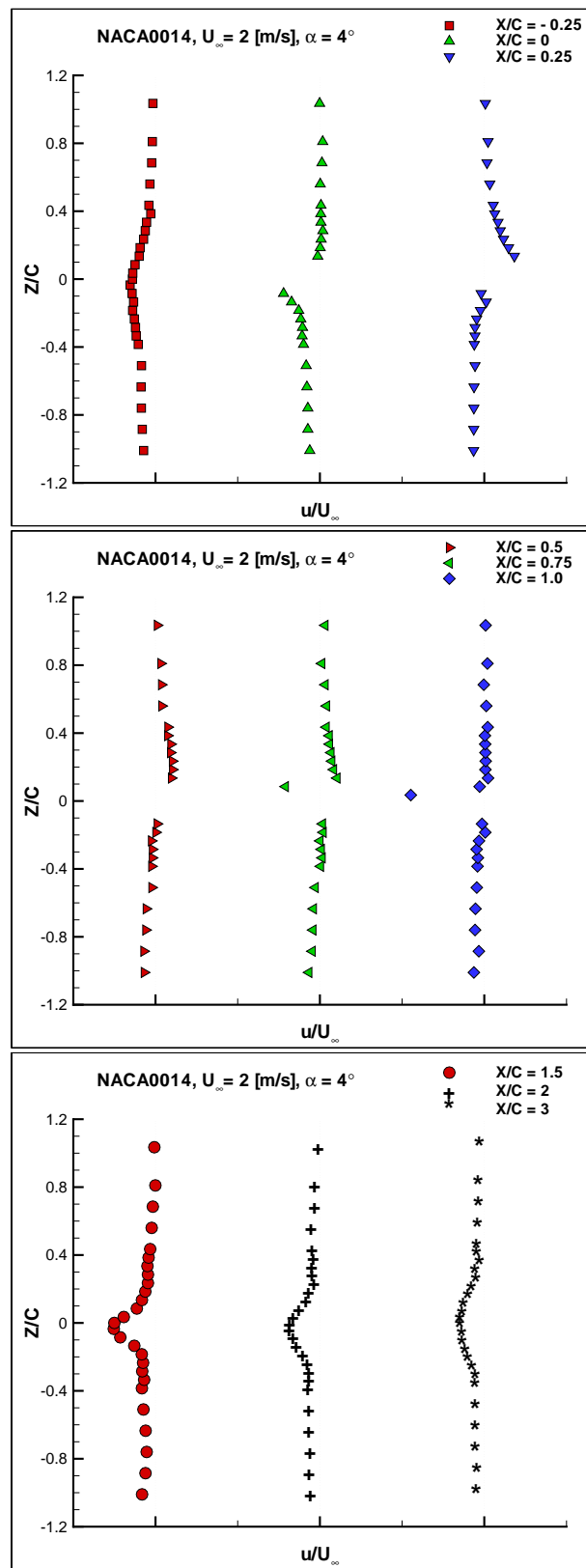


Figure 5.12. Axial Velocity Profile at $U_\infty = 2$ m/s and $\alpha = 4^\circ$

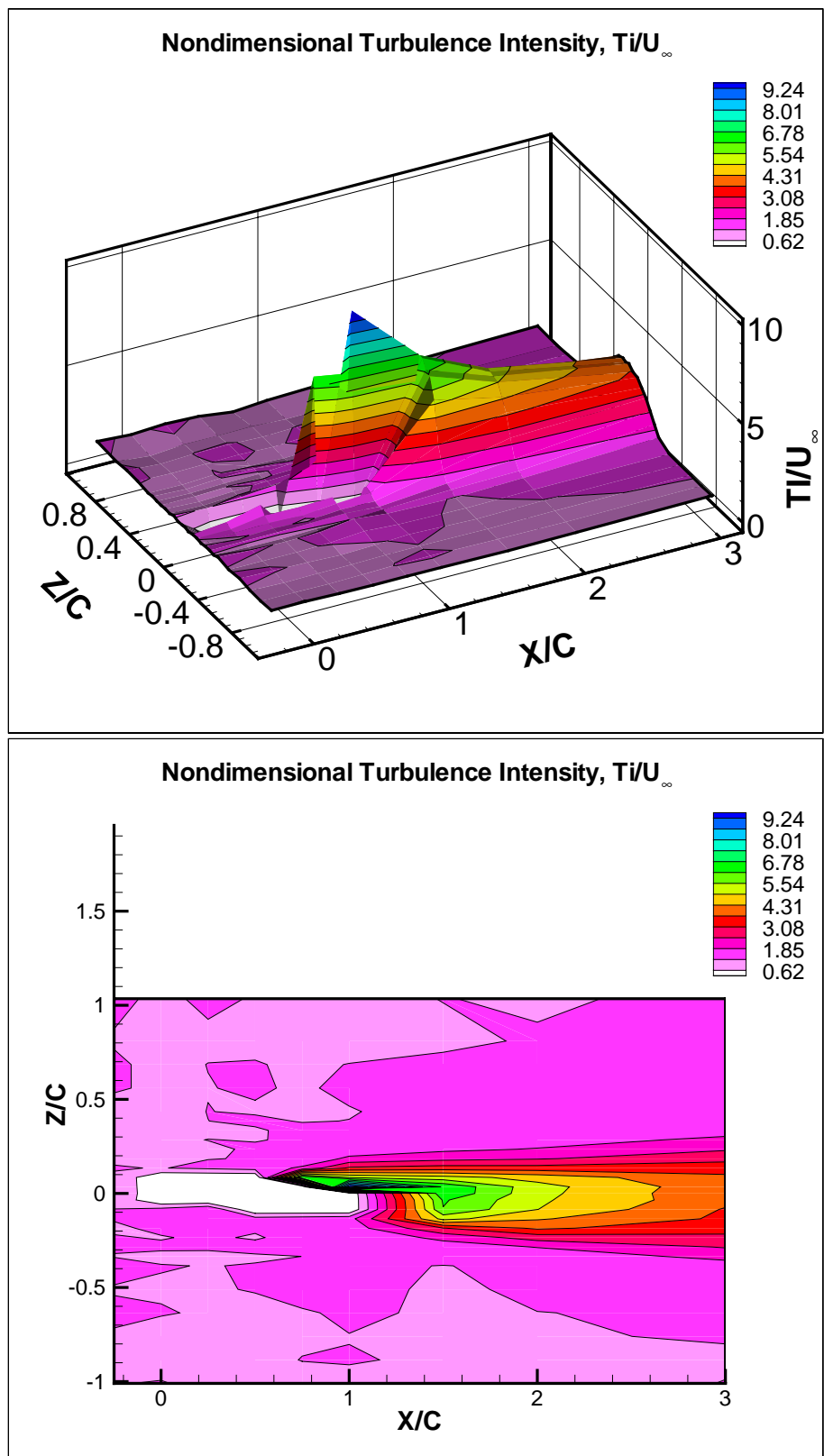


Figure 5.13. Normalized Turbulence Intensity at $U_{\infty} = 2m/s$ and $\alpha = 4^{\circ}$

Table 5.1. Biplane Configuration

X/C	$u/U\infty Vs.\Phi$	u/U as carpet and contour plots	Ti/U_∞
-0.25	Fig. B.1	Fig. 5.14	Fig. 5.15
0.0	Fig. B.2	Fig. 5.16	Fig. 5.17
0.25	Fig. B.3	Fig. 5.18	Fig. 5.19
0.5	Fig. B.4	Fig. 5.20	Fig. 5.21
0.75	Fig. B.5	Fig. 5.22	Fig. 5.23
1.0	Fig. B.6	Fig. 5.24	Fig. 5.25
1.5	Fig. B.7	Fig. 5.26	Fig. 5.27
2.0	Fig. B.8	Fig. 5.28	Fig. 5.29
3.0	Fig. B.9	Fig. 5.30	

Ti/U_∞ is presented as carpet plot at each location. The related figures for each axial position X/C is presented in Table 5.1

The two wings start flapping above the middle point for each one of them at plunge phase angle, $\Phi = 0$ in opposite directions. This means that the upstroke starts at $\Phi = 0$.

a. Average Velocity

The data extracted from the LDV measurements was used to calculate the average velocity profile at each location. The obtained velocity profiles are given in Fig. 5.32.

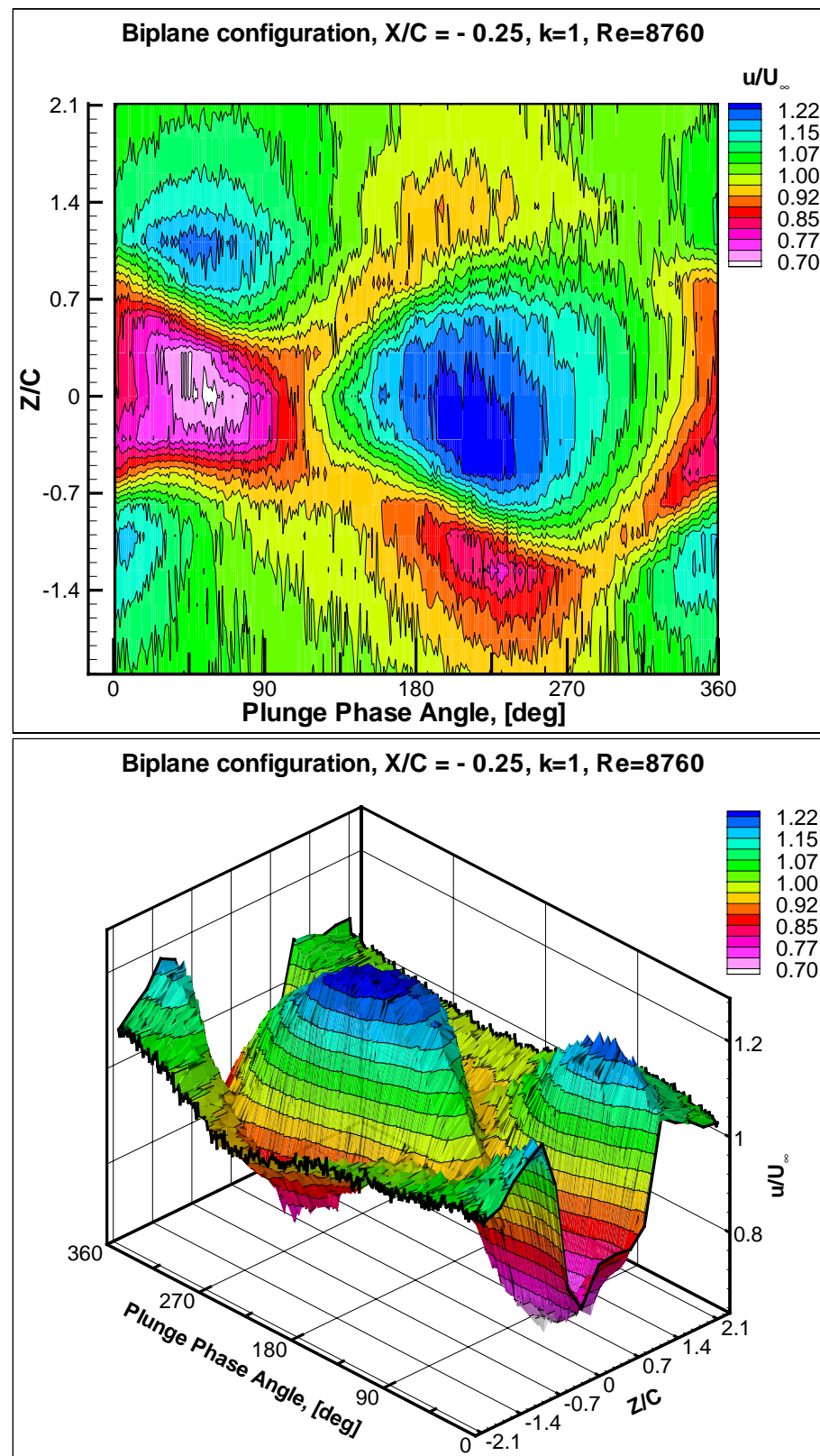


Figure 5.14. Measured Axial Velocity Component, u , at $X/C=-0.25$

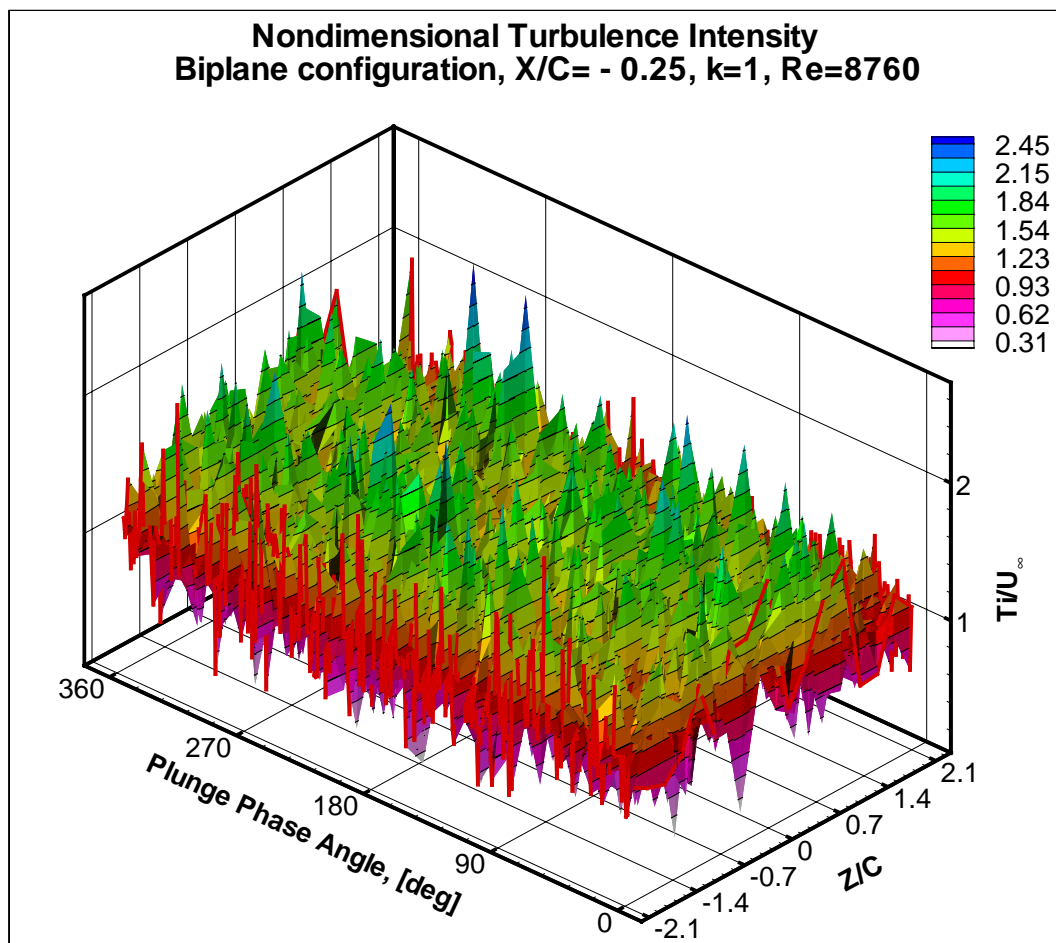


Figure 5.15. Nondimensional turbulence intensity at $X/C=-0.25$

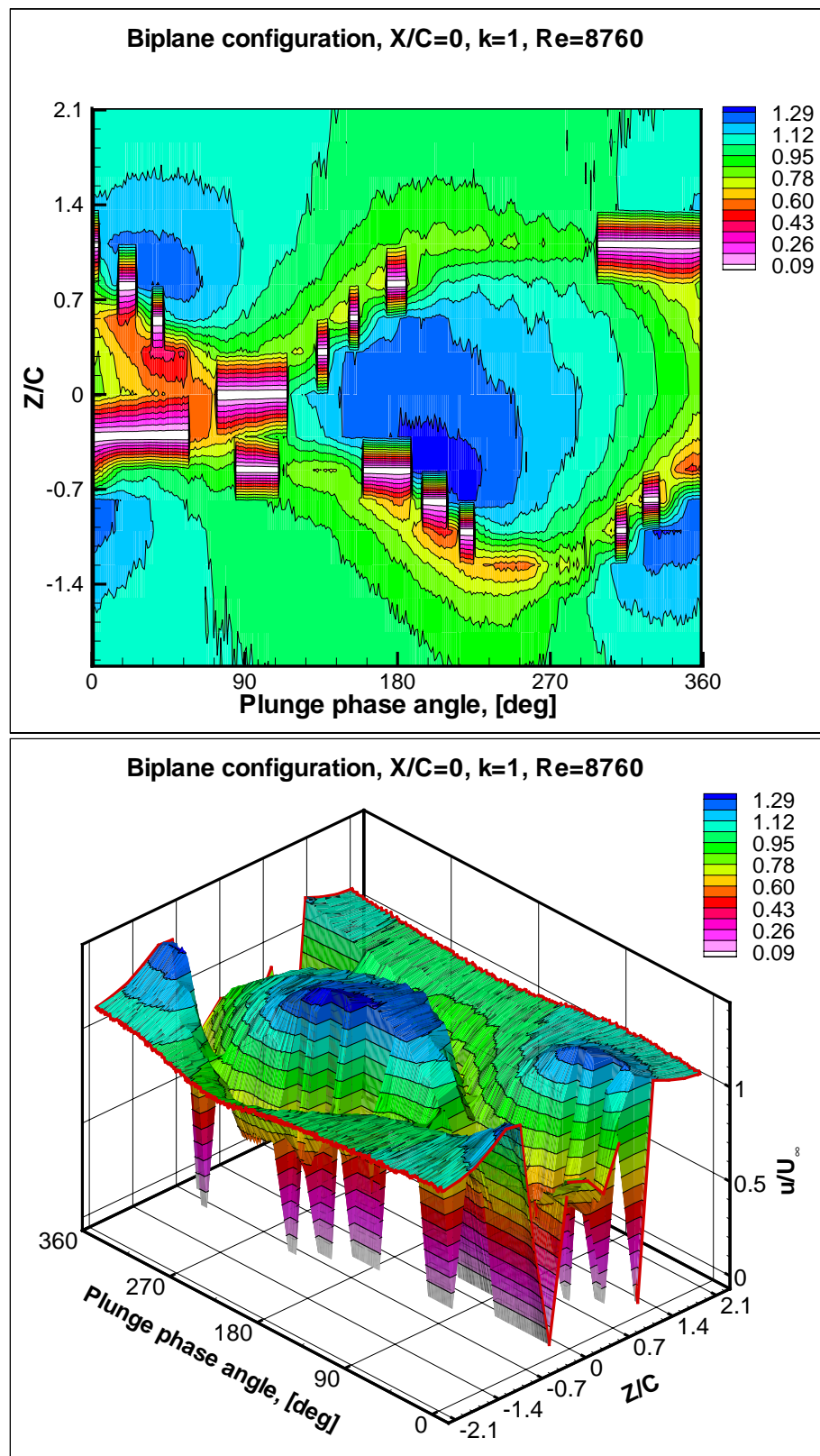


Figure 5.16. Measured Axial Velocity Component, u , at $X/C=0$, the Leading Edge

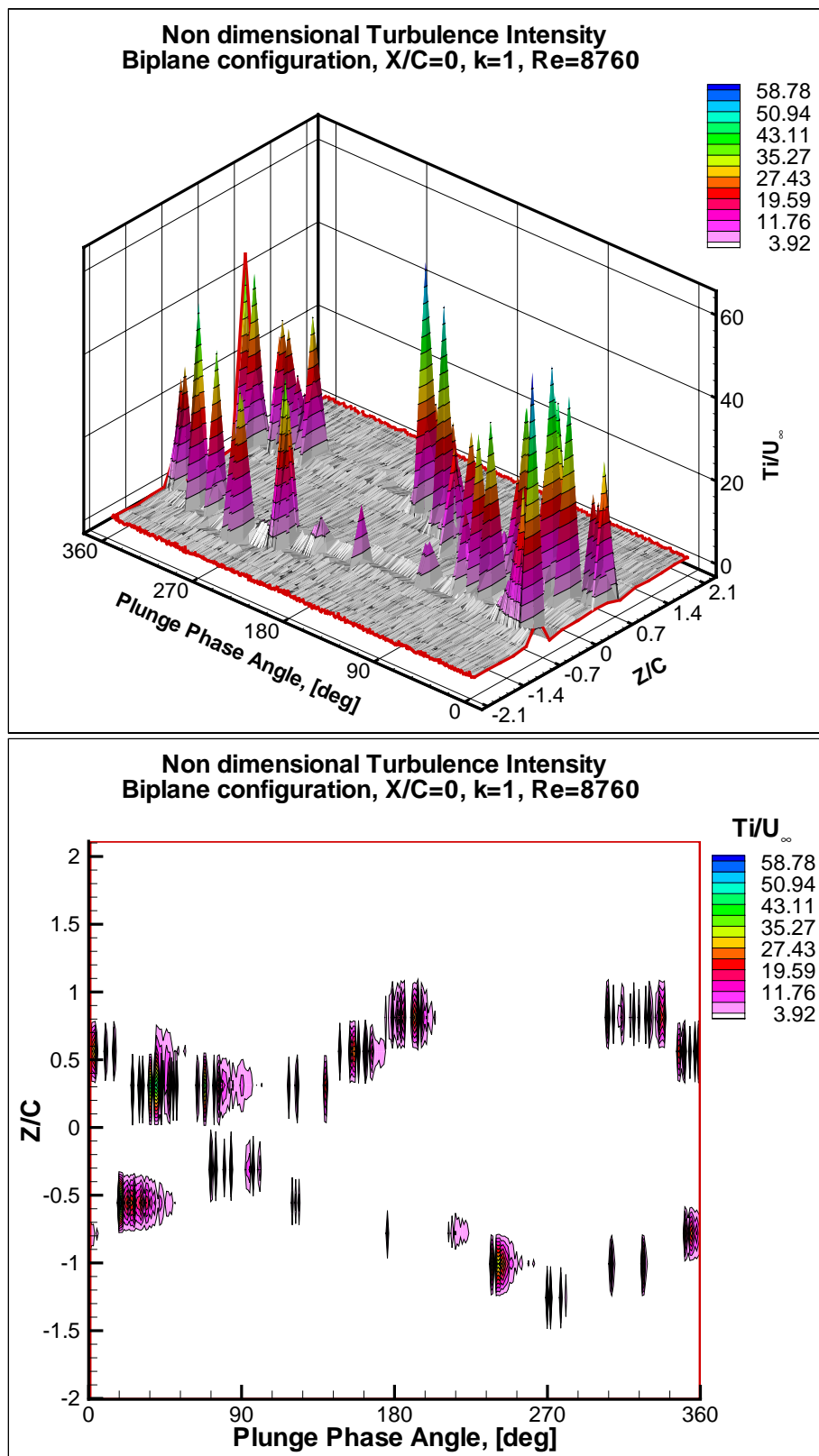


Figure 5.17. Nondimensional Turbulence Intensity at the Leading Edge

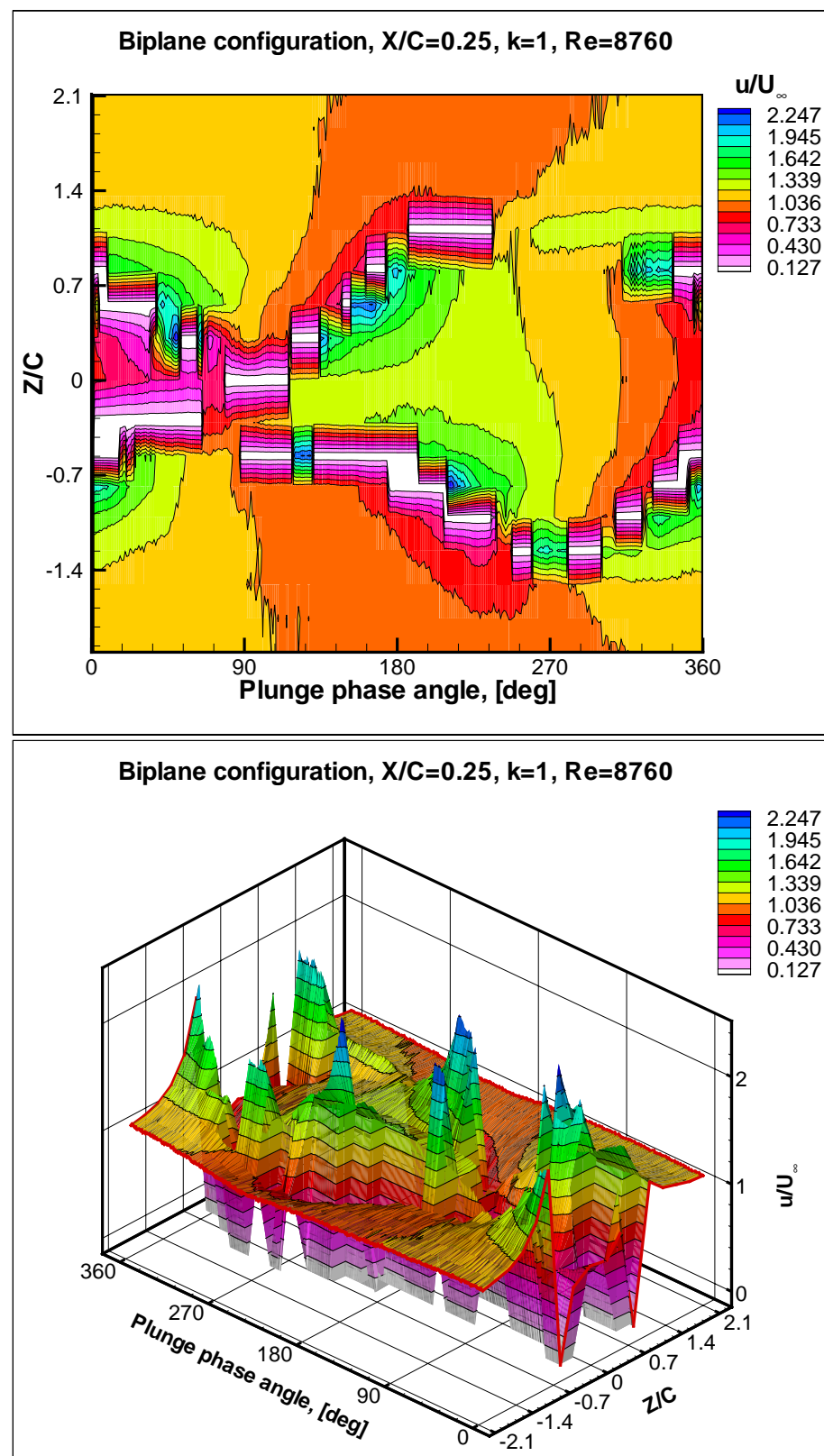


Figure 5.18. Measured Axial Velocity Component, u , at $X/C=0.25$

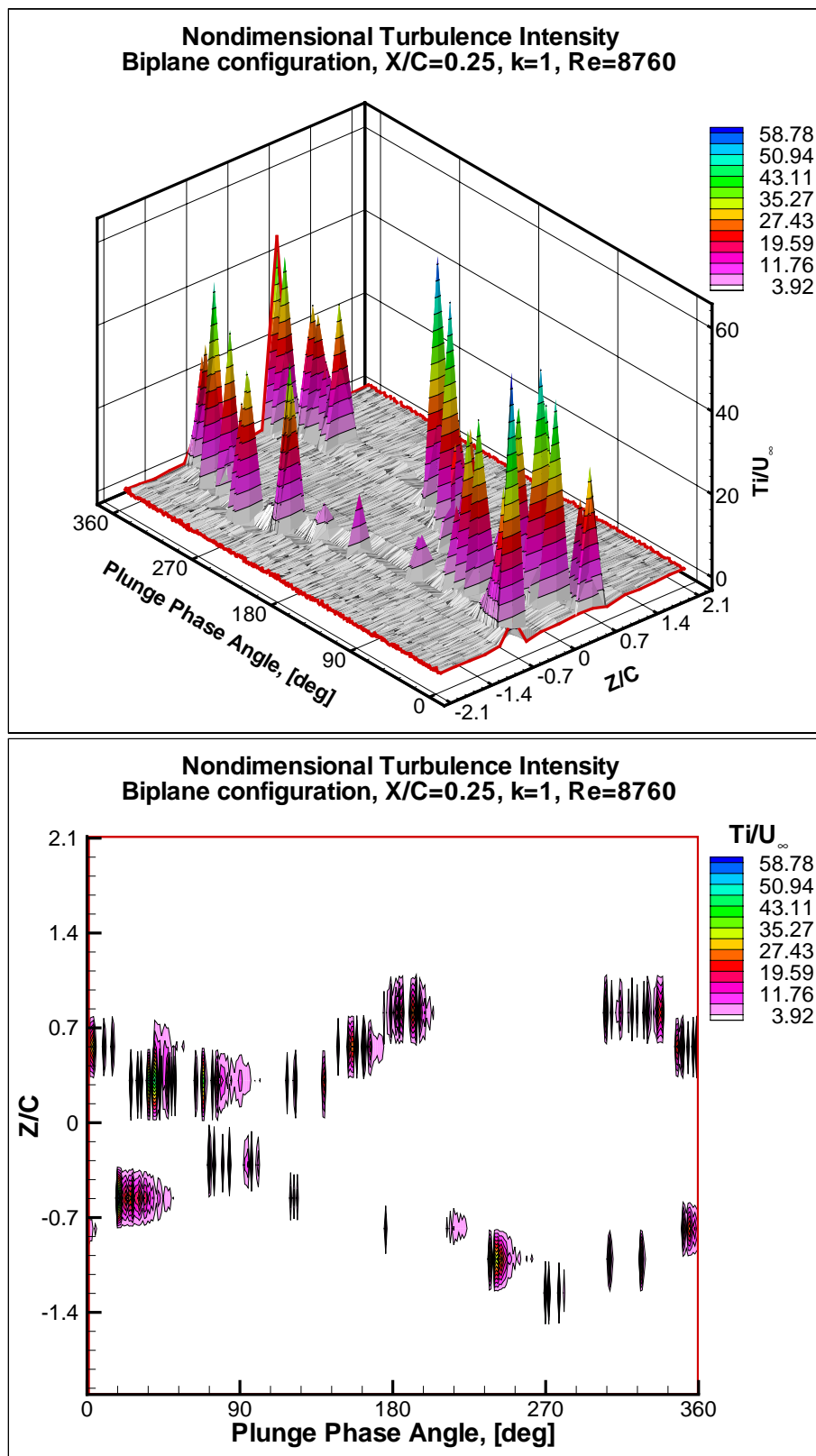


Figure 5.19. Nondimensional Turbulence Intensity at $X/C=0.25$

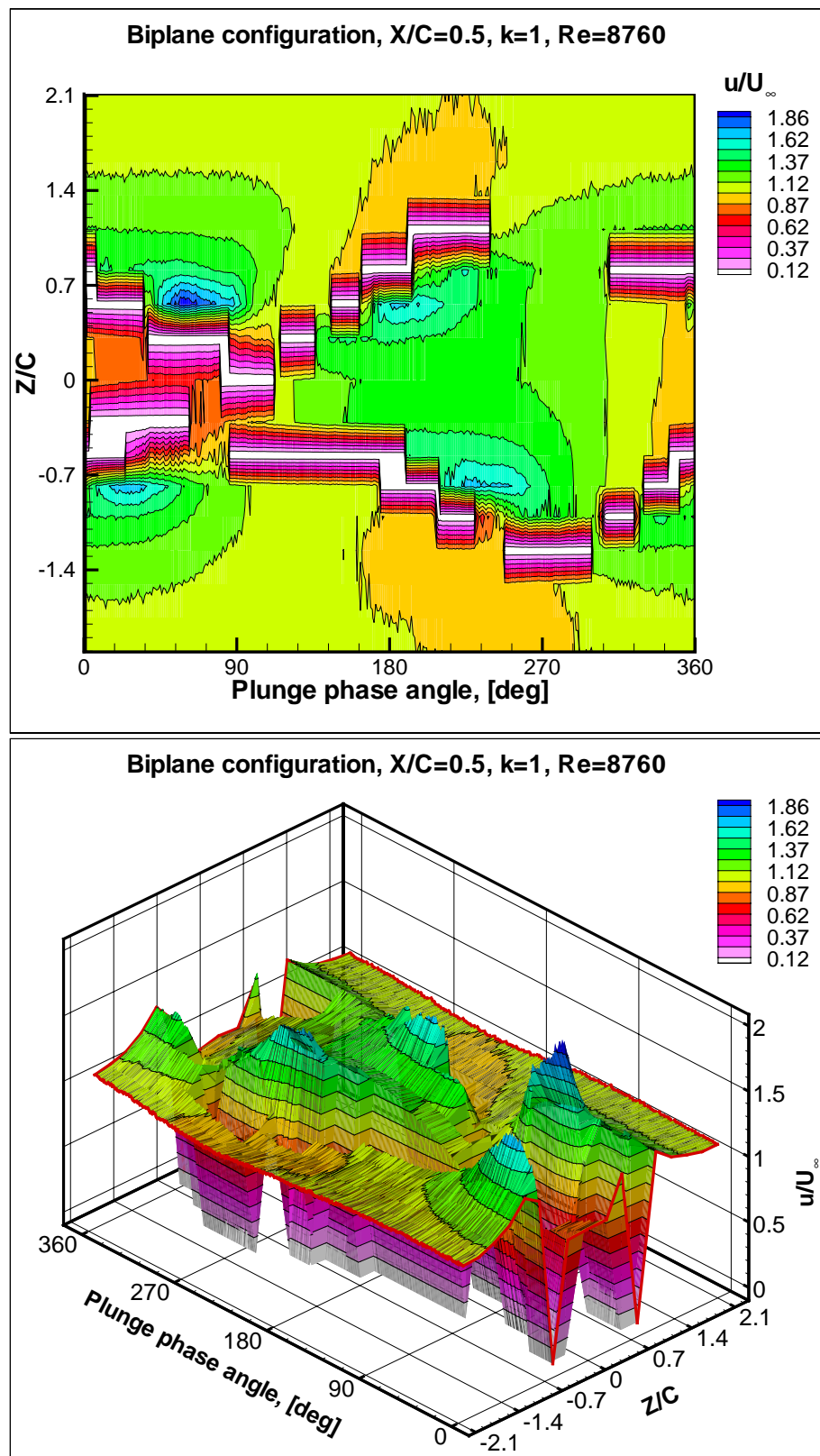


Figure 5.20. The Measured Velocity over the Complete Domain at $X/C = 0.5$

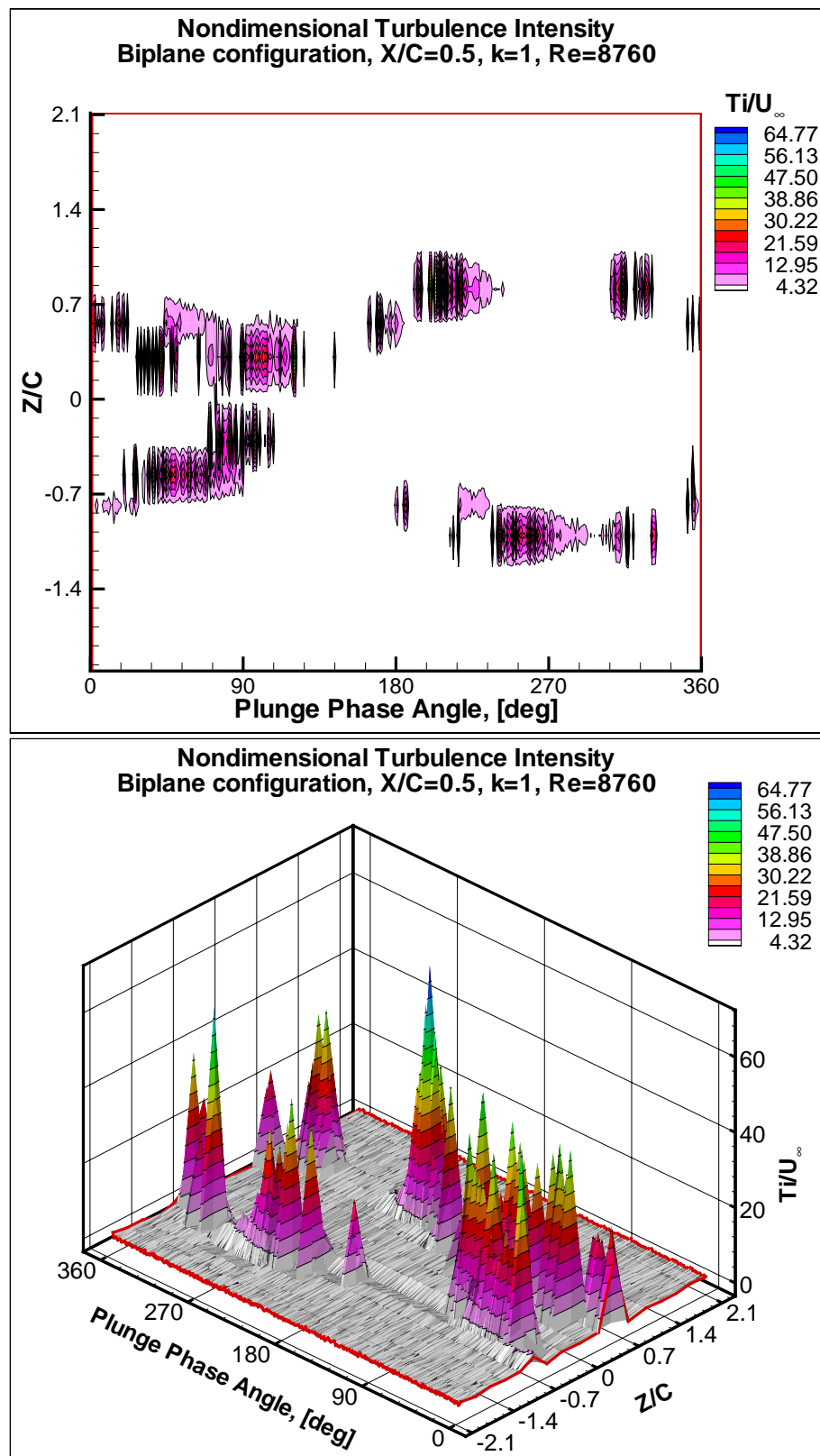


Figure 5.21. Nondimensional Turbulence Intensity, Ti/U_∞ at $X/C = 0.5$

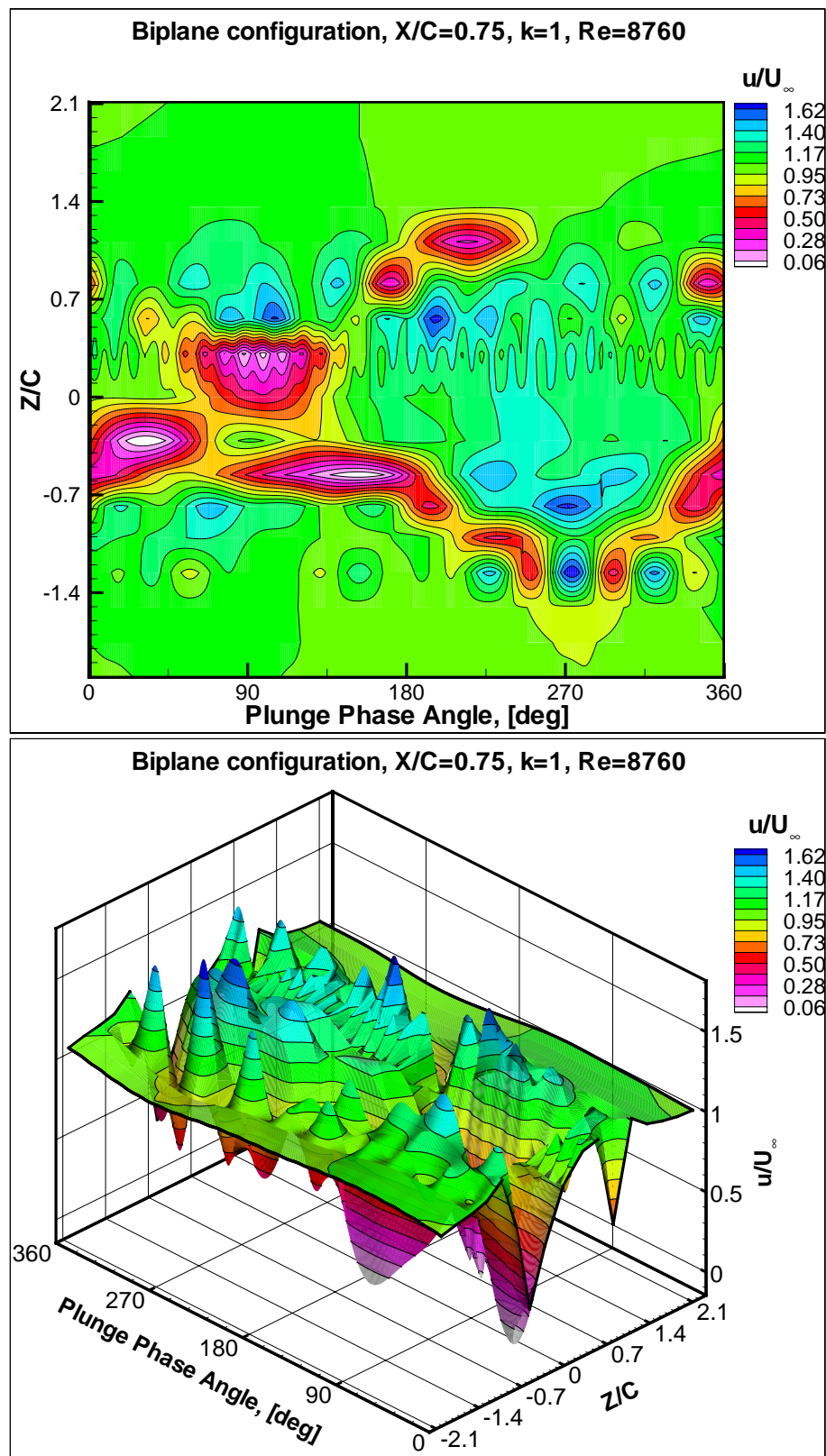


Figure 5.22. The Measured Axial Velocity Component over the Complete Domain at $X/C=0.75$

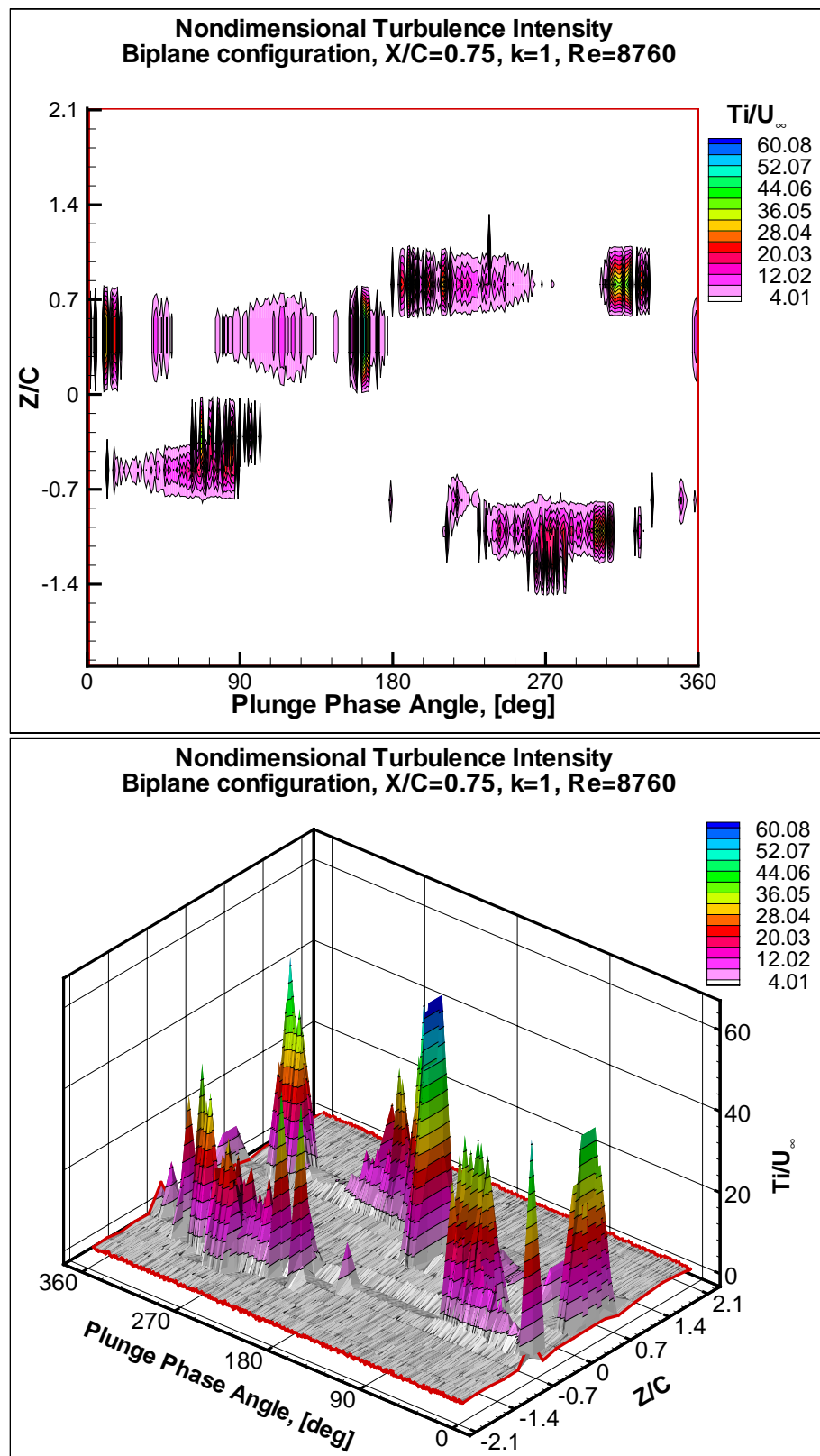


Figure 5.23. Nondimensional Turbulence Intensity at $X/C=0.75$

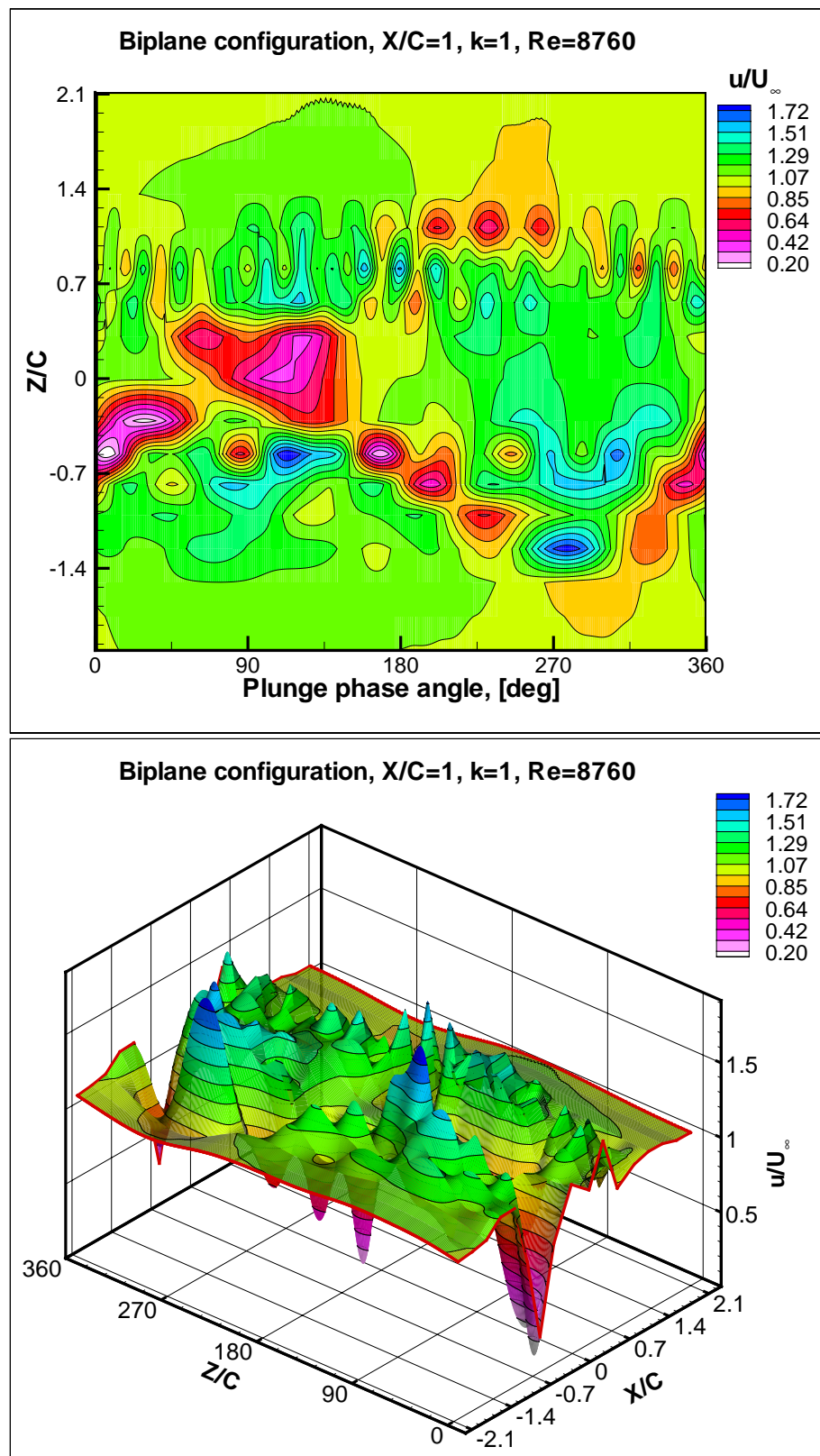


Figure 5.24. Measured Velocity over the Complete Domain

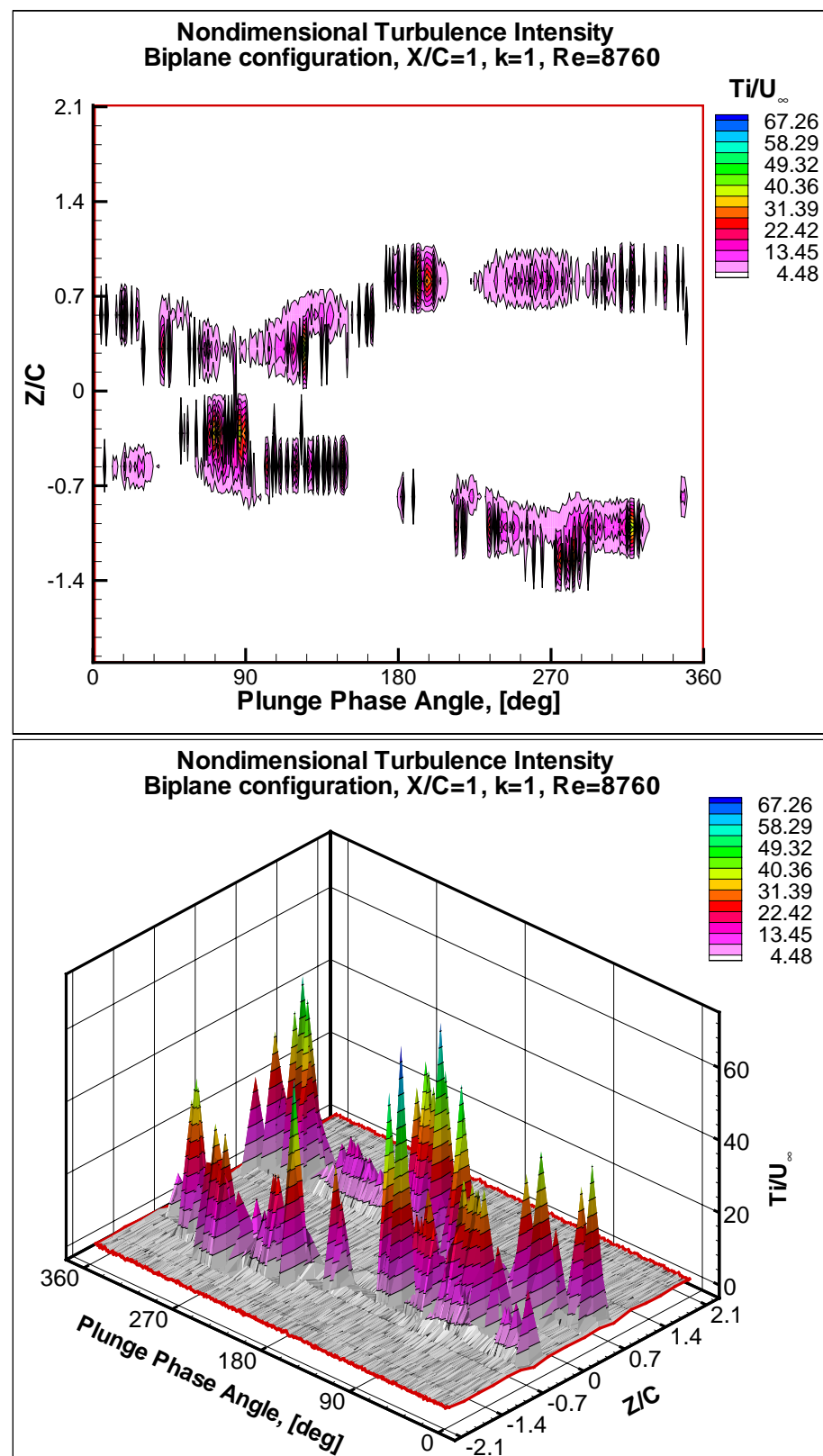


Figure 5.25. Nondimensional Turbulence Intensity

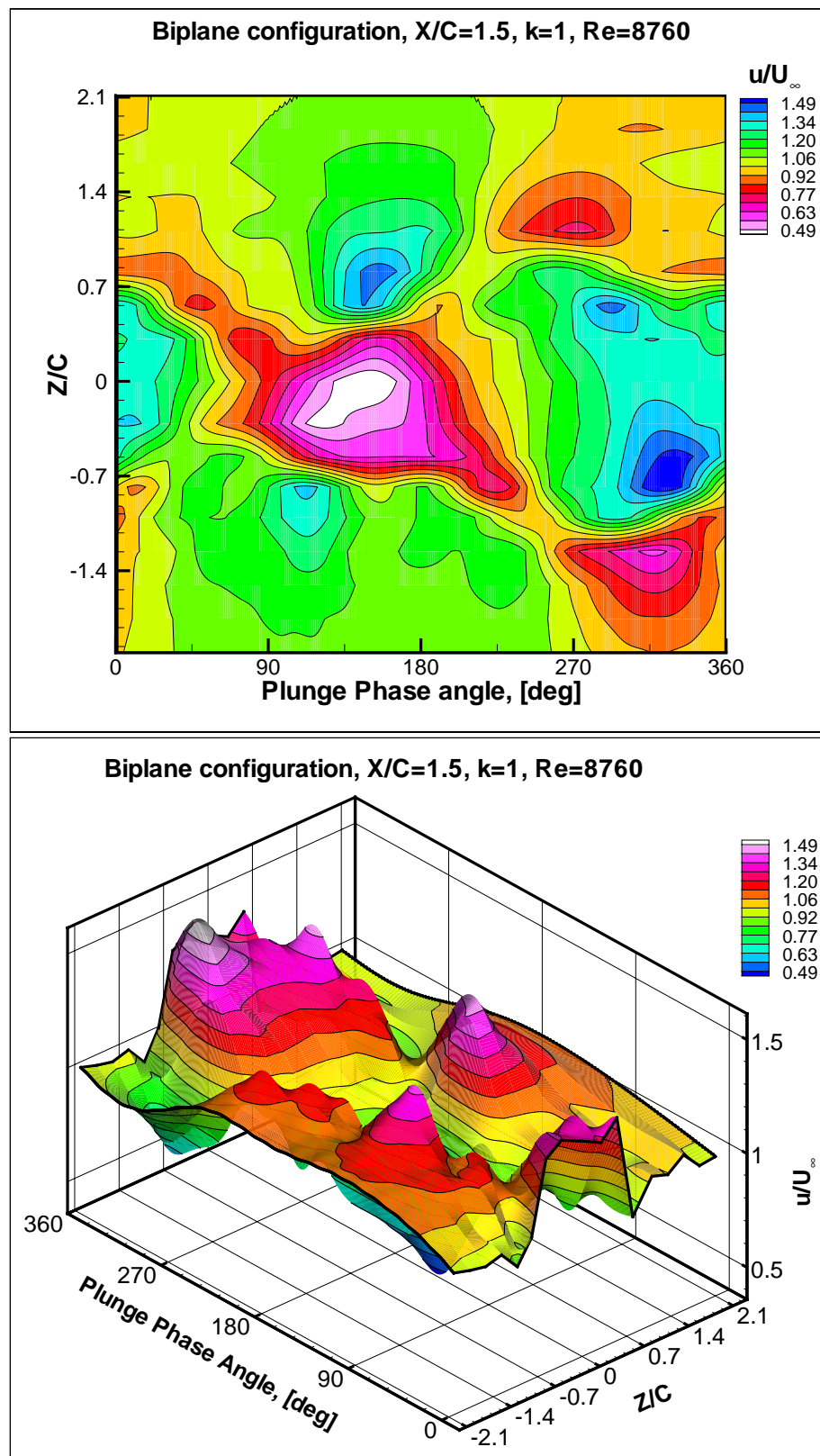


Figure 5.26. Measured Velocity over the Complete Domain at $X/C = 1.5$

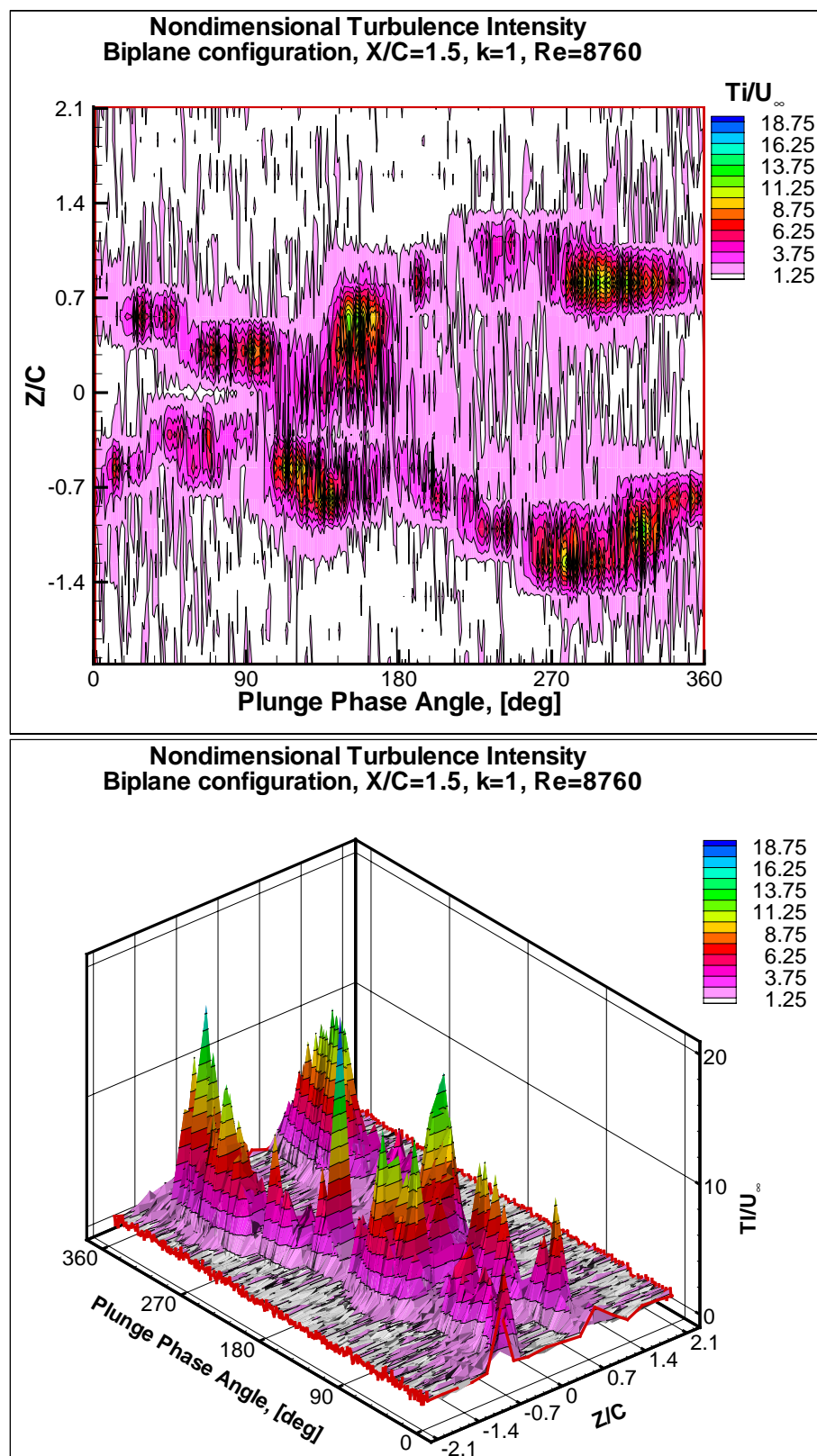


Figure 5.27. Nondimensional Turbulence Intensity at $X/C = 1.5$

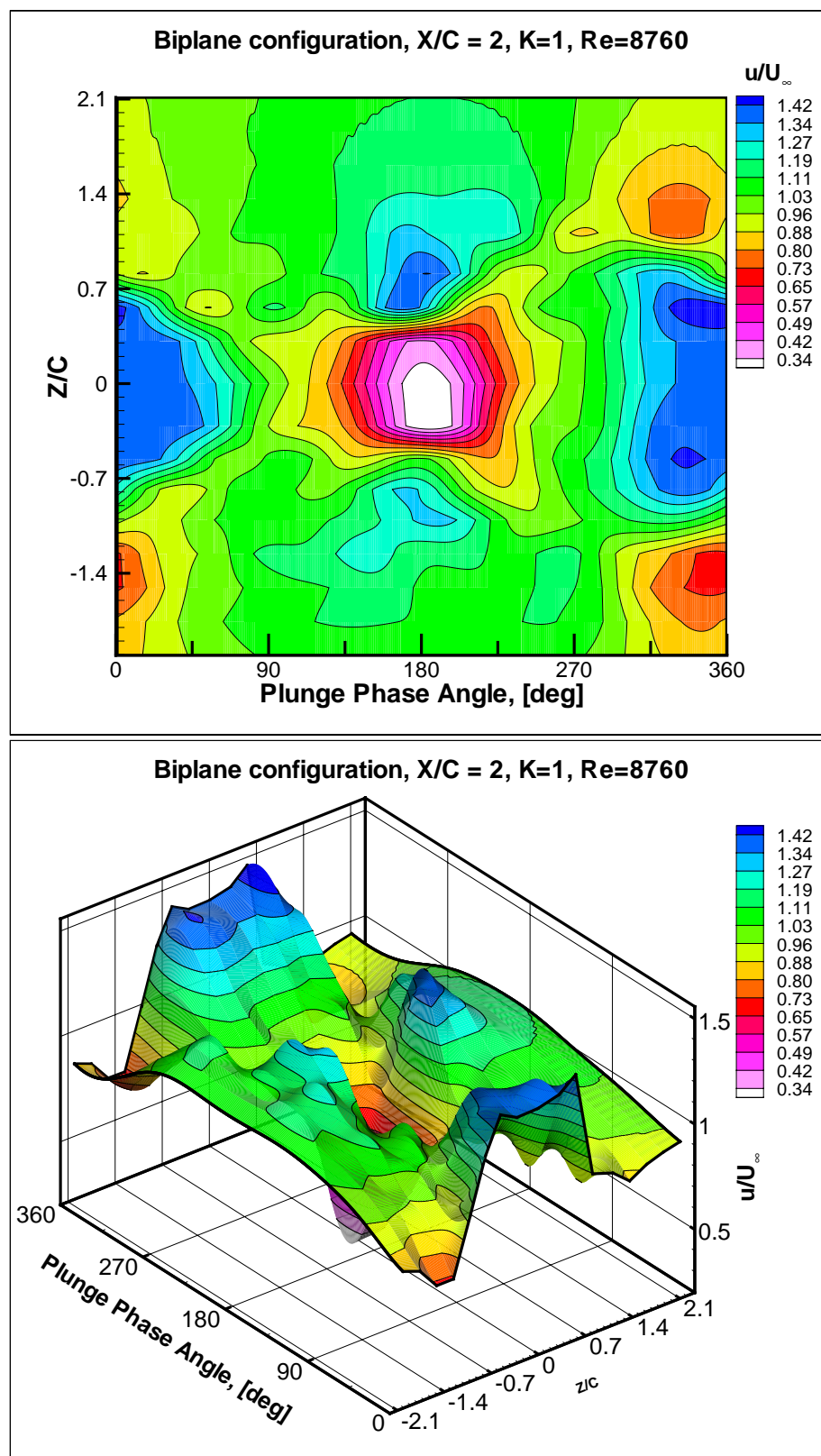


Figure 5.28. Measured Velocity over the Complete Domain at $X/C=2.0$

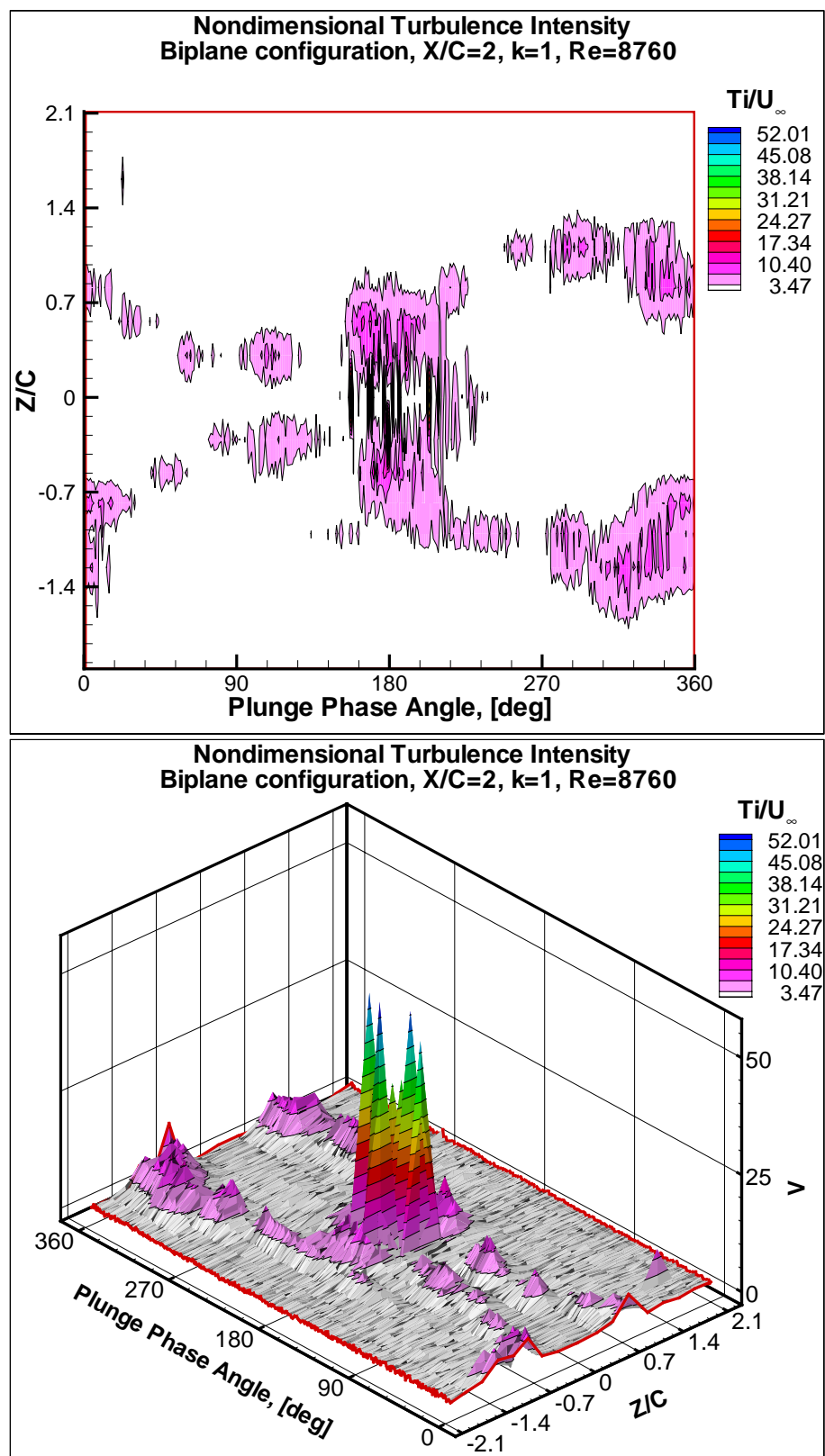


Figure 5.29. Nondimensional Turbulence Intensity

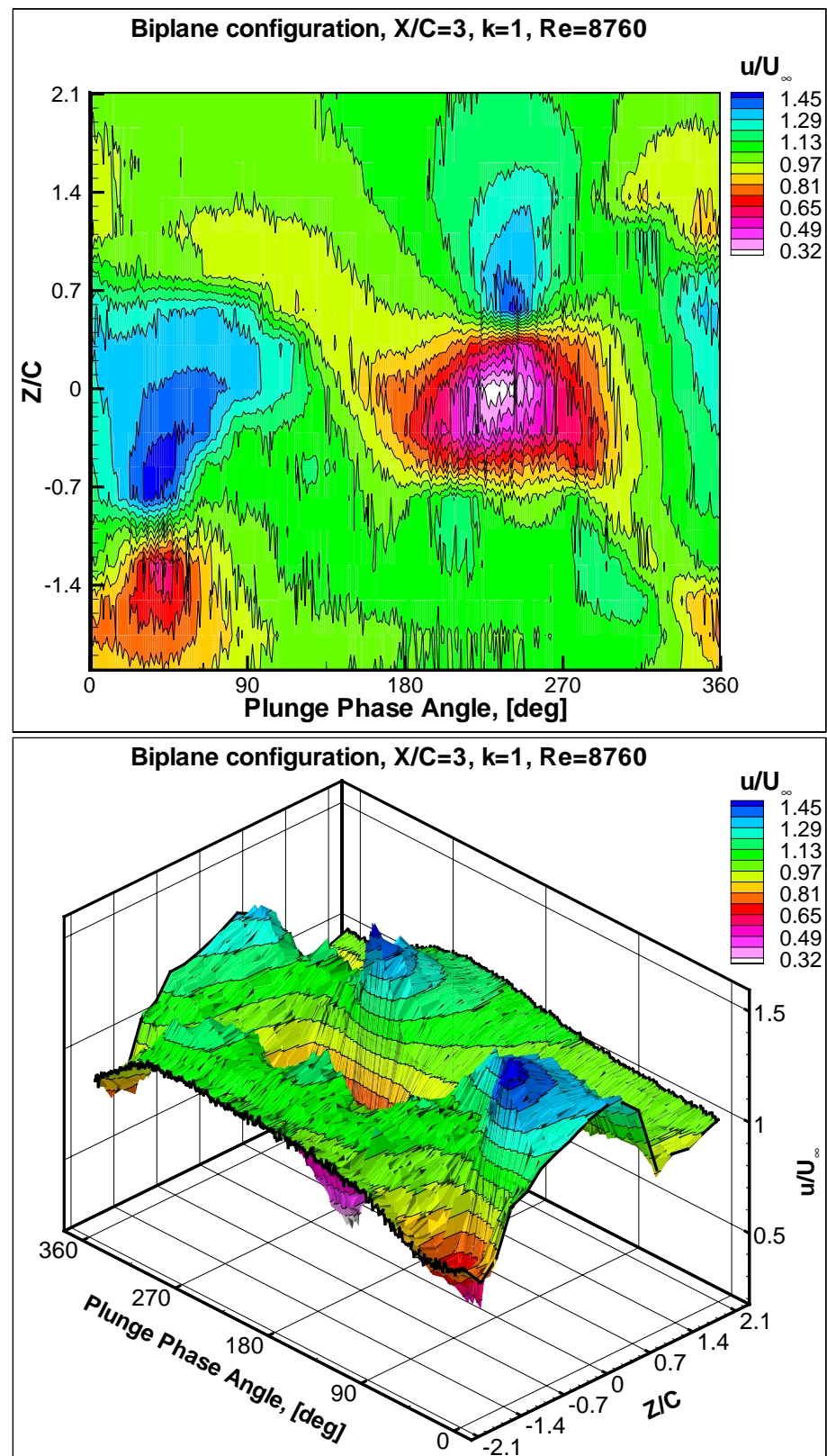


Figure 5.30. Measured Velocity over the Complete Domain at $X/C = 3.0$

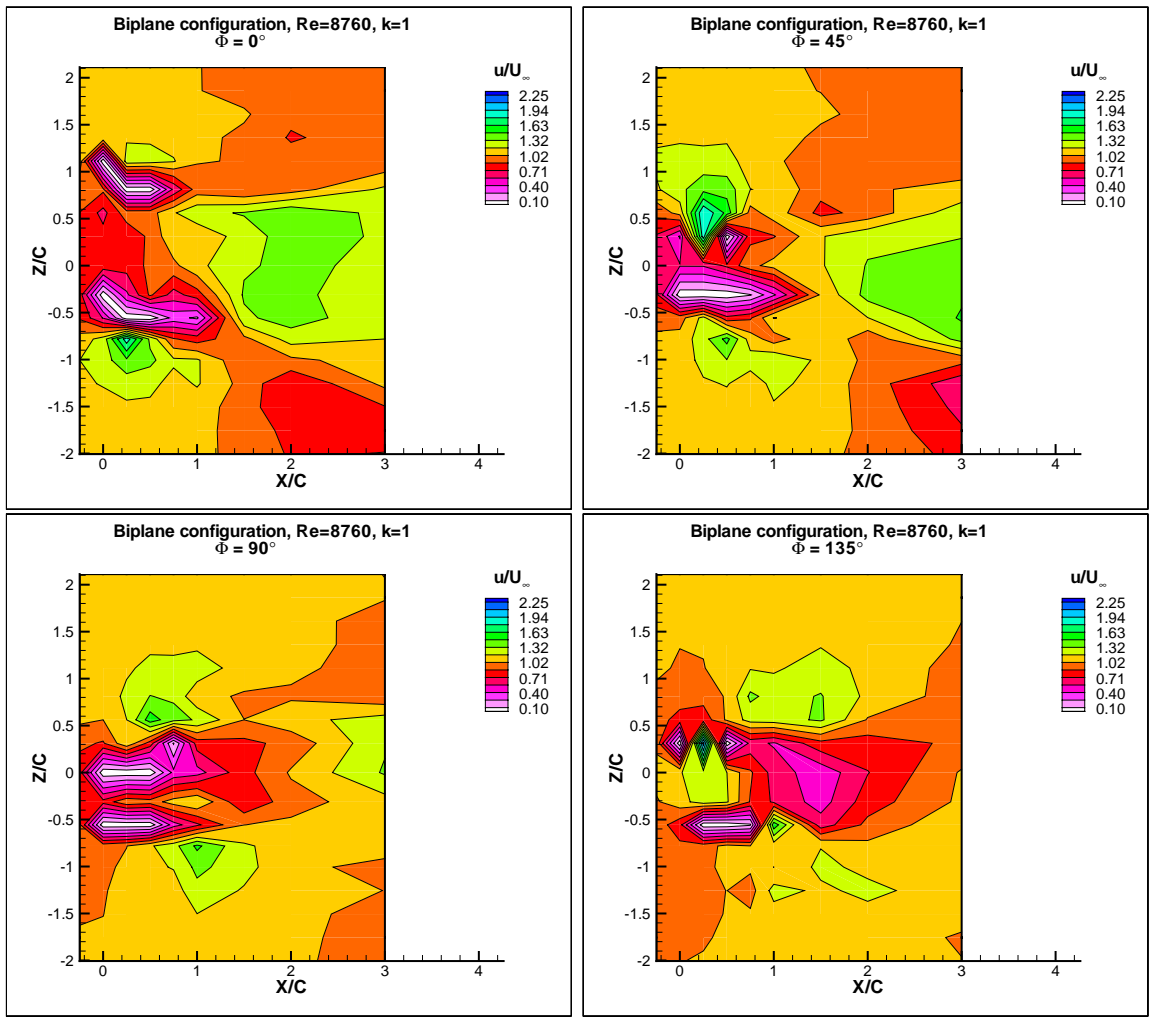


Figure 5.33. Flow Around NACA0014 in the Upper Flapping Stroke for Biplane Configuration

b. Summary

The measured instantaneous velocities were used to obtain the flow field over the whole airfoil at different angles, Φ , which helps to understand the flapping motion. The flow around the airfoil is illustrated over a complete flapping cycle in Fig. 5.33, and Fig. 5.34.

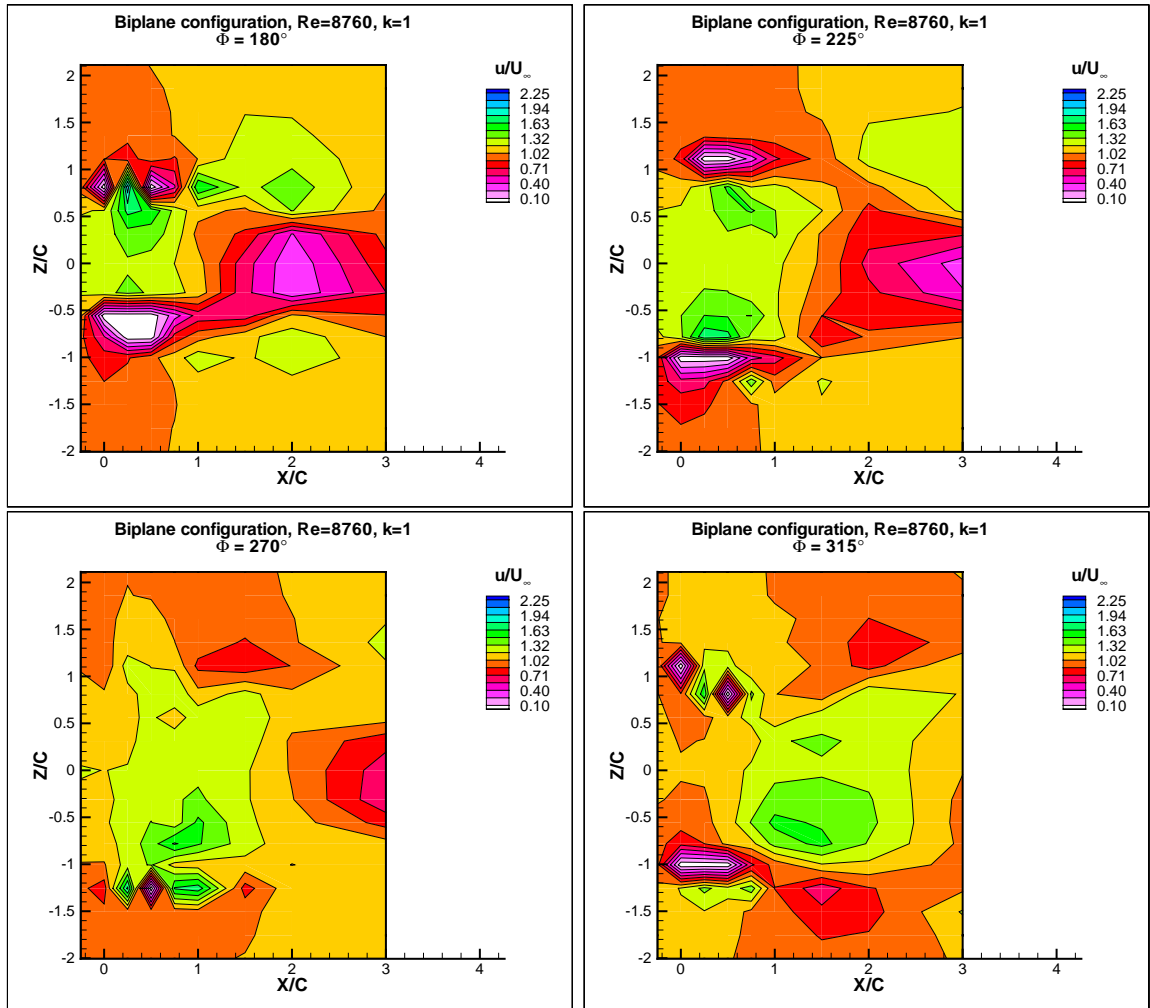


Figure 5.34. Flow Around NACA0014 in the Lower Flapping Stroke for Biplane Configuration

2. Wing in Ground Effect

For this experiment, the flapping model was configured to use only one wing. A brass block with the same weight as the removed wing was added to the model to ensure stability. A fixed flat plate was mounted underneath the wing such that the distance between the plate and the flapping wing in the lowest point in the downstroke was 22 mm.

At first, the boundary layer over the flat plate was studied. The velocity profile was measured at two different locations, namely at $X/C = 5$ and $X/C = 13$, where X is the distance measured from the leading edge of the flat plate, and C is the airfoil chord. The velocity profile at $X/C = 5$ was measured twice, once with the flapping wing at the lowest point of the downstroke, while the other was at the highest point of the upstroke. For $X/C = 13$, the velocity profile was measured only once when the wing was at the highest point.

The velocity profile is shown in Fig. 5.35. The standard deviation is presented as error bars. The turbulence intensity is presented in the same figure. The distance between the ground plane and the flapping-wing mid-point was $Z/C = 0.84$. This value was selected such that the wing will be immersed in the boundary layer in the downstroke part of the flapping cycle.

After the boundary layer was investigated, the model was set to flap at 5 Hz which corresponds to a reduced frequency, $k = 1$, at the used tunnel speed of 2 m/s. The Reynolds number therefore was 8874. The flow around the flapping airfoil was probed in 80 points by LDV, distributed as a set of ten points at eight different axial locations, namely, $X/C = -0.25, 0, 0.25, 0.5, 0.75, 1.0, 1.5, 2.0$. At each location, the flow was investigated in the vertical direction between $-0.69 \leq Z/C \leq 1.4$. The closest point of measurements to the ground plane was at a distance of 3 mm.

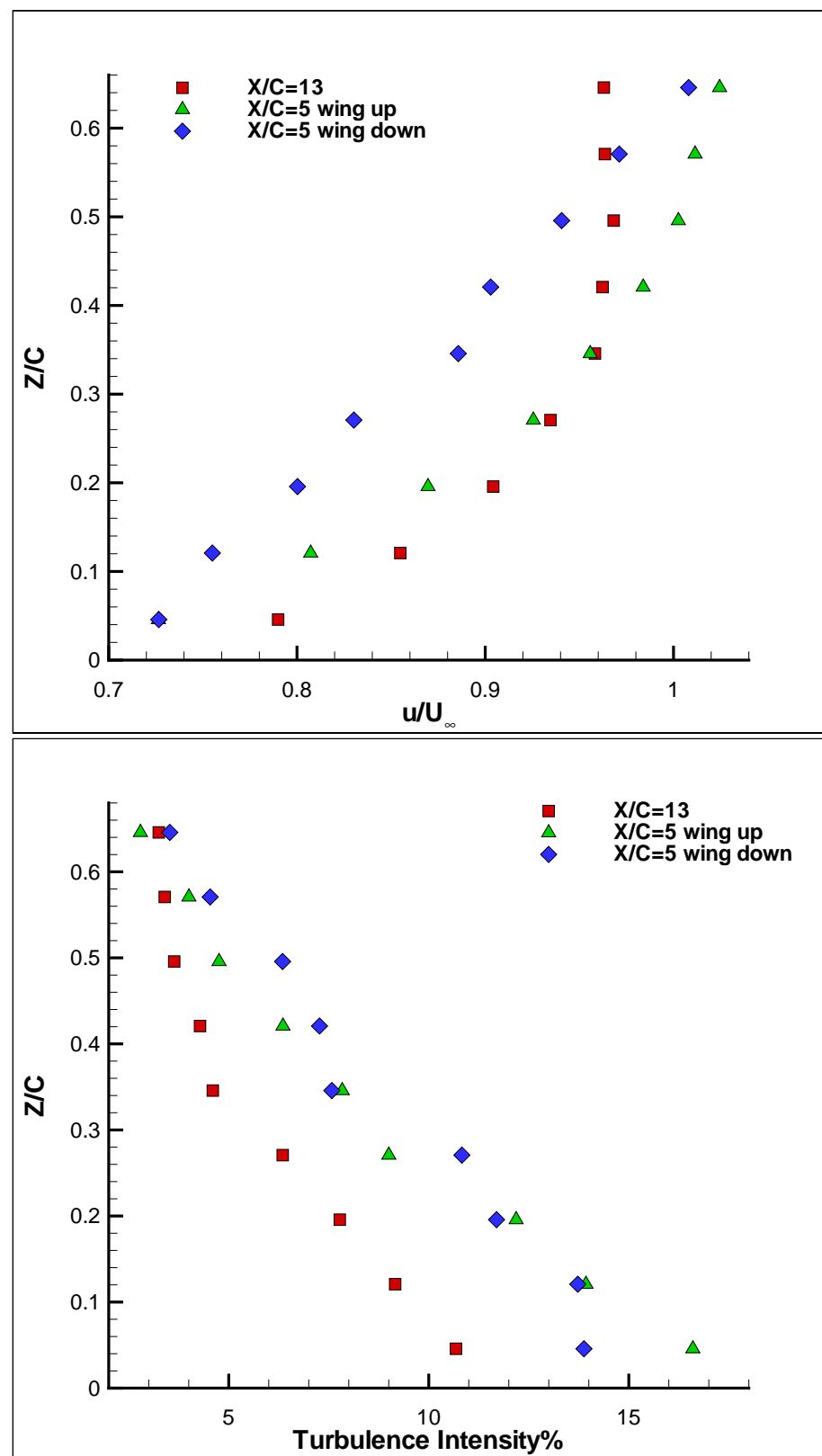


Figure 5.35. Boundary Layer over the Ground Plane

Table 5.2. Flapping Wing in Ground Effect

X/C	$u/U_\infty V s. \Phi$	u/U as carpet plot
-0.25	Fig. D.1	Fig. 5.36
0	Fig. D.2	Fig. 5.37
0.25	Fig. D.3	Fig. 5.38
0.50	Fig. D.4	Fig. 5.39
0.75	Fig. D.5	Fig. 5.40
1.0	Fig. D.6	Fig. 5.41
1.5	Fig. D.7	Fig. 5.42
2.0	Fig. D.8	Fig. 5.43

The axial velocity component, u , was measured as a function of the encoder position which is related to the plunge phase angle at each probed point. The results are presented in the subsequent figures shown in table 5.2

The obtained measurements was integrated together to build a three dimensional block of the nondimensional velocity u/U_∞ . The integration of the measurements in 3D block with X/C as the first coordinates, Z/C as the second coordinates and Plunge Phase Angle as the third coordinates, allows information extraction in different useful directions. Eight slices were taken at different plunge phase angle, starting at zero and by incremental step of 45 degree to illustrate the changes in the velocity distribution around the airfoil in both upstroke and downstroke, which is illustrated in Fig. 5.44 and Fig. 5.45.

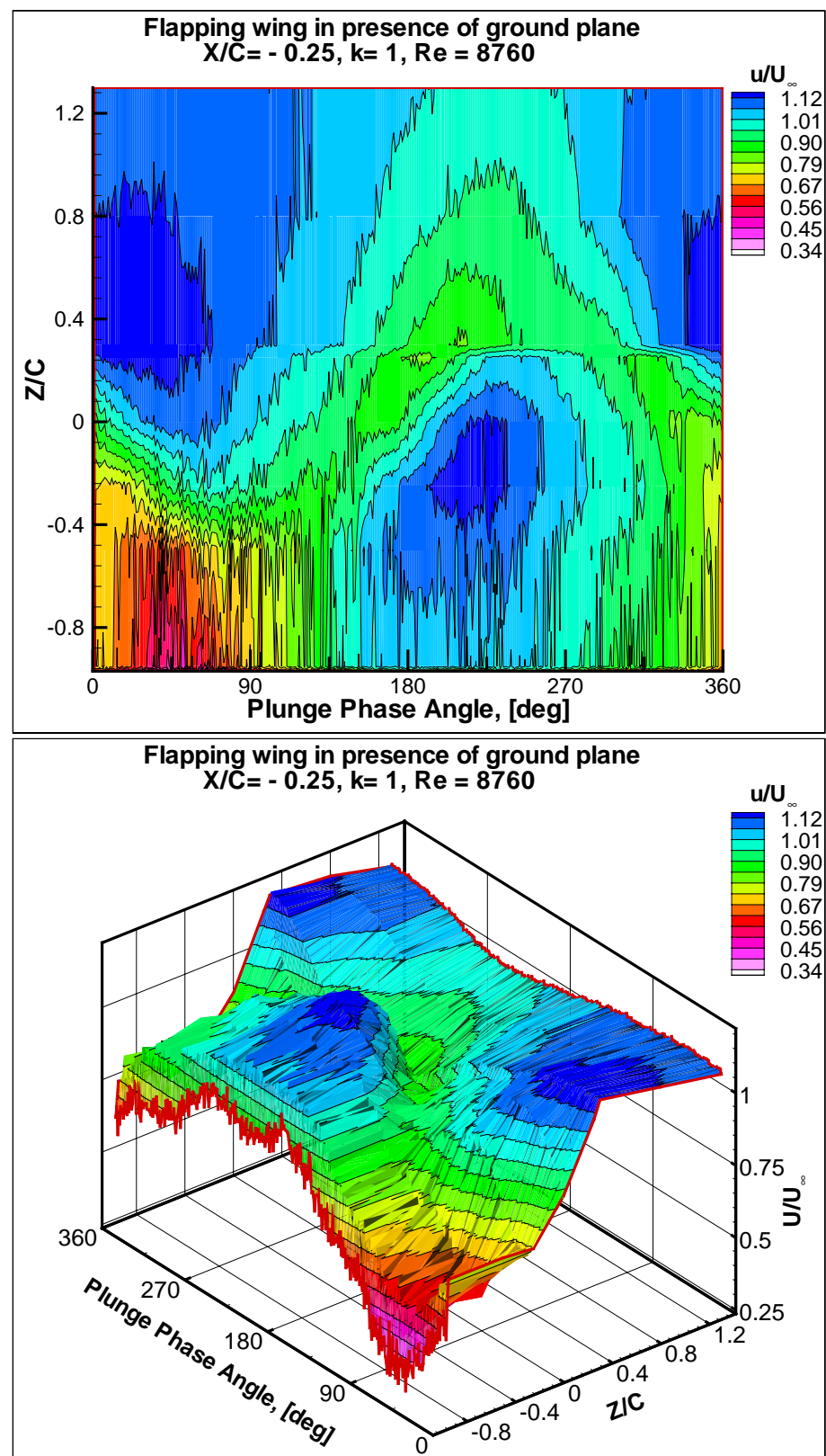


Figure 5.36. Nondimensional Axial Velocity at $X/C = -0.25$ for Flapping Wing in Presence of Ground Effect

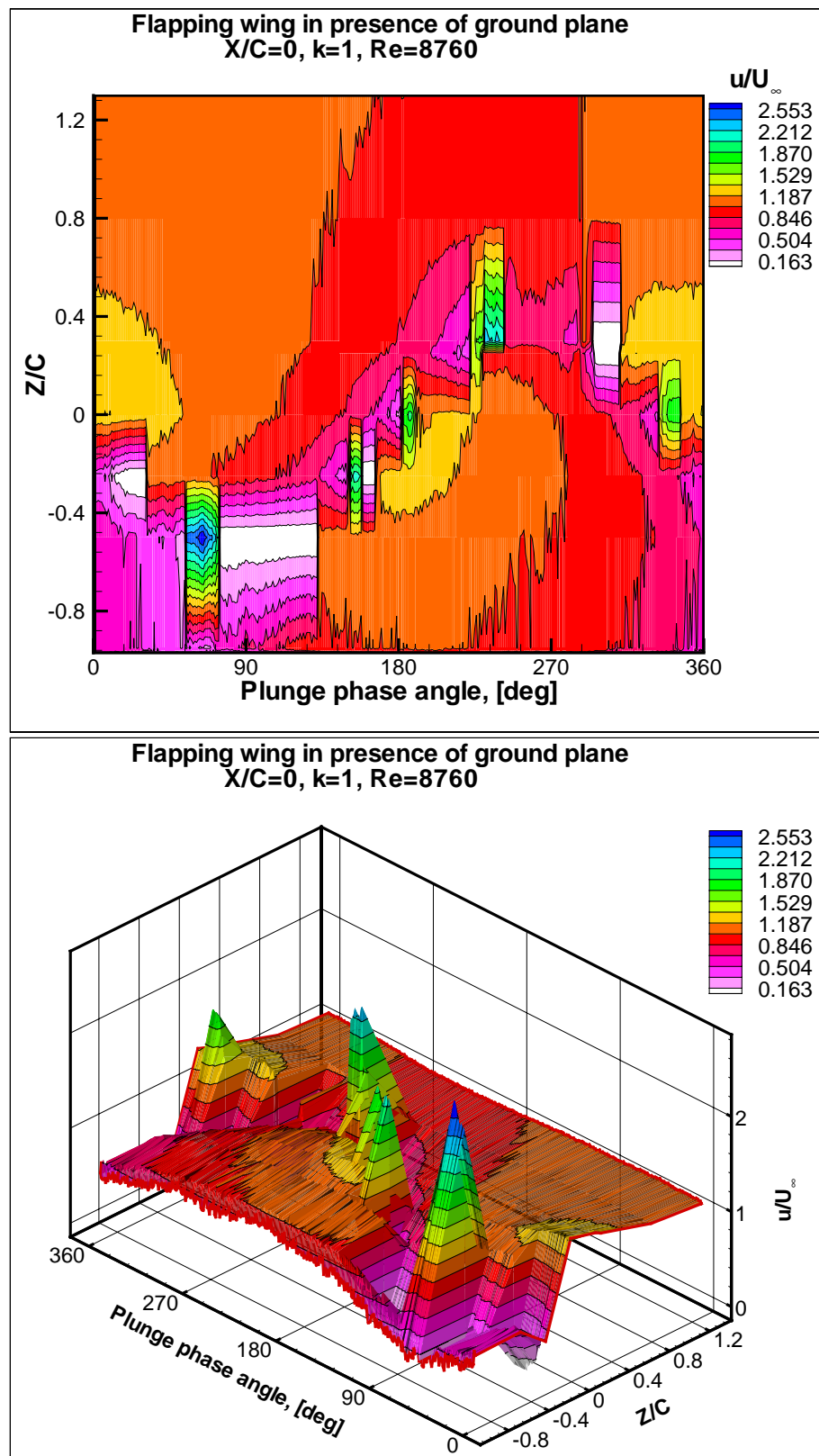


Figure 5.37. Flapping Wing in Presence of Ground Effect, $X/C=0$

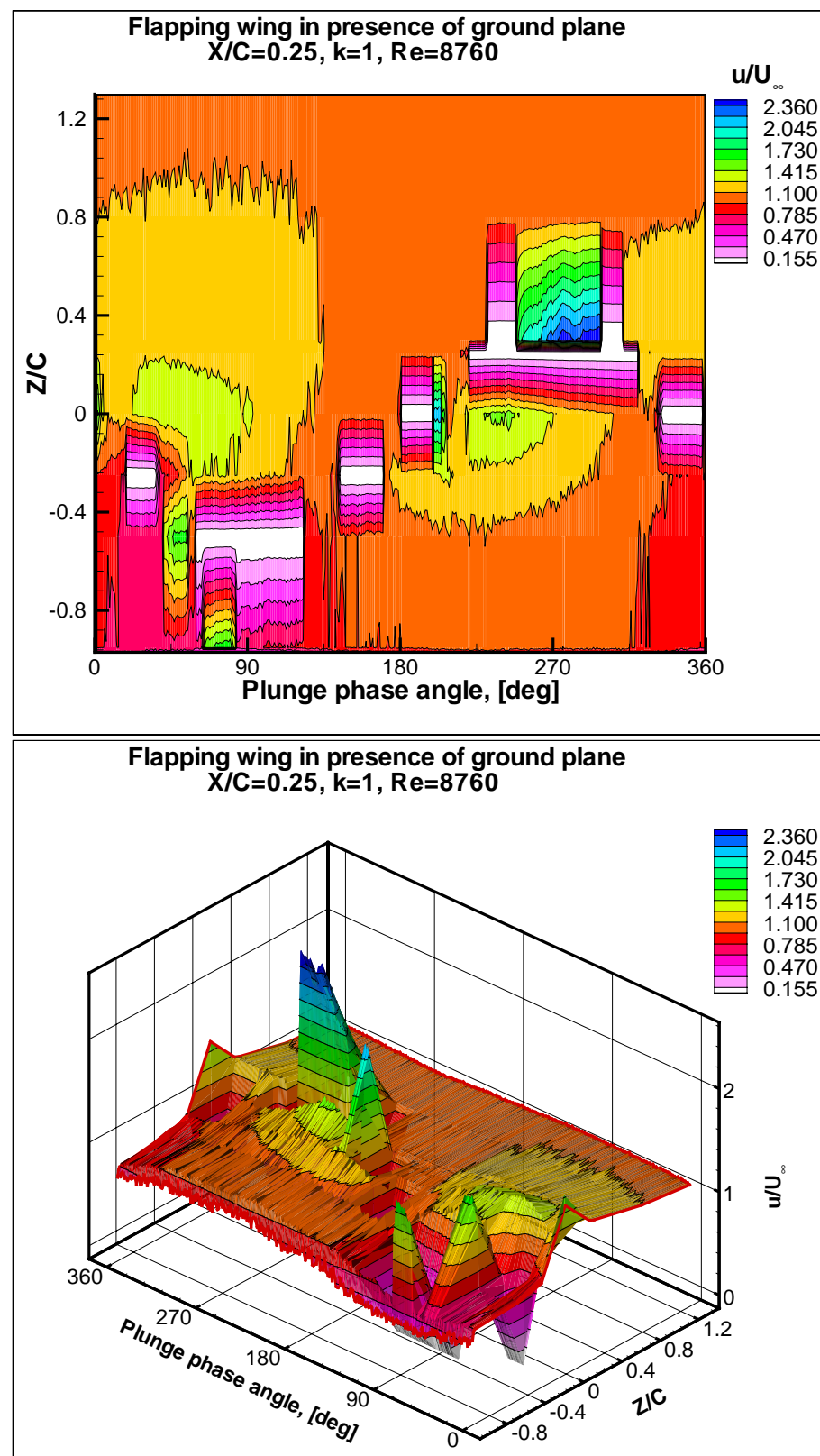


Figure 5.38. Flapping Wing in Presence of Ground Effect, $X/C=0.25$

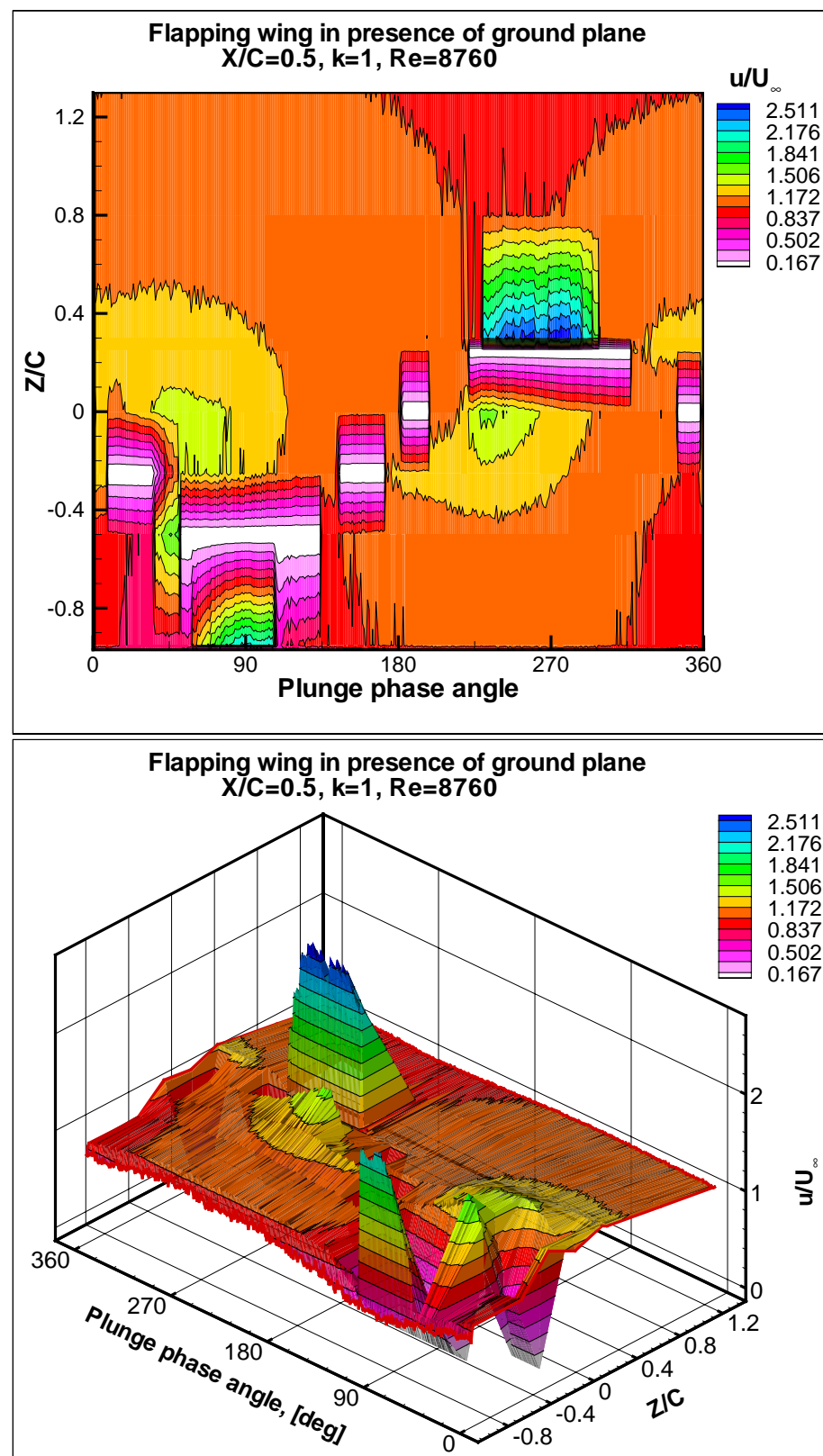


Figure 5.39. Flapping Wing in Presence of Ground Effect, $X/C=0.5$

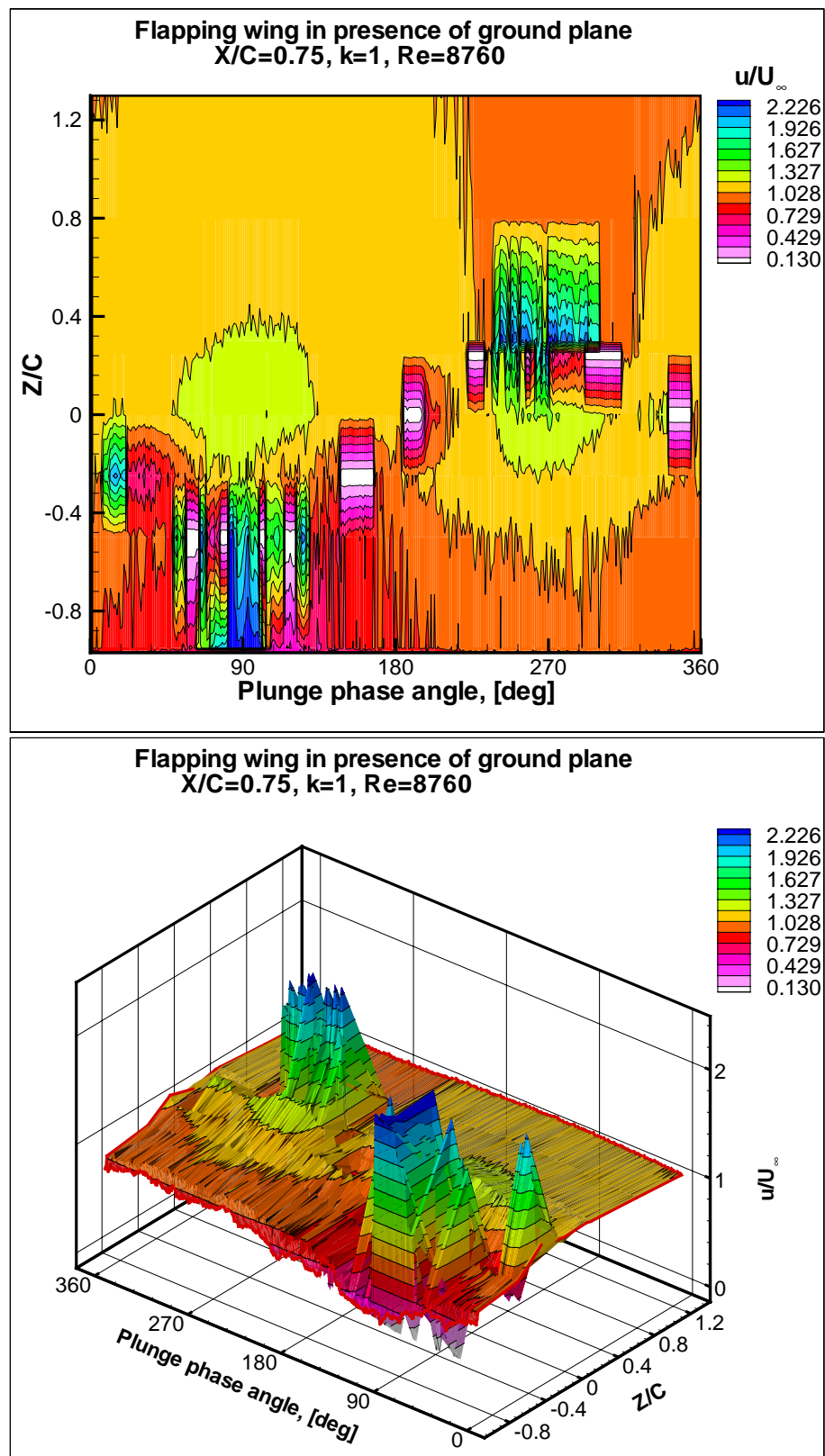


Figure 5.40. Flapping Wing in Presence of Ground Effect, $X/C=0.75$

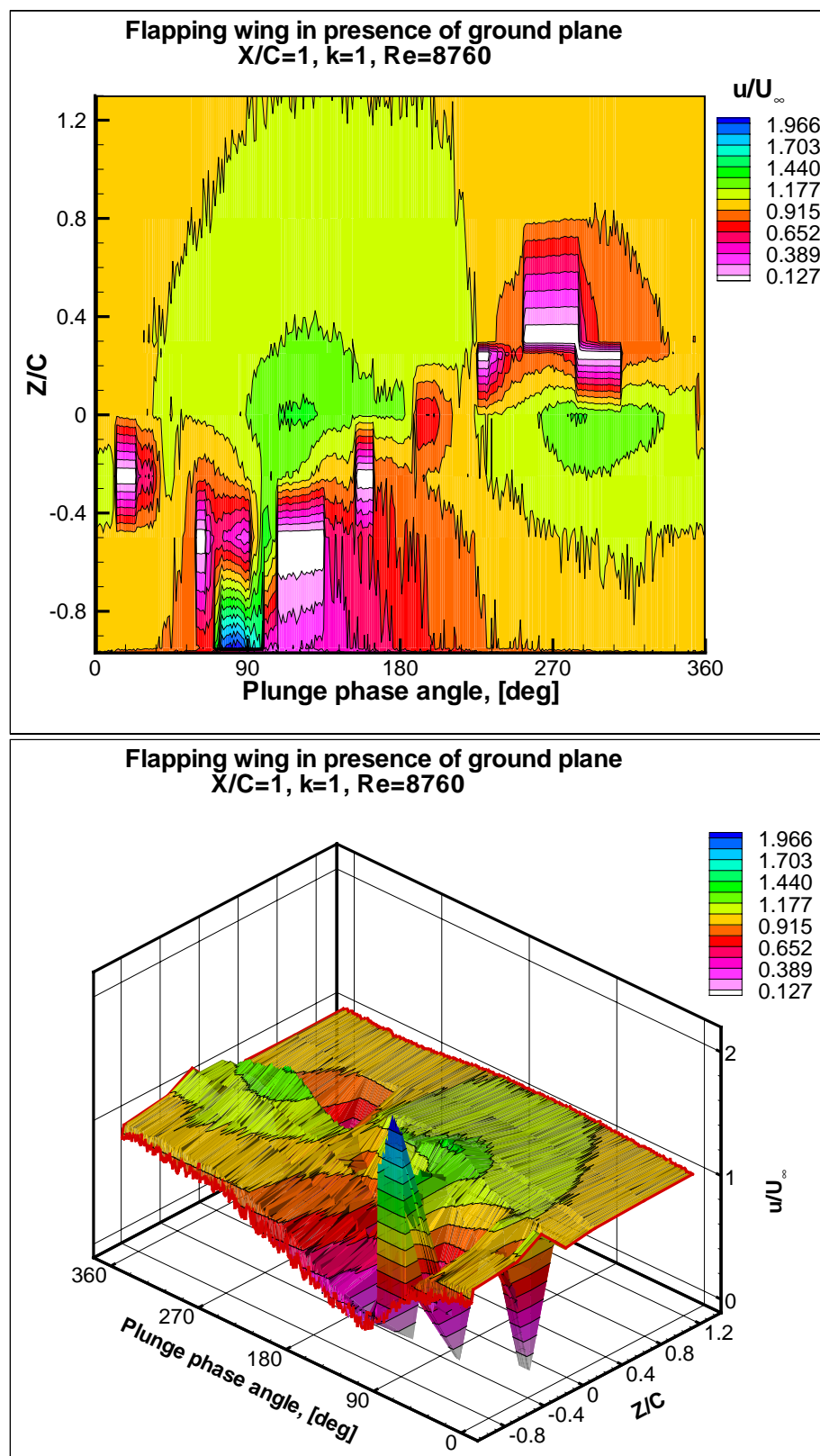


Figure 5.41. Flapping Wing in Presence of Ground Effect, $X/C=1$.

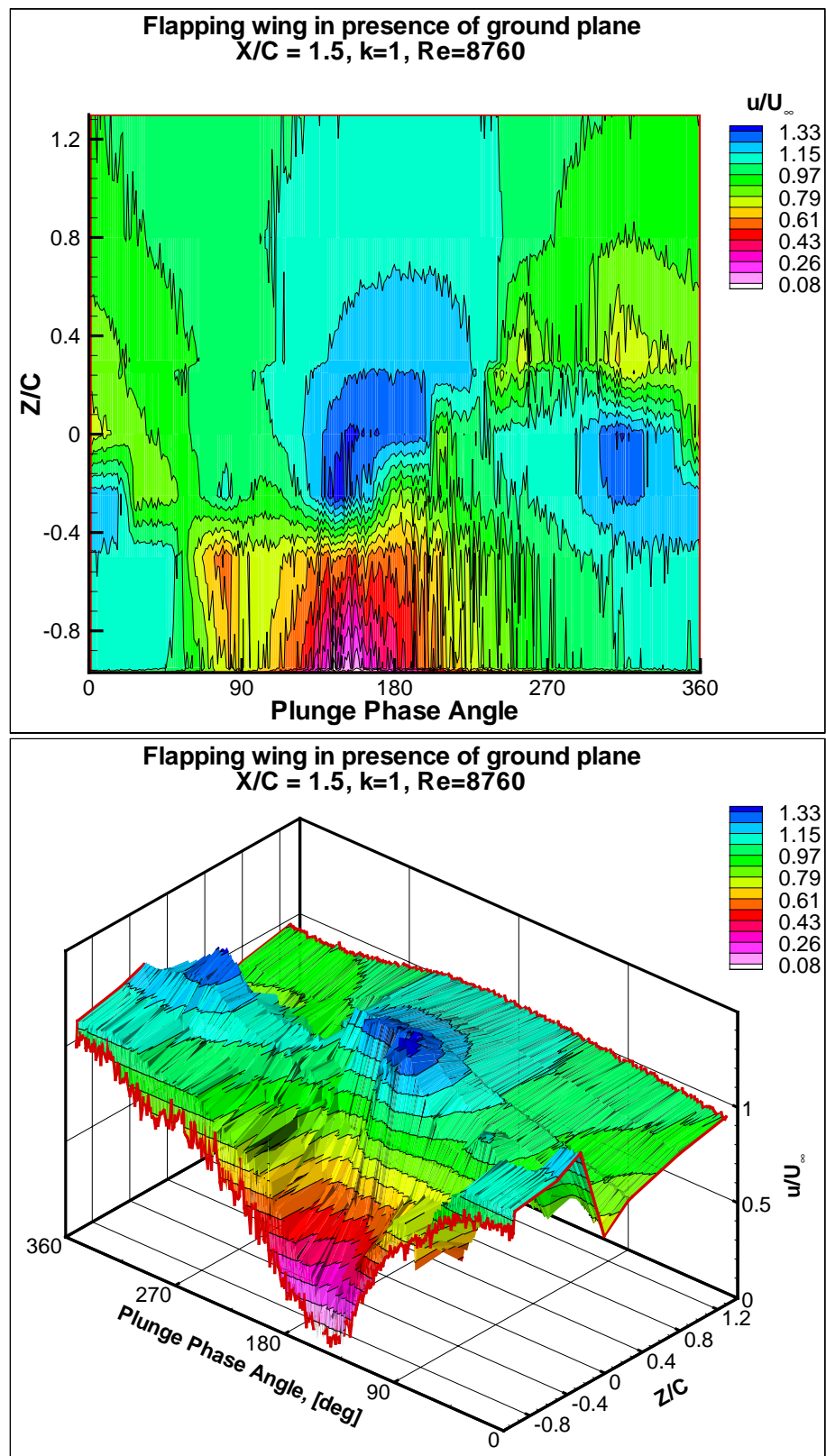


Figure 5.42. Flapping Wing in Presence of Ground Effect, $X/C=1.5$.

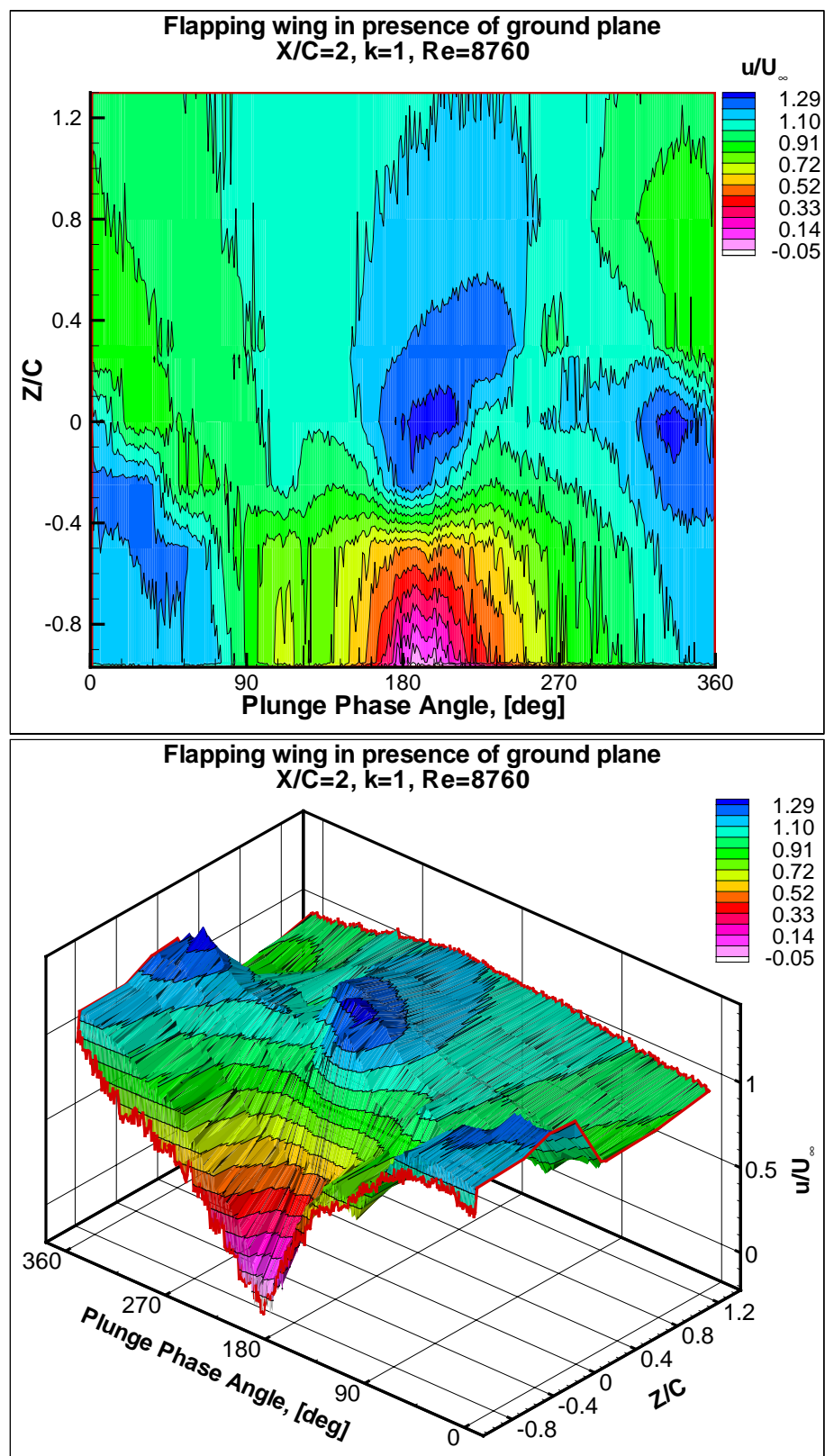


Figure 5.43. Flapping Wing in Presence of Ground Effect at $X/C=2.0$

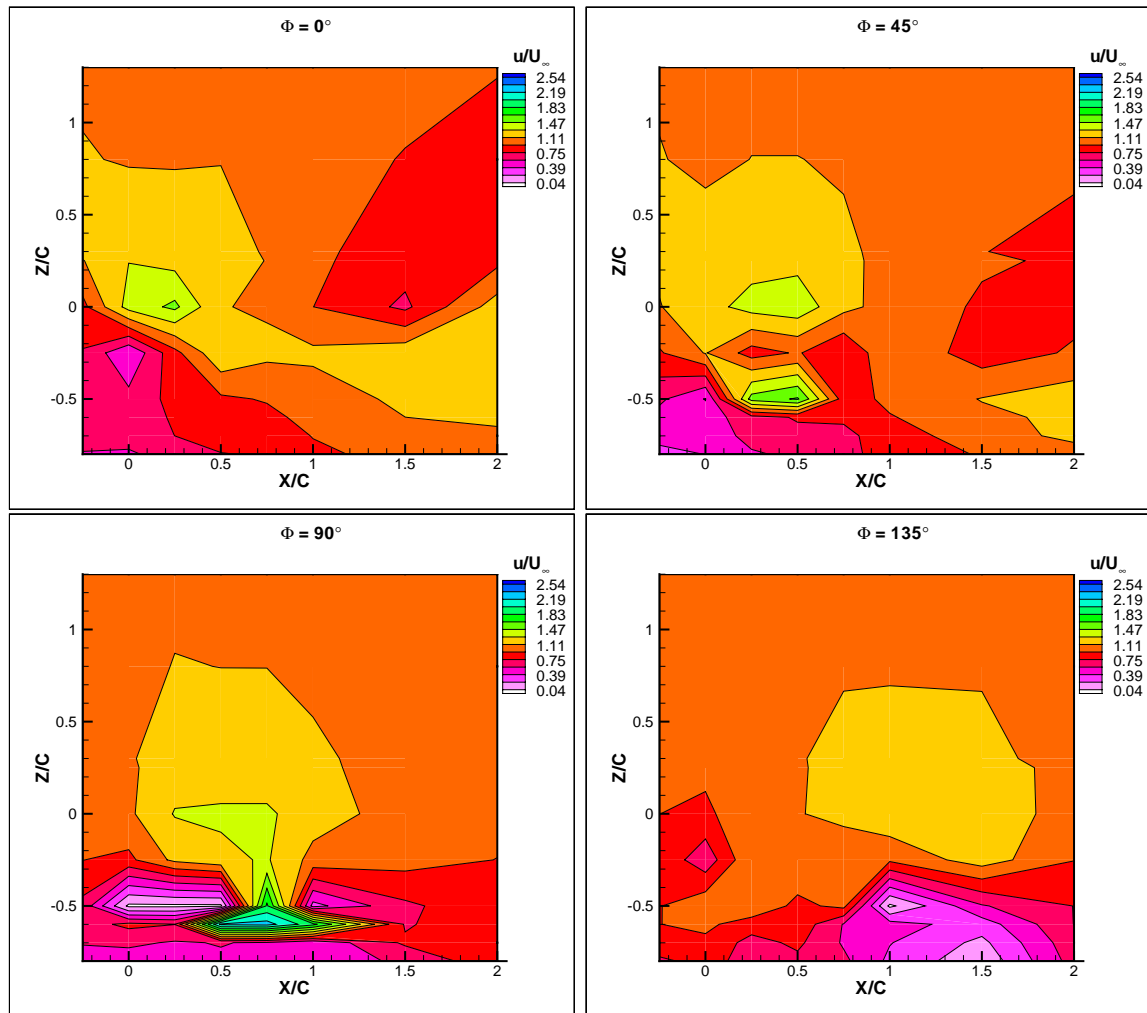


Figure 5.44. Flapping Wing in Ground Plane During Upstroke.

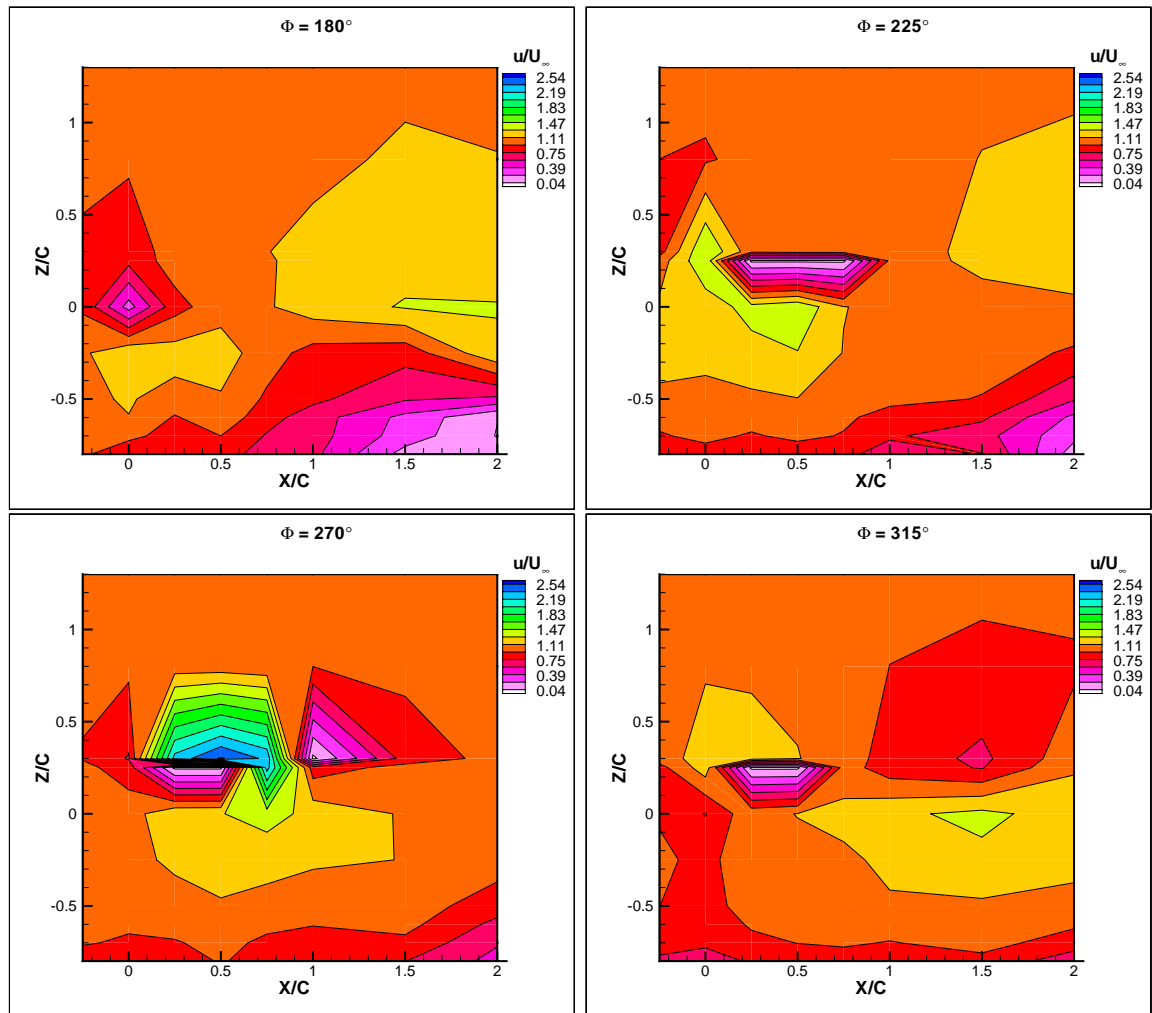


Figure 5.45. Flapping Wing in Ground Plane During Downstroke.

Table 5.3. Single Flapping Wing

X/C	$u/U \propto Vs.\Phi$	u/U as carpet plot
-0.2	Fig. C.1	Fig. 5.49
0	Fig. C.2	Fig. 5.50
0.2	Fig. C.3	Fig. 5.51
0.6	Fig. C.4	Fig. 5.52
1.0	Fig. C.5	Fig. 5.53

3. Single Wing Configuration

In the third experiment a single sinusoidally plunging wing was investigated at a reduced frequency of $k = 1.0$. The same wing previously used for the ground effect was set to flap at a frequency of 5Hz, while the wind tunnel speed was set to 2 m/s. The LDV along with the RMR was used to measure the velocity at 5 locations in the axial direction. Namely at $X/C = -0.2, 0, 0.2, 0.6$ and 1.0 . At each location, 15 points were investigated in the vertical direction to cover $-1.4 \leq Z/C \leq 1.4$. The flapping range was $-0.4 \leq Z/C \leq 0.4$.

The non-dimensional axial velocity distribution is shown in Fig. 5.46 and Fig. 5.47. At each position X/C , the instantaneous velocity is given for each measurement point Z/C as mentioned in table 5.3.

The average velocity profile around the airfoil is shown in Fig. 5.48. It is presented at the axial locations X/C to show how the variation occurs in the flow around the airfoil. The non-dimensional turbulence intensity around the airfoil is represented as well. The turbulence intensity at the free stream was used to non-dimensionalize the measured values.

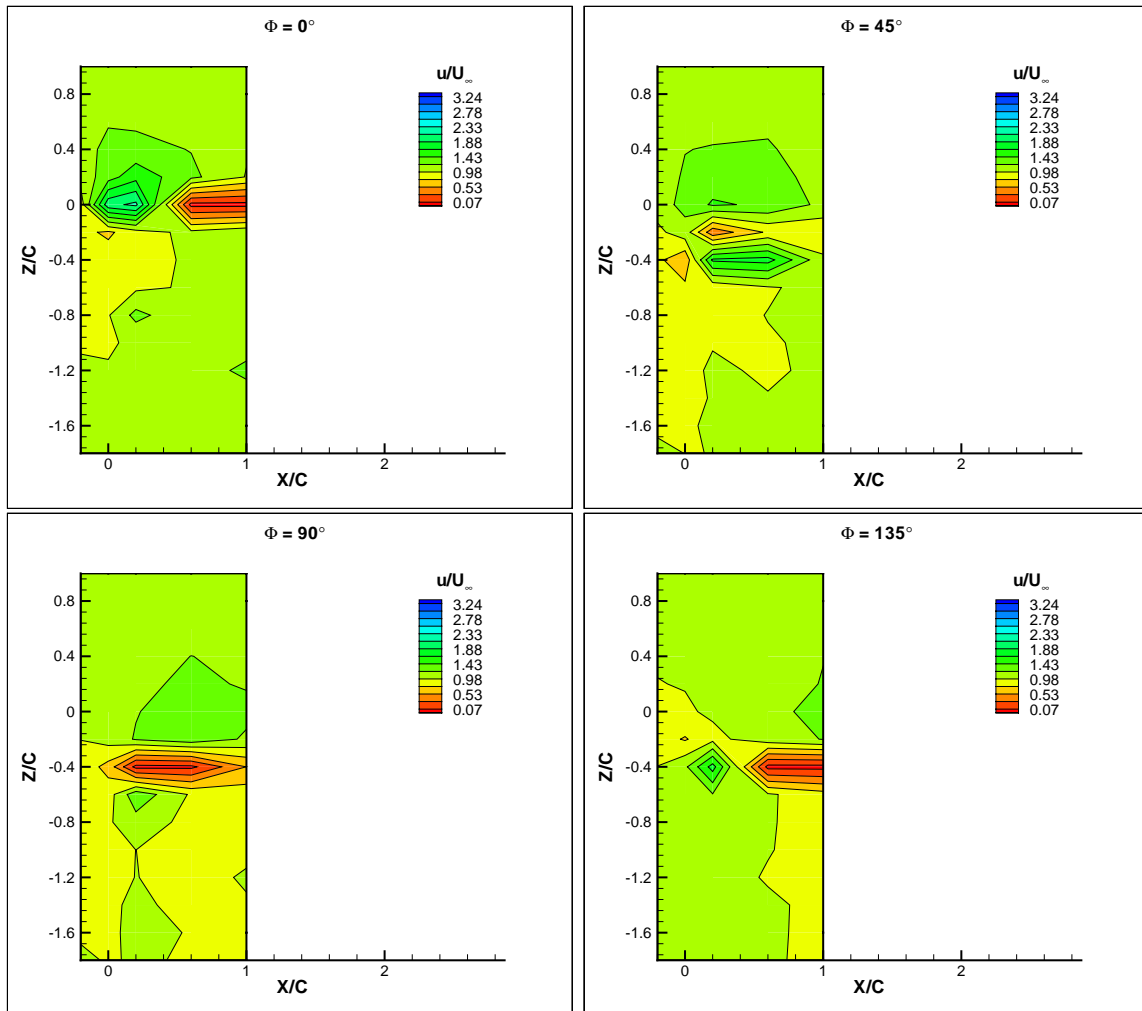


Figure 5.46. Single Flapping Wing During Upstroke, $k=1$, $u=2$ [m/s], $f=5$ [Hz], $Re=8760$

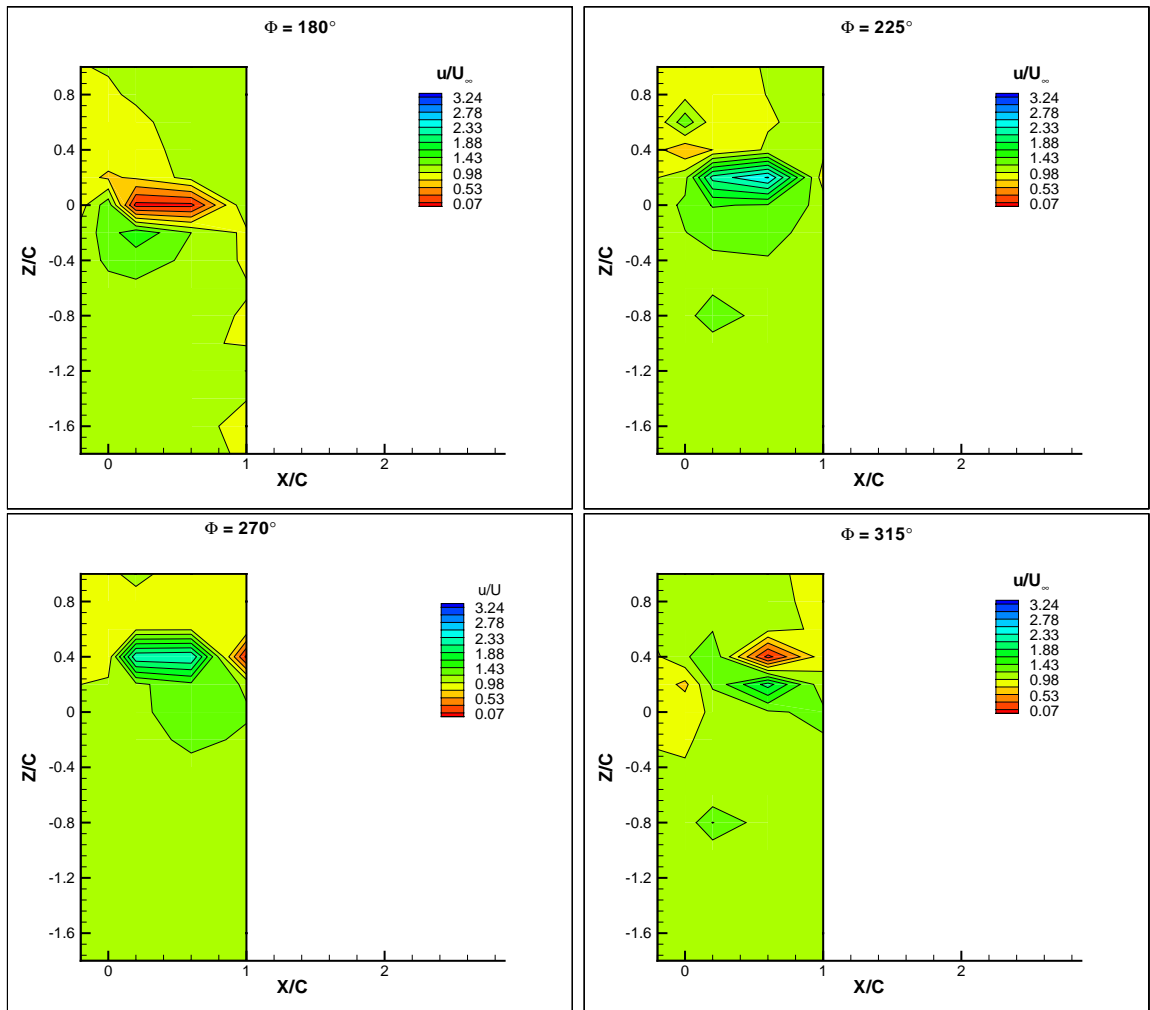


Figure 5.47. Single Flapping Wing During Downstroke, $k=1$, $u=2$ [m/s], $f=5$ [Hz], $Re=8760$

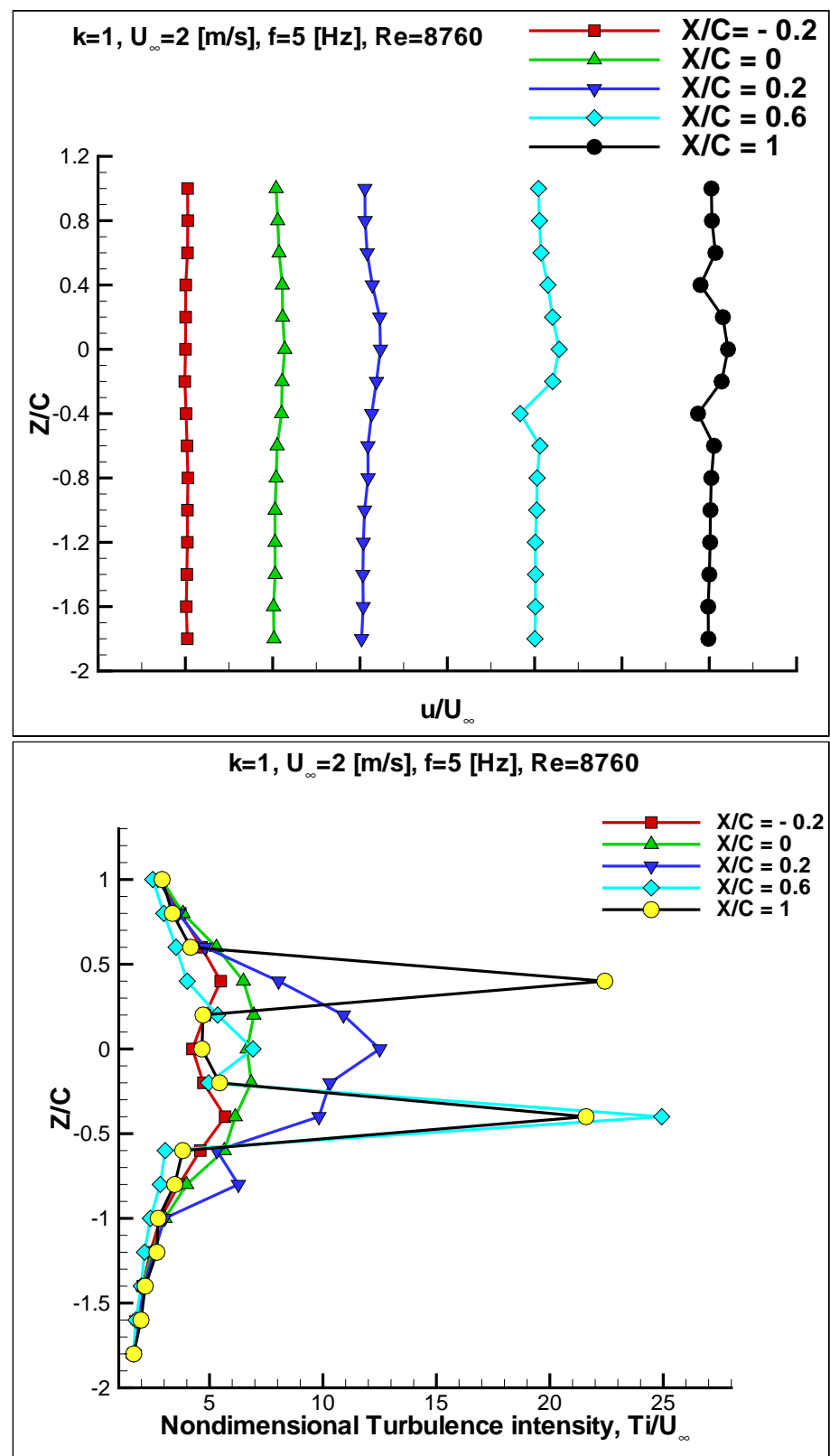


Figure 5.48. Average Velocity Profile and the Associated Turbulence Intensity Around Single Flapping Wing, $k=1$, $u=2$ m/s, $f=5$ Hz

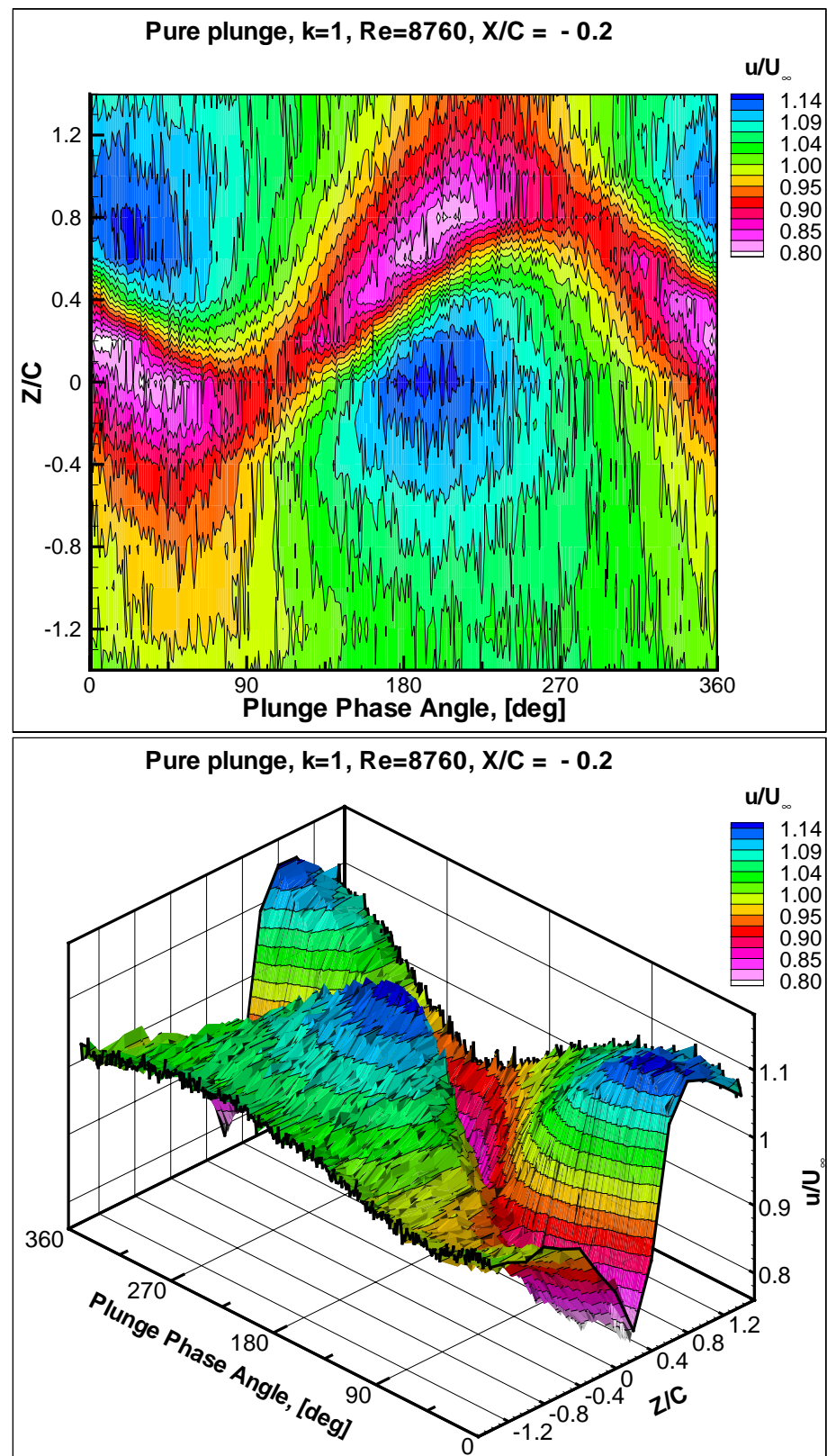


Figure 5.49. Single Flapping Wing at $X/C=-0.2$, $k=1$, $u=2$ [m/s], $f=5$ [Hz], $Re=8760$

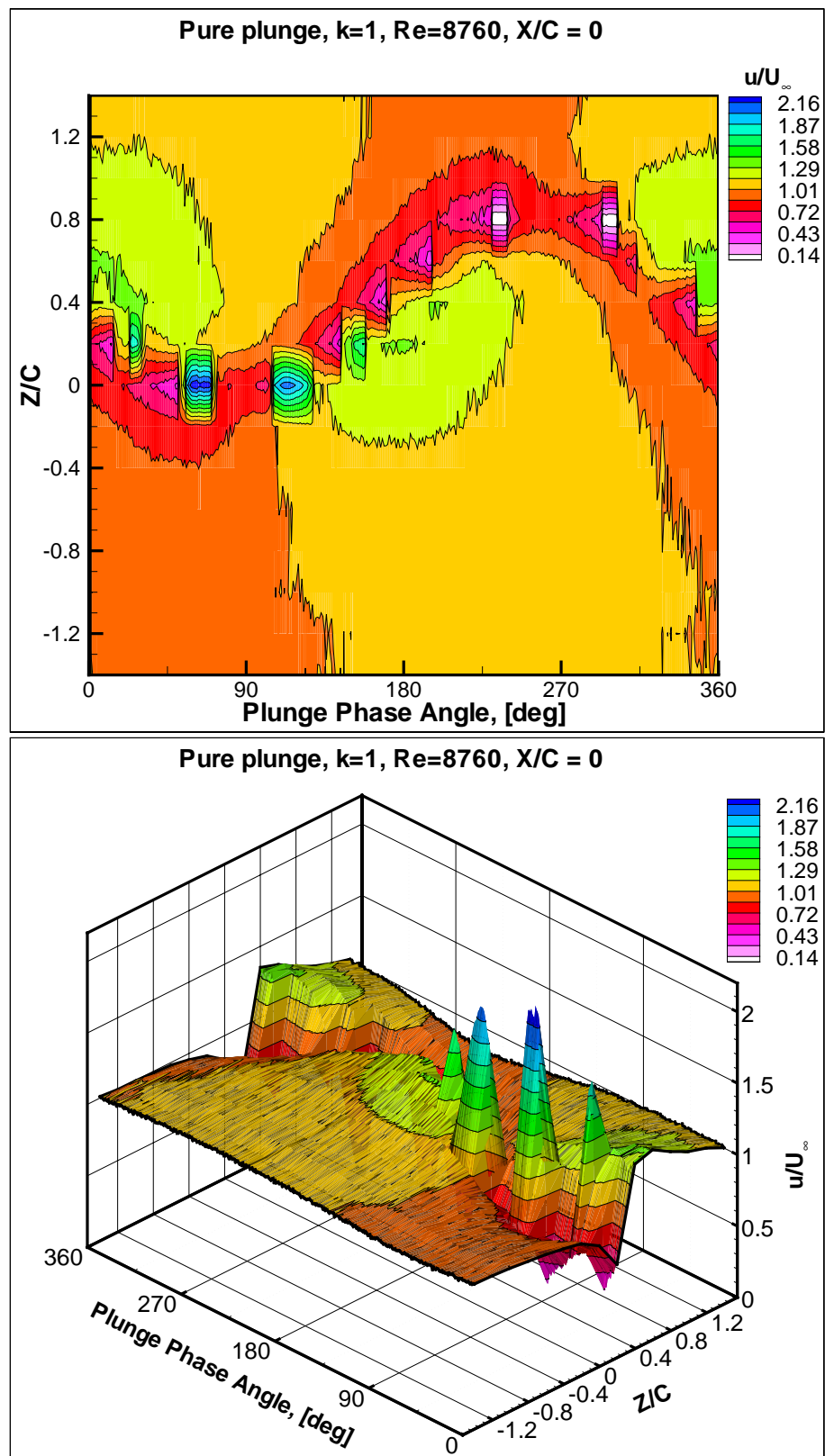


Figure 5.50. Single Flapping Wing at $X/C=0.0, k=1$, $u=2$ [m/s], $f=5$ [Hz], $Re=8760$

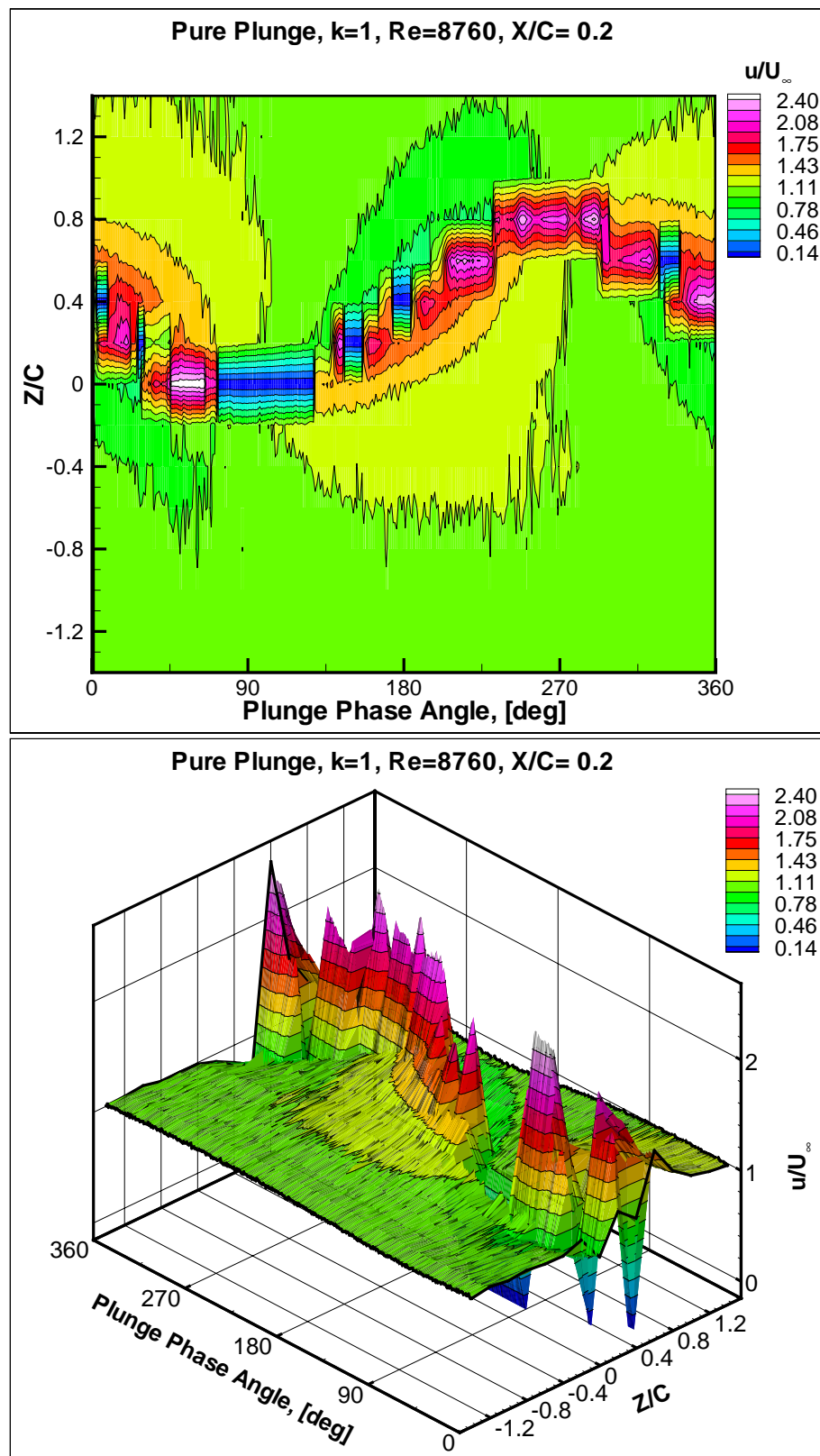


Figure 5.51. Single Flapping Wing at $X/C=0.2$, $k=1$, $u=2$ [m/s], $f=5$ [Hz], $Re=8760$

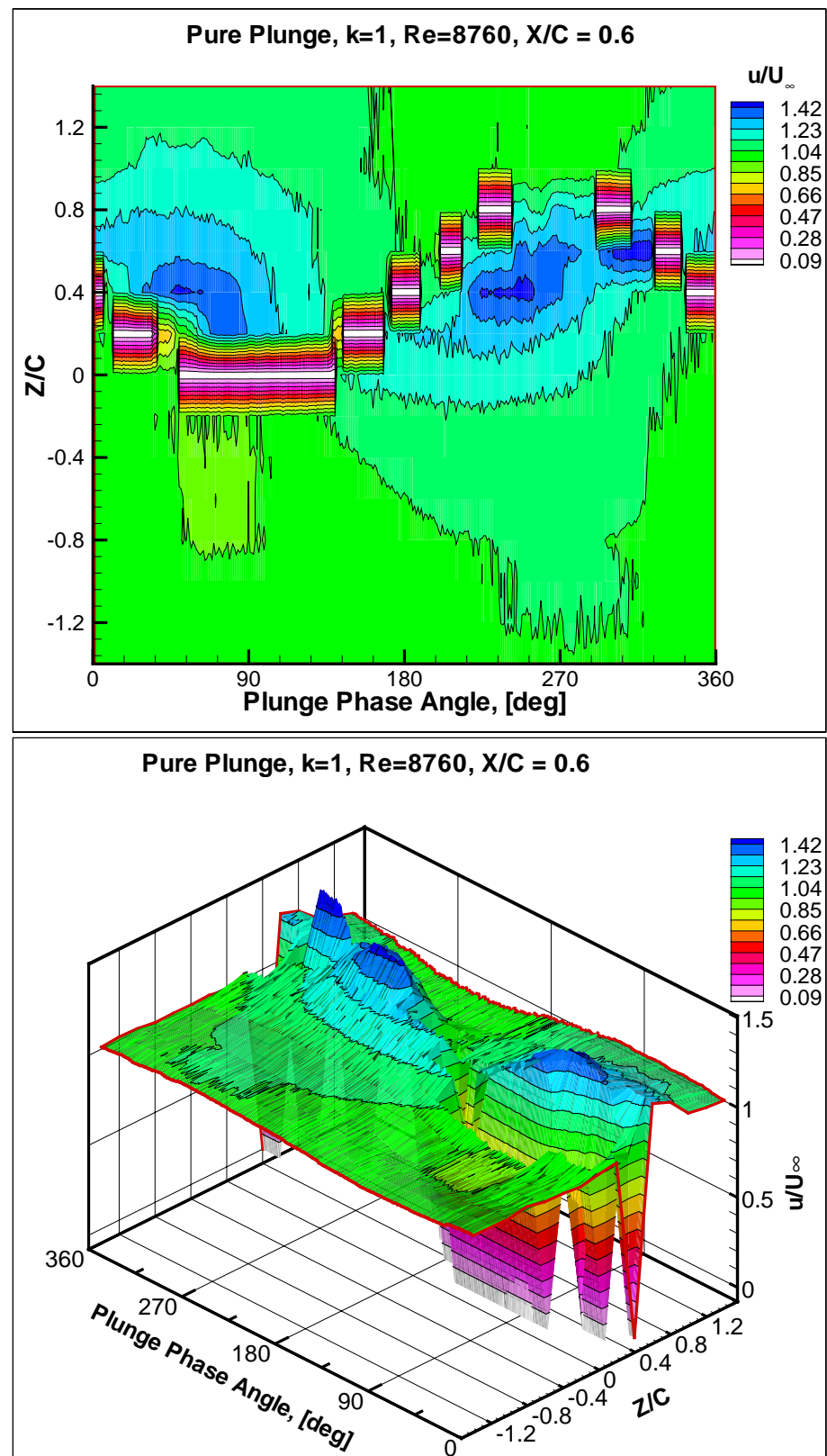


Figure 5.52. Single Flapping Wing at $X/C = 0.6$, $k=1$, $u=2$ m/s, $f=5$ Hz, $Re=8760$

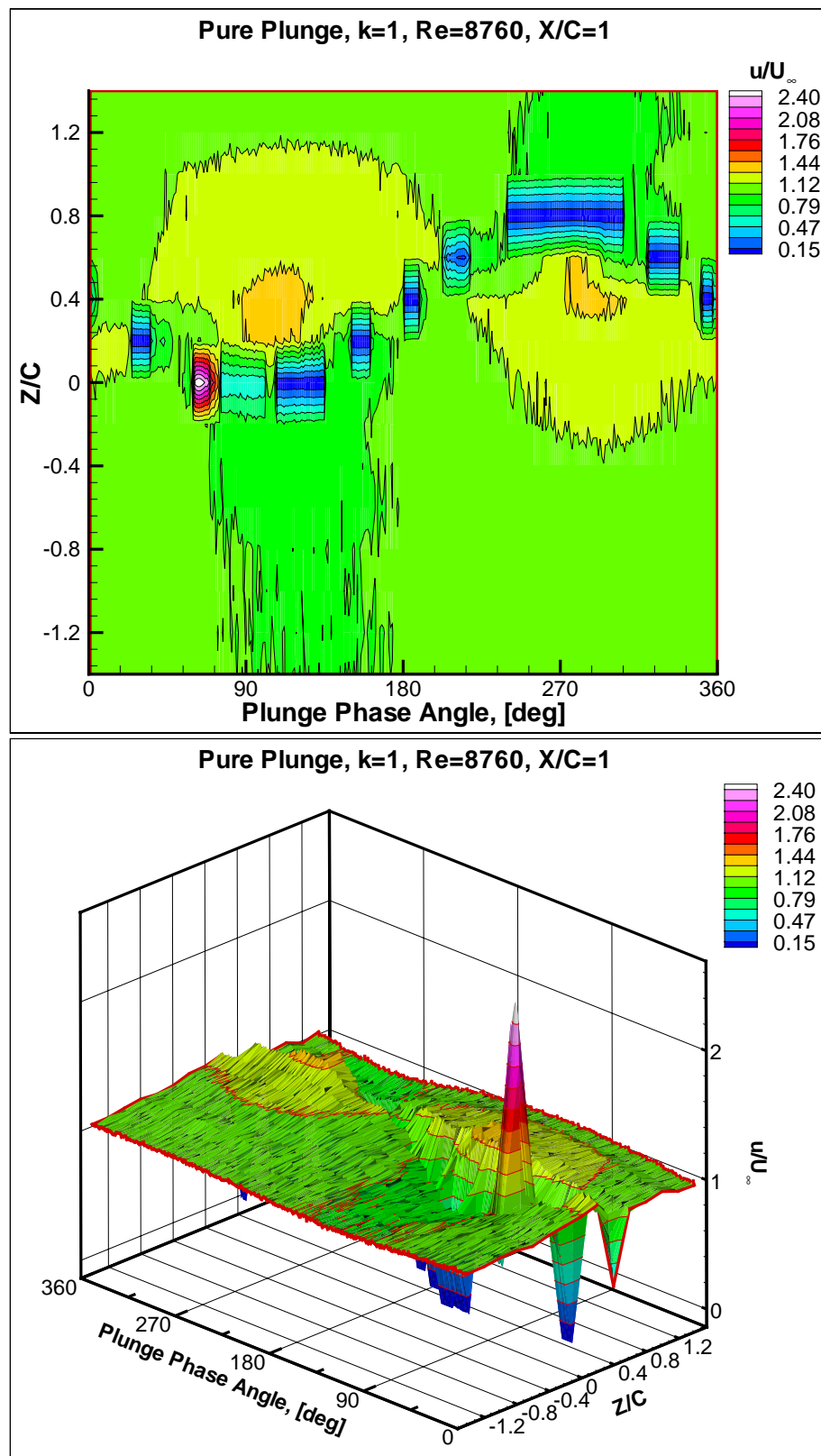


Figure 5.53. Single Flapping Wing at $X/C = 1.0$, $k=1$, $u=2\text{m/s}$, $f=5\text{ Hz}$, $Re=8760$

VI. ANALYSIS OF THE EXPERIMENTAL RESULTS

A. STEADY FLOW MEASUREMENTS

In the steady flow investigation, the axial velocity component, u , and the turbulence intensity were measured at 2 m/s freestream velocity at two different angles of attack, namely 0° and 4° . It was also measured at 5 m/s for zero degree angle of attack.

The obtained results are presented in Fig. 5.3 through Fig. 5.12. For the three cases the turbulence intensity has the highest value in the wake, as expected. Also, a high velocity area can be seen on the upper and lower surfaces for the airfoil at zero angle of attack for $U=2$ and 5 m/s, Fig. 5.3 and Fig. ???. Meanwhile, for the case of angle of attack $=4^\circ$ the highest value for the velocity can be seen on the upper surface only, as shown in Fig. 5.10.

The normalized velocity profiles, u/U_∞ are presented in Fig. 5.4, Fig. 5.8 and Fig. 5.12. For the case of 4 degrees angle of attack, the changes in the wake behind the airfoil are clearly distinguished. For the case of $U_\infty = 2$ and $\text{AOA}=0^\circ$, the highest value of the turbulence intensity is found on the lower surface near the mid chord position. Also, two areas with high velocity and high turbulence intensity can be seen at one chord behind the trailing edge in Fig. 5.6.

B. THRUST MEASUREMENTS

The thrust generation by wing flapping was investigated as well. The thrust coefficient as function of flapping frequency and reduced frequency is presented for different Reynolds numbers in Fig. 5.1 through Fig. ???. It can be seen that as the reduced frequency increases, the thrust coefficient increases for the same Reynolds number. Also, for the same reduced frequency, the thrust coefficient increases as the Reynolds number increases.

C. FLAPPING BIPLANE FLOW MEASUREMENTS

The flow between and around the two flapping airfoils was investigated. The axial velocity component, u , is presented over the whole domain as contour and carpet plots to present the changes during a complete flapping cycle at each location X/C . The same for the turbulence intensity. Also, at each location, X/C , the measured velocity component u is presented as nondimensional value at different vertical locations Z/C . It is important to note that in some plots, like in Fig. B.2, some velocity measurements yield zero velocity values. This is due to the fact that the LDV system was unable to detect any scattered light from the particles passing through the laser probe. This might be due to the fact that the measurements are made in high vortical regions with too few seed particles. It might also be due to laser beam blockage as the wings pass through the beams during the flapping cycle.

All the velocity measurements were processed and the velocity distributions around the airfoil at different plunge phase angles were extracted and presented in Fig. ??, and Fig. ?? for a complete cycle. Since the flow around the two airfoils is antisymmetric around the plane of symmetry, the flow around the upper airfoil will only be described here. Further-

more, it is important to recognize the difficulty in identifying the precise flow characteristics based on the axial flow field information only. Therefore, in the following paragraphs we — describe the locations of high and low axial velocities — of distinct vortices (which could be better identified with u - and v -velocity information).

At plunge phase angle, $\Phi = 0^\circ$, the upper airfoil is located at $Z/C = 1.1$. It is noticed that the velocity near the upper surface is higher than that near the lower surface. The wake area behind the airfoil has a high velocity value. As the wing moves down to $\Phi = 45^\circ$, the velocity increases on the upper surface while the area of high velocity in the wake is moving downstream. As the wing reaches the mean position at $\Phi = 90^\circ$, $Z/C = 0.7$, the high velocity region still exists on the upper surface but moves downstream towards the trailing edge. An area of low velocity is noticed on the lower surface. The area of high velocity in the wake is moving further downstream. As the wing keeps moving down during the downstroke, $\Phi = 135^\circ$, $Z/C = 0.5$, the high velocity region on the upper surface is moving further downstream. The velocity underneath the wing is lower than that above it. A low velocity area is noticed in the wake behind and between the two airfoils. Meanwhile, the velocity between the two airfoils starts to increase, especially within the first quarter chord. The increase in the axial velocity along the centerline between the two airfoils can also be seen quite clearly in Fig. 5.16, Fig. 5.18 and Fig. 5.20. The highest velocities occur when the two airfoils are close together around $\Phi = 180^\circ$. The wing reaches the lowest point during the downstroke at, $\Phi = 180^\circ$, $Z/C = 0.3$. At this location, it appears that three vortices exist on the upper surface. For two of them, the axial velocity component is small while the third one has a higher value. Comparing with the computational results and the flow visualization, we can conclude that there are two spots with low axial velocity

because we have two clockwise vortices which decreases the axial velocity. The opposite situation happens with the third vortex which is a counterclockwise vortex.

As the wing starts the upstroke, $\Phi = 225^\circ, Z/C = 0.5$, the effective angle of attack changes direction and becomes negative. Hence, the velocity starts to increase and build up on the lower surface while the upper surface has a lower velocity. As the airfoil reaches the mean position during the upstroke, $\Phi = 270^\circ, Z/C = 0.7$, the high velocity area between the two airfoils starts to move downstream to almost one chord behind the trailing edge. As the airfoil keeps moving up during the upstroke at $\Phi = 315^\circ, Z/C = 0.9$, the velocity at the lower surface is higher than that on the upper surface. Three vortices can be noticed. Two counterclockwise and one clockwise. The high velocity area between the two airfoils now is moving downstream.

The axial velocity component, u , was measured over a complete cycle at several positions X/C . These instantaneous velocity values were averaged to obtain a velocity profile at each axial location, X/C and presented in Fig. ???. At the leading edge, it is seen that the velocity decreases dramatically within the flapping margin in such a way that there are two peaks in the mean flapping position of the two airfoils. Meanwhile, between the leading and trailing edges the velocity is higher underneath the upper flapping margin than the lower part of it. In the wake behind the airfoil, two increases in velocity can be noticed behind the trailing edge which indicate the shed vortices.

D. FLOW MEASUREMENTS FOR FLAPPING AIRFOIL IN GROUND EFFECT

As the wing starts flapping from the uppermost position it is noticed that the velocity starts to increase between the wing and the ground plane. As the wing keeps moving down during the downstroke to $\Phi = 45^\circ$, it is noticed that an area of high velocity develops near the lower surface of the airfoil downstream of the midchord position. As the wing moves toward the mean position, $\Phi = 90^\circ$, two distinct areas can be seen between the wing and the ground plane. The first is a low velocity region just behind the leading edge. The second is a high velocity region near the trailing edge.

As the wing keeps moving down to, $\Phi = 135^\circ$, the high and low velocity regions between the wing and the ground plane move downstream. As the wing keeps moving down to $\Phi = 180^\circ$, a small area of higher velocity develops on the upper surface close to the leading edge. Meanwhile, the low velocity region keeps moving downstream near the ground plane.

During the upstroke at $\Phi = 225^\circ$, the effective angle of attack changes direction, and the velocity near the upper surface becomes less than the free stream velocity. The velocity starts to increase a little bit on the lower surface. At $\Phi = 270^\circ$, four regions can be distinguished , two with high velocity and two with low velocity. As the wing approaches $\Phi = 315^\circ$, a low velocity region is noticed near the upper surface of the airfoil.

E. SINGLE FLAPPING AIRFOIL FLOW MEASUREMENTS

The wing starts the flapping cycle at $\Phi = 0^\circ$ from the uppermost position, $Z/C = 0.4$. It is noticed that there is a high velocity region near the lower surface of the airfoil.

This vortex was generated during the previous upstroke. As the airfoil moves down, the effective angle of attack increases and the velocity increases on the upper surface. As the airfoil approaches the mean position, $\Phi = 90^\circ$, the velocity near the upper surface becomes higher than the freestream. At the same time the velocity on the lower surface decreases and becomes less than the freestream value.

At $\Phi = 135^\circ$, the velocity on the upper surface is higher than the free stream, indicative of a vortex. At $\Phi = 180^\circ$, the downstroke ends. At that position, a high velocity region is noticed on the upper surface of the airfoil. As the wing starts the upstroke, $\Phi = 225^\circ$, the effective angle of attack changes sign and the velocity near the lower surface starts to increase and becomes higher than that on the upper surface. As the wing keeps moving upward, the velocity increases on the lower surface and the high velocity region starts to sweep backward until it is almost shed from the lower surface at $\Phi = 315^\circ$. The comparison between the biplane measurements and the single airfoil results shows the following significant differences.

A direct comparison between the biplane, flapping wing in presence of ground plane and single flapping wing at different axial locations X/C for different phase angles is presented in Tables 6.1, 6.2, 6.3, 6.4, 6.5 and 6.6. The axial velocities listed in these tables were measured at $Z/C=-0.7$ from the mean flapping position, which is the plane of symmetry for the biplane case. It is readily seen that the biplane configuration, in general, generates larger disturbances than the single airfoil or the airfoil in ground effect, thus giving further quantitative evidence for the greater thrust generation capability of the biplane.

Table 6.1. Measured Axial Velocity Component, u/U_∞ , at Different Plunge Phase Angle, Φ , $Z/C = -0.7$, $k=1$, $Re=8760$, $h=0.4$, $X/C=-0.25$

Plunge phase angle Φ [deg]	Biplane	Ground plane $X/C=-0.25$	Single flapping wing $X/C=-0.2$
	$X/C=-0.25$	$X/C=-0.25$	$X/C=-0.2$
0.83	0.863769619	0.750694541	0.9834992
45.83	0.698112989	0.608992773	0.936257251
90.83	0.804731722	0.741699892	0.961867373
135.83	1.087860634	0.962276964	1.034629426
180.83	1.220980759	1.067223162	1.075115023
225.83	1.244995684	1.08709762	1.073714743
270.83	1.175133207	0.995445301	1.055003501
315.83	1.039729395	0.909875855	1.018581216

Table 6.2. Measured Axial Velocity Component, u/U_∞ , at Different Plunge Phase Angle, Φ , $Z/C = -0.7$, $k=1$, $Re=8760$, $h=0.4$, $X/C=0$, Leading Edge

Plunge phase angle Φ [deg]	Biplane	Ground plane $X/C=0$	Single flapping wing $X/C=0$
	$X/C=0$	$X/C=0$	$X/C=0$
0.83	0.811684173	0.629574881	0.972944589
45.83	0.569932001	0.433633243	0.939377876
90.83	0	0.33616	0.966178236
135.83	1.13911082	1.022446754	1.033916783
180.83	1.261565692	1.114126203	1.077715543
225.83	1.23081558	1.036677854	1.085364573
270.83	1.164183097	0.976808788	1.065453091
315.83	1.020320469	0.883181446	1.027738048

Table 6.3. Measured Axial Velocity Component, u/U_∞ , at Different Plunge Phase Angle, Φ , $Z/C = -0.7$, $k=1$, $Re=8760$, $h=0.4$, $X/C=0.25$

Plunge phase angle Φ [deg]	Biplane	Ground plane	Single flapping wing
	$X/C=0.25$	$X/C=0.25$	$X/C=0.2$
0.83	0.774816871	0.802111299	1.004863473
45.83	0.575344291	1.245323812	0.946941888
90.83	0	0.312615508	0.985342068
135.83	1.256438259	0.861304117	1.066218244
180.83	1.301228459	1.016753033	1.105781156
225.83	1.255636796	1.062136096	1.110977195
270.83	1.179536426	1.050574114	1.098187137
315.83	1.024004303	0.970808273	1.036912382

Table 6.4. Measured Axial Velocity Component, u/U_∞ , at Different Plunge Phase Angle, Φ , $Z/C = -0.7$, $k=1$, $Re=8760$, $h=0.4$, $X/C=0.5$

Plunge phase angle Φ [deg]	Biplane	Ground plane $X/C=0.5$	Single flapping wing $X/C=0.6$
	$X/C=0.5$	$X/C=0.5$	$X/C=0.6$
0.83	0.900424486	0.904803634	1.01315013
45.83	0.734425061	1.263628183	0.95585
90.83	0	0.97328	0.937267453
135.83	1.182476733	0.978371007	0.98485
180.83	1.269807243	1.068632203	1.0282
225.83	1.275504391	1.091999802	1.050573825
270.83	1.213844841	1.079994272	1.05694942
315.83	1.093128082	1.014842246	1.038895279

Table 6.5. Measured Axial Velocity Component, u/U_∞ , at Different Plunge Phase Angle, Φ , $Z/C = -0.7$, $k=1$, $Re=8760$, $h=0.4$, $X/C=0.75$

Plunge phase angle Φ [deg]	Biplane	Ground plane
	$X/C=0.75$	$X/c=0.75$
0.83	0.981739194	0.937109564
45.83	0.97140708	0.805147089
90.83	0.438033383	2.1488
135.83	0.905909197	0.715965832
180.83	1.167707603	0.891507233
225.83	1.273553842	1.016394608
270.83	1.230279662	0.993620106
315.83	1.209224358	1.010877598

Table 6.6. Measured Axial Velocity Component, u/U_∞ , at Different Plunge Phase Angle, Φ , $Z/C = -0.7$, $k=1$, $Re=8760$, $h=0.4$, $X/C=1$, Trailing Edge

Plunge phase angle Φ [deg]	Biplane	Ground plane $X/C=1$	Single flapping wing $X/C=1$
	$X/C=1$	$X/C=1$	$X/C=1$
0.83	1.132776365	1.008925295	1.037340368
45.83	1.068528958	0.902613539	1.023719744
90.83	0.485672157	1.128697907	0.943016103
135.83	0.665957903	0.49128	0.936744249
180.83	1.073062535	0.763821508	0.96765103
225.83	1.216060934	0.935216116	1.027968094
270.83	1.286237237	1.015900262	1.049592418
315.83	1.267735992	1.028645633	1.066170734

VII. CONCLUSIONS AND RECOMMENDATIONS

A wind tunnel investigation of low speed flow over flapping airfoils and airfoil combinations was performed using flow visualization and laser doppler velocimetry. Specifically, three cases were studied: A NACA0014 airfoil oscillating in a sinusoidal plunge mode, A NACA0014 airfoil oscillating in a sinusoidal plunge mode near a ground plane, and two NACA0014 airfoils arranged in a biplane configuration and oscillating in counterphase in a sinusoidal plunge mode. The plunge amplitude-to-airfoil chord ratio was 0.4, the reduced frequency of oscillation was 1.0 and the Reynolds number based on airfoil chord was set at 8760.

Conditionally sampled measurements of the axial flow velocity were taken at numerous flow field points providing detailed information about the flow features generated by this type of flapping motion. These measurements were complemented by time-averaged flow field data and by visualization of the instantaneous flow field at various points during the flapping cycle. Furthermore, the thrust generated by the sinusoidal plunge motion was measured with a laser range finder. The results shows that vortex shedding occurs both from the airfoil leading and trailing edge.

This experimental evidence for the occurrence of dynamic stall at the chosen test conditions of $h=0.4$, $k=1$ and Reynolds number=8760 provides credence to the Navier-Stokes predictions summarized in Chapter II. Dynamic stall may well be an important, and even critical, ingredient to achieve optimum thrust and lift on low Reynolds number flight vehicles, such as birds, and micro-air vehicles.

However, before more specific conclusions can be stated about the role of dynamic stall for effective thrust and lift generation, the following additional studies should be pursued:

1. Repeat the measurements reported in this thesis with a Particle Image Velocimetry PIV system so that complete flow field information becomes available.
2. Extend the range of test parameters so that the dynamic stall boundary for sinusoidal plunge oscillation can be determined. This requires a repetition of the tests for different values of plunge amplitude and frequency and tunnel speeds. Also, it is recommended to test for plunge amplitudes greater than 0.4 so that the change in flow features can be measured as the airfoil is oscillating in deep dynamic stall. Unfortunately, this requires a significant modification of the model which is currently limited to $h=0.4$.
3. Extend the tests to explore the effect of combined pitch and plunge motions. As shown by the potential flow predictions of Jones and Platzer [13] and the Navier-Stokes predictions of Isogai et al [11] the phase angle between pitch and plunge and the amplitude ratio between pitch and plunge are two additional critical parameters. Detailed experimental flow investigation is needed to verify these predictions.
4. Detailed comparisons between the Navier-Stokes predictions of Castro [5] and the present experiments for sinusoidally plunging airfoils need to be made so that the predictive capability of the Navier-Stokes computations can be assessed.
5. If the Navier-Stokes predictions are found to be reasonably accurate, additional computations are recommended to identify the parameter combination for optimum thrust and lift generation

APPENDIX A: CALIBRATION OF WIND TUNNEL

At the beginning of the experimental work, the wind tunnel test section was calibrated to document the flow quality. The calibration was done in three steps. The first step was a survey of the turbulence characteristics over the whole wind tunnel speed range. In the second step, a pitot tube was used for a velocity survey. The third step consisted of a detailed survey using LDV in one vertical plane located one half chord length upstream of the leading edge location of the wing in all experiments.

A. Turbulence Characteristics

LDV was used to measure the axial velocity component, u , at a fixed point. It was intended to take such measurements at the exact center of the test section but due to traverse mechanism limitations, this point was located at 68 cm height from the floor and 71 cm from the side wall. This is only 7 and 4 cm, respectively from the actual center of the test section. The laser probe was aimed to be located 43 cm underneath the pitot tube. The axial velocity component, u , turbulence intensity, standard deviation and the number of particles passing through the probe volume, were recorded and are presented in Table A.1.

Table A.1. Wind Tunnel Calibration

U mean	Standard deviation	Turbulence Intensity	Number of particles
1.06132	0.0403795	3.80464	2965
2.00892	0.0476697	2.3729	2983
3.00066	0.0808584	2.69469	2979
3.96654	0.103202	2.60182	2997
5.12694	0.134258	2.61867	2990
6.02697	0.158603	2.63155	2993
7.04868	0.193352	2.7431	2980
7.96251	0.215616	2.70789	2990

B. Pitot Tube Survey

In his thesis, Lund [21], refurbished the wind tunnel. He calibrated the wind tunnel using both a pitot tube and LDV and presented an empirical formula (A.1) which relates the pitot tube output voltage to the LDV measurements. He did two sets of calibration. In the first one, the LDV and pitot tube were co-located, with the LDV probe 0.1 [m] above and 0.05 [m] in front of the pitot tube. In the second experiment, the LDV probe was 2.4 [m] downstream and 0.1 [m] lower. The empirical formula for the second case, (A.2), was close to the first one.

$$V = 0.4819 \times (mVolt)^{0.489} \quad (\text{A.1})$$

$$V = 0.4593 \times (mVolt)^{0.4979} \quad (\text{A.2})$$

Where, V , is the velocity in m/s and mVolt is the output of the pitot tube system in millie Volts.

In the present work, the pitot tube was moved 2.4 m downstream from the location used by Lund. The new location was selected such that it is located above the test model. A few measurements were taken for the wind tunnel speed by LDV and compared with the detected pitot tube voltage. It turned out that equation (A.1) is still valid and so it was used in the following survey.

In the present work, a Pitot static tube was used to investigate the flow velocity along the test section. The pitot tube was used to probe 168 locations distributed such that the test section could be surveyed completely. In the streamwise direction, X , 7 locations were investigated with 0.3 m apart. At each X location, a vertical plane (Y, Z) was investigated. Along the lateral direction, Y , six points were investigated. The first and sixth point was located 0.15 m from the side walls, while the distance between the points was 0.3 m. In the vertical direction, Z , four locations were investigated, 0.3 m apart and the first point was 0.3 m from the floor. The investigated points are shown in Fig. A.1.

Since the point located at (0,0.76,0.61) was almost in the middle of the test section, the axial velocity obtained from this point was used as the axial component of the free stream velocity, U . Data obtained from the pitot tube are presented in Fig. A.2. At each X location 24 measurements obtained at the associated (Y, Z) plane are plotted. Obtained data at the same vertical distance Z have the same symbol.

The main purpose of this experiment was to investigate the flow quality in the test section. The obtained velocity measurements are presented as a 3D contour graphs. The highest nondimensional velocity recorded was 1.011 which was located at only one spot close to the side wall, far away from the wing location. It is seen that the non-dimensional

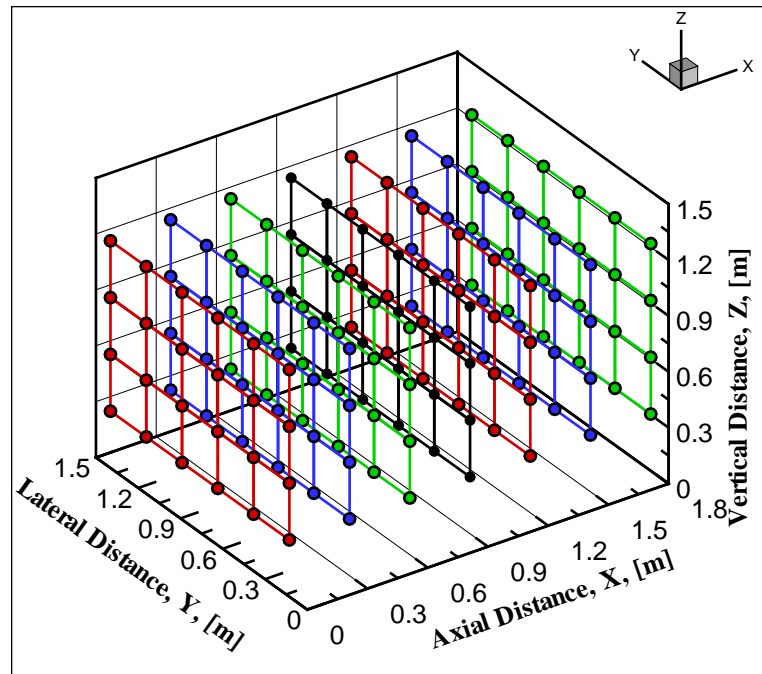


Figure A.1. Locations Probed by The Pitot Tube Along The Wind Tunnel Test Section

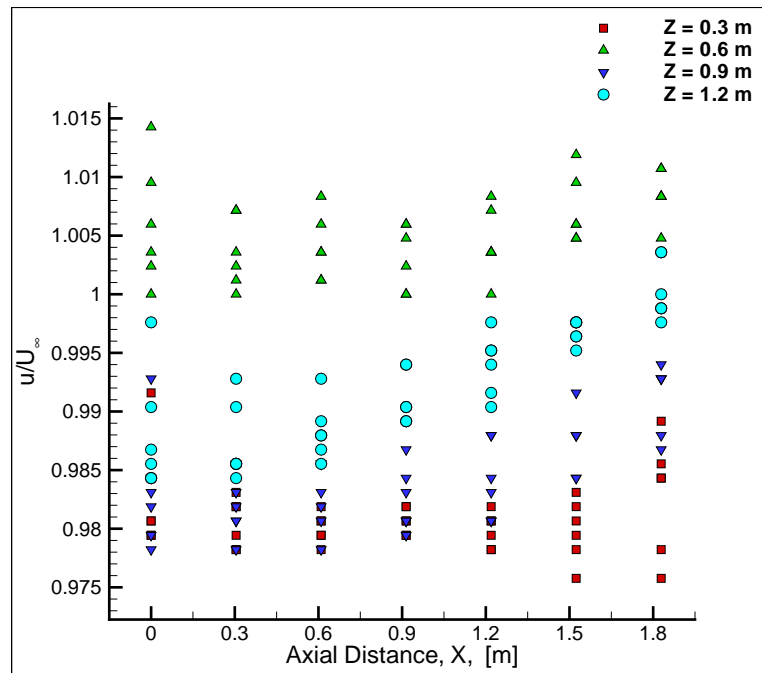


Figure A.2. Nondimensional Axial Velocity Obtained by the Pitot Tube

velocity values range from 0.978 to 1.011. In Fig. A.3 the flow survey in a vertical planes perpendicular to the X axis is presented at different X locations. Also, a set of surveys taken perpendicular to Y and Z is shown in Fig. A.4 and Fig. A.5.

C. LDV Survey

The LDV system was used to scan two vertical planes. One (X, Z) and one (Y, Z) .

For the (X, Z) flow survey, the axial velocity component, u , was measured at the streamwise stations $X = -0.5C$, $X = 0.5C$ and $X = 1.5C$. The measured axial velocity component, u , is presented versus the vertical distance, Z , in Fig. A.6. The turbulence intensity is illustrated in Fig. A.7.

It is seen that the u velocity in the wind tunnel increases with increasing distance from the floor, effectively exposing the model to a slight shear flow. This becomes very obvious when the velocities are non-dimensionalized by the local free stream velocity which is taken at the center of the tunnel. Curve fitting produces the polynomial, Eq. (A.3), as analytical approximation for this shear flow, valid between $0.381 \leq Z \leq 0.508$ [m]

$$u(z) = 11.069 * z^2 - 8.771 * z + 4.6758 \quad (\text{A.3})$$

For the second flow survey, a (Y, Z) plane located a half-chord upstream of the model's leading edge was chosen. Nine points were used to scan the lateral direction Y from 0.508 m to 0.7112 m measured from the tunnel side wall which has the laser probe. The vertical direction Z was scanned with 18 points from 0.5472 m to 0.6858 m. In total, 162 points were used to scan this plane. The scanned plane location for this flow survey is

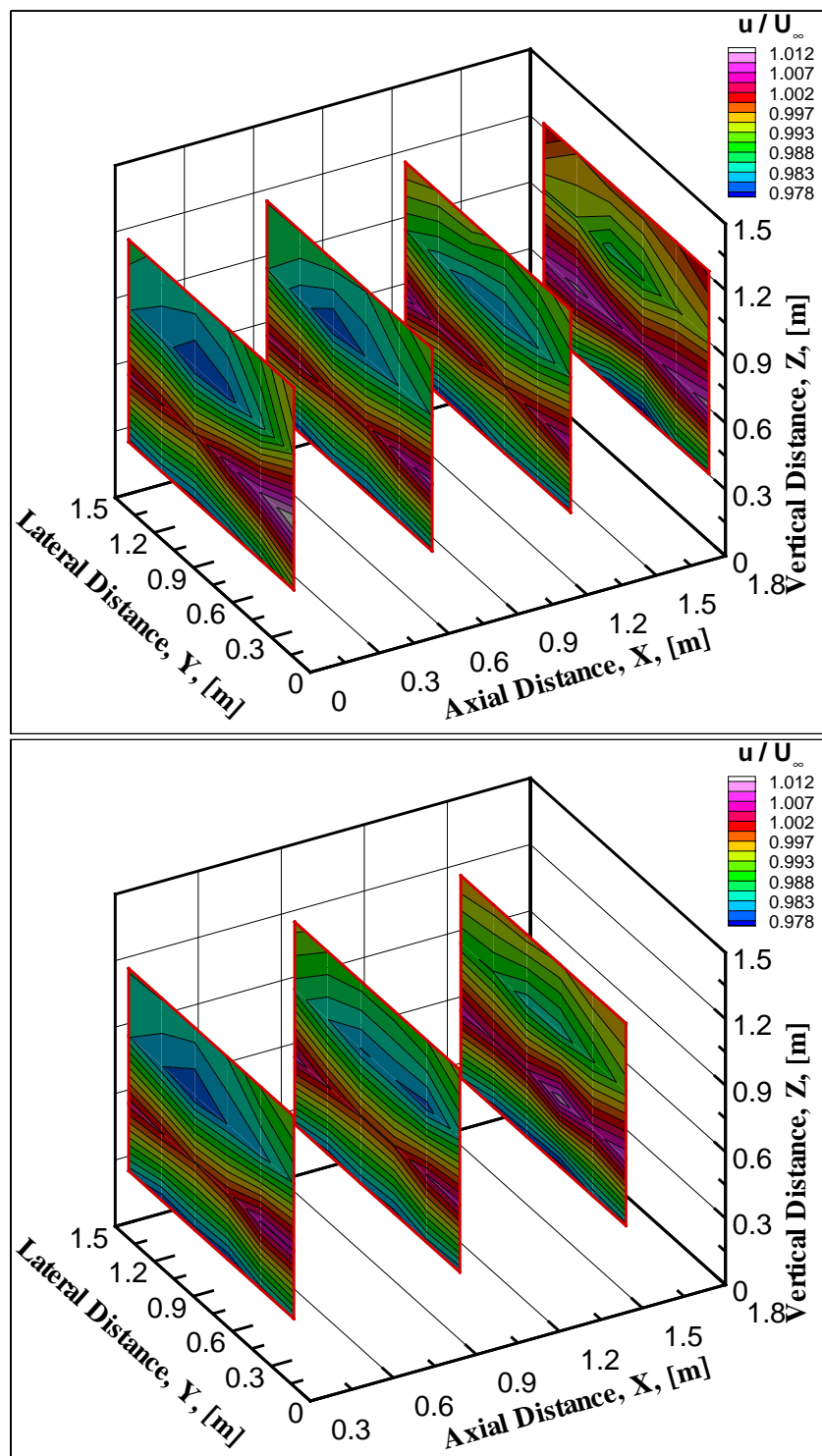


Figure A.3. Nondimensional Axial Velocity Component Measured by Pitot Tube at Different Axial Locations

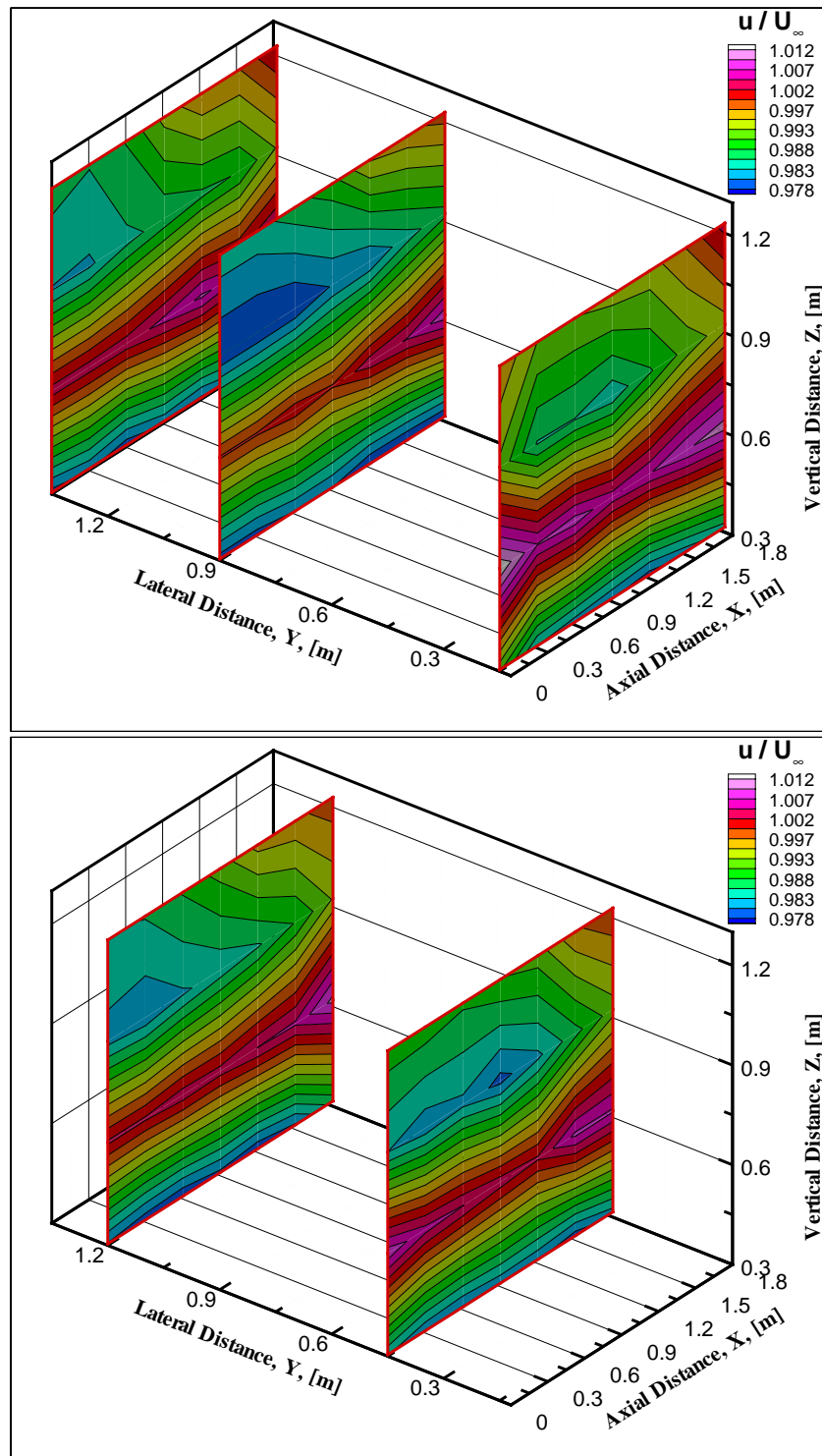


Figure A.4. Nondimensional Axial Velocity Component Measured by Pitot Tube at Different lateral Locations

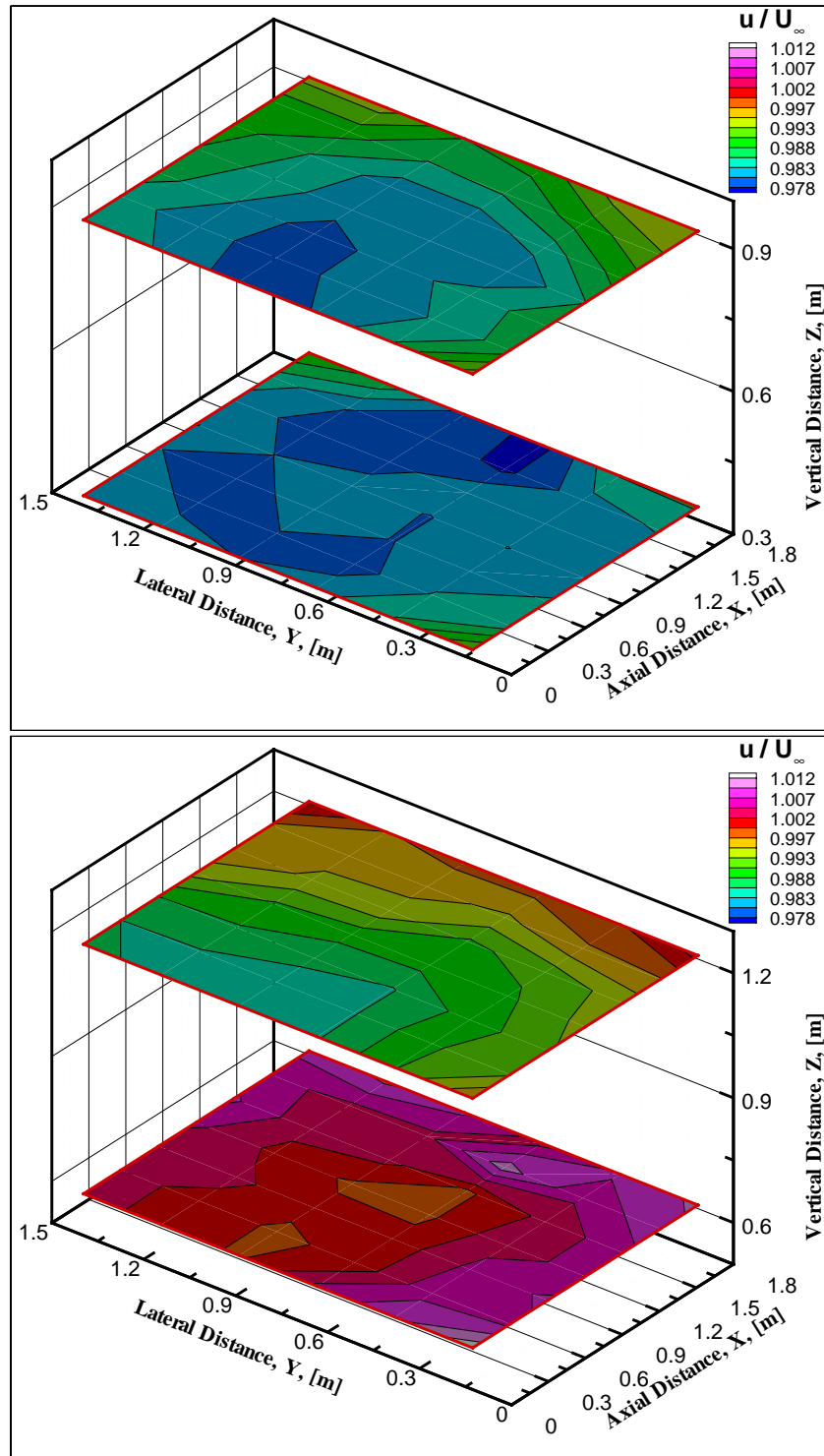


Figure A.5. Nondimensional Axial Velocity Component Measured by Pitot Tube at Different Vertical Locations

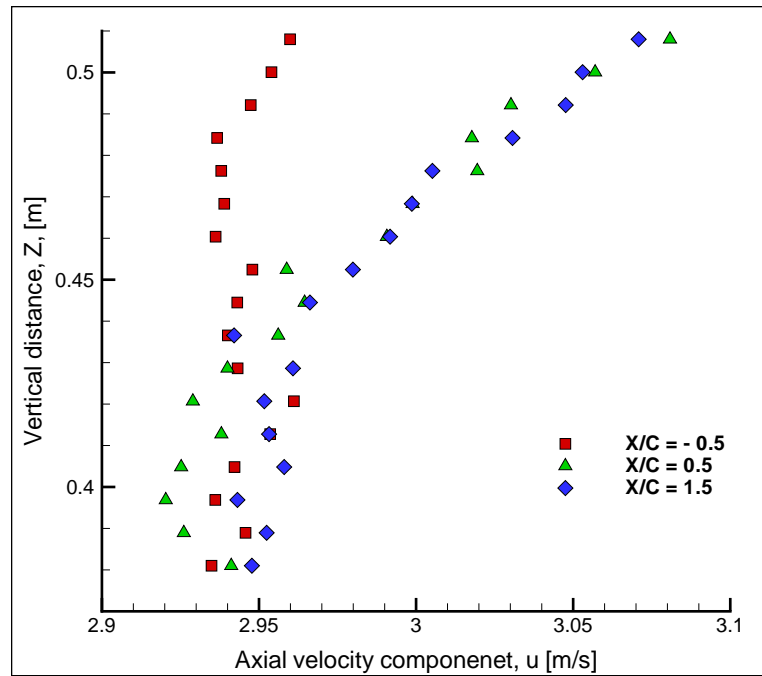


Figure A.6. Measured Velocity

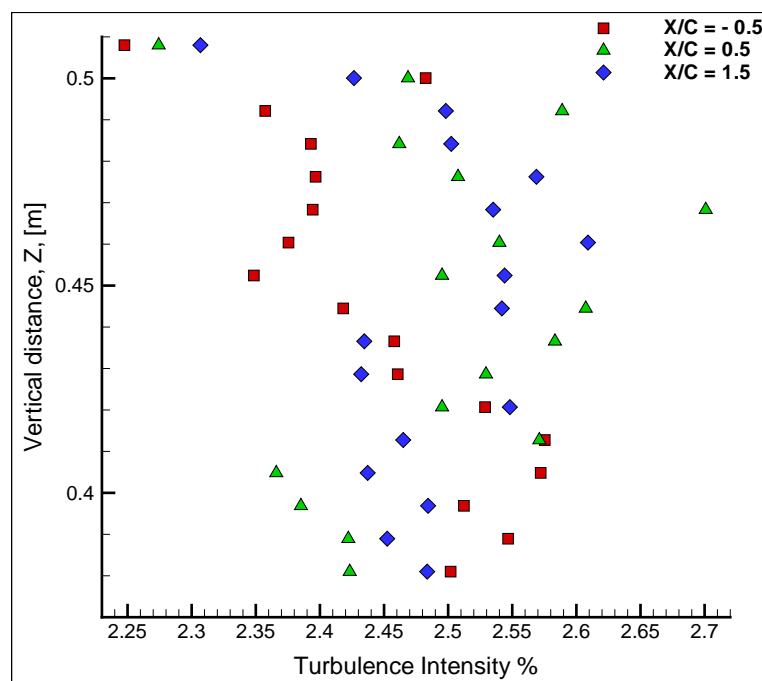


Figure A.7. Turbulence Intensity %

shown in Fig. A.8. The X axis scale is inverted on purpose to make it easy for the reader to compare with the results obtained from the pitot tube measurements.

The measured axial velocity, u , was non-dimensionalized by the measured value at $Y = 0.7112m$ and $Z = 0.6858m$. This point was closest to the center of the test section which can be reached by the LDV probe. This location was used to measure the free stream velocity for all the experiments in the present work.

The non-dimensional axial velocity $u/U\infty$ is presented in Fig. A.9 as it varies with vertical distance. It is noticed that the velocity increases a little as one approaches the center of the tunnel. The wing was located at $Z = 0.45m$ in this work. The standard deviation of the measurements was added as an error bar in the same figure. The non-dimensional axial velocity $u/U\infty$ is shown also as a contour lines in Fig. A.10. The turbulence intensity of the measurements is presented in two ways, as scattered points and as contour lines, in Fig. A.11 gives complete information about the whole domain.

D. DATA SCATTER AND THE STANDARD DEVIATION FOR THE MEASUREMENTS

Testing the validity of the measurements and its scatter was important. The axial velocity component, u , was measured by LDV at three different locations. The first location was at the far upstream almost at the middle of the test section. The second location was at one chord upstream of the leading edge. The third one was at one chord downstream of the trailing edge. The standard deviation for each set was calculated and shown in table A.2. Meanwhile, the measured velocity at the three locations is presented in Fig. A.12.

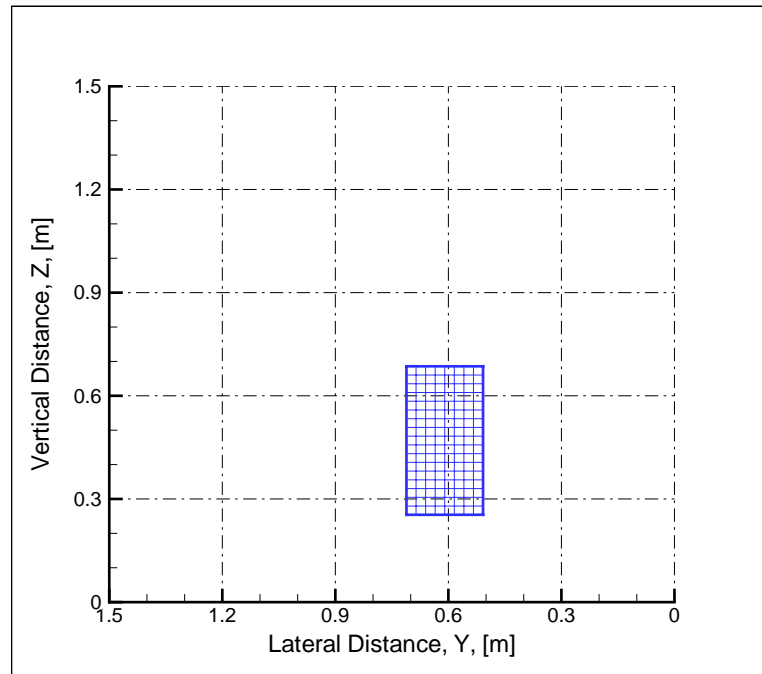


Figure A.8. The Scanned Plane

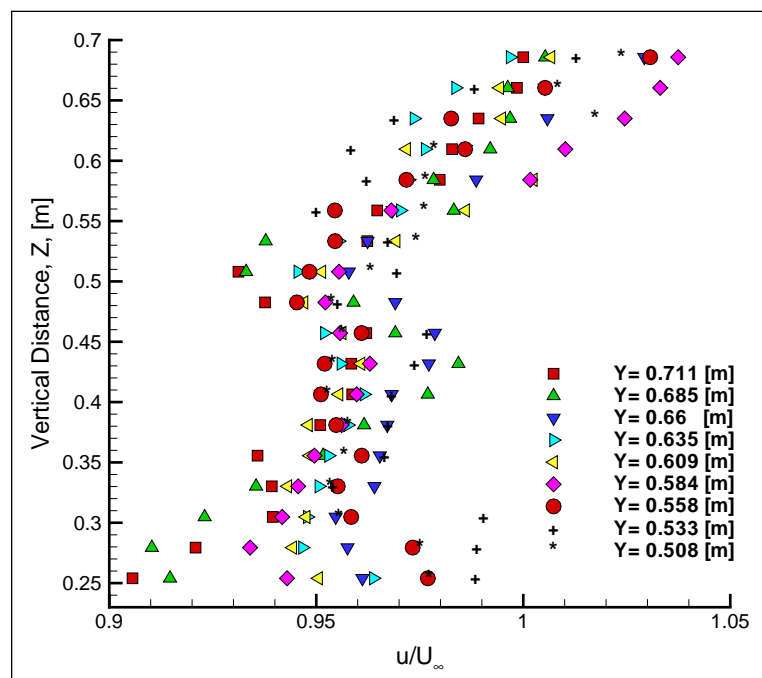


Figure A.9. u/U_{∞}

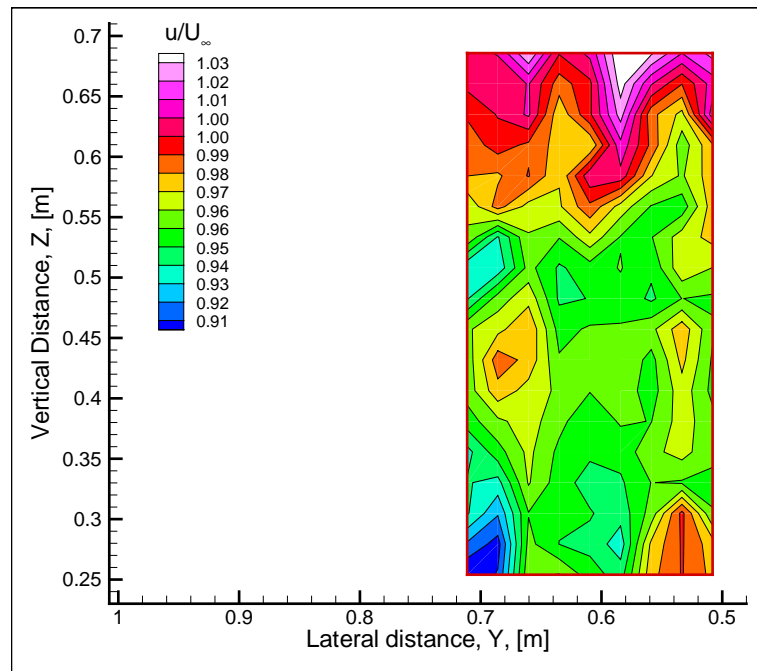


Figure A.10. u/U_∞

Table A.2. Standard Deviation for the Measured Axial Velocity Component

Location of measurements	Standard deviation of measurements
Far free stream	0.01229
One chord upstream of leading edge	0.014044
One chord downstream of the trailing edge	0.010138

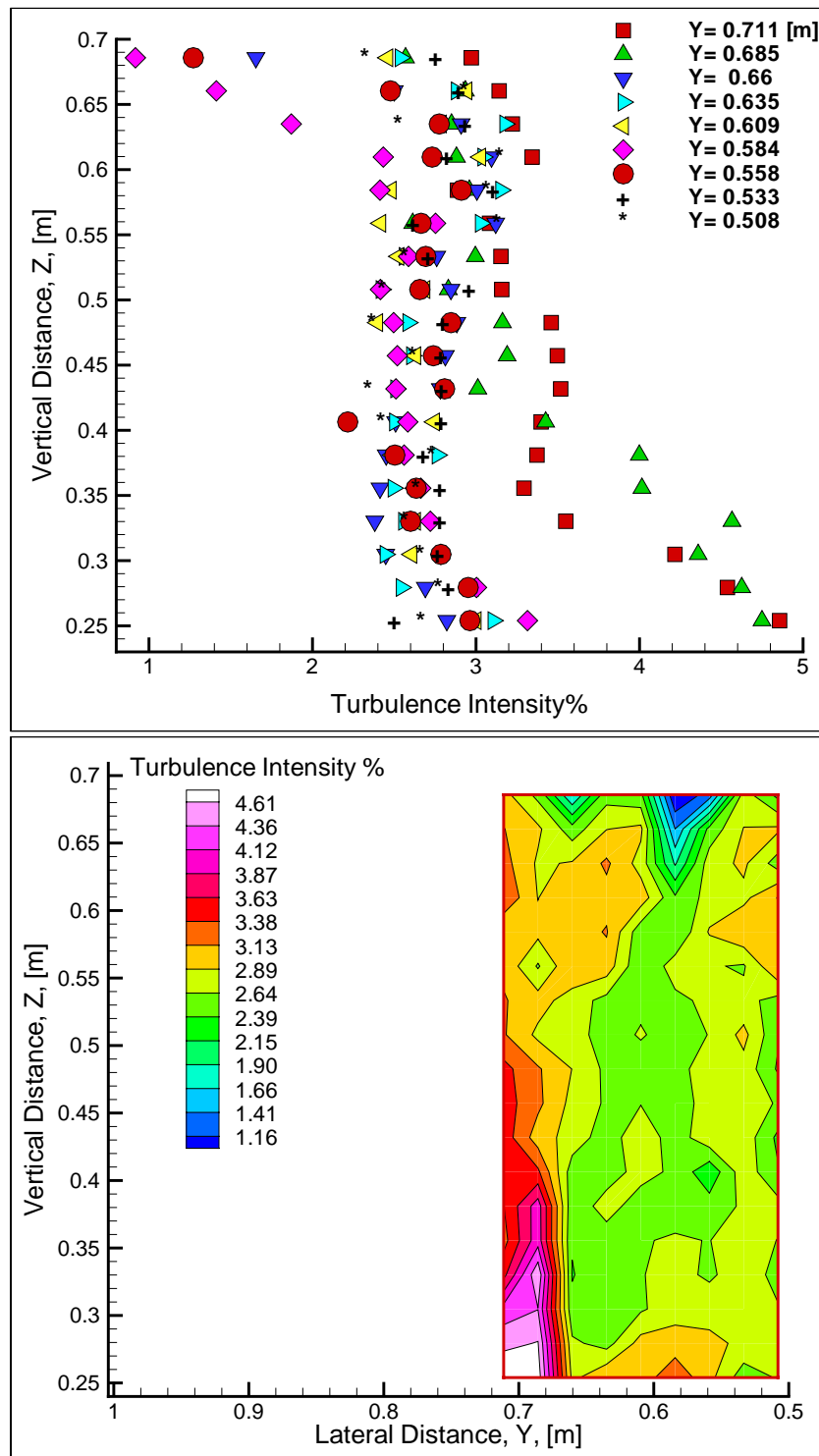


Figure A.11. Turbulence Intensity

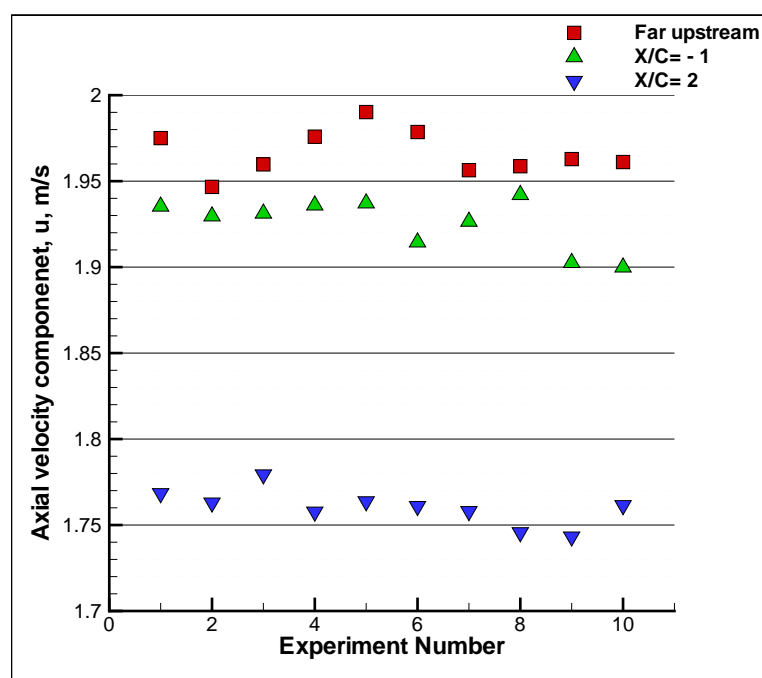


Figure A.12. Measured Axial Velocity Component, u , at Different Locations.

APPENDIX B: UNSTEADY MEASUREMENTS FOR THE BIPLANE CASE

1. First location, $X/C = -0.25$

The measured velocity, u , is presented as function of the plunge phase angle, Φ , at all vertical locations Z/C in Fig. B.1.

2. Second Location, $X/C = 0$, (leading edge)

At this location, the flow was investigated at the leading edge. The measured velocity is illustrated in Fig. B.2 as a function of the plunge phase angle, Φ .

3. Third Location, $X/C = 0.25$

The measured velocity is illustrated in Fig. B.3 as a function of the plunge phase angle, ϕ .

4. Fourth Location, $X/C = 0.5$

The measured velocity is illustrated in Fig. B.4 as a function of the plunge phase angle, ϕ .

5. Fifth Location, $X/C = 0.75$

The measured velocity is illustrated in Fig. B.5 as a function of the plunge phase angle, ϕ .

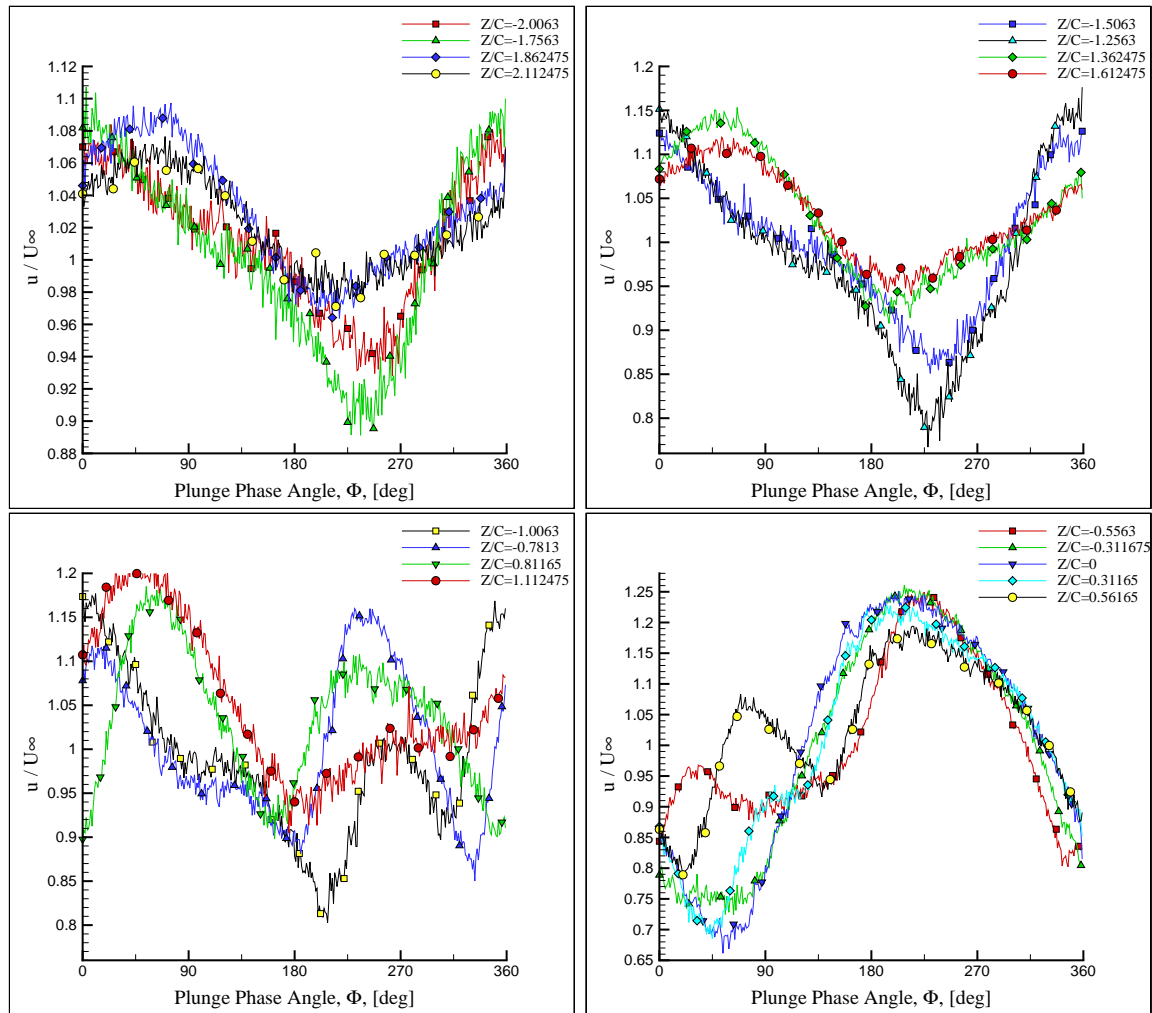


Figure B.1. Measured Axial Velocity, u , at $X/C = -0.25$

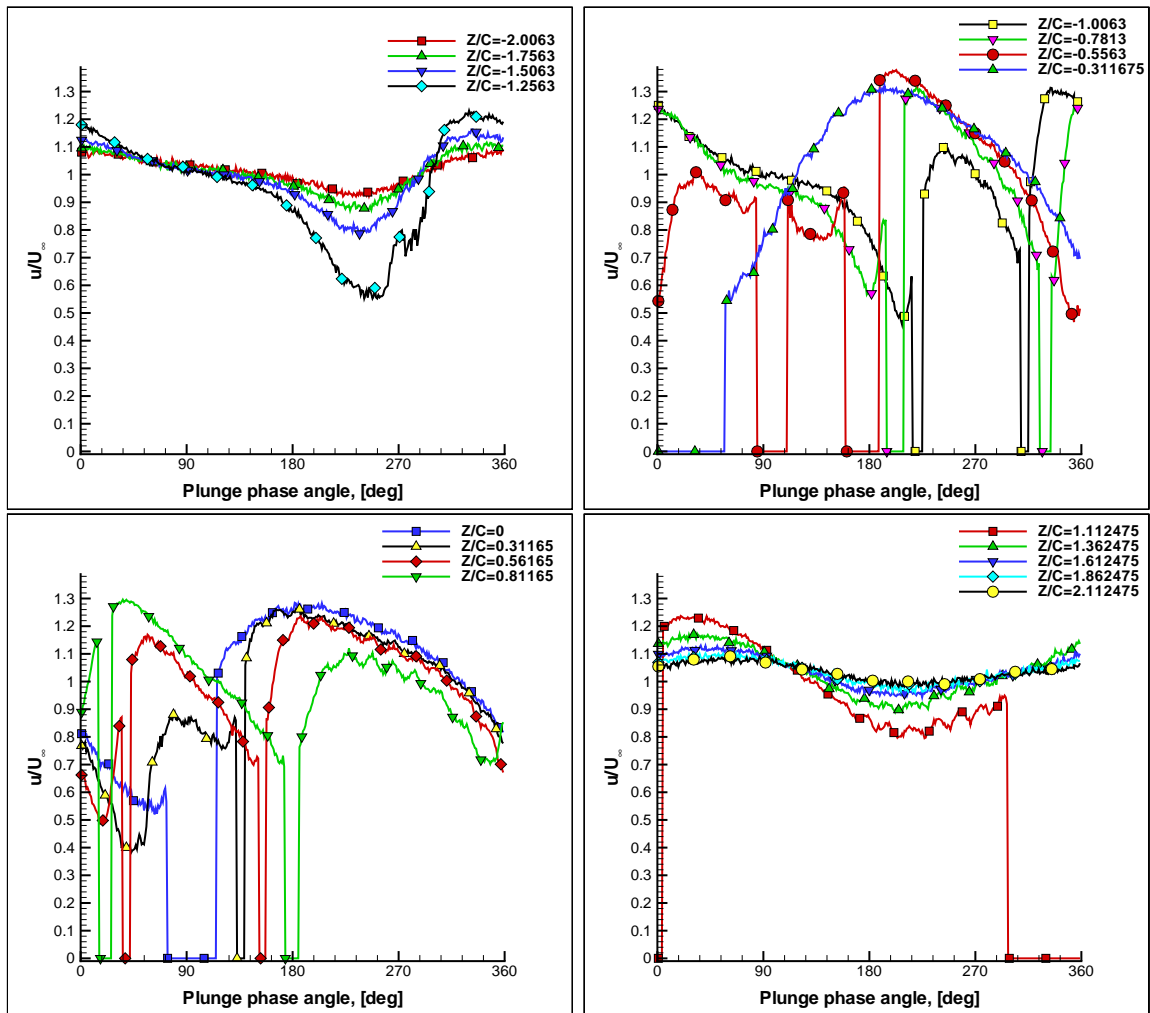


Figure B.2. Measured Axial Velocity, u , at the leading edge

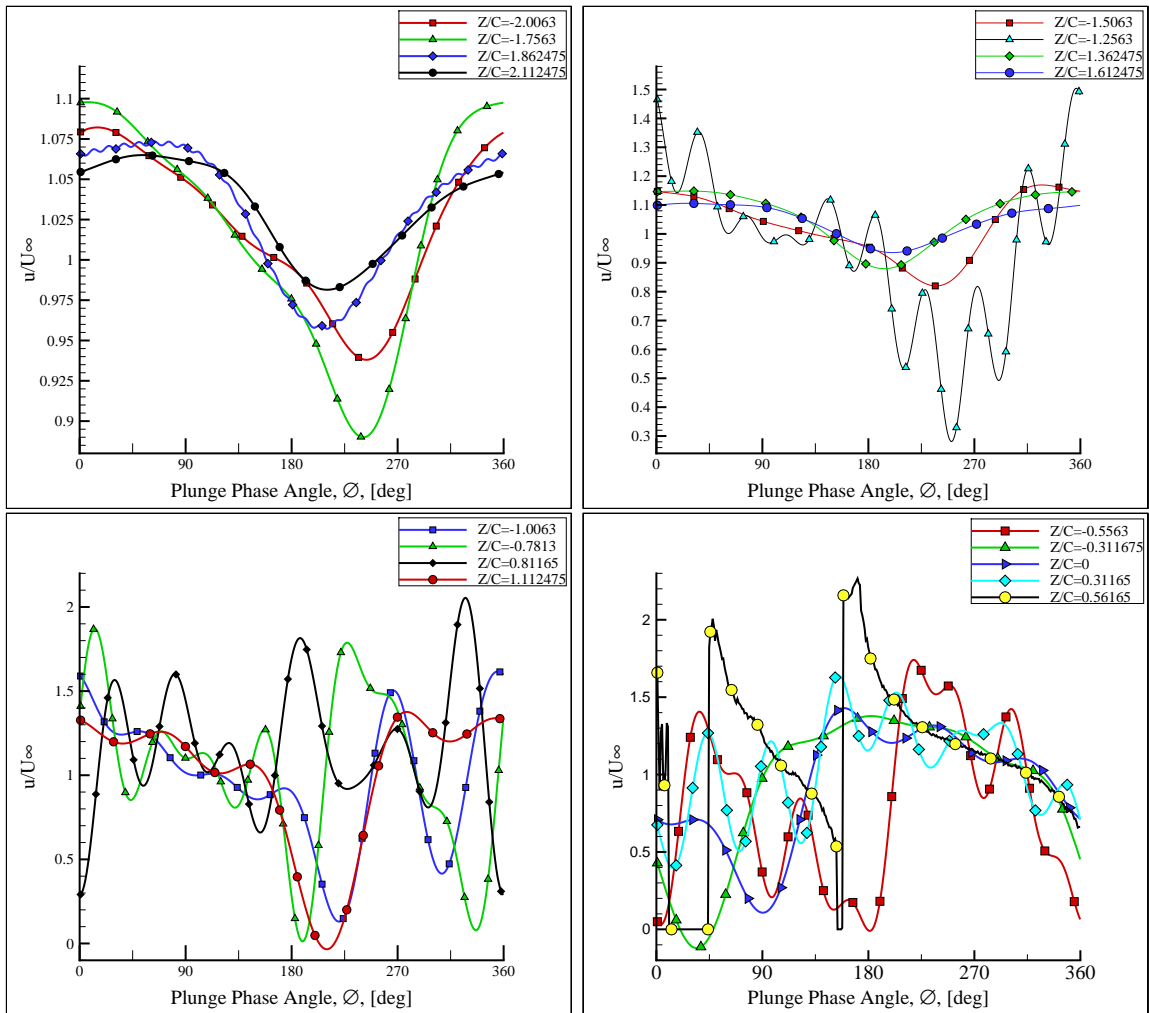


Figure B.3. Measured Axial Velocity, u , at $X/C=0.25$

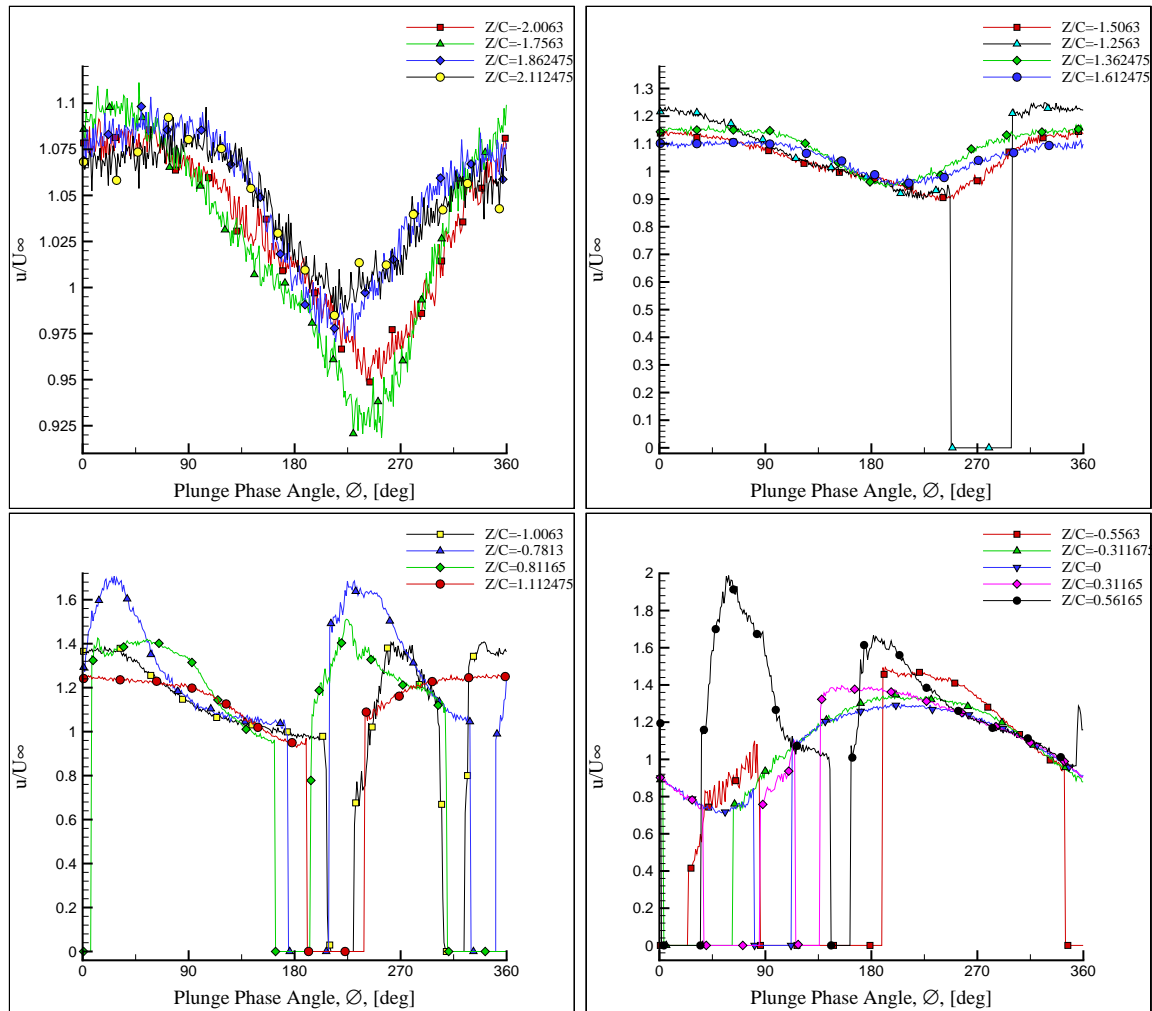


Figure B.4. Measured Axial Velocity, u , at $X/C = 0.5$

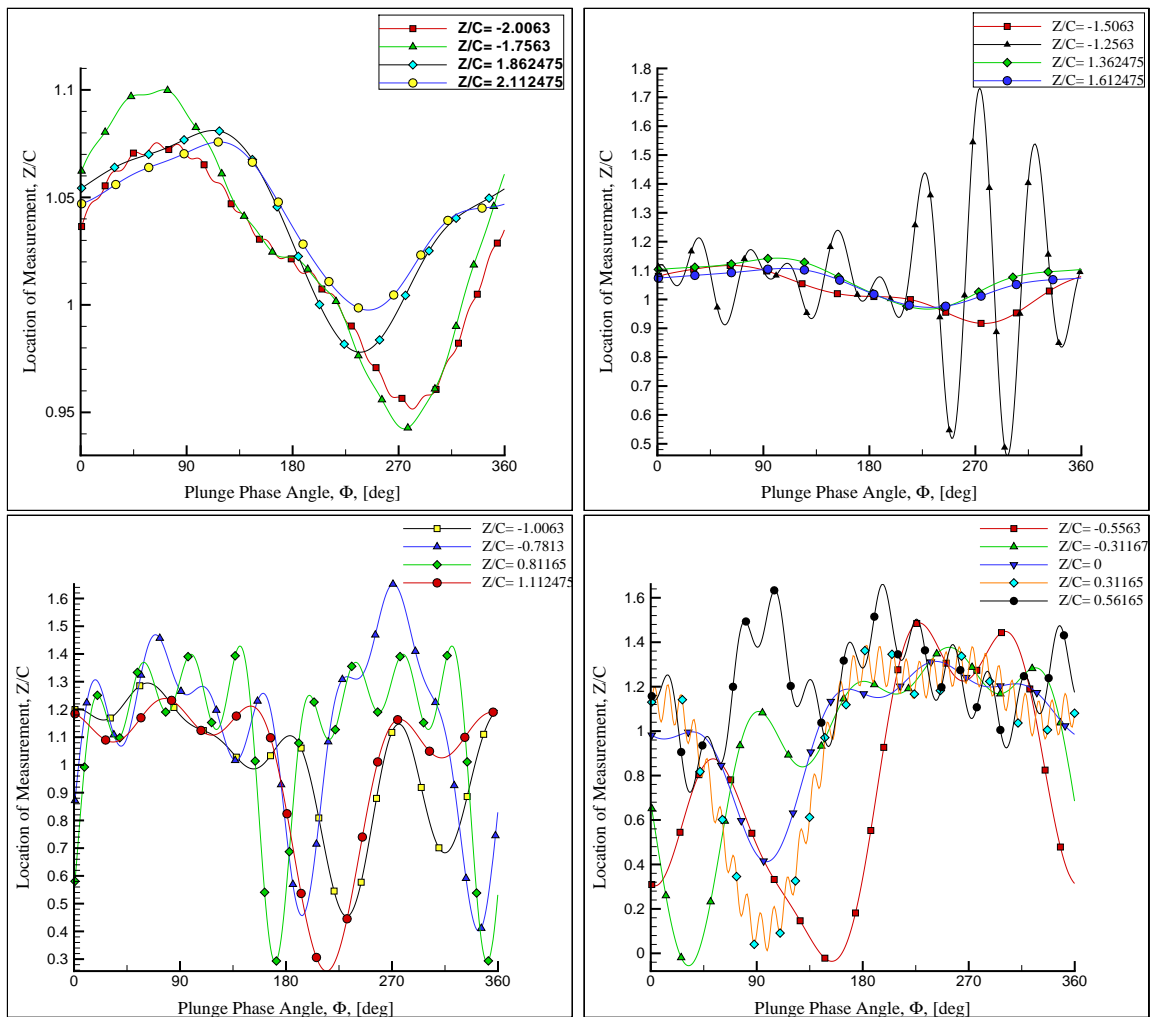


Figure B.5. Measured Axial Velocity, u , at $X/C = 0.75$

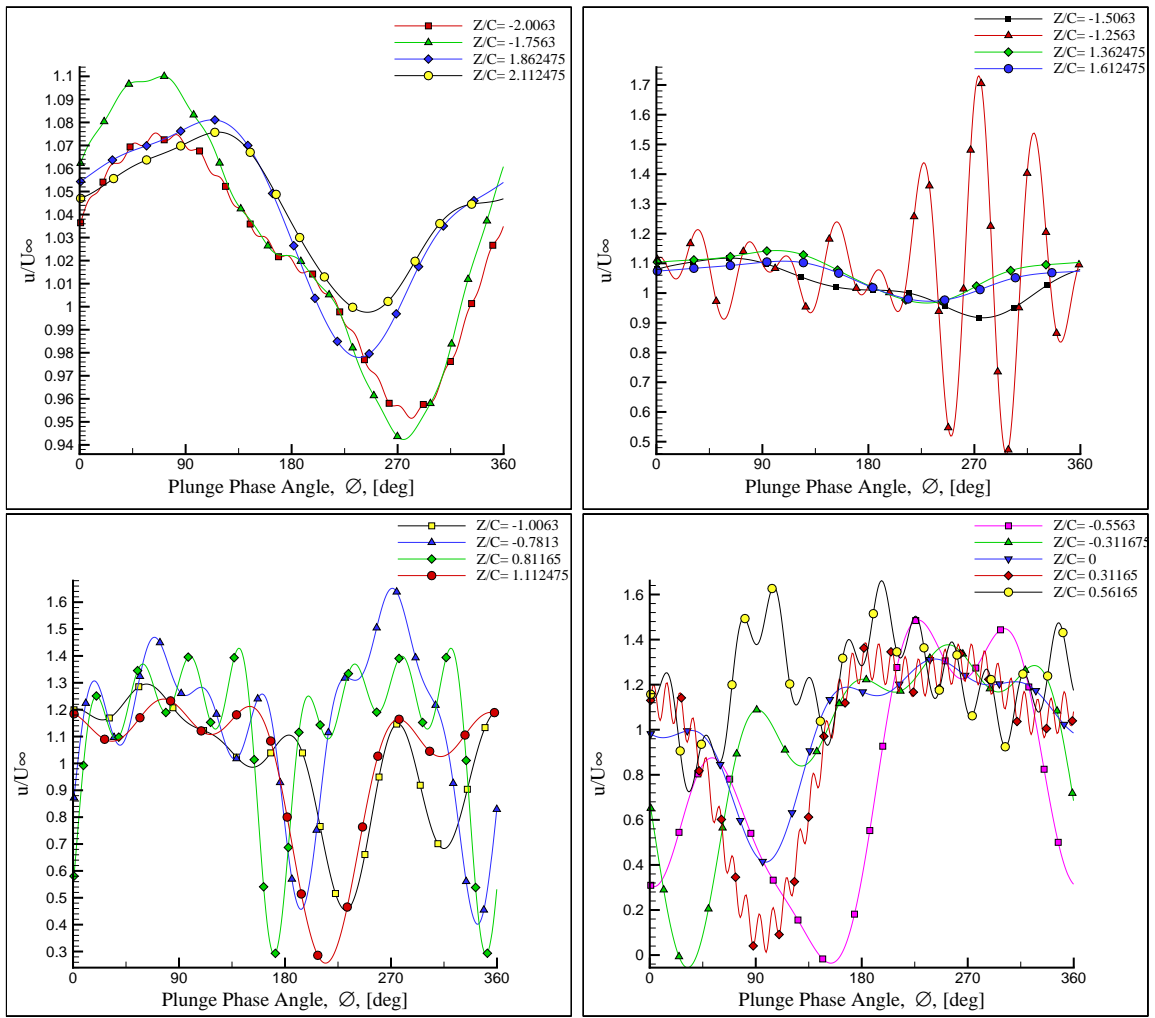


Figure B.6. Measured Axial Velocity, u , at $X/C = 1.0$

6. Sixth Location, $X/C = 1.0$, (trailing edge)

The measured velocity is illustrated in Fig. B.6 as a function of the plunge phase angle, ϕ .

7. Seventh Location, $X/C = 1.5$

The measured velocity is illustrated in Fig. B.7 as a function of the plunge phase angle, ϕ .

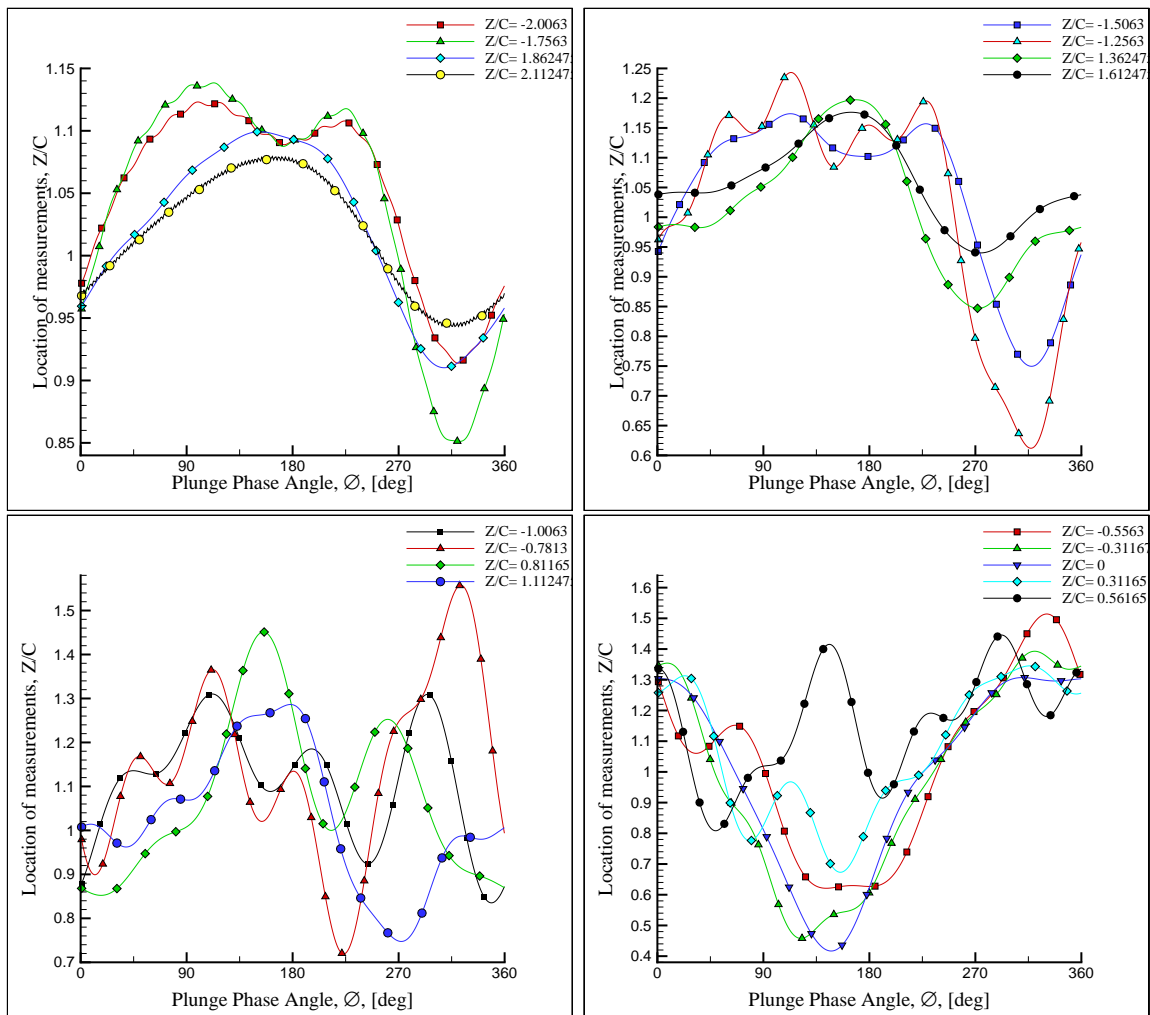


Figure B.7. Measured Axial Velocity, u , at $X/C = 1.5$

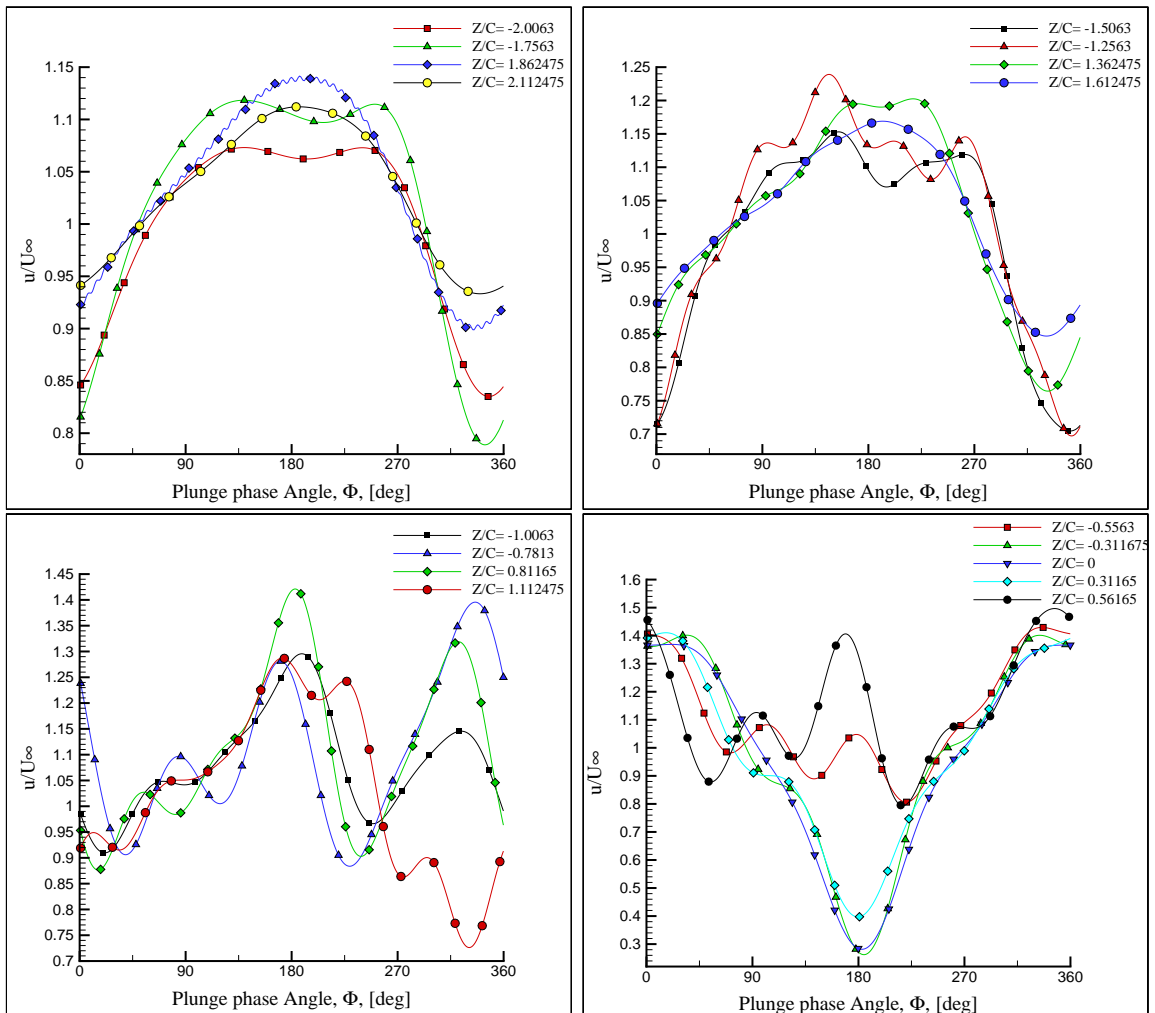


Figure B.8. Measured Axial Velocity, u , at $X/C=2.0$

8. Eighth Location, $X/C = 2.0$

The measured velocity is illustrated in Fig. B.8 as a function of the plunge phase angle, ϕ .

9. Ninth Location, $X/C = 3.0$

The measured velocity is illustrated in Fig. B.9 as a function of the plunge phase angle, ϕ .

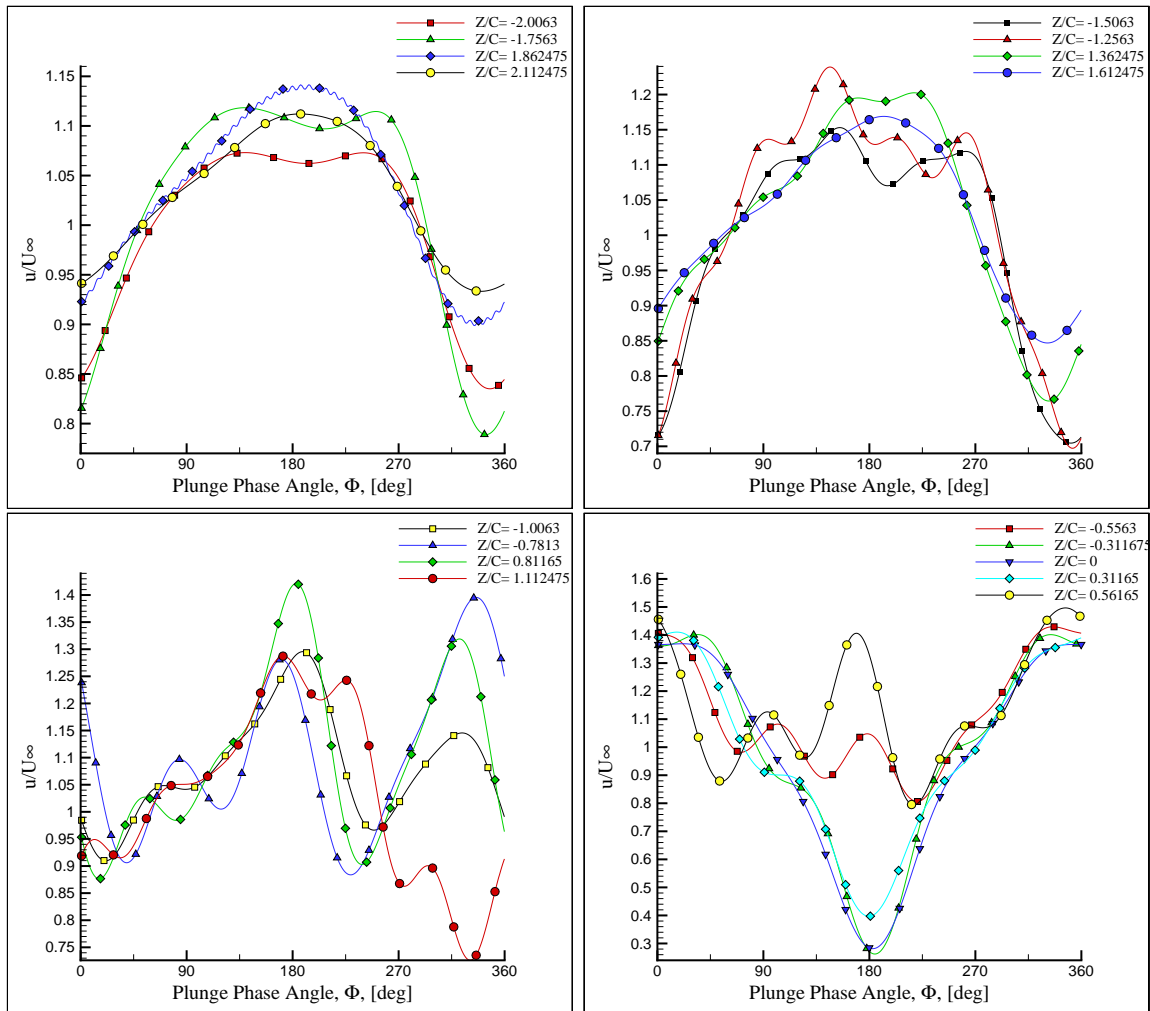


Figure B.9. Measured Axial Velocity, u , at $X/C=3.0$

**APPENDIX C: UNSTEADY MEASUREMENTS
FOR SINGLE FLAPPING WING**

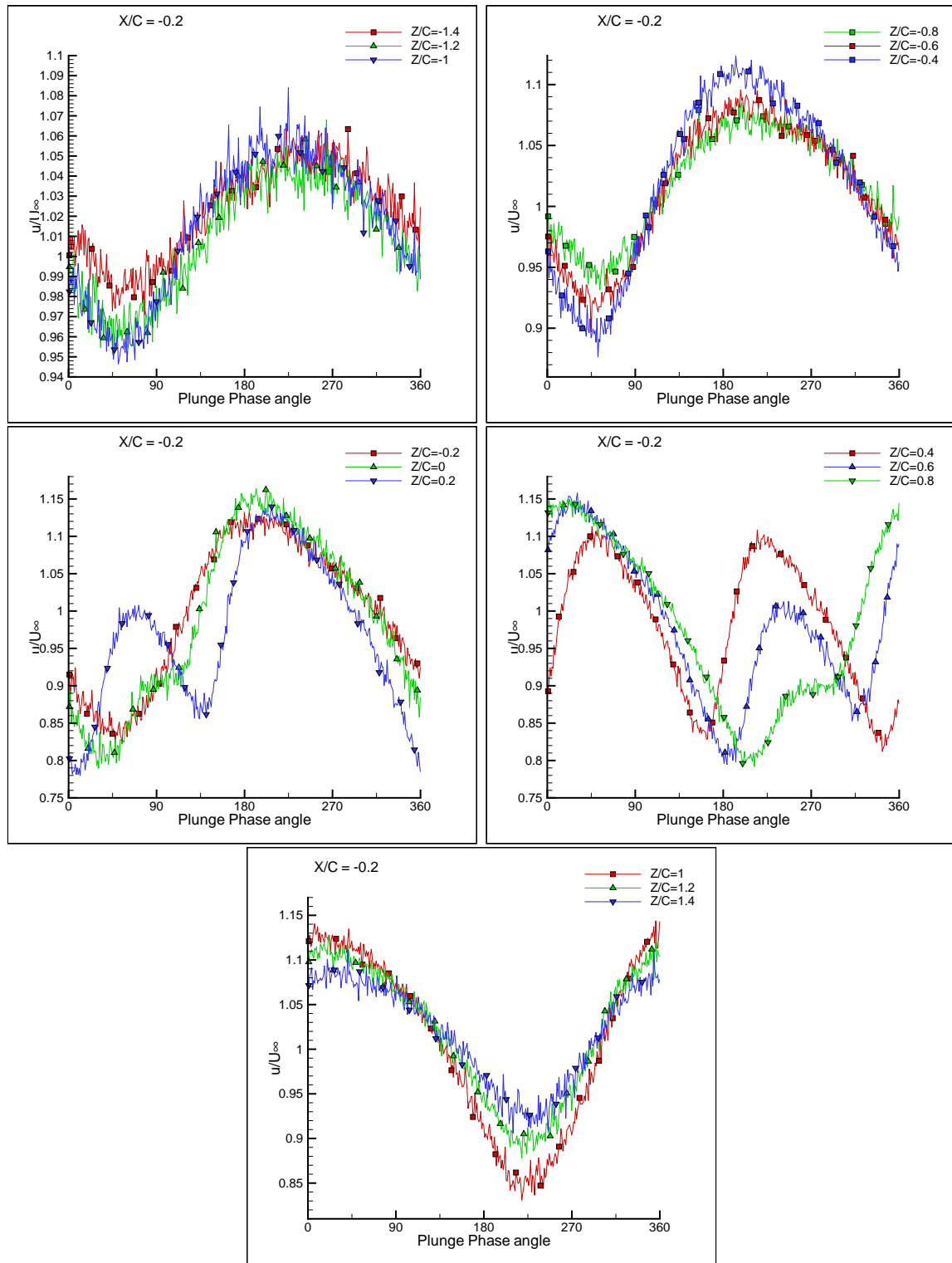


Figure C.1. Single Flapping Wing at $X/C = -0.2$, $k=1$, $u=2$ [m/s], $f=5$ [Hz], $Re=8760$

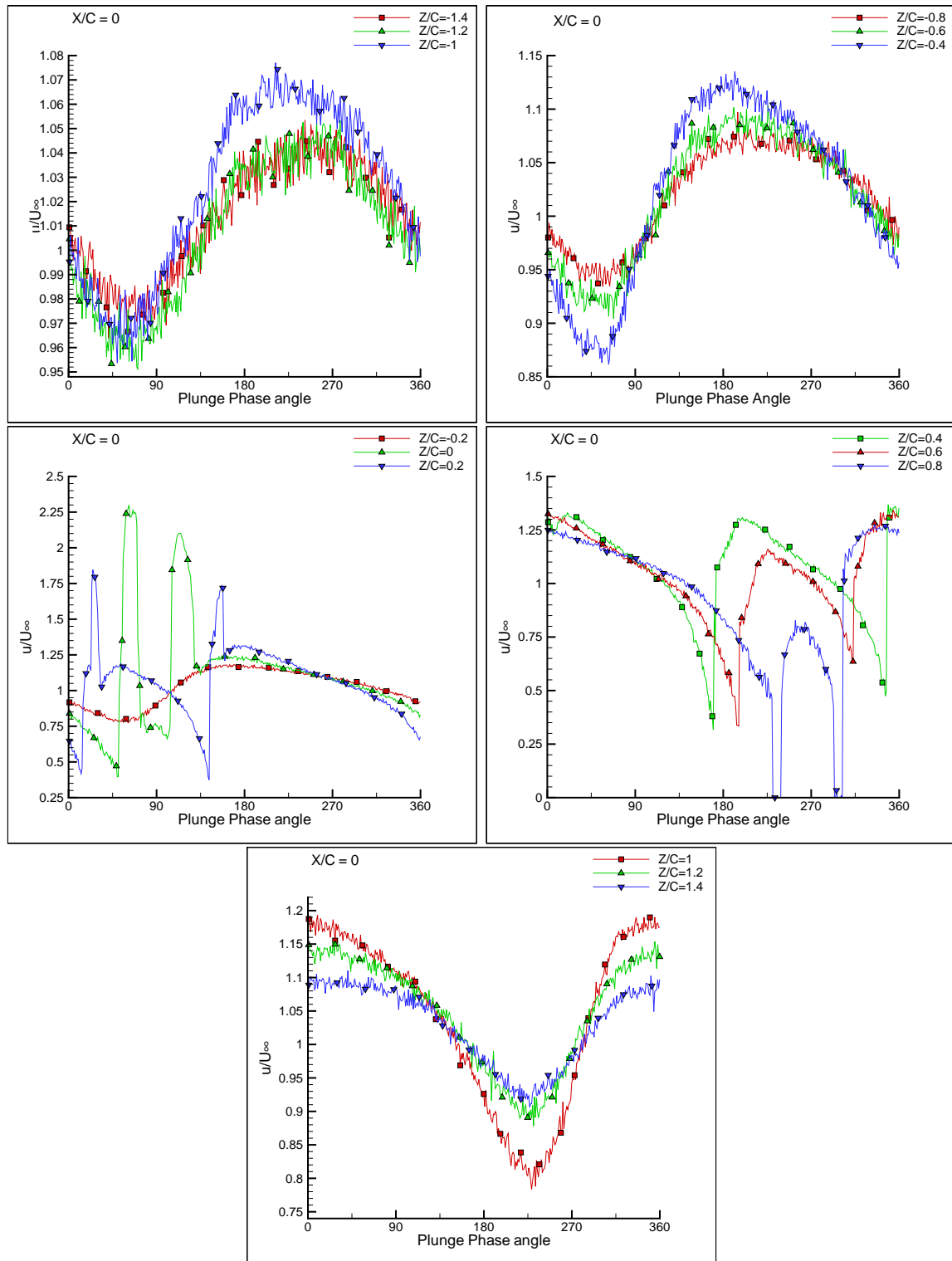


Figure C.2. Single Flapping Wing at $X/C=0$, $k=1$, $u=2[\text{m/s}]$, $f=5[\text{Hz}]$, $\text{Re}=8760$

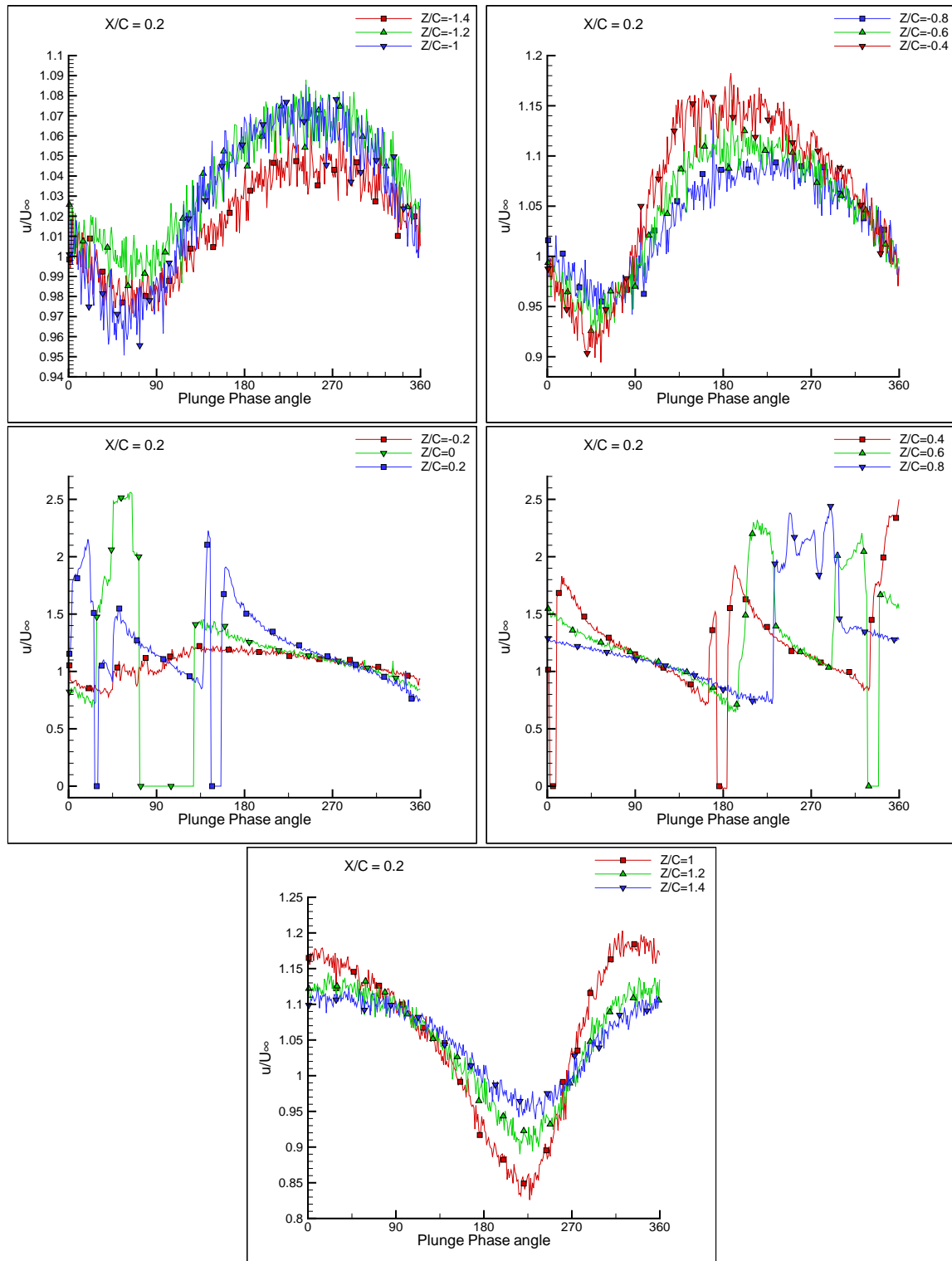


Figure C.3. Single Flapping Wing at $X/C=0.2$, $k=1$, $u=2$ [m/s], $f=5$ [Hz], $Re=8760$

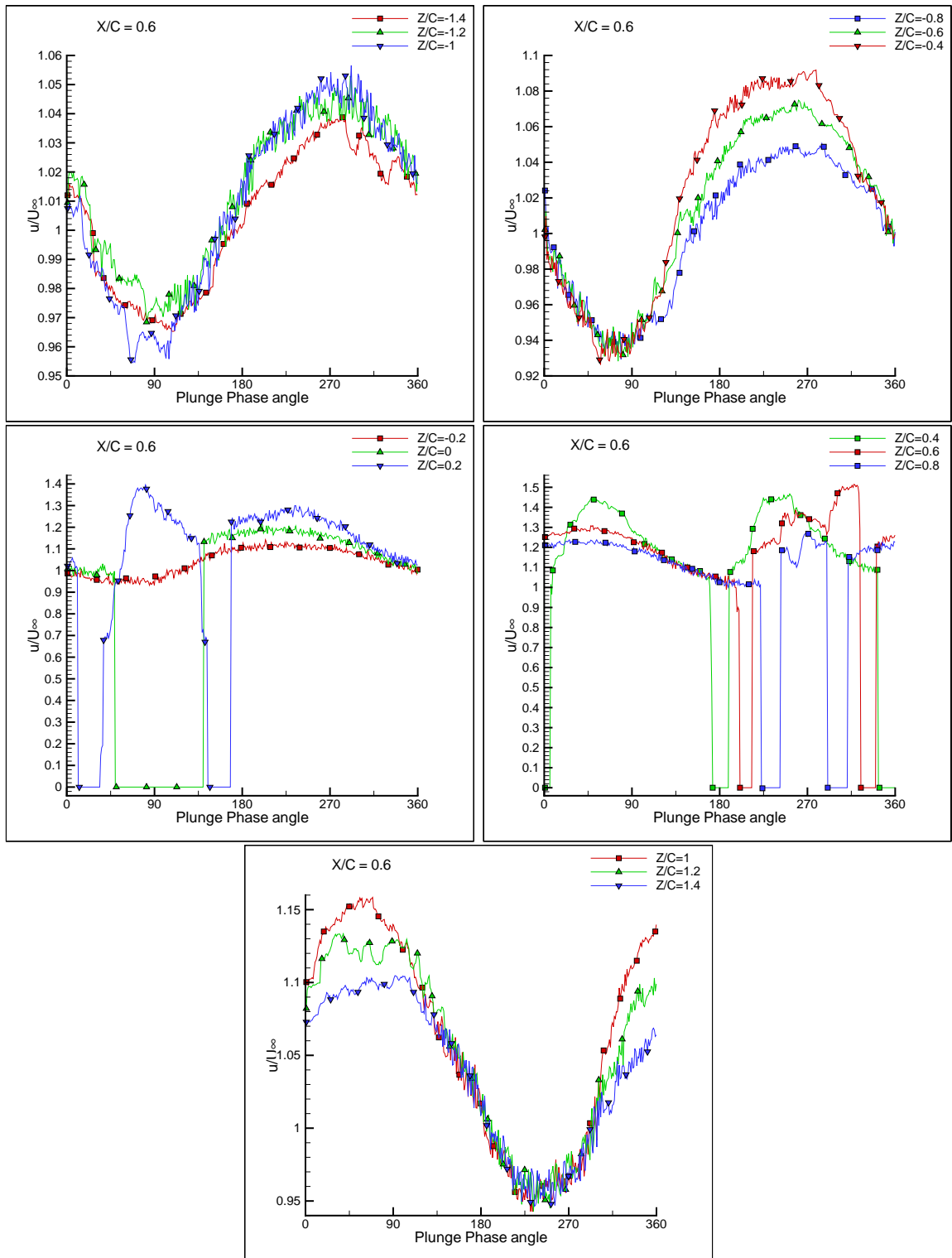


Figure C.4. Single Flapping Wing at $X/C=0.6$, $k=1$, $u=2$ [m/s], $f=5$ [Hz], $Re=8760$

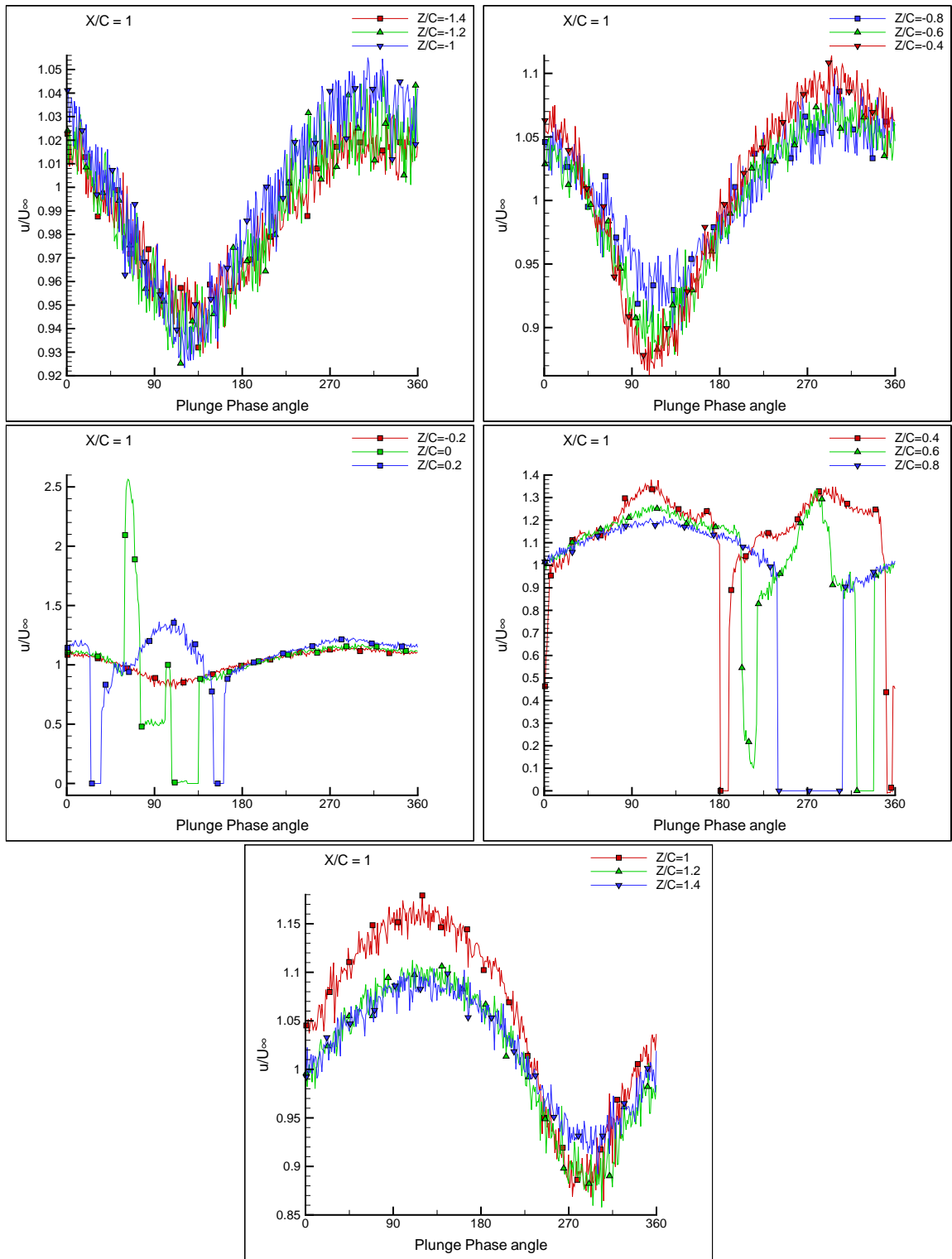


Figure C.5. Single Flapping Wing at $X/C=1.0$, $k=1$, $u=2$ [m/s], $f=5$ [Hz], $Re=8760$

**APPENDIX D: UNSTEADY MEASUREMENTS
FOR THE FLAPPING WING IN PRESENCE
OF GROUND PLANE**

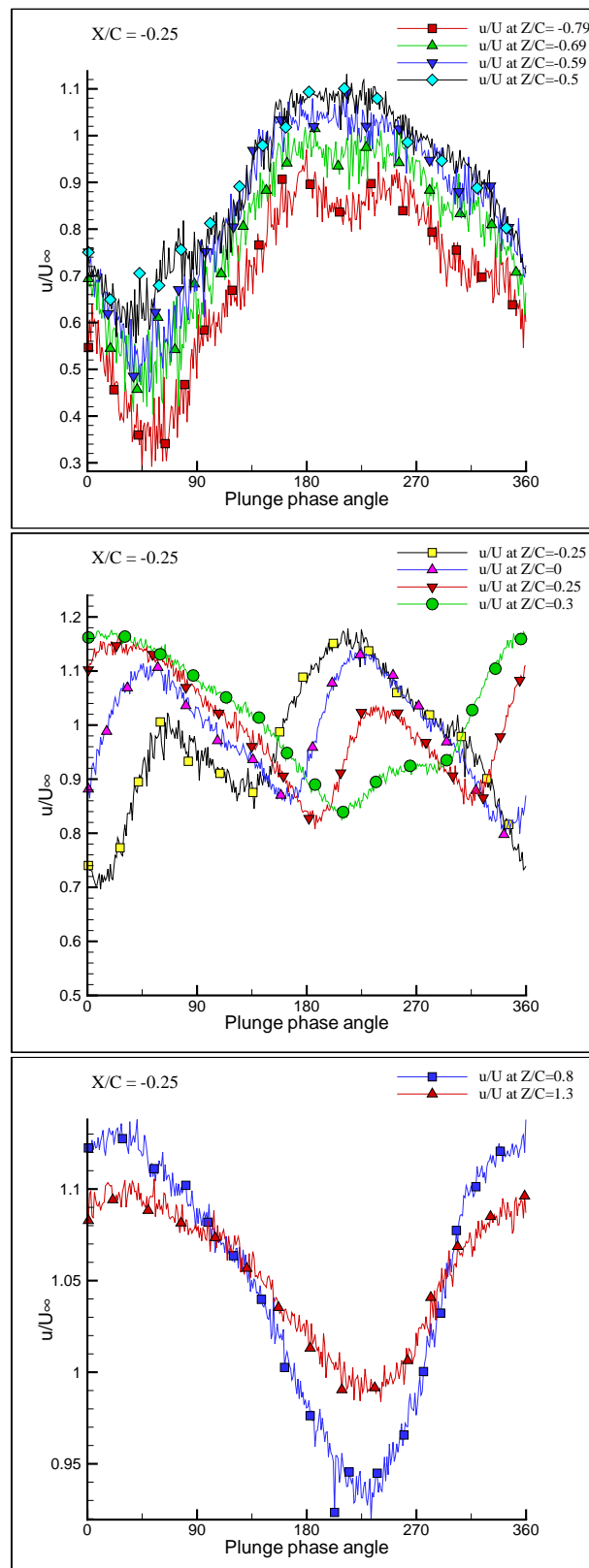


Figure D.1. Flapping Wing in Ground Effect at $X/C = -0.25$

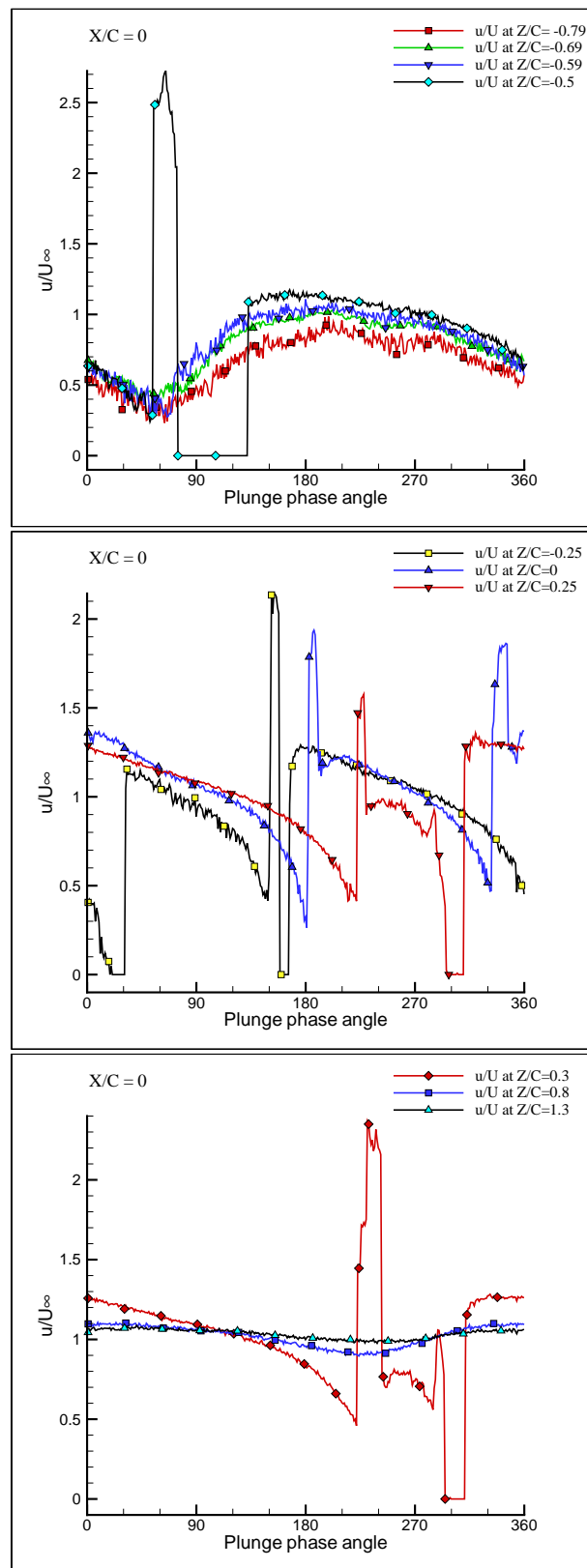


Figure D.2. Flapping Wing in Ground Effect at $X/C=0$

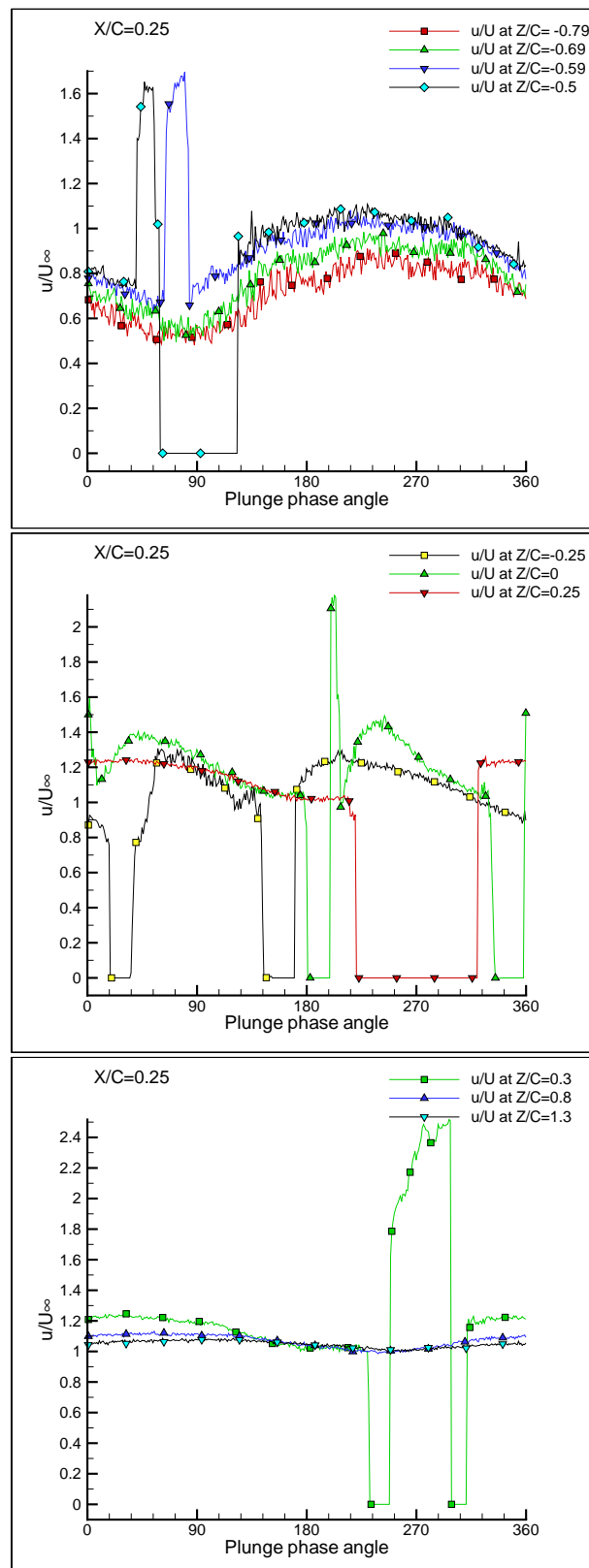


Figure D.3. Flapping Wing in Ground Effect at $X/C=0.25$

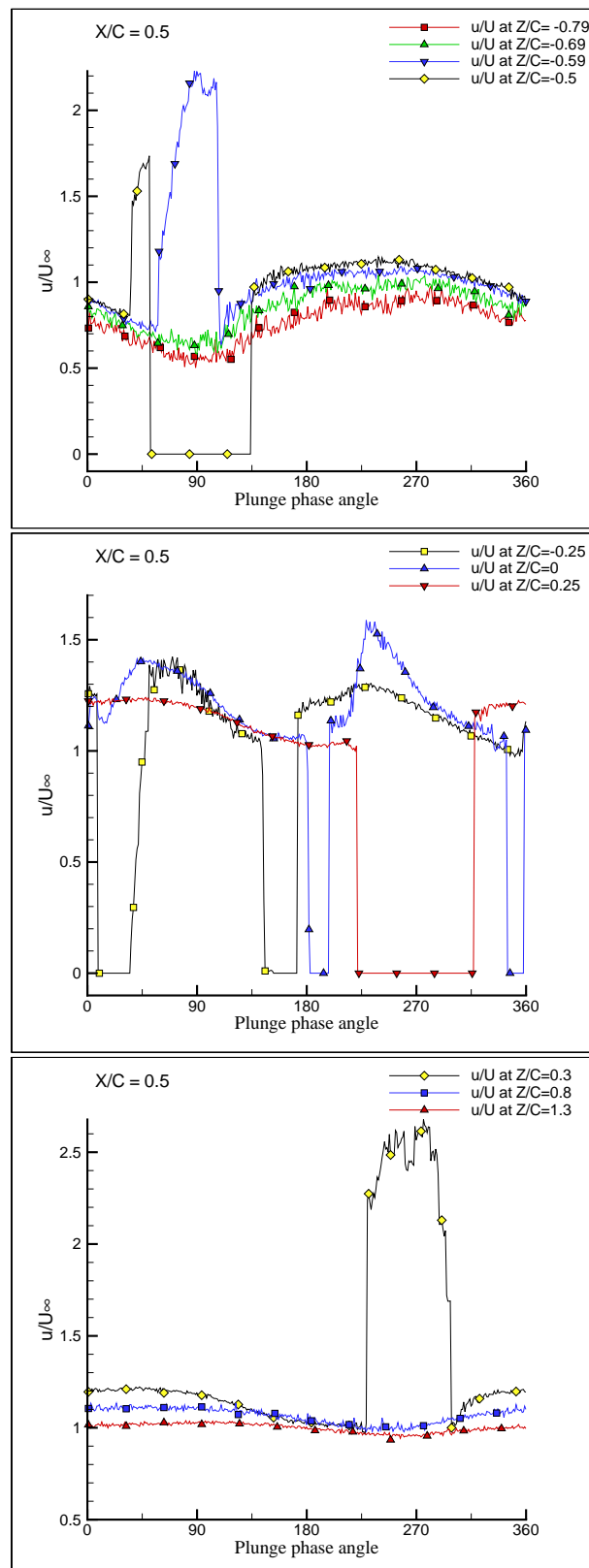


Figure D.4. Flapping Wing in Ground Effect at $X/C=0.5$

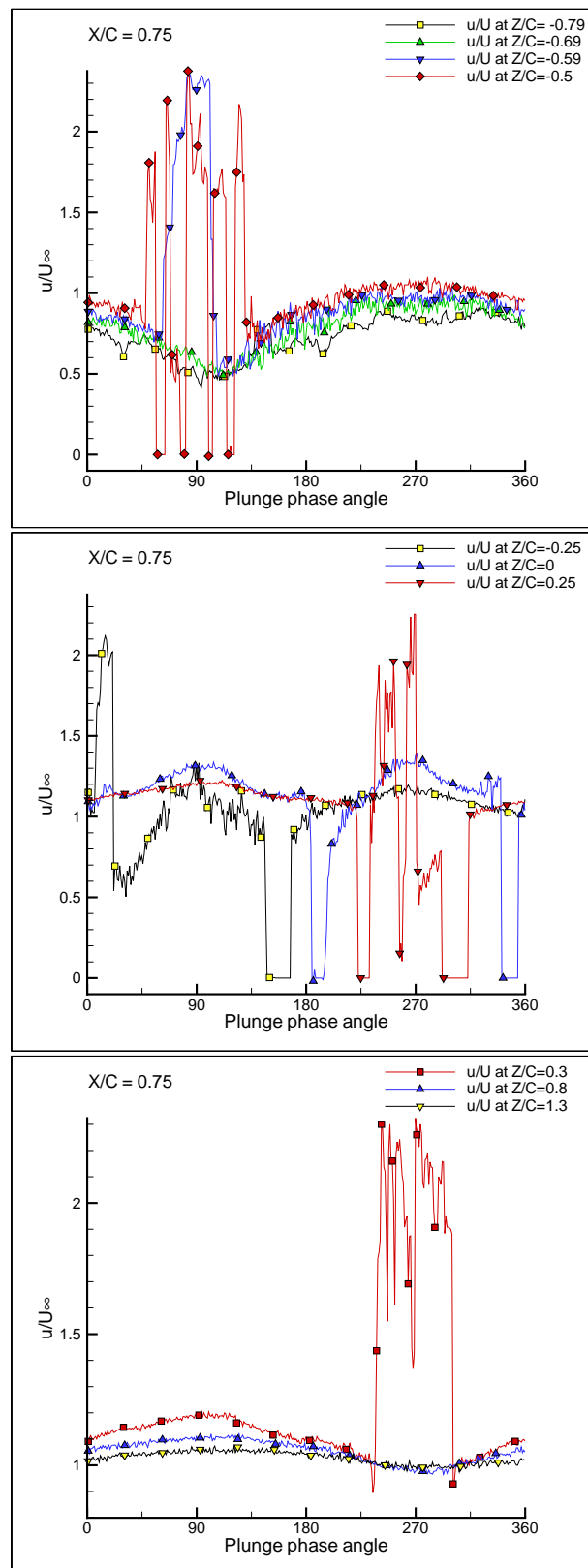


Figure D.5. Flapping Wing in Ground Effect at $X/C=0.75$

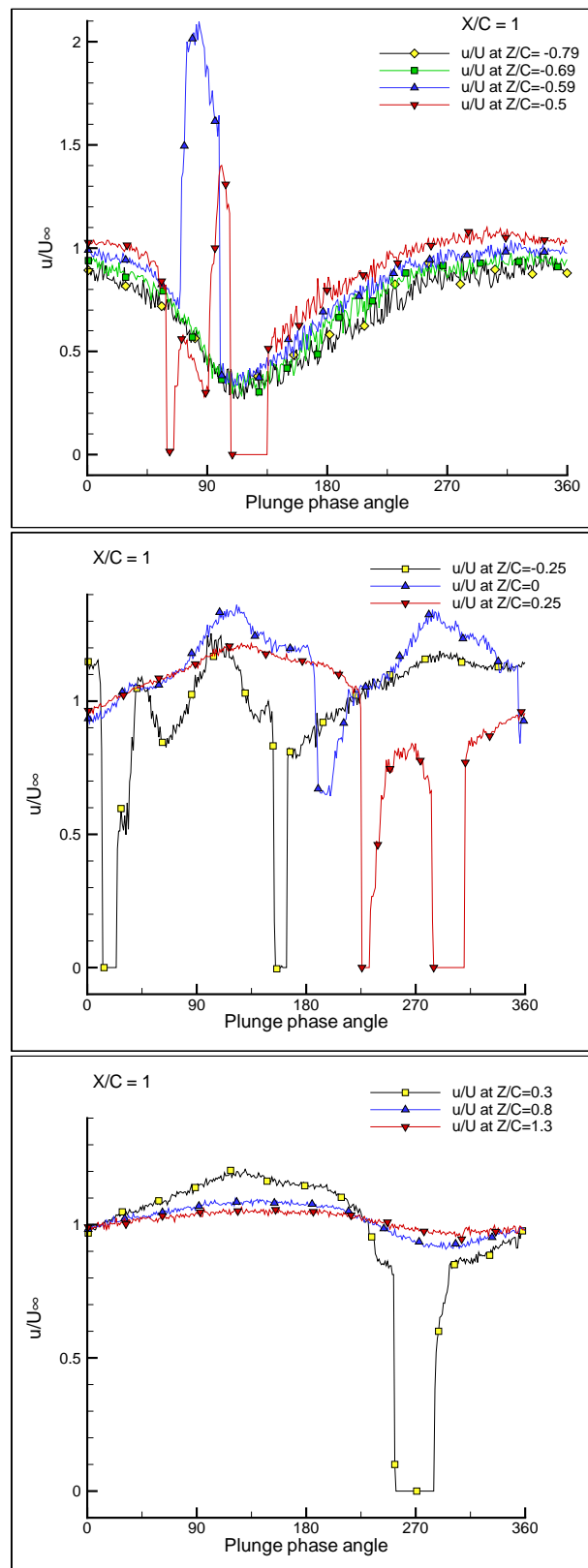


Figure D.6. Flapping Wing in Ground Effect at $X/C=1.0$

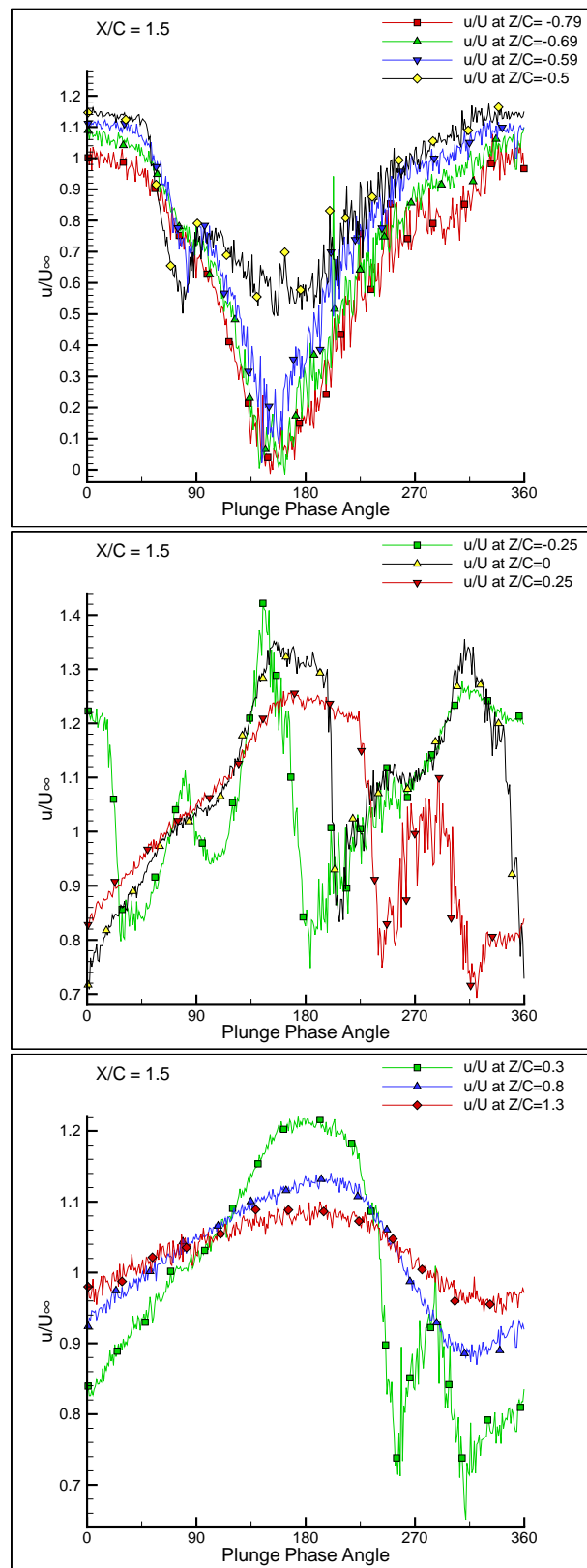


Figure D.7. Flapping Wing in Ground Effect at $X/C=1.5$

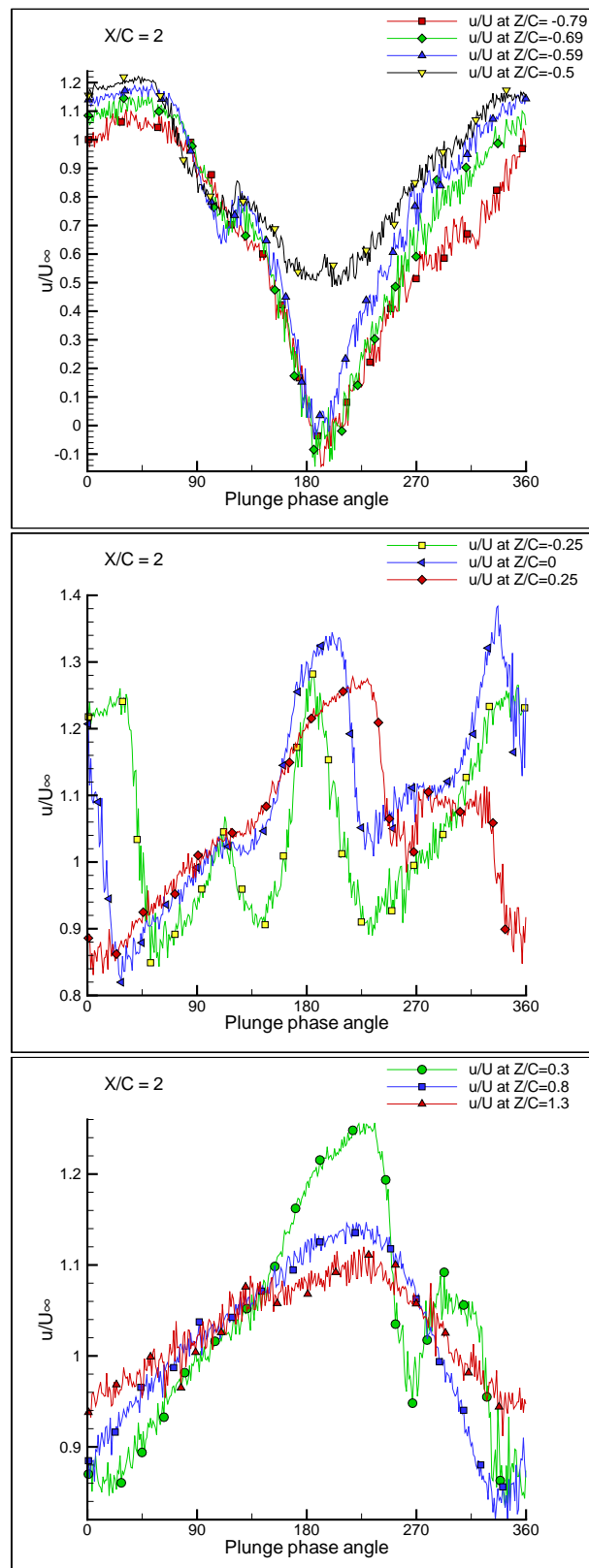


Figure D.8. Flapping Wing in Ground Effect at $X/C=2$

THIS PAGE INTENTIONALLY LEFT BLANK

LIST OF REFERENCES

- [1] J.M. Anderson, K. Streitlien, D.S. Barrett, and M.S. Triantafyllou. Oscillating foils of high propulsive efficiency. *Journal of Fluid Mechanics*, 360:41–72, April 1998.
- [2] A. Betz. Ein beitrag zur erklarung des segelfluges. *Zeitschrift fur Flugtechnik und Motorluftschiffahrt*, 3:269–272, 1912.
- [3] W. Birnbaum. Das ebene problem des schlagenden fluels. *Zeitschrift fur Angewandte Mathematik und Mechanik*, 4(4):277–292, Aug 1924.
- [4] L.W. Carr and M.S. Chandrasekhara. Compressibility effects on dynamic stall. *Progress in Aerospace Sciences*, 32(6):523–573, 1996.
- [5] B. M. Castro. *Multi-Block Parallel Navier-Stockes Simulation of Unsteady Wind Tunnel and Ground Interference Effects*. PhD thesis, Naval Postgraduate School, September 2001.
- [6] J.D. DeLaurier and J.M. Harris. Experimental study of oscillating-wing propulsion. *Journal of Aircraft*, 19(5):368–373, May 1982.
- [7] J.A. Ekaterinaris and M.F. Platzer. Computational prediction of airfoil dynamic stall. *Progress in Aerospace Sciences*, 33(11/12):759–846, 1997.
- [8] I. E. Garrick. Propulsion of a Flapping and Oscillating Airfoil. Technical Report 567, NACA, 1936.
- [9] J.P. Giesing. Nonlinear two-dimensional unsteady potential flow with lift. *Journal of Aircraft*, 5:135–143, 1968.

- [10] J.L. Hess and A.M.O. Smith. Calculation of potential flow about arbitrary bodies. *Progress in Aeronautical Sciences*, 8:1–138, 1966.
- [11] K. Isogai, Y. Shinmoto, and Y. Watanabe. Effects of dynamic stall on propulsive efficiency and thrust of flapping airfoil. *AIAA*, 37(10):1145–1151, 1999.
- [12] K.D. Jones, C.M. Dohring, and M.F. Platzer. Experimental and computational investigation of the knoller-betz effect. *AIAA*, 36(7):1240–1246, 1998.
- [13] K.D. Jones and M.F. Platzer. An experimental and numerical investigation of flapping-wing propulsion. AIAA Paper No. 99-0995, Reno, Nevada, January 1999.
- [14] K.D. Jones and M.F. Platzer. Numerical computation of flapping-wing propulsion and power extraction. (97-0826), Jan 1997. AIAA paper.
- [15] R. Katzmayr. Effect of Periodic Changes of Angles of Attack on Behavior of Airfoils. Technical Report 147, NACA Report, October 1922. translated from **Zeitschrift für Flugtechnik und Motorluftschiffahrt**, March 31, pp. 80–82, and April 13, 1922, pp. 95–101.
- [16] M.F. Platzer K.D. Jones, T.G. Lund. Experimental And Computational Investigation Of Flapping Wing Propulsion For Micro-Air Vehicles. *Symposium of Low-Reynolds Number Vehicles, University of Notre Dame, Indiana*, 2000.
- [17] R. Knoller. Die gesetze des luftwiderstandes. *Flug-und Motortechnik Wien*, 3(21):1–7, 1909.
- [18] J.C.S. Lai and M.F. Platzer. Jet characteristics of a plunging airfoil. *AIAA*, 37(12):1529–1537, 1999.

- [19] C.E. Lan. The Unsteady Quasi-Vortex-Lattice Method with Applications to Animal Propulsion. *Journal of Fluid Mechanics*, 93:747–765, 1979.
- [20] P. Liu. *A Time-Domain Panel Method for Oscillating Propulsors with Both Chordwise and Spanwise Flexibility*. PhD thesis, University of Newfoundland, 1996.
- [21] T. C. Lund. Experimental and computational investigation of flapping-wing propulsion for micro-air vehicles. Master's thesis, Naval Postgraduate School, 2000.
- [22] M.F. Platzer, K.S. Neace, and C.K. Pang. Aerodynamic analysis of flapping wing propulsion. *AIAA paper*, pages 93–0484, Jan 1993.
- [23] A. Pope. *Wind Tunnel Testing*. John Wiley & Sons, Inc., New York, second eddition edition, 1954.
- [24] R. Ramamurti and W. Sandberg. Simulation of flow about flapping airfoils using finite element incompressible flow solver. *AIAA Journal*, 39(2):253–260, 2001.
- [25] W. Schmidt. Der wellpropeller, ein neuer antrieb fuer wasser-land, und luftfahrzeuge. *Zeitschrift fur Flugwiss*, 13:472–479, 1965.
- [26] N.H. Teng. The development of a computer code for the numerical solution of unsteady, inviscid and incompressible flow over an airfoil. Master's thesis, U.S. Naval Postgraduate School, Dept. of Aeronautics and Astronautics, U.S. Naval Postgraduate School, Monterey, CA, June 1987.
- [27] T. Theodorsen. General theory of aerodynamic instability and the mechanism of flutter. Technical Report 496, NACA, 1935.
- [28] I.H. Tuncer and M.F. Platzer. Computational study of flapping airfoil aerodynamics. *Journal of aircraft*, 37(3):514–520, June 2000.

- [29] I.H. Tuncer, R. Walz, and M.F. Platzer. A computational study on the dynamic stall of a flapping airfoil. *AIAA paper*, June, 15-18 1998. AIAA paper 98-2519, 16th Applied Aerodynamics Conference, Albuquerque, New Mexico.
- [30] Ismaiel H. Tuncer and M.F. Platzer. Thrust generation due to airfoil flapping. *AIAA Journal*, 34(2):324–331, 1996.

INITIAL DISTRIBUTION LIST

1. Defense Technical Information Center	2
8725 John J. Kingman Rd., STE 0944	
Ft. Belvoir, Virginia 22060-6218	
2. Dudley Knox Library	2
Naval Postgraduate School	
411 Dyer Rd.	
Monterey, California 93943-5101	
3. Maj. Osama Kamal Mahmoud	7
2 Aly Bahgat St., Hadaique El Qouba,11331,	
Cairo, EGYPT	
4. Prof. Max F. Platzer	4
AA Department - Naval Postgraduate School	
411 Dyer Rd.	
Monterey, California 93943-5101	